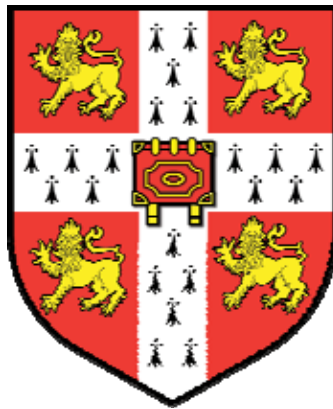


# **IN-SITU PHOTOCATALYTIC REMEDIATION OF ORGANIC CONTAMINANTS IN GROUNDWATER**



*A dissertation submitted for the degree of Doctor of Philosophy in the Department of  
Engineering at the University of Cambridge, UK*

by

**Leonard Lim Lik Pueh**

Clare Hall

May 2010

*Especially dedicated to  
my parents Lim Sze Meng and Foo Eng Hua  
and my brother Dr Lim Lik Thai  
for their love, care, patience, encouragement and support.*

# DECLARATION

I hereby declare that, except where reference is made to the work of others, the contents of this dissertation are a result of my own work and include nothing which is the outcome of work done in collaboration. This dissertation has not been submitted in whole or part for consideration for any other degree, diploma or other qualification to this University or any other institution, except where cited specifically.

This dissertation contains no more than 65,000 words, inclusive of appendices, references, footnotes, tables and equations, and has less than 150 figures.



-----  
Leonard Lim Lik Pueh

May 2010

## Abstract

This research is about the development of a photocatalytic reactor design, Honeycomb, for in-situ groundwater remediation. Photocatalysis, typically a pseudo first order advanced oxidation process, is initiated via the illumination of UVA light on the catalyst, i.e. titanium dioxide ( $\text{TiO}_2$ ). In the presence of oxygen, highly reactive oxidising agents are generated such as superoxide ( $\text{O}_2^-$ ), hydroxyl ( $\text{OH}^\cdot$ ) radicals, and holes ( $h_{\text{vb}}^+$ ) on the catalyst surface which can oxidise a wide range of organic compounds. The target contaminant is methyl tert butyl ether (MTBE), a popular gasoline additive in the past three decades, which gives the water an unpleasant taste and odour at  $20 \mu\text{g L}^{-1}$ , making it undrinkable. This research consists of three major parts, i.e. (i) establishing a suitable catalyst immobilisation procedure, (ii) characterisation and evaluation of reactor models and (iii) scale up studies in a sand tank.

$\text{TiO}_2$  does not attach well onto many surfaces. Therefore, the first step was to determine a suitable immobilisation procedure by preparing  $\text{TiO}_2$  films using several potential procedures and testing them under the same conditions, at small scale. The coatings were evaluated in terms of photocatalytic activity and adhesion. The photocatalytic activity of the coatings was tested using methylene blue dye (MB), which is a photocatalytic indicator. A hybrid coating, which comprises a sol gel solution enriched with Aeroxide  $\text{TiO}_2$  P25 powder, on woven fibreglass exhibited the best adhesion and photocatalytic activity among samples evaluated. Thus, it was used to produce immobilised catalyst for this research. Consequently, the immobilisation procedure was scaled up to synthesize  $\text{TiO}_2$  coatings for the potential photocatalytic reactor design. The photocatalytic activity of the coatings produced from the scaled up immobilisation procedure were reasonably comparable to that produced at small scale.

Due to the UVA irradiation and mass transfer limitations, photocatalytic reactors are typically compact in order to maximise their efficiency to accommodate high flows, particularly in water and wastewater treatment. In the case of groundwater, however, the treatment area can span up to meters in width and depth. Groundwater flow is significantly lower than that of water treatment, as the reactor design does not need to be compact. Considering both factors, a photocatalytic reactor design of hexagonal cross-section (Honeycomb) was proposed, in which the structures can be arranged adjacent to each other forming a honeycomb. A model was constructed and tested in a 4 L column (cylindrical) reactor, using the MB test to characterise the reactor performance and operating conditions. This was followed by a hydraulic performance study, which encompasses single and double pass flow

studies. The single pass flow study involves the photocatalytic oxidation (PCO) of MB and MTBE, while the double pass flow study was focused on the PCO of MTBE only. The double pass can simulate two serially connected reactors. Single pass flow studies found that the critical hydraulic residence time (HRT) for the PCO of MB and MTBE is approximately 1 day, achieving up to 84 % MTBE removal. Critical HRT refers to the minimum average duration for a batch of contaminant remaining in the reactor in order to maintain the potential efficiency of the reactor. Double pass studies showed the reactor can achieve up to 95 % MTBE removal in 48 hours, and that reactor performance in the field of serially connected reactors can be estimated by sequential order of single pass removal efficiency. In groundwater, there are likely to be other impurities present and the effects of groundwater constituents on the reactor efficiency were studied. The MTBE PCO rate is affected by the presence of organic compounds and dissolved ions mainly due to the competition for hydroxyl radicals and the deactivation of catalyst surface via adsorption of the more strongly adsorbed organic molecules and ions. Despite the presence of organic compounds and dissolved ions, the reactor achieved about 80 % MTBE removal in 48 hours. A double pass flow study showed that the overall efficiency of the photocatalytic reactor in the field can be estimated via sequential order of its efficiency in a single pass flow study using the actual groundwater sample in the laboratory.

A sand tank was designed for the simulation of the clean up of an MTBE plume from a point source leakage using the 200 mm i.d. Honeycomb I prototype. Honeycomb I achieved up to 88.1 % MTBE removal when the contaminated groundwater flowed through (single pass) at  $14.6 \text{ cm d}^{-1}$ . The critical HRT for Honeycomb I was also approximately 1 day, similar to that in the column reactor. The response of MTBE removal efficiency towards flow obtained in the column reactor and sand tank was generic, indicating that the reactor efficiency can be obtained via testing of the model in the column reactor. The presence of toluene, ethylbenzene and o-xylene (TEo-X) decreased the MTBE removal efficiency in both the sand tank and column reactor. The same set of catalyst and 15 W Philips Cleo UVA fluorescent lamp was operated for a total of about 582 h (24 d) out of the cumulative 1039 h (43 d) sand tank experiments, achieving an overall MTBE removal efficiency of about 76.2 %.

The experiments in the column reactor and sand tank exhibited the reliability of the immobilised catalyst produced in this research. This research demonstrates the potential of Honeycomb for in-situ groundwater remediation and also proposes its fabrication and installation options in the field.

## Acknowledgements

First of all, my heartfelt gratitude to my supervisor, Dr Roderick Lynch for giving me this rare opportunity to undertake this research. With his profound knowledge on the subject, the timely advice and guidance shown elevated my confidence to complete this research successfully. His great patience and support throughout my research, allowing myself to work closely with him, has constantly kept me in high spirits all the way through.

Special thanks to my advisor, Prof Malcolm Bolton for his kind advices, which are ingenious and practical, and generous support. Many thanks to Chris Knight and Tim Ablett for their assistance in the Environmental Geotechnics Laboratory and Geotechnical Research Office. I would like to thank Prof Kenichi Soga for kindly providing me one of his used computer and some apparatus in the laboratory and Dr M Shahid for his advice on fibreglass. I would also like to thank Amanda Pyatt, Zelda Stuck and Cathy Salkield. My sincere thanks to Davor Dukic of the Electronics Development Group, and Alan Heaver, Leonard Howlett and Anne Bahnweg in the Materials Laboratory. I would like to thank the people in my research group, particularly Srinath Iyengar, Marwa al-Ansary, Kaushal Joshi, Panagiotis Nikolopoulos, Martin Liska, Katka Ondrova, Gue Chang Shin, Tricia Lee, Indrani Pal, Andy Leung, Dilan Robert, Reginald Kogbara, Matthew Kuo, Sidney Lam, Christopher Lo, Ahmed al-Qabany, Khalid Gafar, Abir Osman and Koson Janmonta, for their amity.

My wonderful experience in Cambridge was also enriched by Clare Hall through the collegiate system, in particular would like to thank Irene Hills, Dr Bobbie Wells and Dr Rosie Luff. I am very grateful to my close friends, Jenny Prüfe, Foivi Antoniou, Arjan Abeynaike, Evelyn Chan, Chan Yew Ming, Puli Fuwongcharoen, Elisa Dassie and Peter Hasto, who certainly made my stay a memorable one.

I would like to thank the Cambridge Commonwealth Trust – Special Malaysia Cambridge Bursary and Tunku Abdul Rahman Foundation Sarawak Scholarship for funding my studies, as well as Cambridge Philosophical Society, Board of Graduate Studies (Lundgren Award), Clare Hall and Department of Engineering for the financial assistance during my tenth term.

Above all, I feel grateful and indebt to my parents, Lim Sze Meng and Foo Eng Hua, and my brother, Dr Lim Lik Thai for their care, love, support, encouragement and understanding. I feel blessed to be guided by the teachings of the Buddha and I have my utmost faith in the Goddess of Mercy for the blessings and protection.

Last but not least, I would like to thank everyone who has directly or indirectly contributed to my research.

## Table of Contents

Declaration	iii
Abstract	iv
Acknowledgements	vi
Table of Contents	vii
List of Figures	xvi
List of Tables	xxix
List of Notations	xxxii

### Chapter 1 Introduction

1.0 Overview	1
1.1 Research Background	1
1.2 Methyl Tert Butyl Ether (MTBE)	3
1.3 Existing Groundwater Treatment Technologies	5
1.3.1 Air Stripping	6
1.3.2 Soil Vapour Extraction (SVE)	8
1.3.3 Pump-and-Treat	9
1.3.4 Bioremediation	11
1.3.5 In-situ Chemical Oxidation	13
1.3.6 Adsorption	14
1.3.7 Summary of Advantages and Disadvantages	15
1.4 Photocatalysis and Existing Photocatalytic Reactor Designs	17
1.4.1 Slurry Reactors	20
1.4.1.1 Fountain Photocatalytic Reactor	20
1.4.1.2 Falling Film Reactor	20

1.4.1.3 Solar Parabolic Photocatalytic Reactor	21
1.4.2 Immobilised Reactors	24
1.4.2.1 Optical Fibre Reactor (OFR)	24
1.4.2.2 Multiple Tube Reactor (MTR)	24
1.4.2.3 Rotating Disk Photocatalytic Reactor (RDPR)	25
1.4.2.4 Photocat I	26
1.4.3 Summary	27
1.5 Statement of Need	28
1.6 Aim and Objectives	28
1.7 Scope of Research	29
1.8 Thesis Layout	30

## **Chapter 2 Literature Review**

2.0 Overview	31
2.1 Semiconductor Photocatalysis	31
2.1.1 Photocatalytic Mechanism	34
2.1.2 Photocatalytic Degradation Pathway for MTBE	39
2.1.3 Photocatalytic Degradation Pathway for MB	41
2.2 Photocatalyst: Titanium Dioxide (TiO <sub>2</sub> )	43
2.2.1 Titanium Dioxide Properties	45
2.2.2 Thermal Treatment Terms	46
2.2.3 Film Thickness	47
2.3 Factors Affecting Photocatalysis	48
2.3.1 Surface Area and Morphology	48
2.3.2 Adsorption	49
2.3.3 Dissolved Oxygen Concentration	49

2.3.4	Contaminant Concentration	50
2.3.5	pH	52
2.3.6	Presence of Other Organics, Anions and Cations	53
2.3.7	Light Intensity and Wavelength	54
2.3.8	Temperature	56
2.4	Continuously Mixed Tank Reactor	57
2.5	Contaminant Transport	59
2.5.1	Soil Characteristics	59
2.5.2	Transport Mechanisms	60
2.5.2.1	Advection	60
2.5.2.2	Dispersion	61
2.5.2.3	Peclet Distribution	61
2.5.2.4	Breakthrough Curve	62
2.5.2.5	Retardation Factor	64

### **Chapter 3 Immobilisation of Titanium Dioxide**

3.0	Overview	65
3.1	Introduction	66
3.2	Methodology: TiO <sub>2</sub> Immobilisation Procedure	67
3.2.1	Preparation of Coating Solution	68
3.2.1.1	Sol Gel	68
3.2.1.2	Hybrid	69
3.2.1.3	Reverse Micelles	70
3.2.1.4	Titanium Dioxide Powder Slurry	71
3.2.2	Preparation of Substrates	72
3.2.2.1	Fibreglass	72

3.2.2.2 Aluminum and Glass	73
3.3 Methodology: Testing of Immobilised Catalysts	74
3.3.1 Immobilisation Efficiency	74
3.3.2 Photocatalytic Activity	76
3.3.2.1 Methylene Blue Dye (MB) as Photocatalytic Indicator	76
3.3.2.2 MB Concentration Measurement by Spectrophotometry	77
3.3.2.3 Turbidity Measurement	79
3.3.2.4 2-hours MB Test	80
3.3.2.5 Light Intensity Variation with Distance	82
3.3.2.6 Suitable Combination of Coating Method and Substrate	83
3.3.2.7 Coating Cycles, Calcination Duration and Temperature	83
3.4 Results and Discussion: Coating Method and Substrate Combination	84
3.4.1 Deposition of TiO <sub>2</sub>	84
3.4.1.1 Substrate	85
3.4.1.2 Coating Solution	85
3.4.2 Photocatalytic Activity	87
3.5 Results and Discussion: Coating Cycles, Calcination Duration and Temperature	89
3.5.1 Deposition of TiO <sub>2</sub>	89
3.5.2 Photocatalytic Activity	91
3.5.3 Characterisation of Coating	93
3.5.3.1 Crystal Structure	93
3.5.3.2 Surface Morphology	95
3.6 Scale Up of Hybrid Coating on Woven Fibreglass	96
3.6.1 Materials and Methods	97
3.6.2 Results and Discussion	98
3.6.2.1 Catalyst Performance	98
3.6.2.2 Catalyst Surface Observation	99

3.7 Conclusions	100
-----------------	-----

## **Chapter 4 Evaluation of a Proposed Photocatalytic Reactor**

4.0 Overview	101
4.1 Introduction	102
4.2 Proposed Reactor Design	104
4.2.1 Effect of Surface Area and Light Intensity	106
4.2.2 Scale Effect	107
4.2.3 Reliability	107
4.2.4 Effect of Aeration	108
4.2.5 Effect of Flow	108
4.3 Experimental Methodology	110
4.3.1 Experimental Arrangement	110
4.3.2 Single Pass Flow Study Arrangement	112
4.4 Results and Discussion	113
4.4.1 Experimental Scale Effect	113
4.4.2 Surface Area Study	115
4.4.3 Reliability Study	120
4.4.4 Aeration Study	121
4.4.5 Single Pass Flow Study	123
4.5 Conclusions	127

## Chapter 5 MTBE Degradation using Honeycomb II Model

5.0 Overview	128
5.1 Study Considerations	129
5.1.1 Hydrogeological Aspects	129
5.1.2 Aeration	130
5.1.3 Groundwater Constituents	130
5.1.4 Multiple Pass Photocatalytic Reactor	132
5.2 Experimental Methodology	132
5.2.1 Experimental Arrangement	132
5.2.2 Aeration Experiment Arrangement	133
5.2.3 Single Pass Flow Study Arrangement	133
5.2.4 Double Pass Flow Study Arrangement	134
5.2.5 Selection of Constituents	135
5.2.5.1 Organic Constituents	135
5.2.5.2 Inorganic Constituents	136
5.2.5.3 Combination of Organic and Inorganic Compounds	137
5.2.6 Gas Chromatograph	138
5.2.6.1 Preparation of Standard MTBE Solution	138
5.2.6.2 Configuration of Gas Chromatograph	138
5.2.6.3 Determination of Equilibration Time between Preparation and Analysis of MTBE and TEO-X	139
5.2.6.4 Calibration of Gas Chromatograph	140
5.3 Results and Discussion	141
5.3.1 Considerations Affecting MTBE Vaporisation	141
5.3.1.1 Aeration	141
5.3.1.2 Cell Diameter to Height (D/H) Ratio	142
5.3.1.3 Contaminant Properties	142

5.3.2	Effect of Groundwater Constituents on MTBE Degradation	144
5.3.2.1	Toluene, Ethylbenzene and o-Xylene (TEo-X)	146
5.3.2.2	Cations and Anions	146
5.3.2.3	Combination of TEo-X and Dissolved Ions	150
5.3.3	Single Pass Flow Study	151
5.3.3.1	MTBE only	151
5.3.3.2	MTBE, TEo-X and Dissolved Ions	153
5.3.4	Relationship between Reactor Efficiency and Flow	153
5.3.4.1	Velocity	153
5.3.4.2	Hydraulic Residence Time (HRT)	155
5.3.5	Double Pass Flow Study	157
5.3.6	Catalyst Surface Observation	160
5.4	Conclusions	162

## **Chapter 6 Evaluation of Honeycomb I Prototype in a Sand Tank**

6.0	Overview	164
6.1	Introduction	165
6.2	Experimental Arrangement	166
6.2.1	Setup of Sand Tank Experiment	166
6.2.2	Scaled Up Photocatalytic Reactor	168
6.2.3	Preparation of Homogeneous Aquifer	169
6.2.4	Determination and Preparation of Contaminants	171
6.2.5	Experimental Phases	171
6.3	Results and Discussion	173
6.3.1	MTBE Migration Phase	173

6.3.1.1	Advection, Dispersion and Retardation Factor	178
6.3.1.2	Concentration Distribution Plots	182
6.3.1.3	Within the Photocatalytic Reactor	189
6.3.2	Aeration Phase	189
6.3.3	Photocatalytic Reaction Phase	191
6.3.3.1	Reliability	193
6.3.3.2	Scale Up	194
6.3.4	Flushing Phase	195
6.3.5	Cumulative Performance of Honeycomb I	195
6.3.6	Honeycomb I Observation	196
6.3.7	Comparison of Reactor Performance	196
6.4	Conclusions	198

## **Chapter 7 Proposed Field Scale In-situ Photocatalytic Reactor Installation**

7.0	Overview	200
7.1	Introduction	200
7.2	Design Parameters and Material Specifications	201
7.2.1	UVA Lamp and Shield Tube	201
7.2.2	Aerator	204
7.2.3	Photocatalyst	204
7.2.4	Permeable and Impermeable Liner	205
7.2.5	Sand Filter	206
7.3	Estimating the Number of Cells Required in Series	206
7.4	Installation Approaches	208
7.4.1	Sheet Pile Approach	209

7.4.2 Intensive Clean Up Approach	211
7.5 Monitoring Programme	215
7.6 Material Cost Estimate	215
7.7 Conclusions	216

## **Chapter 8 Conclusions and Recommendations**

8.1 Conclusions	217
8.1.1 Catalyst Immobilisation	217
8.1.2 Evaluation of Honeycomb Reactor Model in a Column Reactor	218
8.1.3 Simulation of MTBE Plume Clean-up in a Sand Tank	219
8.2 Recommendations	219
8.2.1 Field Testing	219
8.2.2 Enhancement of Immobilisation Procedure	220
8.2.3 Process Optimisation	221
8.2.4 Combination with Electrokinetics	222
8.2.5 Study on the Effect of Ethanol	222
8.2.6 Numerical Modelling	223
References	224
List of Publications	236

## List of Figures

### Chapter 1 Introduction

Figure 1.1	Illustration of soil heterogeneity, with high and low hydraulic conductivity zones (Domenico and Schwartz, 1997)	2
Figure 1.2	Illustration of non-aqueous phase liquid (NAPL) migration in aquifer and vadose zone (Domenico and Schwartz, 1997)	2
Figure 1.3	Coupling of air stripping (right) and soil vapour extraction (SVE) (left) in a groundwater remediation project (Fetter, 1999)	7
Figure 1.4	Soil vapour extraction (SVE) system (Fetter, 1999)	8
Figure 1.5	Groundwater extraction using a pump-and-treat system (Fetter, 1999)	10
Figure 1.6	In-situ bioremediation (Fetter, 1999)	12
Figure 1.7	Funnel and gate (left) and trench (right) systems (Bowles et al., 2000)	14
Figure 1.8	Schematic diagram of the fountain photocatalytic reactor model in the laboratory scale experiments (Li Puma and Yue, 2001)	20
Figure 1.9	Schematic diagram of the falling film reactor (Almquist et al., 2003)	21
Figure 1.10a	Geometric profile of a parabolic trough reactor (PTR) (Alfano et al., 2000)	23
Figure 1.10b	View of a PTR, type 'Helioman' (Alfano et al., 2000)	23
Figure 1.10c	Geometric profile of a compound parabolic collecting reactor (CPCR) (Alfano et al., 2000)	23
Figure 1.10d	A CPC prototype (100 m <sup>2</sup> ) at Hydrocen factory in Madrid (Robert and Malato, 2002)	23
Figure 1.10e	Field experiment using concentrating solar collector at Livermore (Mehos and Turchi, 1993)	23
Figure 1.11	Pilot scale TFFBR for textile wastewater treatment (Bahnemann, 2004)	23
Figure 1.12	Fiber optic bundle array cable reactor used in the laboratory scale experiments (Peill and Hoffmann, 1998) (left) and scaled up OFR2 with solar collector/concentrator, equatorial tracker not shown (Peill, 1996) (right)	24

Figure 1.13	Illustration of multiple tube reactor (MTR) (Ray and Beenackers, 1998a)	25
Figure 1.14	Rotating disk photocatalytic reactor (RDPR) (Dionysiou et al., 2000b)	26
Figure 1.15	Illustration of Photocat I (Chan et al., 2006)	27

## Chapter 2 Literature Review

Figure 2.1a	Typical exponential decay curve of a contaminant	33
Figure 2.1b	Typical linear plot $\ln(C_0/C)$ vs time	33
Figure 2.2	Primary stages in photocatalytic mechanism (modified from Hoffmann et al., 1995); (A) and (B) are detailed in Figure 2.3 and 2.4, respectively	34
Figure 2.3	Primary reactions on the catalyst surface (Hoffmann et al., 1995); Red: reductant (electron donor), Ox: oxidant (electron acceptor)	35
Figure 2.4	The formation of activated oxygen species and their reactions (Hoffmann et al., 1995); R: organic contaminant	37
Figure 2.5	The proposed photocatalytic degradation pathway of MTBE (Barreto et al., 1995)	40
Figure 2.6	The proposed photocatalytic degradation pathway of MB (Houas et al., 2001)	42
Figure 2.7	Schematic diagram showing the potentials for various redox processes occurring on the $\text{TiO}_2$ surface at pH 7 (Fujishima et al., 2000); Standard Hydrogen Electrode (SHE)	43
Figure 2.8	Relationship between absorbance and percent light transmittance	51
Figure 2.9	The rate of acetone formation from isopropyl alcohol photodegradation by pure rutile plotted against incident light intensity (Mills et al., 1993)	56
Figure 2.10	Representative values of permeability for various rocks and unconsolidated sediments (Freeze and Cherry, 1979)	60

Figure 2.11	The behaviour of $D_L/D_d$ and $D_T/D_d$ as a function of Peclet number, with classes of mixing (Domenico and Schwartz, 1997); $v$ is the average linear velocity, $d_m$ is the average grain size, $D_d$ is the molecular diffusion coefficient and $D_L$ is the longitudinal dispersion coefficient. Class 1: the mixing is dominated by diffusion, Class 2: the mixing is influenced by diffusion and dispersion, Class 3: the mixing is dominated by dispersion with $D_L$ values approximately proportional to $v_w^{1.2}$ , Class 4: the mixing is dominated by dispersion with negligible effect of diffusion.	62
Figure 2.12	Breakthrough curve of a contaminant from a continuous point source (Domenico and Schwartz, 1997), $t_{50}$ is the breakthrough time of the contaminant	63

### Chapter 3 Immobilisation of Titanium Dioxide

Figure 3.1	Modified Watson-Marlow 502S peristaltic pump for dip coating, dip coating of a 12 cm <sup>2</sup> aluminium plate in sol gel (inset)	68
Figure 3.2	Sol gel preparation procedure modified from Xagas et al. (1999)	69
Figure 3.3	Hybrid preparation procedure modified from Medina-Valtierra et al. (2006)	70
Figure 3.4	Reverse micelles procedure modified from Yu et al. (2002a)	71
Figure 3.5	TiO <sub>2</sub> slurry procedure modified from Chan (2005)	72
Figure 3.6	Fibreglass	73
Figure 3.7	Woven fibreglass	73
Figure 3.8	Aluminum plate	74
Figure 3.9	Glass slide	74
Figure 3.10	Mettler AE 160 digital balance	75
Figure 3.11	Varian Cary 4000 UV/Vis spectrophotometer	78
Figure 3.12	Unicam 8620 UV/VIS spectrophotometer	78

Figure 3.13	Absorbance spectra of MB solutions at various concentrations	78
Figure 3.14	Determination of constant for MB absorbance measurement at 665 nm	79
Figure 3.15	UVA light transmission reduction with increasing turbidity	80
Figure 3.16	Photo (left) and illustration (right) showing 2-hours MB test setup	81
Figure 3.17	UVA light intensity (peak wavelength of 365 nm) variation with distance	82
Figure 3.18	The linear plot of voltage vs light intensity	83
Figure 3.19	Detachment of TiO <sub>2</sub> for various coating and substrate (refer to Table 3.1 for nomenclature)	84
Figure 3.20	Detachment of some hybrid coating on woven fibreglass	86
Figure 3.21	Illustration of TiO <sub>2</sub> coating arrangement for (a) ideal coating, (b) slurry coating, (c) hybrid coating and (d) illustration of TiO <sub>2</sub> coating detachment (i) weak adhesion, (ii) insufficient sol gel to bind P25 and (iii) excessive coating	87
Figure 3.22	Specific photocatalytic activity of various coating and substrate combinations (refer to Table 3.1 to for nomenclature)	89
Figure 3.23	Detachment of hybrid coating of TiO <sub>2</sub> for various coating cycles, calcination duration and temperature (refer to Table 3.2 for nomenclature)	90
Figure 3.24	Specific photocatalytic activity of various coating cycles, calcination duration and temperature (refer to Table 3.2 for nomenclature)	91
Figure 3.25	MB decolorisation by various coating cycles and calcination temperatures (refer to Table 3.2 for nomenclature)	92
Figure 3.26a	XRD analysis for hybrid coating on woven fibreglass	94
Figure 3.26b	EDX spectroscopic analysis on uncoated woven fibreglass; no Ti peak at about 4.5 keV	94
Figure 3.26c	EDX spectroscopic analysis on hybrid coated woven fibreglass; Ti peak at about 4.5 keV indicate the deposition of hybrid coating	94
Figure 3.27a	SEM micrograph showing the hybrid coating was well attached to the fibreglass	96

Figure 3.27b	SEM micrograph showing fractal surface providing larger effective surface area for photocatalysis	96
Figure 3.27c	SEM micrograph showing some parts are not well coated and some cracking was observed to be uncoated	96
Figure 3.27d	SEM micrograph showing some openings and crossing were uncoated	96
Figure 3.28	Photo showing the scaled up hybrid dip coating on woven fibreglass	97
Figure 3.29	Comparison of MB PCO rate constants and degradation efficiencies of catalysts coated in different batches and scales, obtained using the 60 mL 2-h MB test. The dates of testing and dates of coating (in brackets) are as shown. The samples tested in Nov. 07 were coated in small scale, and the others in larger, "mass production" scale.	98
Figure 3.30a	SEM image showing the catalyst surface after MB test	99
Figure 3.30b	Microscopic image showing MB was adsorbed on the catalyst surface rather than fibreglass	99
Figure 3.31	Microscopic image showing the pristine catalyst surface	99

#### **Chapter 4 Evaluation of a Proposed Photocatalytic Reactor Design**

Figure 4.1	Cross section view of the proposed photocatalytic reactor in a trench for in-situ groundwater remediation	104
Figure 4.2	Elimination of gaps among cylindrical cells using hexagonal structure (left; representing dotted circle on the right) and plan view of the proposed in-situ photocatalytic reactor (right); blue line indicating groundwater flow through reactor, $r_c$ : internal radius of cell and $d_c$ : internal diameter of cell	105
Figure 4.3	Plan view of the proposed hexagonal structure with radial panels, Honeycomb I (left) and without radial panels, Honeycomb II (right)	106
Figure 4.4a	Cross section (left) and plan (right) view of the column reactor using Honeycomb II	111
Figure 4.4b	MB column experiment setup (inset: reactor configuration without catalyst) (left) and the plan view inside the column (right)	111

Figure 4.5	Schematic diagram showing the experimental setup of single and double pass flow experiments; peristaltic pump (P), air pump (AP), air flow meter (AFM)	112
Figure 4.6	Variation of normalised MB concentration and $\ln(C_0/C)$ in an adsorption study conducted in two experimental scales; 60 mL and 4 L. Adsorption only for 50 minutes (60 mL) and 6 hours (4 L).	114
Figure 4.7	The relationship between photocatalytic activity and A/V ratio	116
Figure 4.8	Variation of average normalised MB concentration and $\ln(C_0/C)$ of Honeycomb I and II (2 runs each) in the 4 L column reactor after 8 h. Error bars show the minimum and maximum values.	117
Figure 4.9	Slightly cloudy MB solution after the first Honeycomb I experiment, indicating the precipitation of iron (III) oxides	118
Figure 4.10	The corrosion of radial panel support after the Honeycomb I experiments	119
Figure 4.11	The metal clip from control (left) and after the Honeycomb I experiments (right)	119
Figure 4.12	Reduction of the average normalised MB concentrations with time in the reliability experiments at various air supply intervals (on:off). Error bars show the maxima and minima of replicate measurement.	120
Figure 4.13	Variation of MB PCO rate constant of Honeycomb II with aeration ratio (on:off); from left to right 4:8, 8:4, 11:1 and continuous aeration, 12:0	121
Figure 4.14	Reduction of MB concentration in an experiment which had UV lamp and aeration supply interruption	123
Figure 4.15	$\ln(C_0/C)$ plotted against time for MB degradation using Honeycomb II in the 4 L column reactor at five velocities as specified in Section 4.3.2	124
Figure 4.16	Variation of the MB removal efficiency as a function of velocity using Honeycomb II in the 4 L column reactor	125
Figure 4.17	MB removal efficiency in one HRT cycle using Honeycomb II in the 4 L column reactor for various velocities	126

## Chapter 5 MTBE Degradation using Honeycomb II Model

- Figure 5.1 Normalised concentrations of MTBE and TEO-X measured by the GC at the specified times. The concentrations of MTBE, toluene, ethylbenzene and o-xylene are 100, 30, 10 and 20 mg L<sup>-1</sup>, respectively. The concentration of all the compounds appeared to peak between the 2<sup>nd</sup> and 4<sup>th</sup> hour, which indicated the analysis time of the samples. 139
- Figure 5.2 Peak area to MTBE concentration, analysed at various MTBE equilibration times 140
- Figure 5.3 Calibration of gas chromatograph for MTBE (top left), toluene (top right), ethylbenzene (bottom left) and o-xylene (bottom right), analysed after 2 hours of liquid-gas equilibration time 141
- Figure 5.4 Normalised concentration of MTBE and TEO-X vaporisation during the control batch experiment for aeration, with concentrations of MTBE, toluene, ethylbenzene and o-xylene of approximately 80, 30, 10 and 20 mg L<sup>-1</sup>, respectively. The data was plotted with  $C_0$  being the maximum concentration, not necessarily at  $t = 0$ . 143
- Figure 5.5a Variation of normalised MTBE concentration in the presence of TEO-X (refer to Table 5.1 for TEO-X concentrations) 145
- Figure 5.5b Variation of normalised MTBE concentration in the presence of dissolved ions (refer to Table 5.2 for ion concentrations) 145
- Figure 5.5c Variation of normalised MTBE concentration in the presence of both TEO-X and dissolved ions (refer to Table 5.3 for concentrations) 145
- Figure 5.5d MTBE removal efficiency of Honeycomb II reactor in 8 hours batch (0 m d<sup>-1</sup>) experiments (except for the last three are single pass flow experiments) at various TEO-X and dissolved ions concentrations. Low dissolved ions, low TEO-X (LILO), Low dissolved ions, high TEO-X (LIHO), High dissolved ions, low TEO-X (HILO), High dissolved ions, high TEO-X (HIHO). 145

Figure 5.6	Normalised TEO-X concentration during the control experiment for aeration and the PCO of MTBE at various TEO-X concentrations. The data was plotted with $C_0$ being the maximum concentration, not necessarily at $t = 0$ .	146
Figure 5.7a	Photo of catalyst after double pass flow experiment with HIHO. The yellowish brown area indicates the adsorption of iron on the catalyst while the white surface indicates active sites on the catalyst.	148
Figure 5.7b	Plan view of the bottom of the reactor showing yellowish brown particles in the reactor, indicating precipitation of iron during the photocatalytic reaction	148
Figure 5.8	Normalised iron concentration at various initial dissolved ion concentrations (refer to Table 5.2 for initial ion concentrations)	149
Figure 5.9	Normalised concentration of TEO-X during the photocatalytic degradation of MTBE at various organic compound and dissolved ion concentrations. The data was plotted with $C_0$ being the maximum concentration, not necessarily at $t = 0$ .	151
Figure 5.10	MTBE degradation by Honeycomb II at various velocities. The data was plotted with $C_0$ being the maximum concentration, not necessarily at $t = 0$ . The dotted exponential decay curve was calculated using Eq. 2.3, with $k$ of $0.344 \text{ h}^{-1}$ (Table 5.5), fitted to the experimental data ( $0 \text{ cm d}^{-1}$ ), confirming the PCO of MTBE is a pseudo first order process.	152
Figure 5.11	Effect of flow on the column reactor efficiency in degrading MB and MTBE at various velocities	154
Figure 5.12	The variation of Honeycomb II reactor efficiency in degrading MB, MTBE only and MTBE in the presence of TEO-X and dissolved ions at various HRT	156
Figure 5.13	Normalised MTBE concentration in all the double pass flow experiments, with two (new and used catalyst) in the presence of MTBE only. All the catalysts used in the double pass flow experiments are used catalysts except for the one specified new catalyst.	158
Figure 5.14	Normalised concentrations of MTBE and TEO-X in the double pass flow experiment for organic study. The MTBE:toluene:ethylbenzene:o-xylene concentrations applied were 80:30:10:20 $\text{mg L}^{-1}$ .	159

Figure 5.15a	Microscopic image of catalyst surface after MTBE degradation	160
Figure 5.15b	SEM image of catalyst surface after MTBE degradation	160
Figure 5.16	Microscopic image showing the catalyst surface after degradation of organic compounds, i.e. MTBE and TEo-X	161
Figure 5.17	Microscopic image showing that the catalyst surface was yellowish brown, indicating iron was concentrated on the catalyst surface instead of the fibreglass, after the PCO of MTBE in the presence of dissolved ions.	161
Figure 5.18a	Microscopic image showing that the catalyst surface was yellowish brown after HIHO experiments	161
Figure 5.18b	SEM image of the catalyst surface after double pass flow experiment with HIHO	161

## **Chapter 6 Evaluation of Honeycomb I Prototype in a Sand Tank**

Figure 6.1	(a) Plan view of intended application on site showing how hexagonal units can be linked together in series to achieve the required clean-up level, (b) plan view of the sand tank, which examines the clean-up using a single hexagonal unit (Honeycomb I), (c) side view of the sand tank showing the inflow and outflow chambers, sampling points and reactor, and (d) photo showing the plan view of the sand tank after installation and the location of sampling points.	166
Figure 6.2	Particle size distribution (PSD) of various sand grades using sieve analysis	169
Figure 6.3	Permeability of sand tank obtained before and after the sand tank experiments. Velocity was calculated by dividing flow by the area perpendicular to the flow direction, 0.2 m (W) x 0.22 m (H). Flow, induced using constant head device, was obtained by measuring the volume of water overflowed and time.	170

Figure 6.4	Plot of MTBE concentration with time for six sampling points along $y = 100$ cm (on the tank centre line) and $z = 120$ mm (depth) during 7.3:7.3 experiment. Every series consists of a breakthrough curve, stabilisation phase and flushing phase, except for R120 having aeration and reaction phase between stabilisation and flushing phase; E2120 follows R120; (i) MTBE migration, (ii) aeration, (iii) photocatalytic reaction and (iv) flushing phase (refer to Table 6.1 for sampling point identification).	174
Figure 6.5	Plot of MTBE concentration with time for sampling points at 50, 100 and 150 mm across the 200 mm tank width at depths of 60 and 120 mm (refer to Table 6.1 for coordinates) during the 14.6 (7.3:7.3) experiment (refer to Table 6.3 for flow details)	175
Figure 6.6	Plot of MTBE concentration with time for sampling points at 50, 100 and 150 mm across the 200 mm tank width at depths of 60 and 120 mm (refer to Table 6.1 for coordinates) during the 29.0 (20.0:9.0) experiment (refer to Table 6.3 for flow details)	176
Figure 6.7	Plot of MTBE concentration with time for sampling points at 50, 100 and 150 mm across the 200 mm tank width at depths of 60 and 120 mm (refer to Table 6.1 for coordinates) during the 37.3 (30.0:7.3) experiment (refer to Table 6.3 for flow details)	177
Figure 6.8	Breakthrough curves modelled using CXTFIT (full line) fitted well to experimental data from sampling point D2120 at various average velocities (refer to Table 6.3 for flow details).	179
Figure 6.9	Comparison of MTBE velocity and dispersion coefficients, obtained using CXTFIT, from three sand tank experiments (7.3:7.3, 7.8:7.8V and 7.8:7.8 TEO-X, refer to Table 6.3 for flow details) conducted at similar groundwater velocities indicating similar migration pattern	180
Figure 6.10	The velocity and dispersion coefficient of MTBE and TEO-X, obtained through CXTFIT, at D2120 during sand tank experiment at velocity of $15.6 \text{ cm d}^{-1}$ in the presence of TEO-X	181
Figure 6.11	Peclet distribution in all the sand tank experiments showing the plume migration was influenced by diffusion and dispersion ( $vd_m/D_d$ is within Class 2 - Figure 2.11)	182

Figure 6.12	Plan views of MTBE plume migration at increasing water velocities at depths of 60 mm (top) and 120 mm (bottom) in the sand tank plotted using Matlab. The velocities ( $v_{gw}:v_{MTBE}$ , $\text{cm d}^{-1}$ ) applied were 7.3:7.3 (left column), 20:9 (centre column) and 30:7.3 (right column). The first, second and third rows of plan views show the similar stages of every experiment.	183
Figure 6.13	Concentration plots at specified times showing MTBE plume migration at depths of 60 and 120 mm in the sand tank at velocity of $14.6 \text{ cm d}^{-1}$ ( $v_{gw}:v_{MTBE} = 7.3:7.3$ )	184
Figure 6.14	Concentration plots at specified times showing MTBE plume migration at depths of 60 and 120 mm in the sand tank at velocity of $29.0 \text{ cm d}^{-1}$ ( $v_{gw}:v_{MTBE} = 20.0:9.0$ )	185
Figure 6.15	Concentration plots at specified times showing MTBE plume migration at depths of 60 and 120 mm in the sand tank at velocity of $37.3 \text{ cm d}^{-1}$ ( $v_{gw}:v_{MTBE} = 30.0:7.3$ )	186
Figure 6.16	Surface plot of concentration showing the migration of the organic compounds in the sand tank at a velocity of $15.6 \text{ cm d}^{-1}$ . The migration of toluene, ethylbenzene and o-xylene is similar to that of MTBE, implying that the migration of toluene, ethylbenzene and o-xylene in the tank is assisted by MTBE via the co-solvent effect. TEO-X concentrations obtained at the sampling points were about 10 - 15 % of the initial concentration injected into the sand tank.	188
Figure 6.17	Reduction of MTBE concentration in Honeycomb I from the initiation of the aeration phase. The aeration and UVA lamp was switched on at 96 h, 102 h (7.3:7.3); 120 h, 127 h (20.0:9.0); 72 h, 79 h (30.0:7.3); 72 h, 78 h (7.8:7.8 V); 93 h, 99 h (7.8:7.8 TEO-X), respectively, after MTBE injection started (refer to Table 6.3 for flow details).	190
Figure 6.18	The catalyst surface was slightly brown like the sand colour 10 months after the reactor was installed and including six sand tank experiments	193
Figure 6.19a	Honeycomb I after installation	196
Figure 6.19b	Honeycomb I after two sand tank experiments	196

Figure 6.20	MTBE removal efficiency of the column reactor and sand tank reactor at various HRTs are in agreement, in both cases of MTBE only and MTBE with TEO-X	197
-------------	--	-----

## **Chapter 7 Proposed Field Scale In-situ Photocatalytic Reactor Installation**

Figure 7.1	Cross section view of the proposed internal component of Honeycomb I, which is assembled ex-situ prior to installation by lowering into the housing on site. The housing functions as a secondary filter, in addition to the sand filter, to separate solids from entering the reactor and inhibit UVA light illumination on the catalyst surface. The pointed bottom of the housing is for the accumulation of potential settleable solids in the reactor; allows water to flow through and simple maintenance. Inset: Plan view of the railing for sliding in the immobilised catalyst cassettes. The estimated height of Honeycomb I with housing is 2.0 m, yielding D/H ratio of approximately 0.15. Drawing not to scale.	203
Figure 7.2	Plan (left), 3-dimensional (centre) and cross section (right) view of the sheet pile approach. Plan and 3-dimensional views show the arrangement of Honeycomb I in a trench made using “zero” sheet pile by Giken. Drawing not to scale.	209
Figure 7.3	Proposed installation options using the sheet pile approach: closed end “tubular” pile with “P-P” connection (left) and zero sheet pile (right). Closed end “tubular” pile: (i) driving in “tubular” piles (ii) purging of groundwater in the pile (iii) filling in sand into “tubular” pile as sand filter, and (iv) installation of housing and Honeycomb I. “Zero” sheet pile: (i) driving in “trench” sheet pile, (ii) excavation of soil (iii) filling in sand as base and installation of “zero” sheet pile, (iv) filling in sand at the vicinity of “zero” sheet piles, (v) installation of housing and Honeycomb I, and (vi) removal of “trench” sheet pile. Drawing not to scale.	210

- Figure 7.4 Plan (top) and cross section (bottom) view of the interlocking modules arrangement for intensive groundwater remediation. This arrangement is suitable for the remediation of groundwater with high contamination, typically located near the pollution source. The plan view shows that both sides of the catalyst can be used or shared by adjacent modules, thus maximising the utilisation and cost effectiveness of material. Drawing not to scale. 212
- Figure 7.5 Proposed installation option for intensive clean up approach: (i) driving in “trench” sheet pile, (ii) excavation of soil and purging of groundwater, (iii) filling in sand as base and installation of housing, (iv) filling in sand at the vicinity of the housing, and (v) installation of Honeycomb I. Non-perforated sheets for housing perimeter are only areas parallel to groundwater flow. There is nothing between the interlocking reactors as perimeter panels are slotted into the perimeter panel railing. Drawing not to scale. 214

## List of Tables

### Chapter 1 Introduction

Table 1.1	Physicochemical properties of MTBE (Chan, 2005)	4
Table 1.2	Project duration and cost data for completed stand alone technology applications for MTBE remediation (US EPA, 2004)	5
Table 1.3	Performance data for completed stand alone technology applications for MTBE remediation (US EPA, 2004)	6
Table 1.4	Summary of advantages and disadvantages of existing remediation technologies	15
Table 1.5	Specification and operating conditions of existing photocatalytic reactor designs; HRT: hydraulic residence time, A/V: surface area to volume ratio, e: exposed to sunlight, r: recirculation flow	19

### Chapter 2 Literature Review

Table 2.1	Properties of methylene blue (MB)	41
Table 2.2	Properties of anatase and rutile TiO <sub>2</sub> (Chan, 2005)	45
Table 2.3	Range of grain size (in µm) of sand grades (David Ball Plc.)	59

### Chapter 3 Immobilisation of Titanium Dioxide

Table 3.1	Sample nomenclature for study of coating method and substrate	83
Table 3.2	Sample nomenclature for study of calcination duration and temperature	84

## **Chapter 4 Evaluation of a Proposed Photocatalytic Reactor Design**

Table 4.1	Comparison of experimental specifications and conditions applied in a small test, Honeycomb I and II	107
-----------	--	-----

## **Chapter 5 MTBE Degradation using Honeycomb II Model**

Table 5.1	TEo-X concentrations used in the organic compound study; LO: Low Organic and HO: High Organic are used in the combination of TEO-X and dissolved ion study	135
Table 5.2	Dissolved ion concentrations used in the dissolved ion study, LI: Low Ion and HI: High Ion is used in the combination of TEO-X/dissolved ion study	136
Table 5.3	Concentrations of dissolved ion and organic compounds in the four solutions used in combined study	137
Table 5.4	Preparation of standard MTBE solutions for GC calibration	138
Table 5.5	PCO rate constants of MB and MTBE using column reactor at various velocities in 8 hours experiments, except for 64.8 and 136.1 cm d <sup>-1</sup>	155

## **Chapter 6 Evaluation of Honeycomb I Prototype in a Sand Tank**

Table 6.1	The coordinates and nomenclatures of sampling points	167
Table 6.2	Characteristics of Grade 'C' sand used in this study	169
Table 6.3	Flow profile applied in the sand tank experiments. Velocity refers to Darcy's velocity except for total average linear velocity and porosity is 0.42	171
Table 6.4	The initiation times (hours) of experimental phases for the three sand tank experiments	172
Table 6.5	Sand tank experimental details and performance of Honeycomb I	192

## Chapter 7 Proposed Field Scale In-situ Photocatalytic Reactor Installation

Table 7.1	Material cost estimate for 1 m width photocatalytic reactor (2 m deep) with 3 arrays (Figure 7.4)	216
-----------	---	-----

## List of Notations

$\{>\text{Ti}^{\text{III}}\text{OH}\}$	Surface trapped conduction band electron
$\{>\text{Ti}^{\text{IV}}\text{OH}\}^+$	Surface bound hydroxyl radical
$>\text{Ti}^{\text{IV}}\text{O}_2^-$	TiO <sub>2</sub> surface with the dioxygen reduced by $e_{\text{cb}}^-$
$\gamma_l$	Zero-order production term for liquid phase [ $\text{M L}^{-3} \text{T}^{-1}$ ]
$\gamma_s$	Zero-order production term for adsorbed phase [ $\text{M M}^{-1} \text{T}^{-1}$ ]
$\theta$	Volumetric water content [ $\text{L}^3 \text{L}^{-3}$ ]
$\lambda$	Light wavelength [L]
$\mu\text{g}$	Microgram [M]
$\mu_l$	First-order decay coefficient of solute in liquid phase [ $\text{T}^{-1}$ ]
$\mu\text{m}$	Micron(s) or micrometer(s) [L]
$\mu_s$	First-order decay coefficient of solute in adsorbed phase [ $\text{T}^{-1}$ ]
$\zeta$	Molar absorptivity constant [ $\text{L}^3 \text{M}^{-1} \text{L}^{-1}$ ]
$\rho_b$	Soil bulk density [ $\text{M L}^{-3}$ ]
$\tau$	Hydraulic residence time [ $\text{T}^{-1}$ ]
$\Omega$	Ohm [ $\text{M L T}^{-2}$ ]
$^\circ\text{C}$	Degree Celcius [ $\theta$ ]
$a$	Conversion ratio of concentration over peak area [ $\text{M L}^{-3} \text{L}^{-2} \text{T}^{-1}$ ]
$A$	Absorbance measurement
$A$	Area [ $\text{L}^2$ ]
a.u.	Absorbance unit
$A/V$	Surface area to volume ratio [ $\text{L}^2 \text{L}^{-3}$ ]
BTEX	Benzene, Toluene, Ethylbenzene and Xylenes
$c$	Molar concentration [ $\text{M L}^{-3}$ ]
$c$	Speed of light [ $\text{L T}^{-1}$ ]
$C$	Concentration in aqueous phase [ $\text{M L}^{-3}$ ]
$c/c$	Centre to centre (of hole)
$C_0$	Initial concentration [ $\text{M L}^{-3}$ ]
Ca	Calcium
$\text{Ca}^{2+}$	Calcium ion
CB	Conduction Band
$C_F$	Final concentration [ $\text{M L}^{-3}$ ]

CHCl <sub>3</sub>	Chloroform
Cl <sup>-</sup>	Chloride ion
cm	Centimeter(s) [L]
cm <sup>2</sup>	Square centimeter(s) [L <sup>2</sup> ]
$C_N$	Required clean-up concentration, after $N$ units of photocatalytic cells [M L <sup>-3</sup> ]
$C_s$	Concentration of the adsorbed phase [M M <sup>-1</sup> ]
CO	Carbon Monoxide
CO <sub>2</sub>	Carbon Dioxide
CPCR	Compound parabolic collecting reactor
$C_v$	Concentration in vapour phase [M L <sup>-3</sup> ]
d	Day(s) [T]
$D$	Dispersion coefficient [L <sup>2</sup> T <sup>-1</sup> ]
D/H	Cell diameter to height ratio [L L <sup>-1</sup> ]
$d_{10}$	Sieve size passed through by the first 10 % by weight of soil
$d_{50}$	Sieve size passed through by the first 50 % by weight of soil
$d_{85}$	Sieve size passed through by the first 85 % by weight of soil
$d_c$	Internal diameter of photocatalytic cell [L]
$D_d$	Diffusion coefficient [L <sup>2</sup> T <sup>-1</sup> ]
$D_L$	Longitudinal dispersion coefficient [L <sup>2</sup> T <sup>-1</sup> ]
$d_m$	Average grain diameter [L]
DOC	Dissolved Organic Carbon
DWI	Drinking Water Inspectorate
$E$	Energy level of photon in electron volt
EDX	Energy-Dispersive X-ray spectroscopy
$e_{cb}^-$	Conduction band electron
$E_g$	Energy bandgap
EIA	Energy Information Administration
$e_{tr}^-$	Electron trapped in the conduction band
eV	Electron volt
Fe	Iron or ferrum
Fe <sup>2+</sup>	Ferrous ion
Fe <sup>3+</sup>	Ferric ion
g	Gram(s) [M]

GC	Gas chromatograph
GC-FID	Gas chromatograph with flame ionisation detector
h	Hour(s) [T]
H	Height [L]
H	Henry's law constant [ $M L^{-3} (M^{-1} L^{-3})$ ]
H <sup>+</sup>	Hydrogen ion
H <sub>2</sub> O	Water
H <sub>2</sub> O <sub>2</sub>	Hydrogen peroxide
H <sub>3</sub> O <sup>+</sup>	Hydronium ion
Hg	Mercury
HO <sub>2</sub> <sup>-</sup>	Hydroperoxyl or perhydroxyl radical
HRT	Hydraulic residence time [T]
h $\nu$	Energy of a photon
h <sub>vb</sub> <sup>+</sup>	Valence band hole
<i>i</i>	Hydraulic gradient [ $L L^{-1}$ ]
<i>I</i>	Transmitted light intensity [ $M L^2 T^{-3} L^{-2}$ ]
<i>I</i> <sub>0</sub>	Incident light intensity [ $M L^2 T^{-3} L^{-2}$ ]
i.d.	Internal or inner diameter [L]
J	Joule [ $M L^2 T^{-2}$ ]
<i>J</i> <sub>w</sub>	Volumetric water flux density [ $L T^{-1}$ ]
<i>k</i>	Observed first order photocatalytic reaction rate constant [ $T^{-1}$ ]
<i>k</i>	Permeability [ $L T^{-1}$ ]
K	Kelvin [θ]
<i>K</i> <sub>d</sub>	Distribution coefficient for the solute with the soil [ $L^3 M^{-1}$ ]
kg	Kilogram [M]
<i>K</i> <sub>OC</sub>	Organic carbon partition
<i>K</i> <sub>OW</sub>	Octanol-water partition
<i>l</i>	Length of light path through a cuvette [L]
L	Litre(s) [ $L^3$ ]
L <sub>a</sub>	Litre(s) of air [ $L^3$ ]
m	Meter [L]
m <sup>2</sup>	Square meter [ $L^2$ ]
m <sup>3</sup>	Cubic meter [ $L^3$ ]

MB	Methylene Blue
mg	Miligram(s) [M]
min	Minute(s) [T]
mm	Milimeter(s) [L]
mol	Mole [M]
mmol	Milimole [M]
MPE	Multi Phase Extraction
MTBE	Metyl Tertiary Butyl Ether
MTR	Multiple Tube Reactor
mW	miliWatt [ $M L^2 T^{-3}$ ]
$n$	Total porosity [unitless]
$N$	Number of photocatalytic cells in series
NAPL	Non-Aqueous Phase Liquid
$n_e$	Porosity [unitless]
NHE	Normal Hydrogen Electrode
nm	Nanometer(s) [L]
$NO_3^-$	Nitrate ion
NTU	Nephelometric turbidity unit
$O_2$	Oxygen
$O_2^{\cdot-}$	Oxygen radical or superoxide
o.d.	External or outer diameter [L]
$OH^-$	Hydroxyl ion
$O_3$	Ozone
$OH^{\cdot}$	Hydroxyl radical
Ox	Oxidant or electron acceptor
$Ox^-$	Reduced oxidisable molecule
PCO	Photocatalytic oxidation
ppb	Parts per billion
ppm	Parts per million
PSD	Particle Size Distribution
PTR	Parabolic trough reactor
$Q$	Volumetric flow [ $L^3 T^{-1}$ ]
$Q_0$	Incoming volumetric flow [ $L^3 T^{-1}$ ]

$Q_e$	Effluent volumetric flow [ $L^3 T^{-1}$ ]
$r$	Radius of cell [L]
$r$	Ratio of reactor volume (section exposed to sunlight) to feed tank volume
$r$	Recirculation flow
$R$	Gas constant [ $L^3 M^{-1} \theta^{-1}$ ]
$R$	Generation rate [ $M L^3 T^{-1}$ ]
$R$	Retardation factor [unitless]
$R$	Organic compound
$R^2$	Correlation coefficient
$r_c$	Internal radius of photocatalytic cell [L]
RDPR	Rotating Disk Photocatalytic Reactor
Red	Reductant or electron donor
ROI	Radius of Influence
$R_N$	Removal efficiency of reactor after $N$ units of photocatalytic cells in series
$s$	Second(s) [T]
SEM	Scanning Electron Microscopy
SHE	Standard Hydrogen Electrode
SVE	Soil Vapour Extraction
$t$	Time [T]
$T$	Light transmittance
$T$	Temperature [ $\theta$ ]
TBA	Tertiary Butyl Alcohol
TBF	Tertiary Butyl Formate
TEL	Tetraethyl Lead
TEo-X	Toluene, Ethylbenzene and o-Xylene
TFFBR	Thin-Film Fixed-Bed Reactor
TiO <sub>2</sub>	Titanium Dioxide
TiOH	Primary hydroxylated TiO <sub>2</sub> surface
US EPA	United States Environmental Protection Agency
USD	United States Dollar
UV	Ultraviolet light
UV/Vis	Ultraviolet visible
UVA	Ultraviolet light A with wavelength longer than 315 nm

UVC	Ultraviolet light C with wavelength shorter than 254 nm
$V$	Reactor volume [ $L^3$ ]
V	Volt [ $M L T^{-2}$ ]
$v$ or $v_w$	Average linear water velocity [ $L T^{-1}$ ]
$v/v$	Volume by Volume [ $L^3 L^{-3}$ ]
VB	Valence Band
$v_c$	True contaminant transport velocity [ $L T^{-1}$ ]
$v_D$	Darcy's velocity [ $L T^{-1}$ ]
$v_{gw}$	Darcy's velocity of groundwater [ $L T^{-1}$ ]
$v_{MTBE}$	Darcy's velocity of MTBE [ $L T^{-1}$ ]
VOC	Volatile Organic Compound
$V_T$	Feed tank volume [ $L^3$ ]
W	Watt [ $M L^2 T^{-3}$ ]
W	Width [L]
$w/w$	Weight by Weight [ $M M^{-1}$ ]
$x$	Distance [L]
XRD	X-ray Diffraction crystallography
XPS	X-ray Photoelectron Spectroscopy
yr	Year [T]

# CHAPTER 1

## INTRODUCTION

### 1.0 Overview

This chapter provides the research background, which emphasizes the need for in-situ groundwater remediation. It begins with a general overview of the groundwater remediation issues, the identification of the target contaminant in this research and the existing groundwater remediation technologies typically applied in MTBE groundwater clean-up projects. This is followed by the introduction of photocatalysis as a potential alternative for MTBE degradation as well as a brief description of several existing photocatalytic reactor designs, leading to the need for a photocatalytic reactor design for in-situ groundwater remediation. The aim and objectives as well as the scope of research are also included in this chapter, and concludes with a thesis layout to portray the organisation of this thesis.

### 1.1 Research Background

Remediation of contaminated groundwater is an uphill challenge, especially when it involves a highly soluble and mobile contaminant, which is also persistent in the environment such as MTBE. Apart from bioremediation (Deeb et al., 2000; Prince, 2000; Puig-Grajales et al., 2000; Kane et al., 2001), phytoremediation (Rubin and Ramaswami, 2000; Yu and Gu, 2006) and chemical oxidation, most of the remediation technologies do not degrade the contaminant in-situ, thus requiring combination of technologies leading to higher remediation cost. Various technologies for removing MTBE were developed to remove contaminants from contaminated ground, such as air sparging, soil vapour extraction (SVE) and pump-and-treat (US EPA, 2004). The removal efficiency of a contaminant using these technologies can be affected by various factors such as ground and contaminant properties (Mackay and Cherry, 1989; Domenico and Schwartz, 1997; US EPA, 2004).

Ground properties can be categorised into physical, chemical and biological properties. The physical properties encompass the distribution of grain size and soil layering, which influences the permeability of soil and contaminant migration. The soil heterogeneity (Figure 1.1) can sometimes limit the coverage of a remediation project (Mackay and Cherry, 1989; Domenico and Schwartz, 1997). Chemical properties include the pH and constituents of groundwater based on the geologic formation, which can affect the transportation of a contaminant or inhibit a treatment process. Biological properties are usually concerned with the degradation of a contaminant by naturally existing microbial activities.

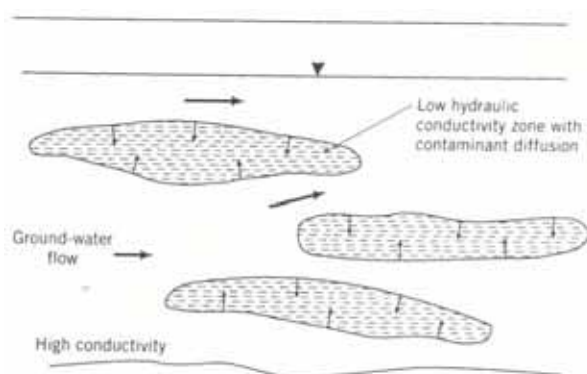


**Figure 1.1** Illustration of soil heterogeneity, with high and low hydraulic conductivity zones (Domenico and Schwartz, 1997)

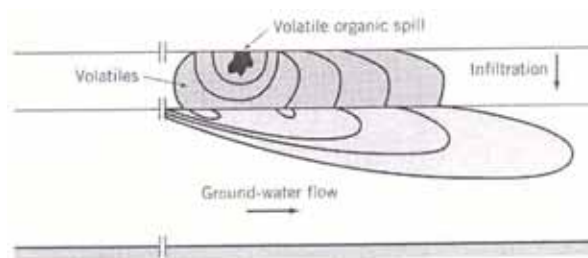


**Figure 1.2** Illustration of non-aqueous phase liquid (NAPL) migration in aquifer and vadose zone (Domenico and Schwartz, 1997)

Contaminant properties, such as Henry's law constant and solubility, can also affect the efficiency of a treatment technology and plume migration (Figure 1.2). Henry's law constant, usually expressed as the ratio of the saturated vapour pressure to the water solubility, determines the tendency of a contaminant to volatilise from groundwater into the vadose zone (soil gas). For instance, it is difficult for soil vapour extraction (SVE) alone to effectively remove a contaminant with low Henry's law constant as the contaminant tends to partition in water. It is also difficult for in-situ bioremediation alone to effectively remove a contaminant recalcitrant to biodegradation with high solubility, which is likely to have high mobility in water, at high groundwater flow. A contaminant with these properties is difficult to eliminate using a sole treatment, thus groundwater remediation projects for such contaminants require a combination of technologies.

Methyl tert butyl ether (MTBE), the target contaminant in this research, is a groundwater contaminant of concern which embodies the above mentioned contaminant properties (Johnson et al., 2000; Jacobs et al., 2001). A groundwater contaminant of concern can be a

contaminant which is persistent and affects the aesthetic value, whilst not necessarily highly toxic. MTBE is among the groundwater contaminants of concern mainly due to its (i) ability to make groundwater undrinkable as it gives the water an unpleasant taste and odour at concentrations above  $20 \mu\text{g L}^{-1}$  (Johnson et al., 2000; Jacobs et al., 2001; Da Silva and Alvarez, 2002), (ii) persistence in the environment and (iii) high solubility and mobility in groundwater. MTBE was extensively used as oxygenate in gasoline formulation to produce cleaner emission in many countries such as the United States (Jacobs et al., 2001), Denmark (Juhler and Felding, 2003) and Europe (Schmidt et al., 2003). This is also reflected by the number of groundwater contamination cases involving MTBE reported in many countries, such as Germany, United Kingdom (Schmidt et al., 2003) and the United States (Squillace et al., 1999; Johnson et al., 2000; Jacobs et al., 2001). MTBE is the second most frequently detected chemical in shallow ambient groundwater samples from urban areas (Deeb et al., 2000; Sahle-Demessie et al., 2002a). Despite the elimination of its consumption in the United States in 2006 (EIA, 2010), MTBE groundwater contamination from spillage and leakage still exists until it is cleaned up. The MTBE concentration varies from below 1 (Juhler and Felding, 2003) to  $830 \text{ mg L}^{-1}$  (Schmidt et al., 2003), depending on the location monitored, i.e. near or away from a pollution source. A MTBE contamination survey in the UK shows MTBE was detectable at 13 % of monitoring locations from 800 site investigations and 3,000 samples from public water supply and monitoring boreholes (Chan, 2005). MTBE concentrations in the UK sites are generally below  $1 \text{ mg L}^{-1}$ . The main concern of MTBE contamination is the destruction of odour and taste of water as there is no concrete scientific evidence of its threat on human health. MTBE does not bioconcentrate as it is released through exhalation and urine excretion (Jacobs et al., 2001).

## 1.2 Methyl Tert Butyl Ether (MTBE)

MTBE is an organic chemical compound, which is synthesized either from the oxidation of methanol ( $\text{CH}_3\text{OH}$ ) and isobutylene (isobutene or 2-methylpropene:  $((\text{CH}_3)_2\text{CCH}_2)$ ) or methanol or tertiary butyl alcohol ( $\text{C}_4\text{H}_9\text{OH}$ ) (Jacobs et al., 2001). Methanol is derived from natural gas while isobutylene is a petroleum refining by-product. Therefore, MTBE was widely used as oxygenate because it is easily and economically manufactured at the refinery and blends well with gasoline due to its relatively low polarity (Johnson et al., 2000). In addition, MTBE has low chemical reactivity with oxygen materials except strong oxidants such as hydrogen peroxide ( $\text{H}_2\text{O}_2$ ), resulting in a low tendency to form peroxides during storage and enables gasoline to be conveyed through existing pipelines (Chan, 2005).

MTBE is a clear, colourless, flammable and combustible liquid. Table 1.1 shows the physicochemical properties of MTBE. The chemical formula shows MTBE has a CH<sub>3</sub>-C-CH<sub>3</sub> bond of propane molecule and a CH<sub>3</sub>-O-C bond of an ether linkage, which contributes to its relatively low polarity of 2.5, compared to water of 10 (Jacobs et al., 2001). The one carbon long branches of MTBE molecule make MTBE very resistant to biodegradation, resulting in MTBE being persistent in groundwater.

**Table 1.1** Physicochemical properties of MTBE (Chan, 2005)

Properties	MTBE
Chemical Formula	
Structural Formula	(CH <sub>3</sub> ) <sub>3</sub> COCH <sub>3</sub>
Molecular Weight (g mol <sup>-1</sup> )	88.15
Density (kg m <sup>-3</sup> or g L <sup>-1</sup> ) at 20 °C	740
Aqueous Solubility (mg L <sup>-1</sup> or ppm)	42,000 to 54,300
Henry's Law Constant at 25 °C	0.0184
Octanol-water Partition Coefficient log(K <sub>ow</sub> )	1.05
Organic Carbon Partition Coefficient log(K <sub>oc</sub> ) (K <sub>oc</sub> in mL g <sup>-1</sup> )	0.94
Odour Threshold in Water (µg L <sup>-1</sup> or ppb)	20 to 50
Taste Threshold in Water (µg L <sup>-1</sup> or ppb)	10 to 100

According to Jacobs et al. (2001), molecules with molecular weight lower than 150 g mol<sup>-1</sup> are likely to have low melting and boiling temperatures, high vapour pressure and low adsorption coefficient. Therefore, MTBE, which has a molecular weight of 88.15 g mol<sup>-1</sup>, does not sorb or bind to soil particles and readily migrates or volatilises to the atmosphere from liquid state. However, MTBE has a Henry's Law constant lower than 0.05 indicating its tendency to remain or partition substantially into water (Jacobs et al., 2001). MTBE is readily soluble depending on the temperature, having high aqueous solubility ranging from 42,000 to 54,300 mg L<sup>-1</sup>, which is more than 30-fold that of benzene. However, the effective solubility of MTBE in the petroleum is about 3,300 mg L<sup>-1</sup> based on Raoult's law (Chan, 2005). Low log(K<sub>oc</sub>) (Table 1.1) implies MTBE does not adsorb significantly to carbon, partitions weakly to the organic fraction in vadose zone (soil) and migrates at the groundwater flow. It also indicates that activated carbon adsorption is not effective in removing MTBE from groundwater.

The resistance to biodegradation, low Henry's law constant, high solubility, low  $\log(K_{oc})$ , and low adsorption coefficient contribute to the persistence and high mobility of MTBE in groundwater, with kilometer-scale plumes have been documented (Johnson et al., 2000). Despite having specific density of 0.74, MTBE does not float and volatilise in an aquifer. The odour and taste thresholds of MTBE in water shows that MTBE could be detected at trace concentration below  $100 \mu\text{g L}^{-1}$  (Table 1.1).

### 1.3 Existing Groundwater Treatment Technologies

In order to eliminate MTBE from groundwater, several soil and groundwater treatment technologies have been used, for instance air stripping, soil vapour extraction (SVE), bioremediation, in-situ chemical oxidation and pump-and-treat (US EPA, 2004). Some of the technologies are listed in Table 1.2 and described in the following sections. Besides the afore-mentioned site characteristics, the selection of groundwater remediation technologies depends on the objective of the remediation project. As most of these technologies extract VOCs from soil and groundwater, it is appropriate for chemical recovery projects. The volatile organic compounds (VOCs) extracted are typically treated using above-ground technologies such as adsorption, biofilter and thermal oxidation (US EPA, 2004).

The selection of groundwater remediation technologies in a groundwater remediation project also depends on the time frame to achieve the desired clean-up level and available budget. Table 1.2 provides an overview of the project duration and cost of the existing technologies, and shows that some of the technologies could be more expensive and/or require longer treatment duration. However, the project duration and cost are not related as the documented data are not from the same projects. It should also be noted that the cost of the respective system was provided for information only, not for comparison as the scale of the projects was unknown.

**Table 1.2** Project duration and cost data for completed stand alone technology applications for MTBE remediation (US EPA, 2004)

Technology	Median Project Duration (months)	Total Project Cost (USD)
Air Stripping	22	247,000
Soil Vapour Extraction (SVE)	21	206,000
Multi-Phase Extraction (MPE)	45	257,000
Bioremediation	6	137,000
In-situ Chemical Oxidation	12	103,000
Pump-and-Treat	31	327,000

Another consideration involved in selecting an appropriate technology is the contaminant removal efficiency. Table 1.3 shows the efficiency of the technologies represented by the median initial MTBE concentration ( $C_0$ ) and final concentration ( $C_F$ ) from 109 completed stand alone remediation projects in the United States. All these remediation technologies achieved more than 99% MTBE removal in groundwater in some of the projects.

**Table 1.3** Performance data for completed stand alone technology applications for MTBE remediation (US EPA, 2004)

Technology	No. of Projects	Median $C_0$ ( $\mu\text{g L}^{-1}$ )	Median $C_F$ ( $\mu\text{g L}^{-1}$ )
Air Stripping	19	2,100	16
Soil Vapour Extraction (SVE)	23	2,600	21
Multi-Phase Extraction (MPE)	3	55	435
Bioremediation	35	3,880	30
In-situ Chemical Oxidation	8	11,700	75
Pump-and-Treat	21	1,610	11

Some of the technologies are not applicable in other countries due to the regulations. For instance, the pump-and-treat method applied in some of the projects in the United States is not appropriate in the United Kingdom and Europe because groundwater is not allowed to be extracted, partially treated and recharged into the ground based on the Water Framework Directive (European Commission, 2000; European Commission, 2006).

### 1.3.1 Air Stripping

Air stripping, also known as air sparging, involves the injection of air into groundwater to vaporise volatile organic compounds (VOCs) into the vadose zone. Air stripping is conducted by injecting compressed air through one or more pipes, into the ground (soil) or in a borehole, trench or well screened below the groundwater level (Figure 1.3). Consequently, the dissolved VOCs partition to the injected air based on their properties such as Henry's law constant. Some oxygen in the injected air dissolved into groundwater, which stimulates the biodegradation of contaminants. Pilot-scale testing of an air stripping system is required to determine the radius of influence (ROI) of an air stripping well under site conditions.

The treatability of contaminants are dependent on the tendency of a contaminant to volatilise into the soil gas determined by their Henry's law constant, and also the soil heterogeneity. Henry's law constant is the ratio of volatility/solubility, or the ratio of partial pressure in the vapour phase to the concentration in the liquid phase at a specific temperature. This affects the air flow requirement whereby higher air flow is required for a lower Henry's Law constant, and vice versa, to drive the compound into the vapour phase from groundwater. The

Henry's law constant of MTBE is lower than 0.05, thus indicates high air flow is required to steer MTBE into vadose zone as it tends to partition substantially into groundwater (Jacobs et al., 2001). MTBE requires about 5 to 10 times higher air flow (as high as  $1 \text{ m}^3 \text{ min}^{-1}$ ) than that of BTEX (US EPA, 2004), implying that air stripping can be an energy intensive process in removing MTBE (Shih et al., 2003).

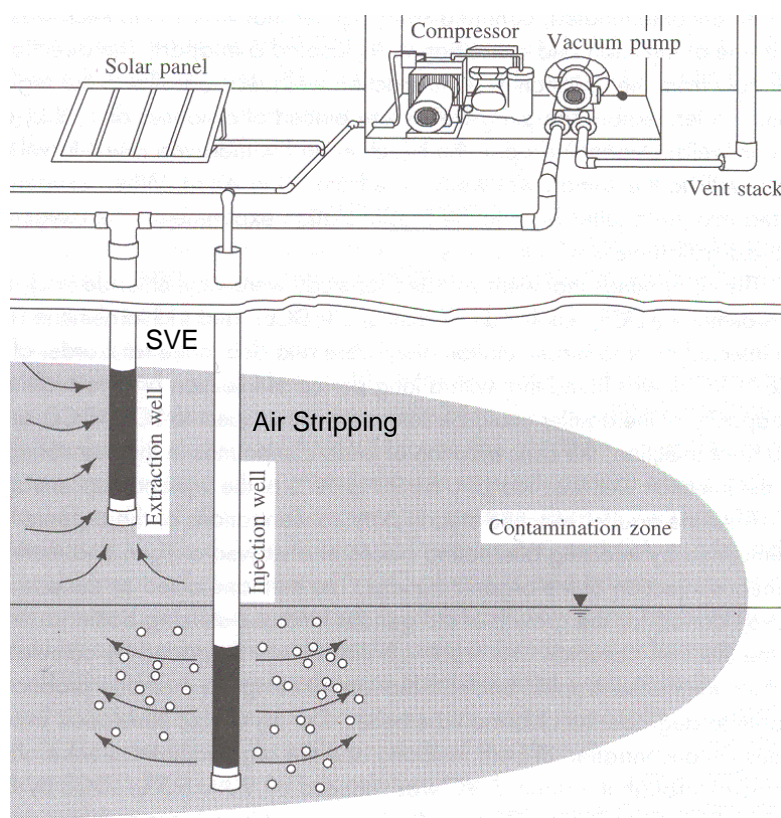


**Figure 1.3** Coupling of air stripping (right) and soil vapour extraction (SVE) (left) in a groundwater remediation project (Fetter, 1999)

Air stripping is generally simple to implement compared to other technologies as it involves physical processes. Contaminants stripped from groundwater could attenuate naturally in the vadose zone, particularly for low concentration contaminants. This is because the injection of air into groundwater also promotes aerobic degradation by microbes. However, VOCs are usually not biodegradable under oxic conditions (Domenico and Schwartz, 1997) and more unlikely for MTBE degradation due to its recalcitrance towards biodegradation.

Air stripping is only effective in conveying VOCs from groundwater to the vadose zone, rather than degrading the VOCs. Therefore, most of the groundwater remediation projects

involving air stripping require combination with another technology, for instance with soil vapour extraction (Gibbs et al., 2001; Lambert et al., 2009). Only 20 of 123 air sparging projects used the technology as stand alone system for groundwater with low contamination (US EPA, 2004). 74 of 123 air sparging projects involved coupling with SVE (US EPA, 2004). It is also combined with technologies, such as thermal oxidation (US EPA, 2004) and bioremediation, known as biosparging (Lambert et al., 2009), in groundwater remediation projects to degrade the contaminant. The requirement to combine with other technologies increases the total remediation project cost.

The median cost of an air sparging system is approximately USD 250,000, ranging from USD 100,000 to USD 350,000 (US EPA, 2004). The median project duration ranged from 1 to 5 years (US EPA, 2004).

### 1.3.2 Soil Vapour Extraction (SVE)

Soil vapour extraction (SVE) applies vacuum in the vadose zone to extract and gather VOCs prior to decomposition by aboveground treatment. SVE systems (Figure 1.3 and 1.4) consist of vapour extraction wells, connected to a vacuum pump to withdraw vapour from the vadose zone, and air vent wells, which provide a pathway of least resistance to allow circulation of air through the soil being remediated. The construction of air vent wells are similar to that of vapour extraction wells, except for the opening above-ground being capped with an inverted U-trap to avoid rain instead of connected to a vacuum pump.

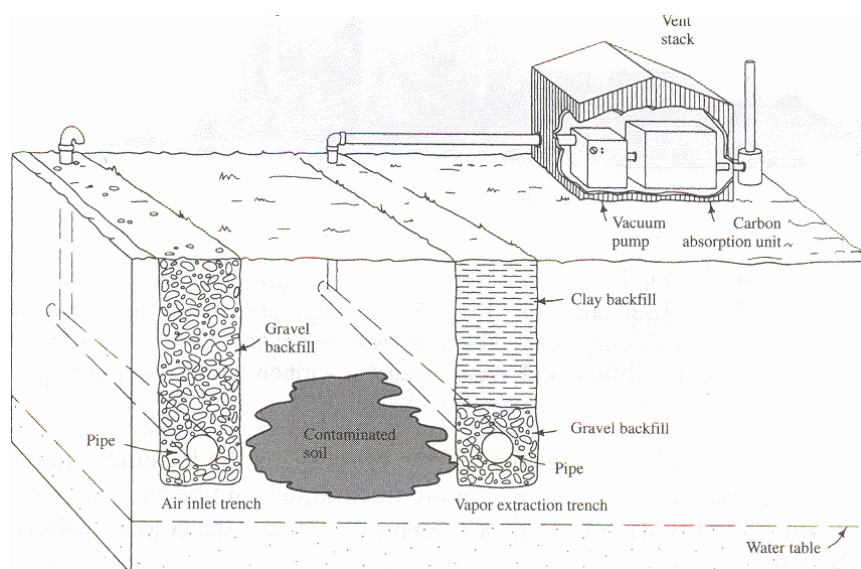


**Figure 1.4** Soil vapour extraction (SVE) system (Fetter, 1999)

The extraction of vapour is expected to be more efficient in removing contaminant from the ground than that of pump-and-treat, which withdraw contaminated groundwater. This is because VOC vapour migrates more easily through the vadose zone than groundwater through pores among soil grains; more pore volumes of air can be migrated through the similar dimension of soil than water, for the same duration. In addition, the extraction of VOC vapour in the vadose zone can minimise groundwater contamination via infiltration of dissolved VOC vapour by rainfall (Figure 1.2) (Mackay and Cherry, 1989; Domenico and Schwartz, 1997; Fetter, 1999).

SVE is suitable for extracting VOCs with vapour pressures greater than 10 mm Hg (US EPA, 2004), to control contaminant spread in the vadose zone, which if they accumulate in basements can lead to fire or explosion hazard, especially hydrocarbon vapours (Fetter, 1999). Therefore, SVE is expected to be effective in extracting MTBE, with vapour pressure of about 250 mm Hg, from the ground. It is among the most popular remediation technologies as it is applied in 42% of the remediation projects in the United States (US EPA, 2004). However, the low volatility (Henry's law constant) of MTBE due to the formation of hydrogen bonds by MTBE and water (Jacobs et al., 2001), implies that SVE needs to be coupled with air stripping in order to enhance the MTBE removal from the ground. As both technologies do not destroy MTBE, a combination with above-ground technologies is required to destroy MTBE, which increases the remediation project costs. SVEs are not effective for sites with high groundwater level (Fetter, 1999).

It is relatively more cost-effective and economical than other remediation technologies. The median cost of a SVE system is approximately USD 206,000, ranging from USD 100,000 to USD 400,000 (US EPA, 2004). The median project duration from 22 projects was 21 months, ranging from 3 to 66 months (US EPA, 2004).

### 1.3.3 Pump-and-Treat

Pump-and-treat shares a similar concept to that of SVE as in the withdrawal of contaminant from the ground, in the form of groundwater. A pump-and-treat system consists of vertical groundwater recovery wells, which groundwater is extracted and conveyed to an above-ground technology to be treated (Figure 1.5). The initial decline in the concentration of a contaminant using pump-and-treat systems is typically rapid, indicating the removal of contaminants from the larger pores. The concentration will eventually reach a steady-state, as contaminants are removed to the smaller pores, where the contaminant removal rate is equal to its release rate; contributing to the tailing. Therefore, pump-and-treat systems are more suitable for contaminant migration control instead of groundwater remediation as it

could not completely remove contaminant (Mackay and Cherry, 1989) due to tailing caused by the presence of non-aqueous phase liquids (NAPLs), effect of sorption and heterogeneity in hydraulic conductivity (Domenico and Schwartz, 1997).

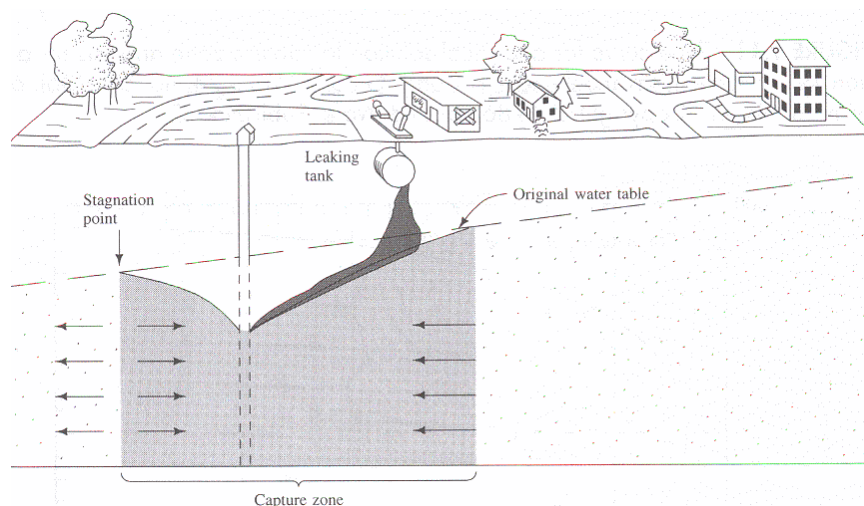


**Figure 1.5** Groundwater extraction using a pump-and-treat system (Fetter, 1999)

Unlike SVE, pump-and-treat is suitable for the withdrawal of less volatile contaminants, to limit the migration of contaminants. It is effective in removing large amount of contaminants from a permeable aquifer, particularly during the initial phase of pumping; suitable for contaminant migration control. It is usually coupled with an above-ground treatment technology for the elimination of contaminants from the extracted groundwater, prior to use or disposal. Examples of the incorporation of pump-and-treat in groundwater remediation projects include air stripping, adsorption, chemical oxidation and biotreatment (US EPA, 2004). It was also coupled with a falling film reactor (Almquist et al., 1993) and field scale solar photocatalytic reactor (Mehos and Turchi, 1993), which intended to eliminate MTBE and trichloroethylene (TCE), respectively. However, the contaminant removal efficiency from the ground is usually not mentioned in these studies, presumably because the mass of contaminant in groundwater is unknown.

The efficiency of a pump-and-treat system is usually limited by the presence of DNAPLs and heterogeneity of soil (Mackay and Cherry, 1989; Domenico and Schwartz, 1997). Projects involving pump-and-treat technology generally requires higher costs and longer times especially for sites with heterogeneous soil, which requires withdrawal of more pore volumes of groundwater prior to achieving the goal of the clean-up especially in removing a strongly sorbed contaminant (higher retardation factor) to the porous mediums (Mackay and Cherry,

1989; Domenico and Schwartz, 1997). Coupling of pump-and-treat system with barriers or wells may be required to isolate a pollution source, in order to enhance the removal efficiency in the presence of NAPLs (Domenico and Schwartz, 1997).

A pump-and-treat system is also relatively more expensive than other groundwater remediation technologies (US EPA, 2004), needless to mention the total remediation project costs as it requires combination with an above-ground technology to destroy contaminants. The median cost of a pump-and-treat system is approximately USD 500,000, ranging from USD 72,000 to USD 1,120,000 (US EPA, 2004). The median project duration, from 17 projects, was about 31 months, with the range from less than 1 to 75 months (US EPA, 2004).

#### 1.3.4 Bioremediation

Bioremediation is an enhanced biodegradation of organic contaminants by stimulating the microbial activities through supply of air and other amendments such as nutrients, pH or conditioner into groundwater. Although MTBE is known to be persistent towards biodegradation in general, bioremediation is surprisingly among the popular groundwater remediation technologies, notably due to the economical treatment (US EPA, 2004) and typical MTBE concentrations below  $1 \text{ mg L}^{-1}$  (Juhler and Felding, 2003; Ruiz-Aguilar et al., 2002). Bioremediation can be configured ex- or in-situ, such as activated sludge in a bioreactor (Davis and Erickson, 2002) and permeable barriers (Bowles et al., 2000; Guerin et al., 2002; Liu et al., 2006; Saponaro et al., 2009), respectively. However, the latter is typically applied in groundwater remediation projects. Bioremediation is applied in-situ in 73 of 323 projects in the United States (US EPA, 2004). Unlike other technologies, 92 % of bioremediation systems were applied as stand alone systems (US EPA, 2004). It is often combined with extraction type technology for degrading extracted contaminants.

In-situ bioremediation can be initiated by introducing a bacterial culture (Liu et al., 2006; Saponaro, 2009) or relying on the local microbial activities of the soil, also known as natural attenuation (Schirmer et al., 1999; Kane et al., 2001; Guerin et al., 2002). Nevertheless, both methods require certain soil conditioning such as air stripping, pH and/or nutrient adjustment (Deeb et al., 2000). Figure 1.6 shows an in-situ bioremediation system using injection and withdrawal wells. The bacteria in groundwater and soil is stimulated by addition of nutrients and injection of compressed air. Groundwater can be withdrawn to be discharged or recirculated. Aerobic biodegradation is preferred to anaerobic biodegradation due to the faster degradation rate of the former and risk of more toxic product formation by the latter. Therefore, aeration (Bowles et al., 2000; Guerin et al., 2002) or addition of

oxygen-releasing compounds (Liu et al., 2006) is required due to the low dissolved oxygen concentration in groundwater, which is not sufficient to maintain aerobic biodegradation of organic contaminants (Liu et al., 2006).

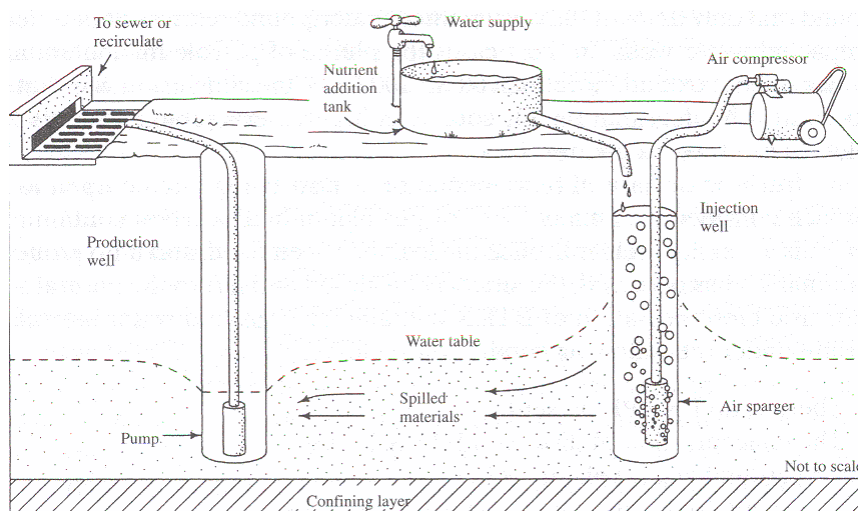


**Figure 1.6** In-situ bioremediation (Fetter, 1999)

Bioremediation is typically significantly slower than chemical oxidation, which implies longer project duration and larger remediation area (footprint) involved. Kane et al. (2001) obtained almost complete MTBE removal in two of their four samples in 15 days (batch experiment,  $C_0 = 4.5 \text{ mg L}^{-1}$ ), while Liu et al. (2006) and Saponaro et al. (2009) achieved about 50 % MTBE removal using a biological two-layer permeable layer in 800 hours (33 days) ( $C_0 = 160 \text{ mg L}^{-1}$  and  $25.0 \text{ cm d}^{-1}$ ) and a 11.4 L column in 40 days ( $C_0 = 950 \text{ mg L}^{-1}$ ,  $5.9 \text{ cm d}^{-1}$  and  $20.3 \text{ d HRT}$ ), respectively. The first order aerobic biodegradation rate of MTBE varies between  $0.005$  and  $0.4 \text{ d}^{-1}$  (Davis and Erickson, 2004), however, the higher rates were obtained in controlled laboratory scale experiments. Schirmer et al. (1999) found that the rates obtained in their laboratory experiments were about 1.5 times greater than that in the field; but still relatively slower than that of advanced oxidation processes.

Among the major disadvantages of bioremediation is the inconsistencies of the results and findings (Deeb et al., 2000). While many studies found that the microbes would be selective in biodegrading readily biodegradable contaminants prior to the harder ones (Deeb et al., 2000; Da Silva and Alvarez, 2002; Ruiz-Aguilar et al., 2002), some found that simultaneous MTBE and tert butyl alcohol (TBA) biodegradation or the MTBE was degraded significantly prior to TBA, which leads to the accumulation of the more toxic TBA (Saponaro et al., 2009).

Deeb et al. (2000) reported that  $0.15 \text{ mg L}^{-1}$  BTEX can inhibit the biodegradation of MTBE. Longer MTBE plumes are expected due to the inhibition of MTBE biodegradation in the presence of ethanol as ethanol is biodegraded first (Ruiz-Aguilar et al., 2002). Ethanol could also deplete available electron acceptors and stimulate anaerobic biodegradation processes (Ruiz-Aguilar et al., 2002). In addition, the anaerobic biodegradation process, which occurs in the deeper zone in the ground is not well understood and could produce toxic products, which could affect the ecology in the subsurface and worsen the contamination issue.

The median cost of a bioremediation system is approximately USD 125,000, ranging from USD 50,000 to USD 350,000 (US EPA, 2004). The median project duration from 24 projects was 6 months, ranging from less than 1 to 60 months (US EPA, 2004).

### 1.3.5 *In-situ Chemical Oxidation*

In-situ chemical oxidation involves the introduction of chemicals, such as hydrogen peroxide (Yeh and Novak, 1995) and permanganate (Yan and Schwartz, 1999), into the subsurface to oxidise the contaminants. There are several methods of introducing oxidants, namely groundwater well injection (similar to air sparging in Figure 1.6 except introducing oxidants), soil mixing and permeable reactive barrier (US EPA, 2004). In some cases, the chemical reaction is also assisted by ultraviolet C (UVC) light, such as ozone and UVC (Garoma et al., 2008). It is a rapid and mildly selective process, which can oxidise all ether and alcohol based oxygenates to the target concentration within several months to a year. It is also applied to degrade inert contaminants which are not effective using bioremediation. 67 % of 21 in-situ chemical oxidation projects was applied as stand alone systems for treating MTBE concentration up to 10,000 ppb (US EPA, 2004).

As an in-situ chemical oxidation is a mildly selective process, a large amount of oxidant is required particularly for sites with high concentration of oxidisable groundwater constituents, resulting in higher project cost. Besides health and safety mitigating measures in handling the oxidants, special precautions in injecting the oxidants need to be considered as concentrated oxidant injection can cause violent subsurface reactions. An off-gas system may be required for the extraction and treatment of potential toxic vapour (by-products) from the chemical reactions in groundwater, for instance bromate during ozone oxidation (Shih et al., 2003; US EPA, 2004).

The cost of an in-situ chemical oxidation system is approximately USD 146,000, based on the only project cost reported (US EPA, 2004). The median project duration from seven projects is about 12 months, ranging from 2 to 18 months (US EPA, 2004).

### 1.3.6 Adsorption

Adsorption is a physicochemical process involving the adhesion of contaminant molecules, in the form of either gas, liquid or dissolved solid, to a surface, driven by equilibrium forces. An adsorption process is commonly used in barriers, such as trench and funnel and gate systems (Figure 1.7), for contaminant containment projects (Boulding, 1995). However, the adsorbed contaminants are not degraded; only transferred through media. An adsorbent has a saturation limit, which is dependent on the contaminant loading, and groundwater conditions and flow. Activated carbon is a popular adsorbent used in water and wastewater treatment to immobilise organic substances and non-polar adsorbates. Its efficiency relies upon several factors such as the adsorptivity of the contaminant molecule and the porosity of the adsorbent.

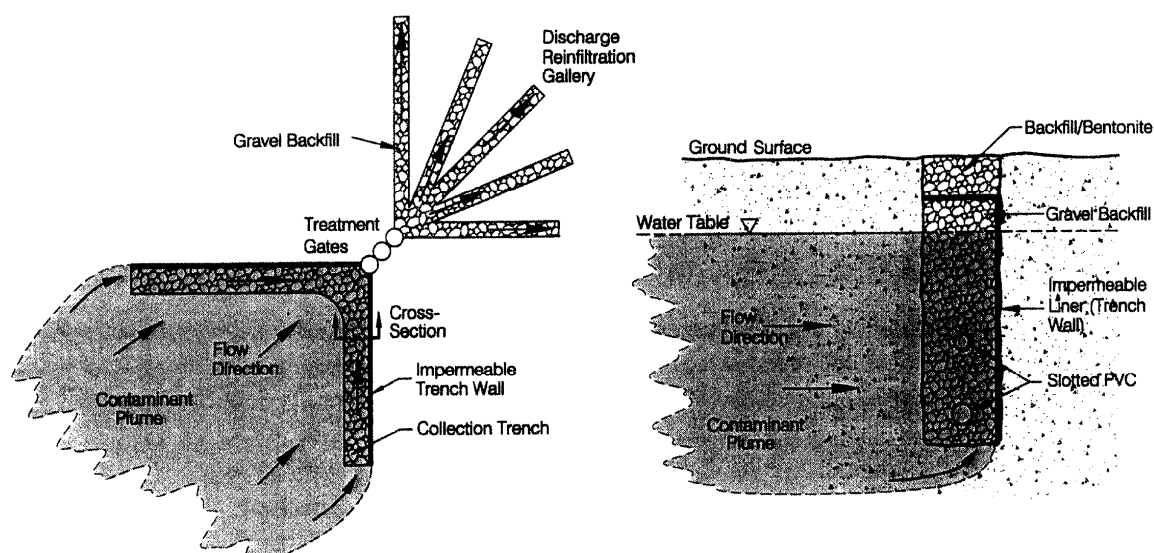


**Figure 1.7** Funnel and gate (left) and trench (right) systems (Bowles et al., 2000)

MTBE, an organic compound with low polarity, does not adsorb well to many surfaces. Only about 8 % MTBE present in an aquifer would be adsorbed to a subsurface material compared to 40 % of benzene (Jacobs et al., 2001). The adsorptivity of MTBE appears to increase with the organic carbon content of the adsorbent. Even then, only activated carbon made from coconut shell is claimed to be effective in adsorbing MTBE, among all the other types of activated carbon (Shih et al., 2003). Similar to biodegradation, it is also a common groundwater remediation technology, typically used in trenches, known as permeable reactor barrier. However, adsorption is not suitable for removing MTBE from groundwater (Shih et al., 2003).

One of the major disadvantages of using an adsorbent is that the spent adsorbent typically requires replacement; involving removal and landfill. When saturated, the adsorbate becomes inactive and it is either; regenerated, disposed in landfill or left in the ground. In addition, there is a risk of desorption of contaminant molecules especially in the saturated phase of certain adsorbent, leading to leaching of contaminant in the long term without careful monitoring. The permeability of adsorbent packing decreases gradually with clogging by solids (Boulding, 1995) and formation of biofilm, which is possible with the contaminant concentrated by the adsorbent. Similar to other treatment technologies, the removal efficiency of MTBE by an adsorbent can also be affected by the presence of more strongly adsorbed constituents (Shih et al., 2003).

### 1.3.7 Summary of Advantages and Disadvantages

In order to assist the selection of technologies in a groundwater remediation project, the pros and cons of the technologies needs to be listed for thorough considerations. As mentioned earlier, the efficiency of most technologies are affected by soil heterogeneity. The advantages and disadvantages of the above-mentioned technologies are summarised in Table 1.4.

**Table 1.4** Summary of advantages and disadvantages of existing remediation technologies

<b>Technology</b>	<b>Advantages</b>	<b>Disadvantages</b>
Air Stripping	<p>Cost effective technology for groundwater remediation</p> <p>Effective removal of VOCs from groundwater</p> <p>Enables recovery of contaminants</p> <p>Encourages aerobic biodegradation by increasing dissolved oxygen concentration</p> <p>Minimal disturbances to site operations</p>	<p>Requires coupling soil vapour extraction or off-gass system to remove contaminant from the ground, and with above-ground technology for decomposition of VOCs; increasing the total project cost</p> <p>Air injection into groundwater causes lateral spread of dissolved or separate phase contaminants plume</p> <p>High air flow could cause fracture leading to non-uniform flow</p> <p>Removal efficiency affected by soil heterogeneity</p>
Soil Vapour Extraction	<p>Controls migration of vapour into buildings or leaching into groundwater by extracting the VOC vapour in the vadose zone</p> <p>Cost effective technology in removing VOC from site</p> <p>Enable recovery of contaminants</p> <p>Minimal disturbance to site operations</p>	<p>Incapable of complying with very rigorous soil clean-up levels as soil concentrations could achieve an asymptotic level which is higher than the legislated level</p> <p>Requires air sparging to drive VOCs from groundwater and above-ground technologies to decompose VOCs;</p>

	as it is implemented in the subsurface	<p>increasing the total project cost</p> <p>Not suitable for sites with high or fluctuating groundwater table as it extracts VOCs from the vadose zone and is prone to upwelling and interference with air flow</p> <p>Removal efficiency affected by soil heterogeneity consisting low permeability layers</p>
Pump-and-Treat	<p>Rapid removal of large amount of contaminant from the ground to control the spread</p> <p>Enable recovery of contaminant</p>	<p>Construction, operation and maintenance cost is relatively more expensive than other technologies</p> <p>Require coupling with above-ground treatment technologies for destruction of contaminants; increasing total treatment cost</p> <p>Require extended operation and maintenance duration</p> <p>System performance can be affected by biofouling or mineral precipitation in the extraction wells</p> <p>Contaminant removal efficiency from ground is affected by soil heterogeneity (Domenico and Schwartz, 1997)</p>
Bioremediation	<p>Economical technology</p> <p>Able to treat soil and groundwater</p> <p>Minimum energy requirement</p> <p>Simple installation using commercially available material</p> <p>Does not pose much obstruction to site operation (US EPA, 2004)</p> <p>Bacteria are most likely to be concentrated on areas with higher concentration</p> <p>Does not require pumping of groundwater for disposal</p> <p>Not affected by soil heterogeneity if applied in a trench</p>	<p>Immobilisation of bacteria forms biofilm, which gradually reduces soil permeability by clogging the pores</p> <p>Relatively more selective and slow organic degradation rates compared to chemical oxidation; requires preliminary studies to confirm the applicability and dependent on site conditions; difficult to implement in aquifers with hydraulic conductivity slower than <math>10^{-4} \text{ cm s}^{-1}</math> (US EPA, 2004)</p> <p>Slow and sometimes unstable microbial growth of oxygenate-degrading microorganisms under aerobic condition (Liu et al., 2006); require a substantial period for microorganisms to acclimatise as it may not be present natively at all sites</p> <p>Require long term monitoring and maintenance as bioremediation is a relatively slow treatment and sensitive to site conditions</p> <p>Vulnerable to inhibition by certain chemicals (Deeb et al., 2000)</p> <p>Highly variable degradation rates under different environmental conditions (Liu et al., 2006)</p> <p>Require conditioning of soil such as nutrient addition and pH control between</p>

		<p>ph 6.5 and 8.5 (Liu et al., 2006)</p> <p>Long term effects on the environment unknown</p>
In-situ Chemical Oxidation	<p>Mildly selective in the oxidation of organic compounds, thus can be used as sole in-situ clean-up technology</p> <p>Can be commissioned within a short period of time and does not require preliminary studies to confirm its applicability in terms of contaminant type; the required amount of oxidant to achieve complete oxidation is determined by the stoichiometric proportion to the number of carbon atoms in the oxygenate from chemical equation</p> <p>Rapid oxidation rates imply shorter project duration to achieve clean-up goal</p> <p>Can be a cost effective technology for sites not amenable to bioremediation</p> <p>Minimal disturbances to site operations</p> <p>Not affected by soil heterogeneity if applied in a trench</p>	<p>Continual oxidising agent addition is required for on-going pollution</p> <p>Special precautions need to be taken for occupational health and safety of worker and during oxidant injection as it involves highly reactive oxidants (US EPA, 2004)</p> <p>Larger amount of oxidant could be required for sites with high concentration of native organic matter in groundwater</p> <p>Risk of producing toxic by-products, which could affect the ecology in the area and worsen the contamination issue (Liu et al., 2006); might require an off-gas system for extraction and treatment</p> <p>Removal efficiency affected by soil heterogeneity; not suitable for sites with heterogeneous media or low permeability as inhibition in aqueous movement limits the contact between oxidant and contaminant</p>
Adsorption	<p>Low cost material</p> <p>Effective retardation of certain compounds</p> <p>Enable recovery of contaminants</p> <p>Not affected by soil heterogeneity if applied in a trench</p>	<p>Saturated adsorbent is eventually removed and landfilled</p> <p>Risk of leaching of contaminant when adsorbent is saturated via desorption</p> <p>Not effective in removing contaminant with low adsorptivity</p> <p>Gradual decrease of permeability of adsorbent packing due to clogging by solids and potential biofilm formation</p> <p>Removal efficiency of contaminant is affected by the presence of more strongly adsorbed groundwater constituents</p>

#### 1.4 Photocatalysis and Existing Photocatalytic Reactor Designs

Photocatalysis is an advanced oxidation process, in which the photocatalytic reaction is initiated when a catalyst is activated via UVA light illumination. It has been proven effective in degrading a plethora of organic compounds (Hoffmann et al., 1995; Herrmann, 2005). It is an environmentally friendly technology in terms of (i) material: the photocatalyst, i.e. titanium dioxide ( $\text{TiO}_2$ ) is safe to handle as it is not a toxic material and can be regenerated

(Bhatkhande et al., 2001), (ii) reaction: a complete aerobic degradation of organic compounds yields carbon dioxide, water and simple mineral acids (Mills et al., 1993; Hoffmann et al., 1995; Barreto et al., 1995), (iii) operation: photocatalysis does not require addition of chemical oxidants (Chan and Lynch, 2003a and b; Sahle-Demessie et al., 2002a; Dionysiou et al., 2002), (iv) localised treatment: its application does not have an effect on its vicinity (Chan, 2005) as it will only be activated upon UVA light illumination; compared to chemical oxidation and biodegradation, and (v) controllable: there is no reaction with photocatalyst when the UVA lamps are switched off except adsorption, which is dependent on the adsorptivity of the compound. In addition, photocatalysis can be operated in both aqueous and vapour phase, therefore the operation is not affected by the fluctuating groundwater level.

Similar to in-situ chemical oxidation, the oxidisation of compounds occurs via contact with oxidising agents, i.e. radicals formed through electron transfer in the case of photocatalysis. The generation of oxidising radicals is detailed in Section 2.1 in Chapter 2. Unlike in-situ chemical oxidation, the oxidising radicals are continuously generated only in the presence of UVA light, oxygen and photocatalyst, i.e. titanium dioxide ( $\text{TiO}_2$ ).  $\text{TiO}_2$ , a semiconductor, is commercially available and a non-toxic material and safe for handling. This implies minimal operation cost and effort, compared to in-situ chemical oxidation. Previous studies have demonstrated effective degradation of MTBE (Barreto et al., 1995; Sahle-Demessie et al., 2002a and b; Chan and Lynch, 2003a and b). The overall chemical reaction equation of complete photocatalytic degradation of MTBE (Chan, 2005) is:



There are two types of photocatalytic reactor configurations, i.e. slurry (Mehos and Turchi, 1993; Mills et al., 1993; Alfano et al., 2000; Almquist et al., 2003) and immobilised catalyst (Peill and Hoffmann, 1998; Ray and Beenackers, 1998a and b; Dionysiou et al., 2000a; Chan and Lynch, 2003a and b; Bahnemann, 2004). A slurry reactor operates with  $\text{TiO}_2$  powder suspended in the contaminated water, while in an immobilised reactor, the  $\text{TiO}_2$  powder is fixed to a support. Although slurry reactors typically demonstrate higher photocatalytic activity than immobilised reactors, the latter are preferred for water treatment due to the requirement of post-treatment solid-liquid separation of nano-sized  $\text{TiO}_2$  particles in the slurry reactor, which can be costly and technically complicated to implement (Balasubramanian et al., 2004). Therefore, this research is focused on immobilised catalyst reactors. To date, there is no photocatalytic reactor designed for in-situ groundwater

remediation. Many compact photocatalytic reactor designs have been proposed and evaluated for water and wastewater treatment where the flow is necessarily high (Table 1.5). In contrast, groundwater flow is significantly slower than that of water and wastewater treatment, providing sufficient time for its clean-up. Most of these designs were not scaled up. Mukherjee and Ray (1999) reviewed that the scale up of a photocatalytic reactor is limited by light intensity and mass transfer of contaminant molecules on the catalyst surface. van Gerven et al. (2007) reported that the efficiency of a photocatalytic reactor can be optimised through the intensification of light intensity and mass transfer. The other possible issue is the immobilisation of TiO<sub>2</sub> onto a support for a large scale reactor, as commercial TiO<sub>2</sub> powder, which is typically photocatalytically more active than laboratory synthesized TiO<sub>2</sub>, does not adhere well onto many surfaces.

**Table 1.5** Specification and operating conditions of existing photocatalytic reactor designs; HRT: hydraulic residence time, A/V: surface area to volume ratio, e: exposed to sunlight, r: recirculation flow

Reactor Type	Flow (mL min <sup>-1</sup> )	HRT (min)	Reactor Volume (L), A/V (m <sup>2</sup> m <sup>-3</sup> )	Removal Efficiency (%)	Target Compound	Comment	Reference
Optical Fiber Reactor	0	Batch	4, 3.2	Complete degradation in 13 h	4-chlorophenol	Scale up (OFR2) described in Section 1.5.1	Peill (1996)
Multiple Tube Reactor	1800 <sup>r</sup>	0.42	1.23, 1087	~ 90 % in 100 mins	Special brilliant blue of Bayer dye	Laboratory scale	Ray (1999)
Solar Parabolic Photocatalytic Reactor	15000	10	74.8 <sup>e</sup> , 0.8 – 0.9 g L <sup>-1</sup> slurry	> 90 %	Trichloroethylene	Not scaled up Pilot scale Single pass	Mehos and Turchi (1993)
Fountain Photocatalytic Reactor	200 <sup>r</sup>	Not given	Not given, 0 - 2 g L <sup>-1</sup> slurry	Not given	Salicylic acid	Pilot scale UVA light intensity 7 mW cm <sup>-2</sup>	Li Puma and Yue (2001)
Falling Film Reactor	240 <sup>r</sup>	7.08	1.7, 0.1 g L <sup>-1</sup> slurry	~ 70 % in 180 mins (actual groundwater)	MTBE	Laboratory scale	Almquist et al. (2003)
Rotating Disk Photocatalytic Reactor	14	360	5, Area not given	Typically from 85 to 97 % for every compound after 24 h	Phenol, 4-chlorophenol, dichlorophenol, trichlorophenol, pentachlorophenol	Laboratory scale UVA light intensity 1.1 mW cm <sup>-2</sup> disk rotation speed 12 rpm	Dionysiou et al. (2002)
Photocat I	18 (5.3 <sup>r</sup> )	20.4	0.48, 5.5	~ 80 % in 14 h (Reactor V in lab scale tank)	MTBE	Laboratory scale Reactor had localised influence on MTBE concentration in the surrounding soil Scale up described in Section 1.5.7	Chan (2005)

### 1.4.1 Slurry Reactors

#### 1.4.1.1 Fountain Photocatalytic Reactor

The fountain photocatalytic reactor (Figure 1.8) was designed and developed by the Li Puma group at the University of Nottingham. The concept of this reactor design is to recirculate the contaminated water with  $\text{TiO}_2$  in suspension to the top of the reactor and create a thin film cascading to the edge of the canopy. The formation of thin film maximises the contact of the slurry with oxygen from atmosphere and UVA light from solar energy for the degradation of the contaminants. However, this design is not suitable for in-situ groundwater remediation as it requires the withdrawal of contaminated groundwater and post-treatment solid-liquid separation.

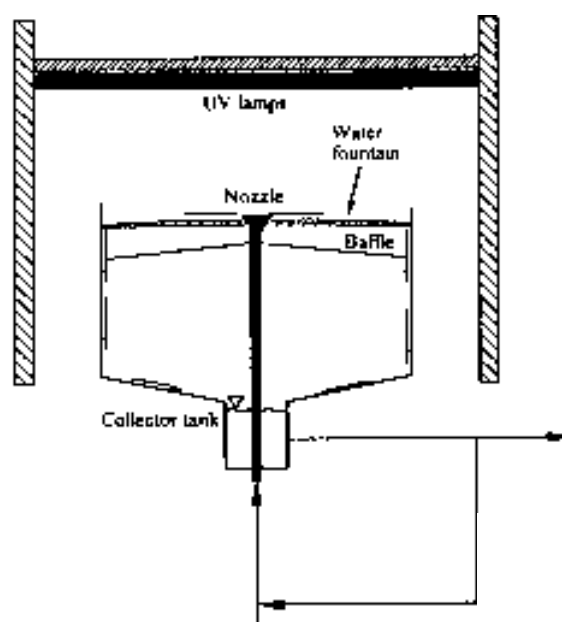


**Figure 1.8** Schematic diagram of the fountain photocatalytic reactor model in the laboratory scale experiments (Li Puma and Yue, 2001)

#### 1.4.1.2 Falling Film Reactor

The falling film reactor (Figure 1.9) (Almquist et al., 2003) by the Sahle-Demessie group uses a similar concept to that of the fountain photocatalytic reactor by the Li Puma group, i.e. treating contaminated groundwater in a thin film by recirculating with  $\text{TiO}_2$  in suspension. These were the few reactor studies addressing the remediation of MTBE contaminated groundwater. However, it is an ex-situ photocatalytic reactor design, which requires a pump-and-treat system to withdraw contaminated groundwater and post-treatment solid-liquid separation. There was no scale up testing for this reactor design and Sahle-Demessie et al.

(2002a) recommended the development of immobilised photocatalytic reactor for groundwater remediation.

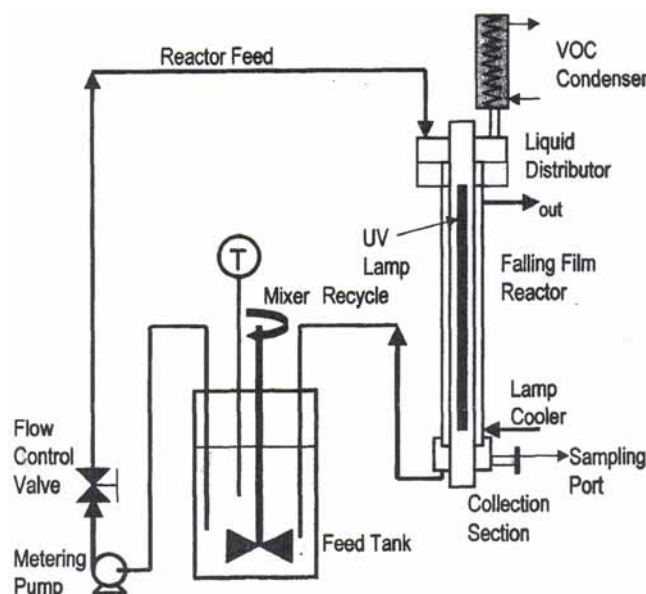


**Figure 1.9** Schematic diagram of the falling film reactor (Almquist et al., 2003)

#### 1.4.1.3 Solar Parabolic Photocatalytic Reactor

The parabolic photocatalytic reactor is notably a popular solar photocatalytic reactor, in which several variations of this reactor design concept were developed to a larger scale in several countries, mostly using slurry  $\text{TiO}_2$  and involving recirculation of contaminated water such as a parabolic trough reactor (PTR) (Figure 1.10a and b) and compound parabolic collecting reactor (CPCR) (Figure 1.10c and d) (Alfano et al., 2000), and parabolic trough (Figure 1.10e) (Mehos and Turchi, 1993). Most of the reactors were designed for wastewater treatment except that of Mehos and Turchi (1993), which was designed for remediating trichloroethylene (TCE) contaminated groundwater in Livermore (Figure 1.10e). Alfano et al. (2000) summarised the main benefits of slurry solar photocatalytic reactor as:

- i. low pressure drop through the reactor;
- ii. larger photocatalytic surface area available for adsorption and reaction, and;
- iii. better mass transfer of the wastewater contaminants from the fluid to  $\text{TiO}_2$

PTR (Figure 1.10a and b) comprises a tubular reactor, in which  $\text{TiO}_2$  is suspended in wastewater flowing in a reaction pipe, solar-illuminated via a light reflecting parabolic trough. It is a light concentrating reactor in which the reaction pipe is located at the focal line of the

light-reflecting parabolic trough (Figure 1.10a). Light concentrating reactors are postulated to employ half of the solar radiation in the UV spectra (Alfano et al., 2000). Therefore, another trough reactor was carried out without complete focusing of solar radiation, i.e. CPCR (Figure 1.10c and d). The only difference is the light reflecting trough consists of two half cylinders set side by side with the center line located closely above the connection of the two parabolic profiles (Figure 1.10c). This configuration enables solar radiation to be reflected into the “focal” line of the CPCR from any direction.

However, the major drawback is the requirement of solids separation as post treatment to retain the nano-sized titanium dioxide. Therefore, later studies were conducted using immobilised  $\text{TiO}_2$  reactor such as thin-film fixed-bed reactor (TFFBR) for textile wastewater treatment (Figure 1.11) (Bahnemann, 2004). Nevertheless, these ex-situ reactor designs require withdrawal of groundwater using pump-and-treat.

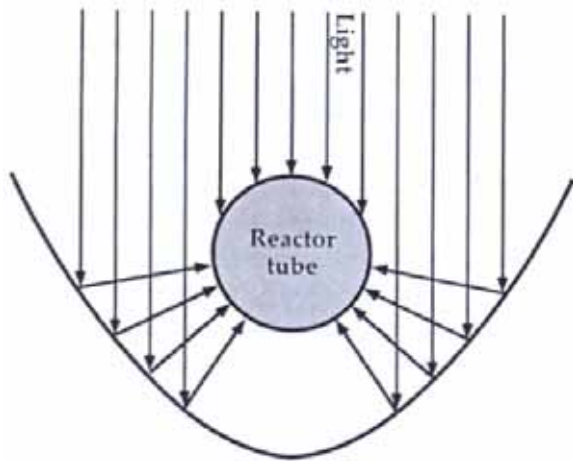


**Figure 1.10a** Geometric profile of a parabolic trough reactor (PTR) (Alfano et al., 2000)

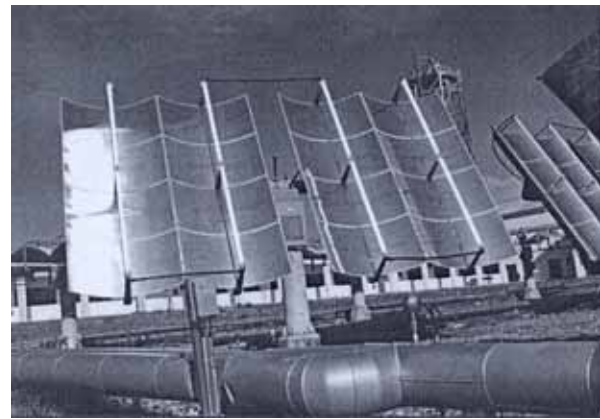


**Figure 1.10b** View of a PTR, type 'Helioman' (Alfano et al., 2000)

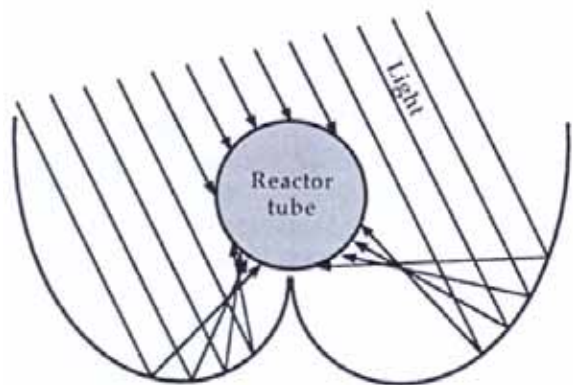


**Figure 1.10c** Geometric profile of a compound parabolic collecting reactor (CPCR) (Alfano et al., 2000)

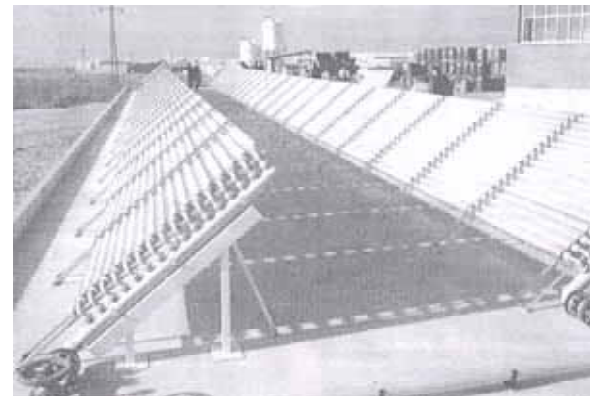


**Figure 1.10d** A CPC prototype (100 m<sup>2</sup>) at Hydrocen factory in Madrid (Robert and Malato, 2002)

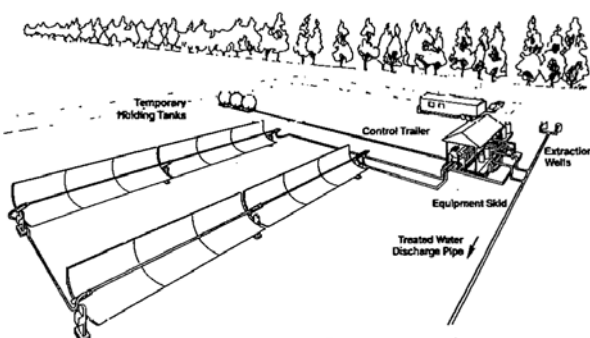


**Figure 1.10e** Field experiment using concentrating solar collector in Livermore (Mehos and Turchi, 1993)



**Figure 1.11** Pilot scale TFFBR for textile wastewater treatment (Bahnmann, 2004)

### 1.4.2 Immobilised Reactors

#### 1.4.2.1 Optical Fibre Reactor (OFR)

The fiber optic bundle array cable reactor (Figure 1.12) patented by Peill and Hoffmann (2000) utilises bundles of optical fibers for light transmission and as a substrate for titanium dioxide. The light is refracted out of the walls of the optical fiber into a photocatalytic coating to activate it. The air is introduced from the bottom of the reactor. The scale up (Figure 1.12) of this compact reactor design for pilot testing uses sunlight as UV light source, but the major limitation is that the treatment area is narrow and shallow, i.e. 30 cm deep (Figure 1.12), which makes it unsuitable for in-situ groundwater remediation. The utilisation of an equatorial sun tracker may be an innovative assistance to obtain maximum UV light intensity from sunlight during a sunny day but not on a cloudy or rainy day.

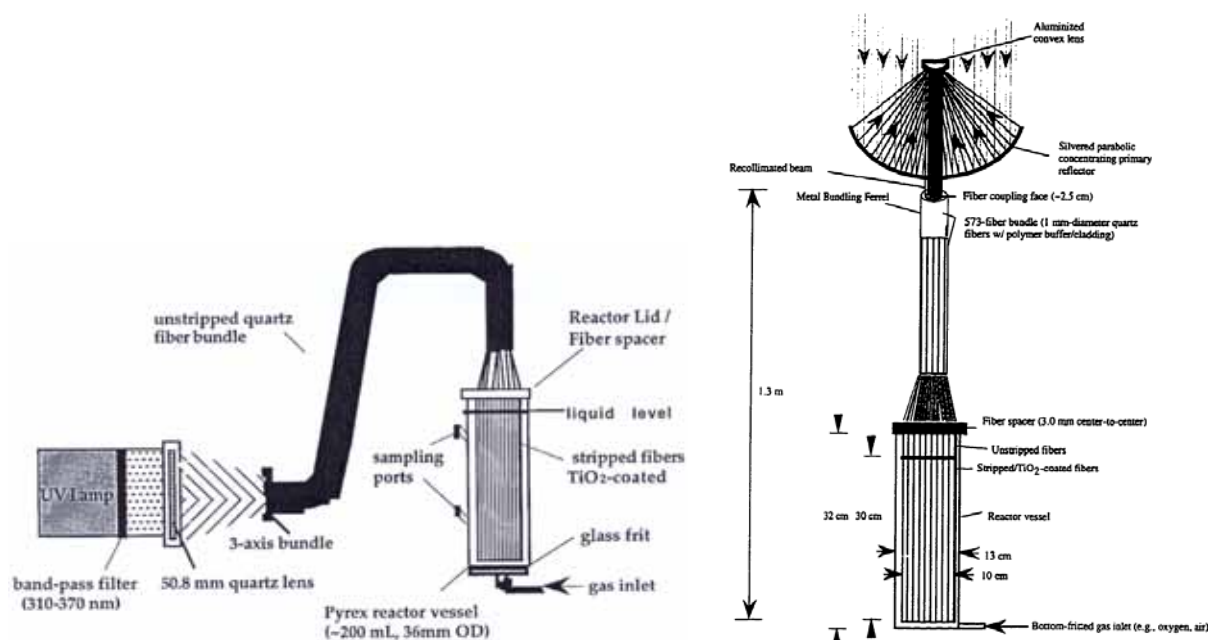


**Figure 1.12** Fiber optic bundle array cable reactor used in the laboratory scale experiments (Peill and Hoffmann, 1998) (left) and scaled up OFR2 with solar collector/concentrator, equatorial tracker not shown (Peill, 1996) (right)

#### 1.4.2.2 Multiple Tube Reactor (MTR)

Ray and Beenackers (1998a) used a distributive type of photocatalytic reactor where glass is applied as a light conducting material in the study, i.e. multiple tube reactor (MTR) (Figure 1.13). The configuration concept is similar to OFR by Peill and Hoffmann (1998), i.e. reflection of UV light by the inner wall of the tubes and configuring the immobilised  $\text{TiO}_2$

between the light source and contaminated water. The 5.6 cm cylindrical vessel consists of fifty-four 0.5 m long 6 mm hollow quartz glass tubes coated with  $\text{TiO}_2$  on its peripheral surface. The more expensive quartz tubes were favoured over Pyrex in terms of light transmissivity and handling of tubes as the price difference is not that appreciable. The catalyst was found to be almost inactive near the end of the tube at 0.5 m away from light source. Similar to the OFR by Peill and Hoffmann (1999), this compact reactor design is not suitable for in-situ groundwater remediation. For large scale reactors, the utilisation of quartz is not encouraged as it is fragile and expensive, thus special consideration for the lighting system is required to prevent contact with water in case one of the quartz breaks. This implies that the whole unit of the reactor needs to be withdrawn for maintenance. The protection system shielding the lamps would minimise the light intensity, which reduces the initial UV light intensity to be reflected by the inner wall of the quartz tubes. This defeats one of the features of this reactor design, which emphasizes effective utilisation of UV light. There was no scale up testing of this reactor design.

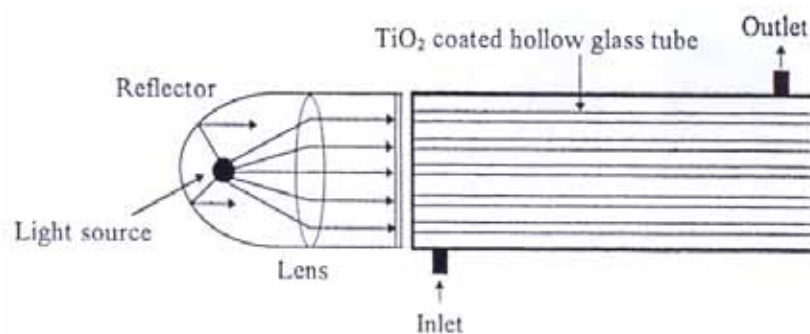


**Figure 1.13** Illustration of multiple tube reactor (MTR) (Ray and Beenackers, 1998a)

#### 1.4.2.3 Rotating Disk Photocatalytic Reactor (RDPR)

The rotating disk photocatalytic reactor (RDPR) (Figure 1.14), using immobilised  $\text{TiO}_2$ , was designed and developed by the Dionysiou group at the University of Cincinnati. This reactor was designed with a  $\text{TiO}_2$  coated circular disk half submerged in contaminated water to be treated and the UVA fluorescent lamps on both sides of the disk. The rotation of the disk creates a thin film of water to enhance the reactor efficiency in degrading contaminants by maximising the contact of  $\text{TiO}_2$  surface with oxygen in the atmosphere and UVA light. However, this reactor design may not be suitable for in-situ groundwater remediation as the plume width and depth of contaminants are in meters scale. The use of a circular disk limits the coverage area of the incoming plume. If this reactor design utilises solar energy, the

reactor efficiency would fluctuate with the UVA light intensity and might be significantly affected by heavy rainfall.

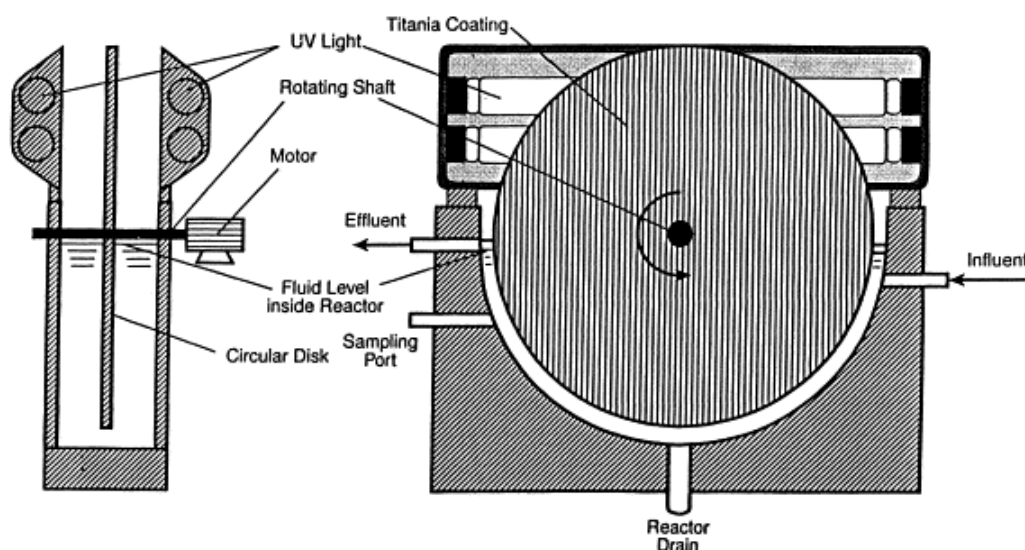


**Figure 1.14** Rotating disk photocatalytic reactor (RDPR) (Dionysiou et al., 2000b)

#### 1.4.2.4 Photocat I

Photocat I is the only immobilised photocatalytic reactor designed for groundwater remediation. A feasibility study using a 48 mm (i.d.) glass cylinder, slurry coated with  $\text{TiO}_2$ , was conducted in laboratory scale tank by Chan and Lynch in the University of Cambridge. This research demonstrated the potential of immobilised  $\text{TiO}_2$  photocatalytic reactor for in-situ groundwater remediation. However, one of the major drawbacks of this reactor was the reliability of  $\text{TiO}_2$  immobilisation on the glass cylinder. In another study, Warren (2006) found that the reactor efficiency decreases significantly after every experiment, indicating fewer active sites for the reaction due to the gradual detachment of the  $\text{TiO}_2$  slurry coating on the glass cylinder. The scaled up photocatalytic reactor (Figure 1.15) used alumina prisms, slurry coated with  $\text{TiO}_2$ , which was fixed to the housing. The pilot scale experiment was unsuccessful because some alumina prisms detached during the operation and the MTBE plume diverted from the reactor.

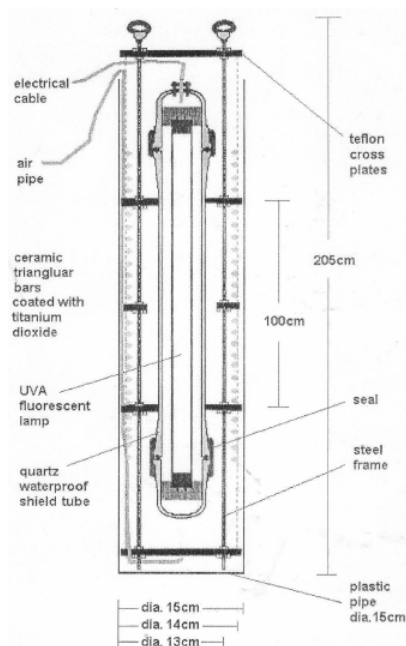


**Figure 1.15** Illustration of Photocat I (Chan et al., 2006)

### 1.4.3 Summary

To summarise, most of the existing large scale photocatalytic reactors were designed for water and wastewater treatment (typically operated using sunlight) using  $\text{TiO}_2$  slurries, requiring expensive post-treatment solid-liquid separation of  $\text{TiO}_2$  nanoparticles. If they were to be used for groundwater, then the reactor becomes the “treat” part of a pump-and-treat system (Section 1.3.3). The uses of slurry photocatalytic reactors and pump-and-treat systems to withdraw contaminated groundwater prior to treatment are drawbacks to groundwater remediation projects.

In view of the limitations of most existing groundwater remediation technologies by soil heterogeneity (Mackay and Cherry, 1989), it is proposed that a reactor in a trench system could overcome this issue. A trench system is usually used to minimise cross over of contaminants into other lands. It may incur substantial capital (installation) cost but is significantly cheaper than a pump-and-treat system in the long term as minimum maintenance is required, suitable for long term passive remediation (Bowles et al., 2000). Therefore, in-situ groundwater remediation using a trench system is proposed to overcome the issue of soil heterogeneity and Henry’s law constant of VOCs. In addition, the significantly lower MTBE concentration after photocatalytic treatment can be further reduced via natural attenuation (Kuburovic et al., 2007).

## 1.5 Statement of Need

In-situ groundwater remediation is preferred over ex-situ groundwater remediation due to several factors, mainly the prohibition of partially treated groundwater recharge by the European Water Framework Directive (European Commission, 2000; European Commission, 2006) and increased remediation project costs due to the combination of technologies.

Photocatalysis, an environmentally friendly technology in many aspects, can potentially be operated as a stand alone groundwater remediation system, as the feasibility of immobilised catalyst in treating MTBE using a laboratory scale model was demonstrated by Chan (2005) in the preceding study. An in-situ photocatalytic remediation system is also cost-effective as it consists of economical material and does not require combination of technologies for MTBE removal from groundwater such as air sparging and SVE, and pump-and-treat (Mackay and Cherry, 1989; US EPA, 2004). Although immobilised titanium dioxide has significantly lower photocatalytic activity than in suspension, due to the amount of active surface area, it eliminates the requirement of post-treatment solid-liquid separation, which reduces the total remediation project cost. In addition, a groundwater flow around  $9 \text{ cm d}^{-1}$  provides sufficient retention time for photocatalytic treatment.

This development of an immobilised photocatalytic reactor is hoped to overcome most of the limitations encountered by existing groundwater remediation technologies. This research is also applicable for the remediation of other organic contaminants as it is a mildly selective process.

## 1.6 Aim and Objectives

This research aims to propose and develop a novel photocatalytic reactor design for in-situ groundwater remediation. The objectives in this research are listed as follows:

- (i) to determine a suitable  $\text{TiO}_2$  immobilisation procedure, followed by its scale up for the reactor design;
- (ii) to propose a photocatalytic reactor design and evaluate its efficiency using a model via laboratory scale experiments;
- (iii) to investigate the effect of groundwater constituents on the photocatalytic degradation of MTBE;

(iv) to scale up the proposed reactor design to the proposed field scale dimension for the assessment of the reactor efficiency through sand tank experiments, which simulate the plume clean-up from underground leakages; and

(v) to propose the installation options of the proposed reactor design in the field.

## 1.7 Scope of Research

This research pioneers a novel photocatalytic reactor design for in-situ groundwater remediation, therefore the development of the proposed photocatalytic reactor was focused on the scale up and evaluation on its efficiency in degrading the target contaminants, as a sole treatment system. Consequently, it does not include investigations on the process optimisation conditioning such as pH adjustment.

This experimental research emphasizes on verifying the feasibility of the proposed photocatalytic reactor design for in-situ groundwater remediation via observations and data from the experiments. As photocatalysis is known to effectively degrade a plethora of organic compounds, only one target contaminant, MTBE, was chosen while MB was used as the photocatalytic indicator, in this study.

As the first research on developing a proposed photocatalytic reactor design, it has provided sufficient evidence to validate the feasibility of this reactor design for in-situ groundwater remediation. However, further experiments needs to be conducted to enable a comprehensive numerical modelling of the reactor design or the clean-up. Installation options for the photocatalytic reactor in the field was proposed, however, field testing was not included in this study due to financial and time constraint.

## 1.8 Thesis Layout

This thesis consists of eight chapters, with the respective summaries below:

**Chapter 2** provides the basic concepts and theories in photocatalysis, reactor engineering and hydrogeology, which were used as foundation for the photocatalytic reactor design in this research.

**Chapter 3** involves the determination of a suitable immobilisation procedure of the catalyst in terms of adhesion and photocatalytic activity by weighing the catalyst and measuring the absorbance of methylene blue solution at 665 nm, respectively. It also involves the scale up of the suitable immobilisation procedure, in which the catalysts were evaluated for its reproducibility in terms of photocatalytic activity.

**Chapter 4** describes the concept of the proposed photocatalytic reactor design, named “Honeycomb”, as well as the design considerations involved. The performance of the proposed photocatalytic reactor was evaluated by measuring the decolourisation rate of the methylene blue solution. Several operating conditions of the proposed photocatalytic reactor was also determined.

**Chapter 5** investigated the performance of photocatalytic reactor in degrading MTBE, which also studied the effect of organics and dissolved ions on the photocatalytic oxidation of MTBE. Similar to Chapter 4, the hydraulic performance of the proposed photocatalytic reactor was studied to obtain its MTBE removal efficiency and compare with MB demineralisation.

**Chapter 6** involves the scale up of Honeycomb I and the simulation of in-situ MTBE plume clean-up in a sand tank. The performance of Honeycomb I prototype was then compared with that of Honeycomb I model in Chapter 5.

**Chapter 7** describes about the general specifications of the proposed photocatalytic reactor components and proposed two installation approaches for the field scale photocatalytic reactor.

**Chapter 8** concludes the thesis and recommends some future research work.

## CHAPTER 2

### LITERATURE REVIEW

#### 2.0 Overview

Chapter 1 has described some of the existing practices in remediating groundwater contaminated by MTBE, as well as the existing photocatalytic reactor designs. This chapter is focused on the theoretical descriptions of photocatalysis and contaminant transport. The first section is about photocatalysis, which encompasses the photocatalytic mechanism, properties of the photocatalyst and factors affecting the process. The photocatalytic mechanism is described chronologically the generation of oxidising agents on the semiconductor catalyst surface. This is followed by the description of the photocatalytic oxidation (PCO) of MTBE and mineralisation of the MB dye, including the proposed pathway and products of the reaction. The properties of the photocatalyst used in this research, i.e. titanium dioxide ( $\text{TiO}_2$ ) is also described. The latter part of this chapter covers the description of contaminant transport mechanisms involved and considered in this research.

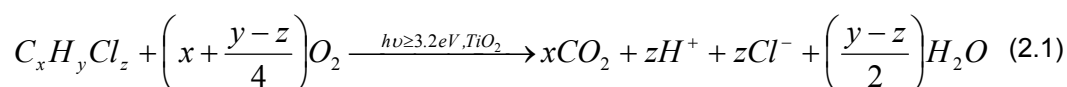
#### 2.1 Semiconductor Photocatalysis

Semiconductor photocatalysis basically involves three stages:

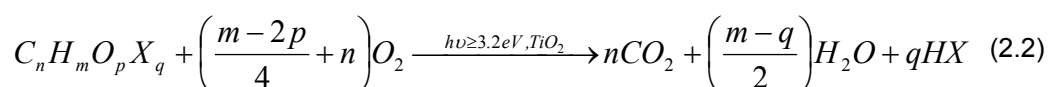
- (i) The activation of the photocatalyst by UV light to generate electrons and holes;
- (ii) The holes oxidise water to generate hydroxyl radicals, and at the same time the electrons reduce oxygen to form other oxidising agents including more hydroxyl radicals;
- (iii) The radicals oxidise the pollutants eventually to carbon dioxide, water and simple mineral acids.

A description of the photocatalytic mechanism is detailed in Section 2.1.1 (main reference: Hoffmann et al., 1995).

Semiconductor photocatalysis, typically uses titanium dioxide (TiO<sub>2</sub>) photocatalyst, has been applied in various processes such as air and water purification, sterilisation, cancer treatment, water photosplitting, noble metal recovery and oil spill clean-up (Hoffmann et al., 1995; Fujishima et al., 2000; Herrmann, 2005). Semiconductor photocatalysis has been applied to the remediation of contaminants and has been proven successful for a plethora of compounds mainly organics such as aliphatic alcohols, aromatic carboxylic acids, halogenated alkanes and alkenes (Mills et al., 1993; Hoffmann et al., 1995), and inorganic such as pesticides and reductive deposition of heavy metals from aqueous solution to surfaces (Bhatkhande et al., 2001; Herrmann, 2005). It is a promising technology for environmental applications particularly due to its ability to completely mineralise complex and persistent organic chemicals, which is hardly biodegraded by microorganisms. An example of the general stoichiometry for the photocatalytic oxidation to yield mineralisation products is a chlorinated hydrocarbon (Eq. 2.1) (Hoffmann et al., 1995).



The overall chemical reaction equation for the photocatalytic oxidation of organics with general formula C<sub>n</sub>H<sub>m</sub>O<sub>p</sub>X<sub>q</sub> (X is a halogen atom) to complete mineralisation (Eq. 2.2) (Chan, 2005).



Photocatalysis is typically a pseudo first order process, in which the reduction of reactant concentration is an exponential curve (Eq. 2.3) (Figure 2.1a).

$$C = C_0 e^{-kt} \quad (2.3)$$

where  $C$  is the reactant concentration at time,  $t$ ,  $C_0$  is the initial reactant concentration,  $k$  is the observed photocatalytic degradation rate and  $t$  is time. Eq. 2.3 can be derived into Eq. 2.4, which justifies that the photocatalytic degradation rate of the reactants,  $k$  can be obtained by plotting  $\ln(C_0/C)$  versus time, typically linear for no flow experiments (Figure 2.1b).

$$kt = \ln\left(\frac{C_0}{C}\right) \quad (2.4)$$

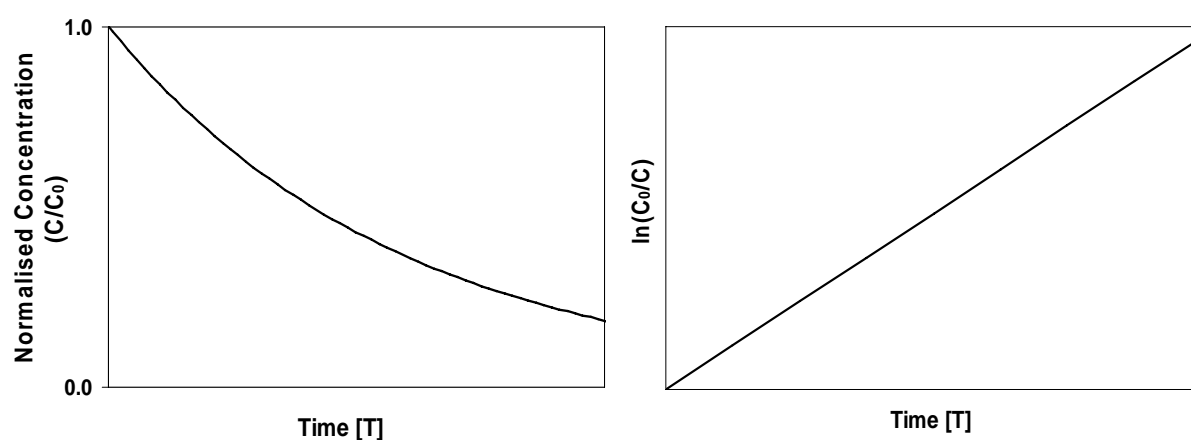


**Figure 2.1a** Typical exponential decay curve of a contaminant  
**Figure 2.1b** Typical linear plot  $\ln(C_0/C)$  vs time

### 2.1.1 Photocatalytic Mechanism

Semiconductors have electronic structures, characterised by a filled valence band and an empty conduction band, which can be sensitive to light induced redox processes. Figure 2.2 illustrates the main stages in the mechanism of photocatalysis occurring on the surface of a photocatalytic semiconductor (Hoffmann et al., 1995), which is explained as follows.

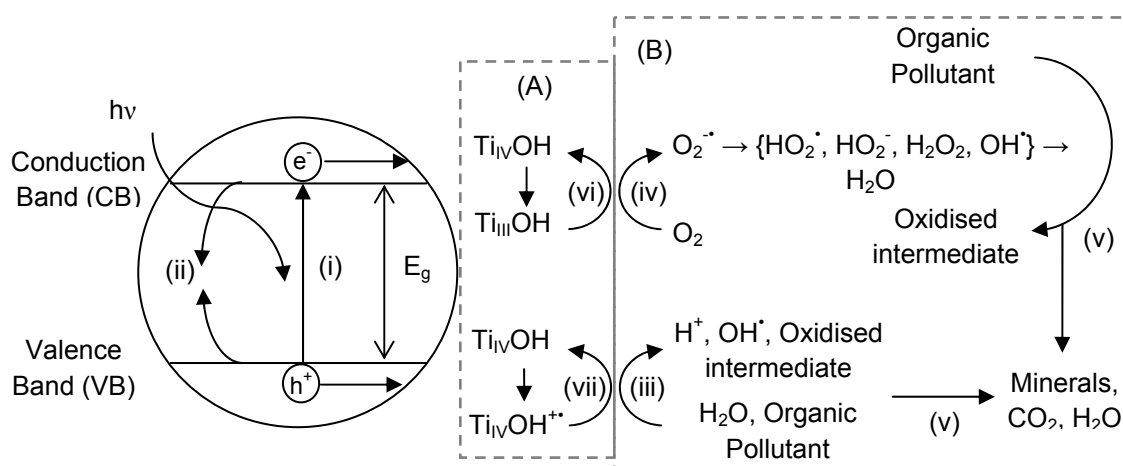


**Figure 2.2** Primary stages in photocatalytic mechanism (modified from Hoffmann et al., 1995); (A) and (B) are detailed in Figure 2.3 and 2.4, respectively.

#### (i) formation of charge carriers by a photon

The irradiation of light induces photons with energy,  $h\nu$ , onto the illuminated semiconductor surface. When the energy of  $h\nu$  is equivalent to or greater than the bandgap energy,  $E_g$ , of the semiconductor, electrons are excited from the valence band (VB) into the conduction band (CB),  $e_{cb}^-$ . As an  $e_{cb}^-$  leaves the valence band, a hole,  $h_{vb}^+$  is generated. Therefore, the charge carriers, i.e.  $e_{cb}^-$  and  $h_{vb}^+$ , are formed (Eq. 2.5) and can react with electron donors and acceptors, or electron and hole scavengers.



The photocatalytic mechanism assumes that contaminant molecules do not go through direct hole transfer and that oxidative electron transfer occurs via surface bound hydroxyl radicals,  $\{>\text{Ti}^{\text{IV}}\text{OH}\}^+$ , or equivalent trapped hole species. When the charged carriers are formed, the possibilities (with characteristic times) are charge carrier recombination, charge carrier trapping and interfacial charge transfer (Figure 2.3).

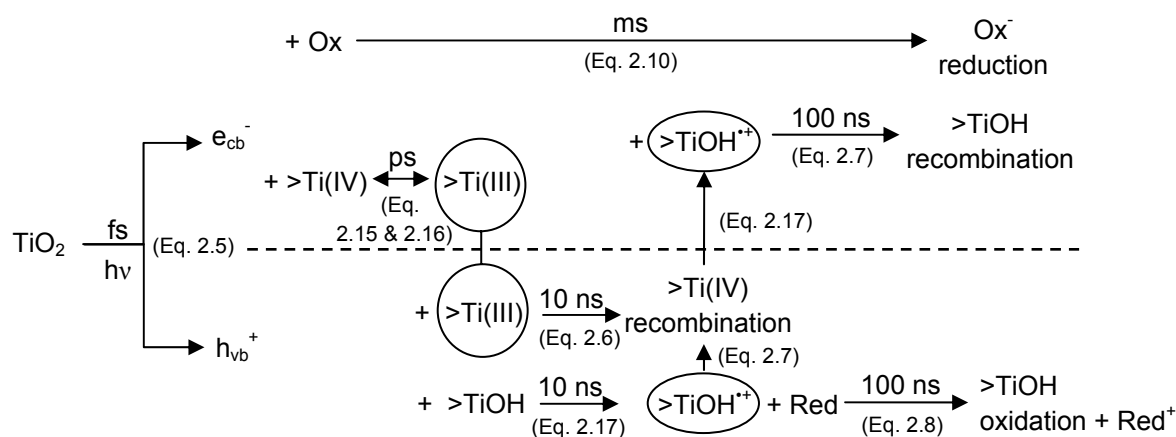


**Figure 2.3** Primary reactions on the catalyst surface (Hoffmann et al., 1995); Red: reductant (electron donor), Ox: oxidant (electron acceptor)

(ii) charge carrier recombination to liberate heat

The illuminated semiconductor surface becomes unstable or activated when the charged carriers are formed with the assistance by input energy of the photons. Among several possibilities which could occur to the excited state conduction band electrons,  $e_{\text{cb}}^-$ , and valence band holes,  $h_{\text{vb}}^+$ , is recombination (Eq. 2.6 and 2.7). Recombination occurs due to the absence of suitable electron and hole scavenger leading to the dissipation of the input energy in the form of heat, which happens within a few nanoseconds. Thus, recombination can be minimised to enable subsequent redox reaction by creating suitable scavenger or surface defect state to trap the electrons and holes.



where  $>\text{TiOH}$  represents the primary hydrated surface functionality of  $\text{TiO}_2$ ,  $\{>\text{Ti}^{\text{III}}\text{OH}\}$  is the surface trapped conduction band electron and  $\{>\text{Ti}^{\text{IV}}\text{OH}^{\cdot+}\}$  is the surface bound hydroxyl radical. Faster recombination rate leads to lower photocatalytic activity as the charged carriers do not react with electron donors or acceptors, and electron and hole scavengers, and vice versa. Degussa P25 has high photocatalytic activity due to slow recombination because it consists of anatase and rutile crystal structures, which promotes charge-pair separation and inhibits recombination (Hoffmann et al., 1995).

(iii) initiation of an oxidative pathway by a valence band hole,  $h_{vb}^+$

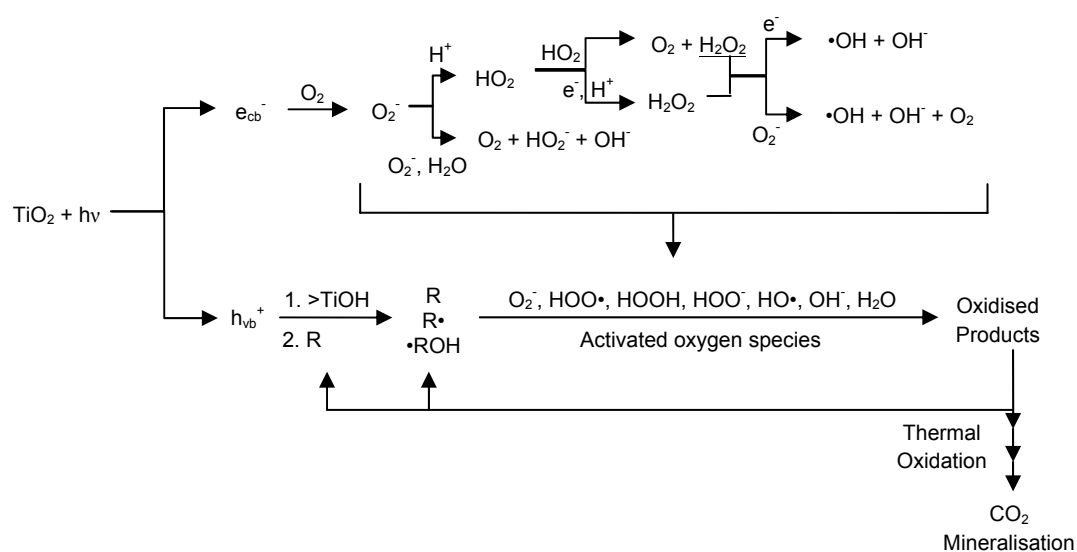
Apart from recombination,  $h_{vb}^+$  can react either with electron donors adsorbed on the surface of the semiconductor, or within the surrounding electrical double layer of the charged particles as described by the following interfacial charge transfer reaction (Eq. 2.8). A valence band hole,  $h_{vb}^+$ , is a strong oxidant with a redox potential ranging from +1.0 to +3.5 V versus normal hydrogen electrode (NHE) depending on the semiconductor and pH, thus, plays an essential oxidising role in photocatalytic degradation. The oxidation can occur due to either indirect oxidation via the surface bound hydroxyl radical  $\{>TiOH\}^+$  (i.e. surface trapped  $h_{vb}^+$ ) or directly via  $h_{vb}^+$  before it is trapped within the particle or at its surface.



Figure 2.4 illustrates the pathways of hydroxyl radicals formation on the surface of  $TiO_2$  by the reaction of  $h_{vb}^+$  with adsorbed water, hydroxide or surface titanol groups ( $>TiOH$ ), and two electron reduction of adsorbed oxygen by  $e_{cb}^-$ . Hydroxyl radicals, with oxidation potential of 2.8 V (Legrini et al., 1993), are likely to be the principle reactive oxidant in photocatalysis, as intermediates typically of hydroxylated structures were detected during the PCO of halogenated aromatic compounds (Hoffmann et al., 1995). Reactive oxygen species such as hydrogen peroxide ( $H_2O_2$ ), which is a strong oxidant by itself, can be formed due to the oxidation of water by  $h_{vb}^+$  (Eq. 2.9).



It could clean the surface as hydrogen peroxide is not stable and will function as a direct electron acceptor oxidising organic and inorganic electron donors through homolytic fission or scission. This process is chemical bond dissociation of a neutral molecule generating two free radicals. The formation of  $H_2O_2$  is inhibited in the absence of oxygen.



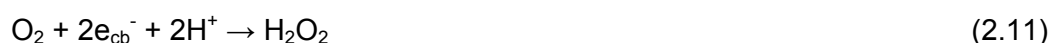
**Figure 2.4** The formation of activated oxygen species and their reactions (Hoffmann et al., 1995); R: organic contaminant

*(iv) initiation of a reductive pathway by a conduction band electron,  $e_{cb}^-$*

Similarly, the excited state electrons which are trapped in the conduction band,  $e_{tr}^-$ , can react with electron acceptors adsorbed on the surface of the semiconductor or electron scavengers, or within the surrounding electrical double layer of the charged particles as shown in the following interfacial charge transfer reaction (Eq. 2.10). Conduction band electrons,  $e_{cb}^-$  are good reducing agents with redox potentials ranging from +0.5 to -1.5 V vs NHE, thus, plays essential reducing role in photocatalytic degradation reaction.



As the interfacial electron transfer occurs, these electrons react with electron acceptors, including oxygen ( $\text{O}_2$ ) and water ( $\text{H}_2\text{O}$ ). In the conduction band, the reactive oxygen species such as superoxide ( $\text{O}_2^-$ ) and  $\text{H}_2\text{O}_2$  can be formed due to a two electron reduction of the adsorbed oxygen by  $e_{cb}^-$  (Eq. 2.11).  $\text{H}_2\text{O}_2$  is also formed on the illuminated  $\text{TiO}_2$  surface through the dioxygen reduction by  $e_{cb}^-$  in the presence of air and suitable electron donor (Eq. 2.12 and 2.13).



(v) reactions of activated oxygen species with reactants to yield mineralisation products

The active oxygen species formed will subsequently oxidise reactants to produce carbon dioxide, water and simple mineral acids (Figure 2.4). The PCO of chlorinated hydrocarbons (Eq. 2.1), such as chloroform (Eq. 2.14) yields mineralisation products; carbon dioxide ( $\text{CO}_2$ ), water and mineral acids.



(vi) trapping of a  $e_{\text{cb}}^-$  in a dangling surficial bond to yield Ti(III)

Another possibility apart from the ones mentioned earlier is that  $e_{\text{cb}}^-$  can be trapped in a metastable surface state forming a surface trapped conduction band electron,  $\{\text{>Ti}^{\text{III}}\text{OH}\}$  (Eq. 2.15 and 2.16).



(vii) trapping of a  $h_{\text{vb}}^+$  at a surficial titanol group

Similarly,  $h_{\text{vb}}^+$  can be trapped in metastable surface state forming surface trapped valence band hole also known as surface bound hydroxyl radical,  $\{\text{>Ti}^{\text{IV}}\text{OH}\}^+$  (Eq. 2.17).



### 2.1.2 Photocatalytic Degradation Pathway for MTBE

MTBE is among the wide range of organic contaminants degradable using photocatalysis (Sahle-Demessie et al., 2002a and b; Almquist et al., 2003; Chan and Lynch, 2003a and b), with the photocatalytic degradation pathway of MTBE being proposed by Barreto et al. (1995) (Figure 2.5). The proposed photocatalytic degradation scheme of MTBE observed in their experiments showed the formation of many intermediates encompassing  $\alpha$ -hydroperoxy MTBE (HyperMTBE), tertiary butyl formate (TBF), tertiary butyl alcohol (TBA) and acetone. Barreto et al. (1995) proposed the structural formula of an intermediate compound as HyperMTBE based on its molecular weight of approximately 120. Barreto et al. (1995) also revealed that TBF is photocatalytically degraded to form TBA and acetone as intermediates. Both TBF and TBA were detected in the studies by Sahle-Demessie et al. (2002a and b) and Almquist et al. (2003). Chan (2005) also observed the formation of acidic TBF and acetone in oxygen-limited experiments through pH measurement and gas chromatograph (GC). MTBE is typically measured using gas chromatography (GC) as it is a volatile compound. Consequently, TBA is also photocatalytically degraded to form acetone and isobutylene, which are both subsequently photocatalytically degraded to CO<sub>2</sub> and H<sub>2</sub>O (Barreto et al., 1995). The initial pseudo first order photocatalytic degradation rate of TBF ( $1.93 \times 10^{-4} \text{ s}^{-1}$ ) and TBA ( $2.34 \times 10^{-4} \text{ s}^{-1}$ ) are slower than MTBE ( $1.23 \times 10^{-3} \text{ s}^{-1}$ ) by an order of magnitude (Barreto et al., 1995). The electrical power of the medium pressure mercury lamp was 450 W, with wavelength cutoff at 290 nm. The lower and upper limits of light wavelengths without initiating photolysis of MTBE are 254 and 400 nm, respectively (Chan, 2005).

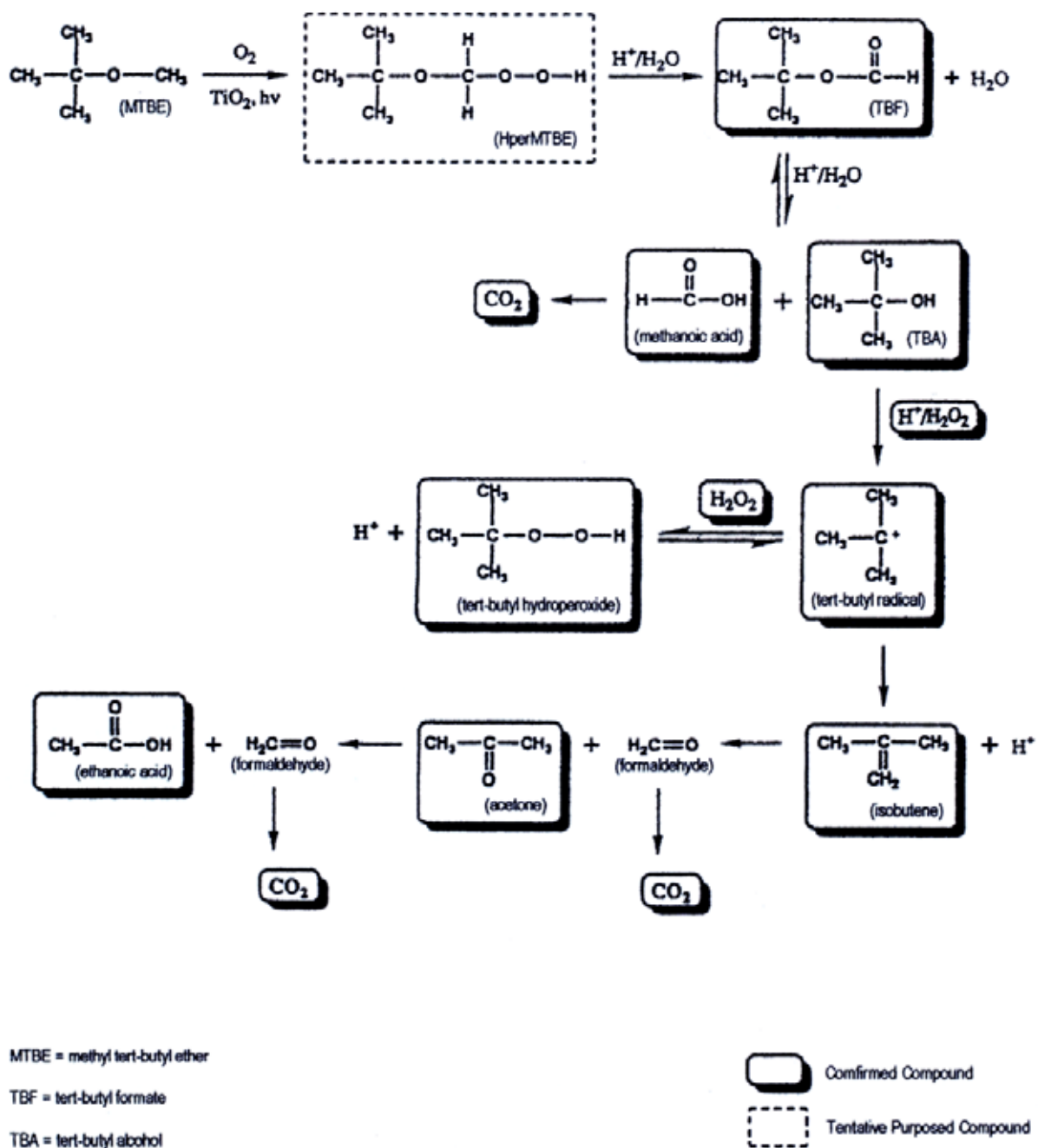
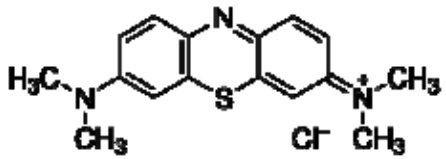


Figure 2.5 The proposed photocatalytic degradation pathway of MTBE (Barreto et al., 1995)

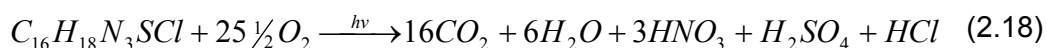
### 2.1.3 Photocatalytic Degradation Pathway for MB

The principle of photocatalysis and the photocatalytic activity of a photocatalyst is often assessed using a common dye, methylene blue (MB) (Mills et al., 1993; de Lasa et al., 2005; Ryu and Choi, 2008). Methylene blue is a basic aniline dye, which appears as a solid, odorless, dark green powder at room temperature and yields a blue solution when dissolved in water. MB solution is blue in an oxidizing environment, but becomes colorless if exposed to a reducing agent. It is a heterocyclic aromatic chemical compound of many uses particularly in biology (antidote for cyanide poisoning and a bacteriological stain) or chemistry (redox indicator in analytical chemistry). The concentration of MB is analysed using a UV/Vis spectrophotometer at light wavelength of 660 (Mills et al., 1993), 664 (Kiriakidou et al., 1999) or 665 nm (Fretwell and Douglas, 2001). The lower and upper limits of light wavelengths without initiating photolysis of MTBE are 300 and 400 nm, respectively (Chan, 2005). Table 2.1 lists some of the properties of MB.

**Table 2.1** Properties of methylene blue (MB)

Properties	Methylene Blue
Chemical Formula	 $C_{16}H_{18}N_3SCl$ 319.85 35.5
Structural Formula	
Molecular Weight ( $g\ mol^{-1}$ )	
Aqueous Solubility in Water at 25 °C ( $g\ L^{-1}$ )	

The complete photocatalytic degradation of MB according to Mills et al. (1993) is shown in Eq. 2.18. Figure 2.6 shows the photocatalytic degradation pathway of MB proposed by Houas et al. (2001). The intermediates were proposed based on the molecular weight and the final products were  $CO_2$  and  $H_2O$ .



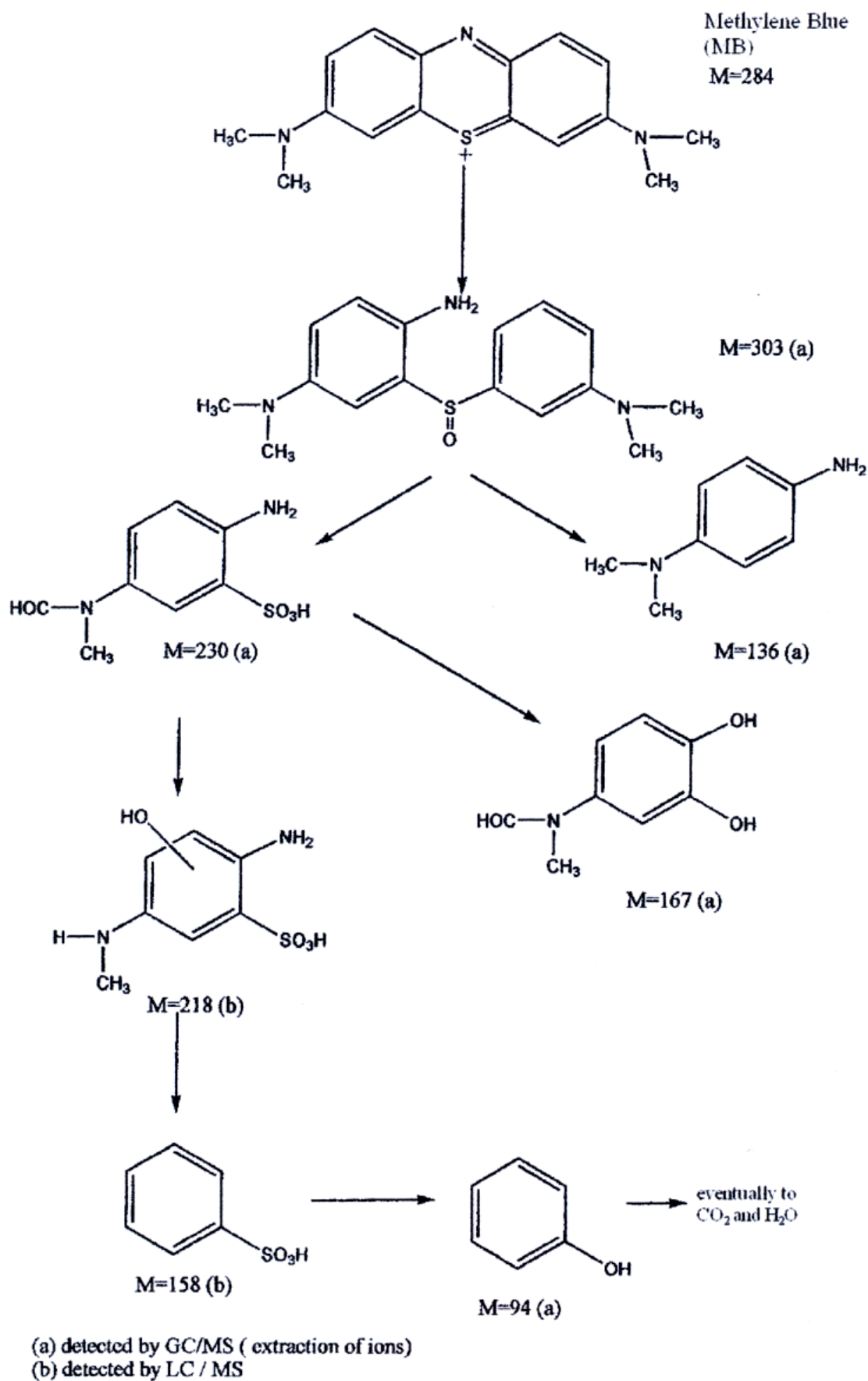


**Figure 2.6** The proposed photocatalytic degradation pathway of MB (Houas et al., 2001)

## 2.2 Photocatalyst: Titanium Dioxide (TiO<sub>2</sub>)

Titanium dioxide (TiO<sub>2</sub>), also known as titanium (IV) oxide or titania, is an n-type semiconductor which has been widely used in photocatalysis (Mills et al., 1993; Hoffmann et al., 1995; Ryu and Choi, 2008). Mills et al. (1993) summarised that TiO<sub>2</sub> is the preferred semiconductor photocatalyst, for the following reasons.

### i. Activity

TiO<sub>2</sub> is the most active among the other semiconductor photocatalysts as the band position of TiO<sub>2</sub> shows the redox potential of (i) photogenerated  $h_{\nu b}^+$  are sufficiently positive to generate adsorbed OH radical and (ii)  $e_{cb}^-$  are sufficiently negative to reduce adsorbed O<sub>2</sub> to superoxide radical anion (O<sub>2</sub><sup>-</sup> or its conjugate acid HO<sub>2</sub>), in which the generated radicals can subsequently react with the organic contaminant (Mills et al., 1993). This is confirmed by Fujishima et al. (2000) that the band position of TiO<sub>2</sub> has the redox potential to generate a variety of oxidizing and reducing couples at pH 7 (Figure 2.7).

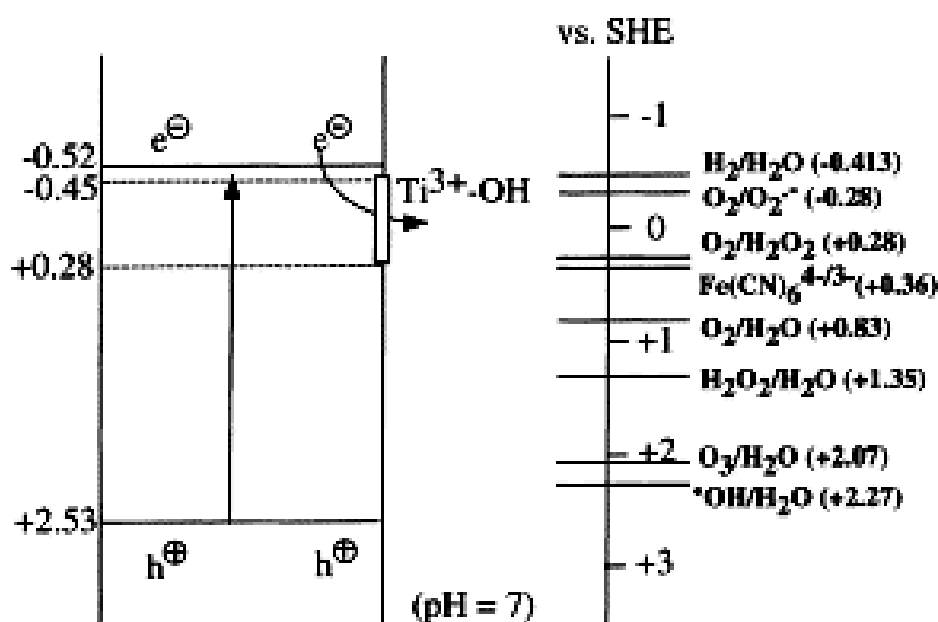


**Figure 2.7** Schematic diagram showing the potentials for various redox processes occurring on the TiO<sub>2</sub> surface at pH 7 (Fujishima et al., 2000); Standard Hydrogen Electrode (SHE)

*ii. Cost*

TiO<sub>2</sub> is inexpensive and commercially available (Mills et al., 1993; Hoffmann et al., 1995). The major advantage of TiO<sub>2</sub> is that it remains intact before and after treatment, thus contributes to the longer lifespan compared to chemical oxidation treatment. The major component of a photocatalytic reactor project cost is the energy consumption of UVA artificial light source, which is one of the shortcomings for rapid commercialisation of photocatalytic water treatment (Bahnemann, 2004). Photocatalytic reactors can also be operated using solar irradiation (Alfano et al., 2000; Bahnemann, 2004).

*iii. Photostability*

TiO<sub>2</sub> is stable towards photocorrosion, implying that it can be recycled. This holds a major advantage as photocatalyst for water purification. Bhatkhande et al. (2001) found no significant reduction in the photocatalytic activity when the TiO<sub>2</sub> slurry was filtered and reused several times. Mills et al. (1993) also reviewed similar findings for TiO<sub>2</sub> reused for 10 successive photomineralisation cycles of 4-chlorophenol. TiO<sub>2</sub> is also biologically and chemically inert (Mills et al., 1993; Hoffmann et al., 1995).

*iv. Manageability*

TiO<sub>2</sub> is manageable as it is insoluble under most conditions and can be separated from liquid, through filtration or sedimentation in the post-treatment of photocatalytic slurry reactors (Bahnemann, 2004), however, the solid-liquid separation process of nano-sized TiO<sub>2</sub> powder is complicated and costly. Consequently, the immobilised TiO<sub>2</sub> reactors became more popular and some researches were focused on developing TiO<sub>2</sub> immobilisation procedures (Balasubramanian et al., 2004). It does not require special health and safety measures in its handling (except respiratory mask to prevent inhalation of nano-sized TiO<sub>2</sub> powder) as it is a non-toxic chemical.

*v. Safety*

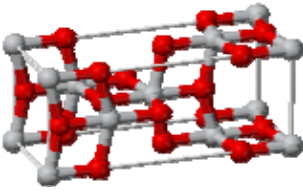
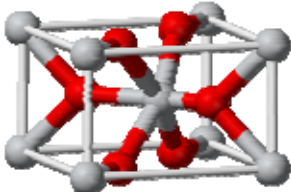
As TiO<sub>2</sub> is a non-toxic material (Mills et al., 1993), there is no special health and safety measures required in the handling of TiO<sub>2</sub>. In addition, it is widely used in a wide range of domestic product and as pigment in paint. Photocatalysis is also applied for cancer treatment by exterminating tumor cells using the redox potential of illuminated TiO<sub>2</sub> (Fujishima et al., 2000).

### 2.2.1 Titanium Dioxide Properties

TiO<sub>2</sub> contains 60 % Ti and 40 % O and appears as a white and insoluble solid at room temperature. It exists in three different crystalline structures, i.e. brookite, anatase and rutile, due to its atomic structure and can vary depending on the calcination temperature. The brookite, anatase and rutile crystal structure can be formed by calcination at 300 ± 50, 500 ± 50 and 700 ± 50 °C, respectively. It has a molecular weight, density and bulk density of 79.87 g mol<sup>-1</sup>, 4.23 g cm<sup>-3</sup> and 0.85 g cm<sup>-3</sup>, respectively. The n-type semiconductor has electric resistivity of 3 x 10<sup>5</sup> Ω at temperature of 773 K. There are several ways of analysing the crystal composition such as x-ray diffraction (XRD) and x-ray photoelectron spectroscopy (XPS).

Anatase TiO<sub>2</sub> has been said to be photocatalytically more active than rutile TiO<sub>2</sub> in degradation of organic chemical compounds (Hoffmann et al., 1995; Bhatkhande et al., 2001), possibly due to the higher electron transfer rate of anatase than rutile and the higher specific surface area of anatase. However, Ryu and Choi (2008) found that this may not be true and that the photocatalytic activity is compound specific. The drawback of this phenomena is the higher electron-hole recombination rate in anatase, which results in deactivation of photocatalytic surface. Therefore, the presence of rutile TiO<sub>2</sub> is essential to minimise the electron-hole recombination due to the different recombination lifetimes and interfacial electron transfer rate constants (Hoffmann et al., 1995); even commercial TiO<sub>2</sub>, Degussa P25, has typical anatase to rutile ratio between 70:30 (Mills et al., 1993; Bhatkhande et al., 2001) and 80:20 (Kiriakidou et al., 1999). Some studies showed that rutile TiO<sub>2</sub> is more effective in photocatalytically degrading inorganic chemical compounds (Ryu and Choi, 2008). Table 2.2 lists some of the properties of anatase and rutile TiO<sub>2</sub>.

**Table 2.2** Properties of anatase and rutile TiO<sub>2</sub> (Chan, 2005)

Properties	Anatase	Rutile
Crystal Structure		
Bandgap Energy (eV)	3.25	3.00 to 3.05
Density (kg m <sup>-3</sup> )	3.90	4.25
Refractive Index	2.5	2.7
Temperature of Stability (°C)	Room temperature to 800 ± 100	Room temperature to above 1000
Appearance under electron spectroscopy inspection	Narrower columnar grains	Wider columnar grains

Ryu and Choi (2008) scrutinized the photocatalytic degradation rate of various organic and inorganic compounds by eight types of commercially available TiO<sub>2</sub> and found that the rates were compound specific and varied with the different photocatalyst; there was no exceptional photocatalyst. Nevertheless, Degussa P25 showed higher photocatalytic degradation rates among the photocatalysts used for a wider range of chemicals in their study. Their study also found that rutile crystal structure generally performed better in photodegradation of inorganic chemicals. In other words, the anatase is not necessarily more photoreactive than rutile, and that the correlation between the activity and common physicochemical properties of photocatalysts is more complex than commonly believed. Ryu and Choi (2008) found that the photocatalytic activities are roughly correlated only among structurally related compounds as the rutile with specific surface area of 2 m<sup>2</sup> g<sup>-1</sup> could perform better than rutile from Degussa P25 with specific surface area of 29 m<sup>2</sup> g<sup>-1</sup> on certain chemicals such as methanol and methylene blue.

Amorphous is the non-crystalline phase which is formed in preparation of TiO<sub>2</sub> from precursor solution such as sol gel and reverse micelles. Its structure lacks crystalline periodicity, i.e. the pattern of its constituent atoms or molecules does not repeat periodically in three dimensions. The amorphous phase is not photocatalytically active and requires calcination at 500 °C to transform to anatase TiO<sub>2</sub>, or 700 °C and above to transform to rutile TiO<sub>2</sub>.

### 2.2.2 Thermal Treatment Terms

Calcination is a thermal treatment process which is conducted below the melting point of material and changes the crystal phase transition and eliminates any volatile fraction. In many literature, different terms are used to address the similar process, i.e. anneal, sinter and calcine, where the typical temperature applied circa 500 °C (Mills et al., 1993; Peill, 1996; Chan, 2005).

Sintering is a process of densification driven by interfacial energy. Material moves by viscous flow or diffusion in such way as to eliminate porosity and thereby reduce the solid-vapour interfacial area. In a gel, that area is enormous, so the driving force is great enough to produce sintering at exceptionally low temperatures, where transport processes are relatively slow. The kinetics of densification of gels are complicated by the concurrent processes of dehydroxylation and structural relaxation. This leads to the remarkable result that faster heating permits complete densification at a lower temperature. For crystalline growth there are further complications of grain growth and phase transformations. It is advantageous to complete sintering before crystallization of the gel.

On heating to 390 °C, the mass and pore volume of the gel decreases due to condensation of hydroxide groups producing water that was expelled. Simultaneously, the skeletal density of the amorphous gel is increased. This indicates that the particles of the hydrous oxide in the gel shrink during dehydration, so there must have been hydroxyl groups within the particles, as well as the surface of the pores. This is also the characteristic of the alkoxide-derived gels, which do not contain particles. Further increases in skeletal density occurred at higher temperatures as the amorphous gel crystallises.

### 2.2.3 Film Thickness

As photocatalysis requires adsorption prior to redox reaction through electron and hole transfer, it is believed that the surface contact area of the coating plays a more important role than the thickness of coating. In other words, an ideal thin coating layer saturated with TiO<sub>2</sub> could provide similar performance to that of a thick coating layer of TiO<sub>2</sub>. The immobilisation of TiO<sub>2</sub> is usually required in thin films because excessive thickness (i) does not enhance photocatalytic activity as photocatalysis is initiated through adsorption and occurs mainly on the surface of the film and (ii) inhibits light and diffusion of a chemical compound through the depth of TiO<sub>2</sub> film, and (iii) would result greater detachment of immobilised TiO<sub>2</sub> especially when the holding limit of film is exceeded. Chang et al. (2000) derived from the numerical modelling of porous thin film photocatalyst that TiO<sub>2</sub> film which is thicker than 2 µm does not further enhance photocatalytic activity.

It is practically very difficult to obtain the ideal thin coating layer, therefore, multi coating is required, especially for a dip coating method. Excessive coating is allowed in this study because UVA light is illuminated on and not through the TiO<sub>2</sub> coating (Peill, 1996; Ray and Beenackers, 1998a), and for the photocatalytic activity can still be maintained despite the potential detachment of TiO<sub>2</sub>. Excessive thickness sorb but does not photocatalytically degrade molecules. The film thickness of immobilised TiO<sub>2</sub> is often associated to the multiple coating cycle. This is because TiO<sub>2</sub> generally does not adhere well to many substrates, thus, single coating is not sufficient for effective photocatalysis. The purpose of multiple coating cycles is to saturate the substrate surface to maximise the effective surface area of the coated substrate as well as to synthesize a thicker coating without compromising the coating quality (Sakka, 1994). Peill (1996) did not observe the multiple coating layering effect in dip coating optical fibers into TiO<sub>2</sub> slurry. Shang et al. (2003) found that the limiting thickness of immobilised TiO<sub>2</sub> using sol gel (Section 3.2.1.1) in terms of light illumination efficiency is approximately 250 nm. This is because the photocatalytic efficiency did not increase significantly beyond 250 nm. 1 to 4 coating cycles yielded TiO<sub>2</sub> film thicknesses of

50, 140, 250 and 360 nm, respectively (Shang et al., 2003). The titanium alkoxide spin coating by Watanabe et al. (1999) was measured using scanning electron microscopy (SEM) and by weighing. The initial coating thickness was approximately 0.15  $\mu\text{m}$ , followed by 0.08  $\mu\text{m}$  for the subsequent layers at withdrawal speed of 2  $\text{mm s}^{-1}$ . The spin coating was repeated for 1, 5 and 10 coating cycles for the substrates.

## 2.3 Factors Affecting Photocatalysis

There are various factors which could affect the photocatalytic activity, which could be classified into two main categories as the name suggests, photo as in light and catalysis as in the catalyst, i.e.  $\text{TiO}_2$ , hence refers to coating. The light factor affecting the photocatalytic activity is usually associated with the light intensity as the light wavelength is typically constant, providing the required energy from the photons. One of the instances which could affect the light intensity from light source to the catalyst is the inhibition of light transmittance, usually referring to the turbidity as total suspended solids could be dealt with simple filtration. Turbidity refers to the cloudiness or murkiness of water or other fluid caused by the light scattering action of individual particles (suspended solids) leading to the extinction of the incident light beam, thus being much like smoke in air. Factors affecting the efficiency of a photocatalytic reactor design are described in Chapter 4, as it is part of the design considerations for the proposed reactor in this research.

### 2.3.1 Surface Area and Morphology

Surface area is among the critical parameters in semiconductor photocatalysis as the surface area is proportional to the total number of active sites for the adsorption of compounds and photocatalytic reaction. The surface area of  $\text{TiO}_2$  is important in photocatalysis as photocatalytic degradation of adsorbed compounds is generally initiated with adsorption of molecules (Herrmann, 2005). The photocatalytic activity is mainly affected by the specific surface area of  $\text{TiO}_2$  rather than its crystal phase of anatase ( $50 \text{ m}^2 \text{ g}^{-1}$ ) and rutile ( $5 \text{ m}^2 \text{ g}^{-1}$ ), particularly in terms of porosity and surface area (Mills et al., 1993). Degussa  $\text{TiO}_2$  P25 is more active than that of Aldrich  $\text{TiO}_2$  as it has five-fold larger surface area due to smaller particle size. The specific surface area varies inversely with the particle size of  $\text{TiO}_2$ . A fractal surface is preferred as it provides larger effective surface area (Xagas et al., 1999). However, a recent study by Ryu and Choi (2008) reported that the adsorption

and specific surface area may not be applicable for compounds which either has low adsorptivity or require electrostatic adsorption.

Several methods of analysing the surface morphology include atomic force microscopy (AFM), scanning electron microscopy (SEM) and transmission electron microscopy (TEM). The crystal composition of TiO<sub>2</sub> can be analysed using X-ray diffraction (XRD) and X-Ray photoelectron spectroscopy (XPS).

### 2.3.2 Adsorption

Adsorption is a process involving the attachment of molecules to a surface by electrostatic forces. It is evidently a vital aspect in the photocatalytic degradation of a strongly adsorbing compound in gaseous and aqueous treatment (Bhatkhande et al., 2001) as the PCO of a compound is postulated to be initiated with the adsorption of compound molecule onto the catalyst surface (Herrmann, 2005; Ryu and Choi, 2008). In other words, the PCO rate of a pollutant is a function of the adsorbed pollutant concentration. Hoffmann et al. (1995) and Ryu and Choi (2008) confirmed that there is a correlation between the degradation rate and concentration of pollutant adsorbed to the TiO<sub>2</sub> surface, implying the availability of photogenerated charge-carriers at the surface. Linsebigler et al. (1995) reviewed the chemisorption studies on TiO<sub>2</sub> surface for variety of molecules including oxygen and water. The formation of superoxides, O<sub>2</sub><sup>-</sup>, requires oxygen adsorption on the active sites prior to partial charge transfer from the surface adsorption site to the oxygen molecule. Similarly, the hydroxyl radicals, OH<sup>-</sup>, are synthesized through the reaction between adsorbed H<sub>2</sub>O molecules with a bridging-oxygen atom. Nevertheless, Ryu and Choi (2008) suggested that the effect of adsorption may not be applicable to the PCO of contaminants with low adsorptivity and the PCO of such compounds can also occur via mobile hydroxyl radicals off the catalyst surface. This may be the case for the PCO of MTBE based on its properties (Section 1.2).

### 2.3.3 Dissolved Oxygen Concentration

The importance of oxygen (O<sub>2</sub>) in photocatalysis is emphasized through the reaction stoichiometry (Eq. 2.19) (Mills et al., 1993) and the photocatalytic kinetics as a function of adsorbed oxygen (Eq. 2.20) (Hoffmann et al., 1995). The significance of adsorbed oxygen in photocatalysis is also mentioned in Section 2.3.2.



The presence of reductants and oxidants plays a vital role in the photocatalytic degradation of chemicals (Eq. 2.20) (Hoffmann et al., 1995).

$$-\frac{d[\text{Red}]}{dt} = -d\frac{[\text{Ox}]}{dt} = k_d \theta_{\text{Red}} \theta_{\text{Ox}} \quad (2.20)$$

where  $k_d$  is the photocatalytic degradation rate constant due to photoexcitation and surface chemical reaction processes,  $\theta_{\text{Red}}$  is the fraction of the electron donating reductants and  $\theta_{\text{Ox}}$  is the fraction of the electron accepting oxidants (oxygen), adsorbed on the catalyst surface. As mentioned in stage (v) of the photocatalytic mechanism, reactive oxygen species such as  $\text{H}_2\text{O}_2$  are not formed in the absence of adsorbed oxygen. Therefore, it is evident that the dissolved oxygen concentration in the system has a significant effect on the reaction rate. The photocatalytic activity in  $\text{O}_2$ -saturated (100 %  $\text{O}_2$ ) conditions appeared to be only 1.7 higher than to that of air-saturated (20 %  $\text{O}_2$ ) conditions (Mills et al., 1993).

There were some studies carried out to study the performance of photocatalysis coupled with strong oxidants. Mills et al. (1993) also reported that hydrogen peroxide ( $\text{H}_2\text{O}_2$ ) enhanced the photomineralisation rate of some organics, however, did not deny that  $\text{H}_2\text{O}_2$  can also function as a hydroxyl radical scavenger for other organics. Agustina et al. (2005) reported that addition of a low concentration of ozone into photocatalysis ( $\text{TiO}_2/\text{UV}/\text{O}_3$ ) increased the dissolved organic carbon (DOC) removal. The DOC removal efficiency increased with the ozone dosage up to  $3 \text{ mg L}^{-1}$ . Higher ozone dosage thereafter did not enhance the photocatalysis ozonation efficiency. This could be due to excessive  $\text{O}_3$  functioning as an hydroxyl radical scavenger, which decreases the photocatalytic activity. The mineralisation rate of dibutyl phthalate using  $\text{TiO}_2/\text{UV}/\text{O}_3$  was about 1.2 to 1.8 times higher than that of  $\text{UV}/\text{O}_3$  with the same ozone concentration (Agustina et al., 2005).

#### 2.3.4 Contaminant Concentration

The PCO of a compound is affected by its concentration and properties such as light absorption spectrum. Mills et al. (1993) reported that the photomineralisation kinetics of an organic pollutant is dependent on its PCO rate and adsorption rate on the  $\text{TiO}_2$  surface. Herrmann (2005) suggested that the reaction rate is pseudo first order for concentrations less than  $5 \times 10^{-3} \text{ M}$ . This is expected in the PCO of strongly adsorbing compounds. Kiriakidou et al. (1999) found that the PCO of acid orange (AO7) dye decreased with increasing initial concentration due to adsorption of dye molecules; inhibiting the illumination

of UV light onto the surface and the contact of molecules with the oxidising radicals formed. Conversely, this effect was significantly reduced when the adsorption of AO7 dye molecules was impeded by increasing the pH of solution; enhancing the PCO rate of acid orange (AO7) dye.

The light absorption spectrum of a pollutant has significant impact on the kinetics of photocatalysis (Mills et al., 1993). The photocatalytic degradation rate varies inversely with strong UV absorber pollutant concentration because the increase in concentration will screen the TiO<sub>2</sub> from UV light (Mills et al., 1993). However, this is unlikely to be a significant issue for organic pollutants which are not strong UV absorber, such as MTBE. UV light inhibition from a catalyst surface, such as screening by UV absorber pollutant or deposition of particulate matter on the TiO<sub>2</sub> surface, is usually an overlooked major drawback of TiO<sub>2</sub> photocatalysis in water purification (Mills et al., 1993). This corresponds to another possible issue in groundwater remediation, i.e. turbidity. The turbidity of the groundwater in reactor can be measured in terms of absorbance using a UV/Vis spectrophotometer, and converted to percent light transmittance, which is expected to be proportional to the light intensity. Absorbance is zero indicating that all the light passes through a solution without any absorption and percent transmittance is 100 %, and vice versa. The relationship between absorbance and transmittance is expressed by Eq 2.21 and illustrated in Figure 2.8.

$$A = -\log_{10}\left(\frac{I}{I_0}\right) = -\log_{10}(T) \quad (2.21)$$

where  $A$  is the absorbance unit (a.u.),  $I$  is the transmitted light intensity,  $I_0$  is the incident light intensity and  $T$  is the light transmittance (%); of a specified wavelength.

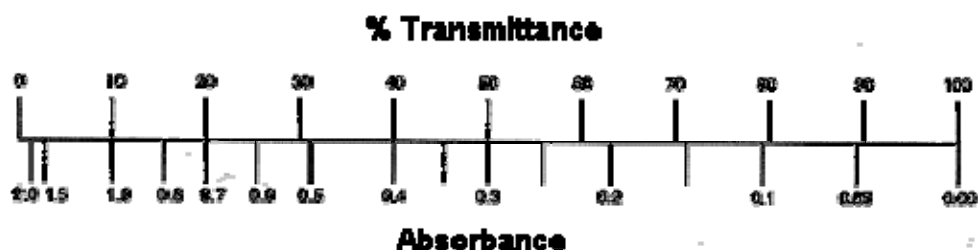


**Figure 2.8** Relationship between absorbance and percent light transmittance

### 2.3.5 pH

Mills et al. (1993) reported that photocatalysis is not strongly dependent on pH, with typical variation by less than an order of magnitude from pH 2 to 12. The PCO rates of nitrotoluenes were found to be pH independent (Kabra et al., 2004). Agustina et al. (2005) concluded that pH adjustment is not necessary for operating photocatalytic reactors due to its negligible effect on photocatalysis. The coupling of photocatalysis ozonation is most effective at pH 7. Bhatkhande et al. (2001) confirmed photocatalysis typically performs best at pH 7 as it is the point of zero charge (PZC) pH, also known as isoelectric point (pI), where adsorption and photocatalytic degradation rate is maximum. The PZC of Degussa P25 is about pH 7 (Wang et al., 2004). Fox and Dulay (1993) reviewed the weak pH effect on photocatalytic degradation rate and the pI for TiO<sub>2</sub> in water is approximately pH 6 (Ryu and Choi, 2008).

Nevertheless, the pH of the aqueous solution can affect photocatalysis in terms of the charge of particles, adsorption and the positions of the conductance and valence bands. pH changes the surface charge of the catalyst and adsorption behaviour of ions. Kiriakidou et al. (1999) found a strong dependence of AO7 dye adsorption on the pH of the solution; AO7 dye adsorption decreased with increasing pH. The adsorption of cations on the catalyst surface is enhanced when the catalyst surface is negatively charged in alkaline conditions and vice versa for anions. Among the common ions present in groundwater are chloride (Cl<sup>-</sup>) and bicarbonate (HCO<sub>3</sub><sup>-</sup>) ions. Liao et al. (2001) found that the OH<sup>-</sup> concentration at pH 6 is about 100 times of that at pH 2 in the presence of Cl<sup>-</sup>, which suggests that the reactor efficiency can be enhanced when operated in neutral or alkaline conditions. This is due to the pK value for deprotonation reaction, which HOCl is the dominant species when pH is greater than 7.2, and Cl<sup>-</sup> and H<sub>2</sub>O becomes the dominant species when pH is less than 7.2. However, the presence of bicarbonate ion, the OH<sup>-</sup> concentration decreased with increasing pH. Therefore, Liao et al. (2001) suggested the optimum pH between 5 and 7 for the operation of photocatalytic reactors in the presence of chloride and bicarbonate ions. Kabra et al. (2004) agreed that the catalyst appears to be more effective in acidic and slightly alkaline condition.

Although pH is an important reactor operation parameter, the effect of pH was not investigated in this study as it is focused on the reliability of the proposed photocatalytic reactor design in ambient conditions.

### 2.3.6 Presence of Other Organics, Anions and Cations

The presence of competitive adsorbates seems to challenge and inhibit the overall reaction rate due to deactivation of reactive sites. For the organic compounds, it is likely that the more strongly adsorbed organic molecules will be degraded first and inhibit the subsequent adsorption of the other organic molecules (Sahle-Demessie et al., 2002b). The other possibility is the increased competition for OH radicals among the molecules (Matthews, 1992). Both phenomena can explain the reduced removal rate of a target contaminant in the presence of more strongly adsorbing organic compounds.

As photocatalysis involves reduction and oxidation (redox) reactions, it is also affected by the presence of dissolved ions (Mills et al., 1993; Litter, 1999). Iron, at certain concentrations (Butler and Davis, 1993; Klauson et al., 2005), is reported to have a beneficial effect on the PCO of a contaminant, thought to be due to iron (III) ( $\text{Fe}^{3+}$ ) reducing electron-hole recombination, thus increasing the OH radical generation rate. Ferrous ( $\text{Fe}^{2+}$ ) and ferric ( $\text{Fe}^{3+}$ ) ions have similar effects on the PCO rate of a contaminant possibly due to an equilibrium established between  $\text{Fe}^{2+}$  and  $\text{Fe}^{3+}$  in acidic aqueous solution in the presence of dissolved oxygen (Scalfani et al., 1991; Butler and Davis, 1993; Vamathevan et al., 2001; Klauson et al., 2005). Bhatkhande et al. (2001) reported that the presence of cations generally decreases the photocatalytic activity, except iron, silver and copper at trace concentrations ranging between 1 and  $5 \times 10^{-6}$  mmol  $\text{L}^{-1}$ . Reduction in photocatalytic activity at higher cation concentration could be resulted from the effect of anion associated with metal ions (metal precipitation) and solution opacity.

Mills et al. (1993) summarised that concentrations of anions, such as sulfate, chloride and phosphate, greater than  $10^{-3}$  mol  $\text{L}^{-1}$  can decrease the photomineralisation rate by 20 to 70 % through adsorption at oxidation sites on  $\text{TiO}_2$  surface. Liao et al. (2001) found that chloride ion inhibited the PCO of n-chlorobutane by scavenging the  $\text{OH}^\cdot$  radical and deactivating active sites via adsorption on the positively charged catalyst surface, especially in acidic conditions. Mills et al. (1993) found that nitrate concentration at 0.4 mol  $\text{L}^{-1}$  can decrease the photomineralisation rate of 4-chlorophenol by 50 % through screening of the  $\text{TiO}_2$  from UV light. Bhatkhande et al. (2001) confirmed that the anions, including bicarbonate ions, affect the adsorption of degrading species, scavenging hydroxyl radical and can screen  $\text{TiO}_2$  from UV light. The effect obeys the order of:  $\text{SO}_4^{2-} < \text{HCO}_3^- < \text{NO}_3^- < \text{Cl}^-$ .

While the effect of organic compounds on the PCO of a target contaminant seems to be straight forward, the effect of dissolved ions is more complicated when a mixture of dissolved ions are present. Sahle-Demessie et al. (2002b) observed that the PCO rate constant of

MTBE was inhibited by an order of magnitude in actual groundwater compared with deionised water and was attributed to dissolved metal ions and chlorides. Mehos and Turchi (1993) found that the PCO rate constant of TCE was enhanced 5 to 7-fold under acidic conditions (pH 5) compared with neutral conditions (pH 7); the catalyst loading and flow effects were negligible. Nevertheless, the PCO rate constant of TCE was still significantly lower when treating actual groundwater, compared to that in deionised water. Matthews (1992) reported that the reactor efficiency varied with different wastewater treated; 10 and 40 % reduction in the PCO rate determined by CO<sub>2</sub> formation when treating 100 mg L<sup>-1</sup> phenol spiked in wastewaters from a paint stripping operation and petroleum refinery, respectively, compared to that in deionised water. Due to the complex matrices in groundwater and wastewater, it is difficult to identify the inhibiting constituent. Some studies have investigated the effect of organics and inorganics, typically dissolved ions (Scalfani et al., 1991; Butler and Davis, 1993; Liao et al., 2001; Vamathevan et al., 2001; Wang et al., 2004; Klauson et al., 2005) on the PCO of a target contaminant. However, these studies usually scrutinise the effect of one type of constituent only, for example chloride (Liao et al., 2001) and iron (Vamathevan et al., 2001; Klauson et al., 2005). Therefore, it would be interesting to observe the inhibition of a contaminant in the presence of organics, dissolved ions and combination of organics and dissolved ions.

### 2.3.7 Light Intensity and Wavelength

Light plays an essential role in photocatalysis as it is required in the photogeneration of charge-carriers to initiate the redox reaction with adsorbed pollutant molecules. The determination of light source wavelength mainly depends on the energy band gap of semiconductor in photocatalysis. Energy band gap,  $E_g$ , is the energy level difference between the conduction and valence band of a semiconductor. In photocatalysis, the semiconductor photocatalyst requires an energy level equal to or greater than  $E_g$ , induced by the photons of light, in order to activate the oxidation and reduction (redox) of the target pollutant. The minimum energy band gap for promoting electrons and holes for anatase and TiO<sub>2</sub> is +3.2 and +3.0 eV, respectively (Bhatkhande et al., 2001). The energy level by the photons of light is directly related to the wavelength of light as shown in Eq. 2.22.

$$E = \frac{hc}{1.602 \times 10^{-19} \cdot \lambda \times 10^{-9}} = \frac{1.24 \times 10^3}{\lambda} \quad (2.22)$$

where  $E$  is the energy level in electron Volt (eV),  $h$  is the Planck's constant ( $6.63 \times 10^{-34}$  Js),  $c$  is the speed of light ( $3 \times 10^8$  m s<sup>-1</sup>),  $\lambda$  is the wavelength of light (nm) and  $1.602 \times 10^{-19}$  J is equivalent to 1 eV. From Eq. 2.25, the light wavelength limit for photocatalysis using TiO<sub>2</sub> is approximately 400 nm, which is the ultraviolet (UV) light range. Although shorter wavelength irradiation at 254 nm is considerably more effective than that at 350 nm (Bhatkhande et al., 2001), the UV lamps emitting the light wavelength of 365 nm, which yields approximately +3.4 eV, is used in this study to ensure the reaction is truly photocatalytic and not photolytic.

Mills et al. (1993) summarised that the photocatalytic degradation rate is usually proportional to  $I^{0.5}$  as the light intensities used are typically greater than  $6 \times 10^{-14}$  ultra-band gap photon cm<sup>-2</sup> s<sup>-1</sup>. Egerton and King (1979) showed that the rate changed from first order to half order with increasing light intensity (Figure 2.9), using the photo-oxidation of isopropyl alcohol to acetone by rutile TiO<sub>2</sub> in air-saturated solution. The photocatalytic degradation rate is proportional to  $I$  below the photocatalytic degradation rate of  $1 \times 10^{-5}$  mol cm<sup>-2</sup> s<sup>-1</sup> and  $I^{0.5}$  above the photocatalytic degradation rate of  $2 \times 10^{-5}$  mol cm<sup>-2</sup> s<sup>-1</sup> for phenol using anatase TiO<sub>2</sub> (Bhatkhande et al., 2001). The proportionality of the photocatalytic reaction rate changes from  $I$  to  $I^{0.5}$  at an approximate light intensity of 25 mW cm<sup>-2</sup> (Herrmann, 2005).

Most of the light distribution reactors utilises high power lamps such as 1000 W Xenon arc lamp (Peill, 1996) while direct illumination reactors utilises low power lamps (Mills et al., 1993; Chan and Lynch, 2003a and b). Nevertheless, Fujishima et al. (2000) reported that TiO<sub>2</sub> photocatalysis is dependent on the energy of the incident photons to a first approximation instead of intensity. This is because photocatalysis can be initiated by several photons of the required energy. Fujishima et al. (2000) demonstrated that a constant maximum quantum yield for photocatalysis was achieved at low light intensity due to minimal recombination losses and high coverage of the adsorbed organic compound.

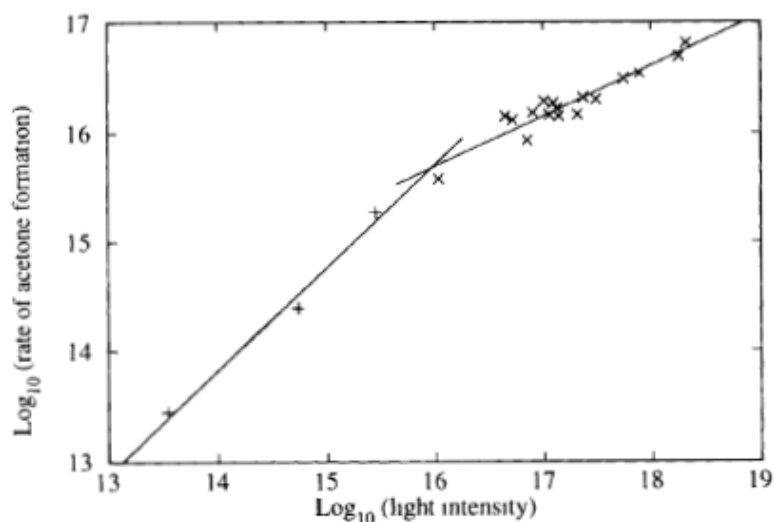


**Figure 2.9** The rate of acetone formation from isopropyl alcohol photodegradation by pure rutile plotted against incident light intensity (Mills et al., 1993)

In addition, its potential of utilising solar energy is well known (Bahnemann, 2004) and many researchers have been modifying  $\text{TiO}_2$  photocatalyst, such as doping, to enhance its application using sunlight by enabling it to be activated by a wider range of light wavelengths (Kiriakidou et al., 1999; Orlov, 2004; Herrmann, 2005).

### 2.3.8 Temperature

Photocatalysis is a process which is initiated through the photonic activation, thus photocatalytic reactors can be operated at ambient temperature and do not require heating (Herrmann, 2005). Most studies found that photocatalysis is not considerably affected by reaction temperature (Mills et al., 1993; Bhatkhande et al., 2001; Herrmann, 2005). Although higher reaction temperature increases all the reactions rates and decreases oxygen solubility in water, it does not appear to have significant effect on photocatalysis. Fox and Dulay (1993) reported that photocatalysis is not dramatically sensitive to small variations in temperature, which are mainly from UV irradiation and thermal effect from chemical reactions involved. The activation energy of semiconductor photocatalysis is often small, typically ranging between 5 and 16  $\text{kJ mol}^{-1}$  (Mills et al., 1993). However, it should be noted that the removal rate of a VOC can be affected by temperature as the volatilisation of a VOC increases with increasing temperature. This can be represented by the Henry's law constant, a parameter to reflect air-to-water partitioning of a compound, for example MTBE 0.012 (10 °C), 0.022 (20 °C) and 0.029 (25 °C) (Fischer et al., 2004); a greater constant indicates a greater tendency to partition into air.

## 2.4 Continuously Mixed Tank Reactor

The proposed photocatalytic reactor design in this research is considered as a continuously mixed tank reactor (CMTR). CMTR, also known as continuously stirred tank reactor (CSTR), refers to ideal reactors typically in steady state, in which the contents of the reactor is uniformly agitated while there is flow through the reactor. The CMTR model assumes constant density, isothermal conditions, steady state, and single, irreversible and first order reaction. Accumulation is assumed zero and the inflow must equal outflow in steady state conditions. Generation rate,  $R$ , is negative when a compound is degraded. The mass balance of reactants equations (Eq. 2.23 and 2.24) assume the reaction proceeds at the reaction rate associated with the effluent concentration.

$$In + Generation = Out + Accumulation \quad (2.23)$$

$$Q_0 C_0 + RV = Q_e C_e + V \frac{dC}{dt} \quad (2.24)$$

where  $Q_0$  is the incoming volumetric flow,  $C_0$  is the initial concentration of the compound,  $Q_e$  is the effluent volumetric flow,  $C_e$  is the effluent concentration of the compound,  $R$  is the rate at which the compound is formed or reduced,  $V$  is the reactor volume and  $C$  is the concentration of compound in the reactor. The concentration of compound is in the units of mol per volume. Eq. 2.24 assumes that the reaction is occurring in the solution.

Vella et al. (2010) developed a mass balance equation (similar to Eq. 2.24) for the differential fixed bed reactor (Eq. 2.25), which considered the surface area of catalyst, concentration of contaminant and photon absorption (light).

$$\int_A R dA = Q(C_0 - C_e) \quad (2.25)$$

where  $Q$  is the volumetric flow through reactor (assuming  $Q_0 = Q_e$ ),  $C_0$  is the initial concentration of the compound,  $C_e$  is the effluent concentration of the compound,  $A$  is the photocatalytic area of the reactor and  $R$  is the degradation rate of the compound, which must be a function of the local reactant concentration on the catalyst surface and the local surface rate of photon adsorption.

The hydraulic residence time (HRT) is the average duration for a molecule to remain in a reactor prior to discharge, which is expressed by the ratio of reactor volume to flow of a compound into the reactor (Eq. 2.26). HRT decreases with increasing flow, and vice versa. In this research, the HRT can also be defined as the average duration to allow for the contact of compound molecules with the oxidising radicals because a compound molecule needs to be in contact with a radical prior to its degradation.

$$\tau = \frac{V}{Q} = \frac{V}{A.v} \quad (2.26)$$

where  $\tau$  is the hydraulic residence time,  $V$  is the reactor volume,  $Q$  is the volumetric flow,  $A$  is the area of section perpendicular to flow direction and  $v$  is the average velocity of flow.

Herrmann (2005) (Eq. 2.27) and Dionysiou et al. (2000a) (Eq. 2.28) used HRT in calculating the efficiency of the compound parabolic collector photoreactor (similar to Figure 1.10c) in the recirculation system and rotating disk photocatalytic reactor (Figure 1.14), respectively.

$$C = C_0 \cdot \exp\left[-\left(\frac{1+r}{r}\right)k.\tau\right] \quad \text{with} \quad r = \frac{V}{V_t} \quad (2.27)$$

where  $C$  is the concentration of the compound,  $C_0$  is the initial concentration of the compound,  $k$  is the first order reaction rate constant,  $\tau$  is the HRT, and  $r$  is the ratio of the reactor volume (section exposed to sunlight),  $V$ , to a feed tank volume,  $V_t$ .

$$\frac{C}{C_0} = \alpha \cdot \exp^{\beta[-(t/\tau)]} \quad (2.28)$$

where  $\alpha$  and  $\beta$  are the coefficients of the equation (both are equal to 1 for an ideal continuously stirred tank reactor) and  $t$  is the time after the pulse input.

## 2.5 Contaminant Transport

As mentioned in Chapter 1, the migration of a contaminant is affected by both soil and contaminant characteristics.

### 2.5.1 Soil Characteristics

In terms of soil properties, the grain size of soil is typically characterised in hydrogeological studies because it affects the soil permeability (term used by engineers), also known as hydraulic conductivity by hydrogeologists. The ranges of permeability is controlled by the soil type (Figure 2.10). The intrinsic permeability of soil can be estimated using the sieve size which is passed through by the first 10 % (w/w) of soil,  $d_{10}$  (Eq. 2.29) (Bolton, 1979), which governs the permeability as it fills the spaces among the larger soil grains.

$$k = 0.01(d_{10})^2 \quad (2.29)$$

where  $k$  is the permeability ( $\text{m s}^{-1}$ ), 0.01 is the proportionality constant of the sphericity and roundness of the grains and  $d_{10}$  is the grain size of the first 10 % by weight of the soil sample measured using PSD (mm). The value of  $d_{10}$  is obtained by a particle size distribution (PSD) chart, plotted using data obtained from sieve analysis. A PSD chart can also reflect how well sorted the soil is. In the case of graded sands, the sand typically falls within a certain range of grain sizes (Table 2.3).

**Table 2.3** Range of grain size (in  $\mu\text{m}$ ) of sand grades (David Ball Plc.)

Grade	E	D	C	B	A
Grain Size	90 - 150	150 - 300	300 - 600	600 - 1180	1180 - 2000

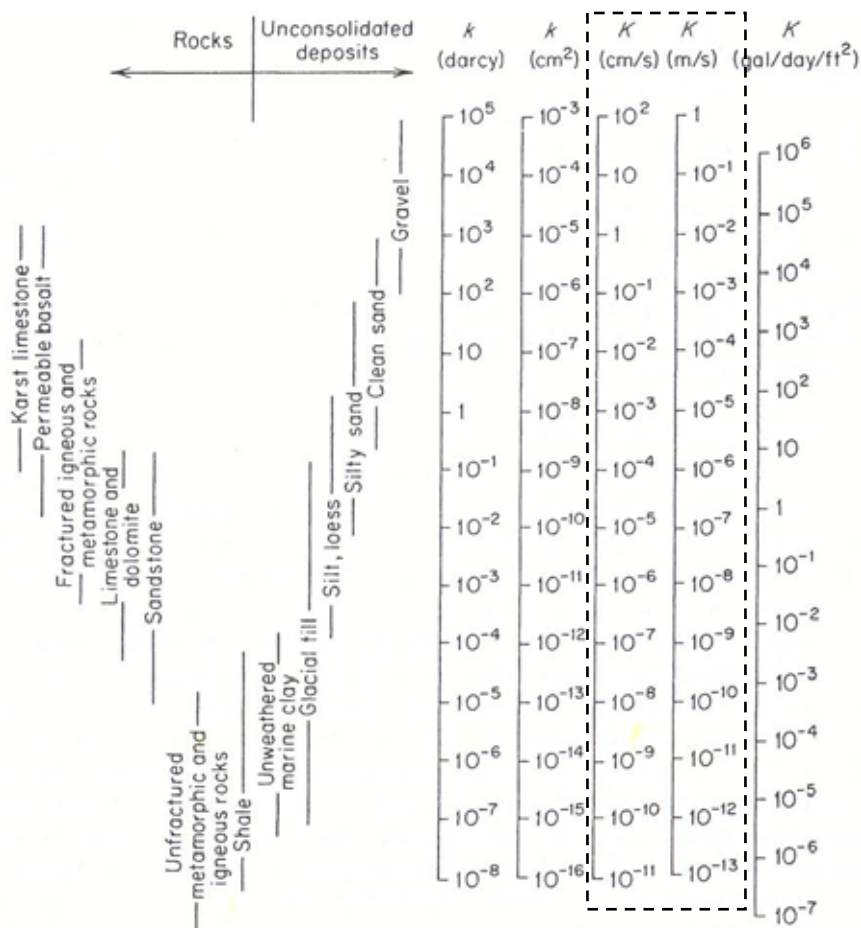


**Figure 2.10** Representative values of permeability (in dotted box) for various rocks and unconsolidated sediments (Freeze and Cherry, 1979)

### 2.5.2 Transport Mechanisms

The migration of a contaminant is usually documented in terms of advection, dispersion and retardation factor.

#### 2.5.2.1 Advection

Advection is a process where solutes are transported by the flowing groundwater. The advective velocity is described by the Darcy's law that a flow velocity is linearly proportional to the dimensionless hydraulic gradient, which yields a constant called permeability,  $k$  (Eq. 2.30).

$$v_D = k \frac{\partial h}{\partial l} = ki \tag{2.30}$$

where  $v_D$  is the Darcy's velocity ( $\text{m d}^{-1}$ ),  $k$  is the permeability ( $\text{m d}^{-1}$ ) and  $\delta h/\delta l$  or  $i$  is the hydraulic gradient. As water flows only through the pore openings among soil grains, a more realistic velocity is the average linear velocity which refers to the volumetric flow per unit area of interconnected pore space. Here, the effective porosity of soil representing the effective flow area (the interconnected pores where flow can occur) is considered (Eq. 2.31).

$$v = \frac{v_D}{n_e} = \frac{k}{n_e} i \quad (2.31)$$

where  $v$  is the average linear velocity ( $\text{m d}^{-1}$ ),  $v_D$  is the Darcy's velocity ( $\text{m d}^{-1}$ ),  $n_e$  is the soil porosity,  $k$  is the permeability ( $\text{m d}^{-1}$ ), and  $i$  is the hydraulic gradient. Porosity is the fraction of the volume of the voids over the total unit volume, representing the void spaces in soil. It ranges from 0 to 1 (decimal fraction) or 0 to 100 % (percentage). The porosity of sand typically ranges between 25 and 50 % (Freeze and Cherry, 1979).

### 2.5.2.2 Dispersion

Dispersion is a process resulting in a dilution of a contaminant when mixed with uncontaminated water as a contaminated fluid flows through a porous medium. There are basically three factors causing the pore-scale longitudinal dispersion, i.e. the pore size, path length and friction in pore. Therefore, similar to advection, the extent of dispersion also depends on grain size, with finer grain size resulting in greater transverse dispersion. There are two types of dispersion, i.e. longitudinal dispersion and transverse dispersion. Longitudinal dispersion refers to the mixing occurring along the flow path directions, while transverse dispersion refers to the mixing in the directions normal to the flow path. In Chapter 6, longitudinal dispersion represents the mechanical dispersion, which is a mixing occurring along the flowpath due to different path lengths and velocities caused by flow through different sized voids. This is because the overall flow is assumed to be a plug flow with minimal transverse dispersion.

### 2.5.2.3 Peclet Distribution

The Peclet number, a useful ratio which relates the advective transport to the diffusive transport, is a dimensionless number in the form of  $v_w d_{50}/D_d$ , where  $v_w$  is the average linear velocity,  $d_{50}$  is the average grain diameter which represent the characteristic flow lengths

and  $D_d$  is the molecular diffusion coefficient. Diffusion is a process involving the migration of solutes from areas of higher concentrations to areas of lower concentrations. By plotting dimensionless dispersion coefficients  $D_L/D_d$  against the Peclet number (Figure 2.11), the relative contribution of dispersion and diffusion to solute transport can be evaluated.  $D_L$  is the longitudinal dispersion coefficient.

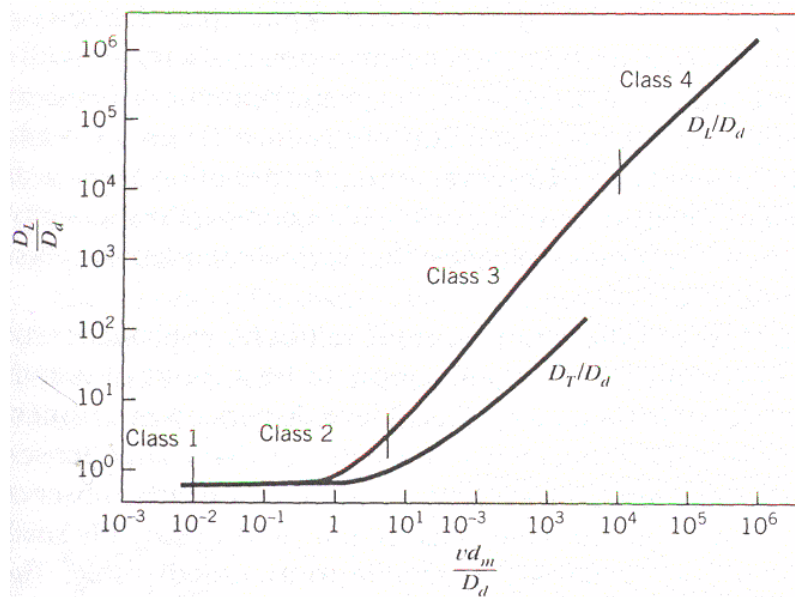


**Figure 2.11** The behaviour of  $D_L/D_d$  and  $D_T/D_d$  as a function of Peclet number, with classes of mixing (Domenico and Schwartz, 1997);  $v$  is the average linear velocity,  $d_m$  is the average grain size,  $D_d$  is the molecular diffusion coefficient and  $D_L$  is the longitudinal dispersion coefficient. Class 1: the mixing is dominated by diffusion, Class 2: the mixing is influenced by diffusion and dispersion, Class 3: the mixing is dominated by dispersion with  $D_L$  values approximately proportional to  $v_w^{1.2}$ , Class 4: the mixing is dominated by dispersion with negligible effect of diffusion.

#### 2.5.2.4 Breakthrough Curve

The advection, dispersion and retardation factor can be determined through breakthrough curves, using a software program CXTFIT (Toride et al., 1999). A breakthrough curve (Figure 2.12) can be obtained by plotting the relative concentration of a contaminant ( $C/C_0$ ) as a function of time for a specific point. The concentration is initially zero, and as the contaminant arrives, will gradually increase to the initial contaminant concentration,  $C_0$ . The first contaminant molecules to arrive traveled through the shortest flow paths. The breakthrough time is when the relative concentration of a contaminant achieves 0.5 (50 % of initial contaminant concentration,  $C_0$ ). It can be said that the dispersion is in the region of

relative concentration between 0.16 and 0.84, while outside this region is considered as diffusion.

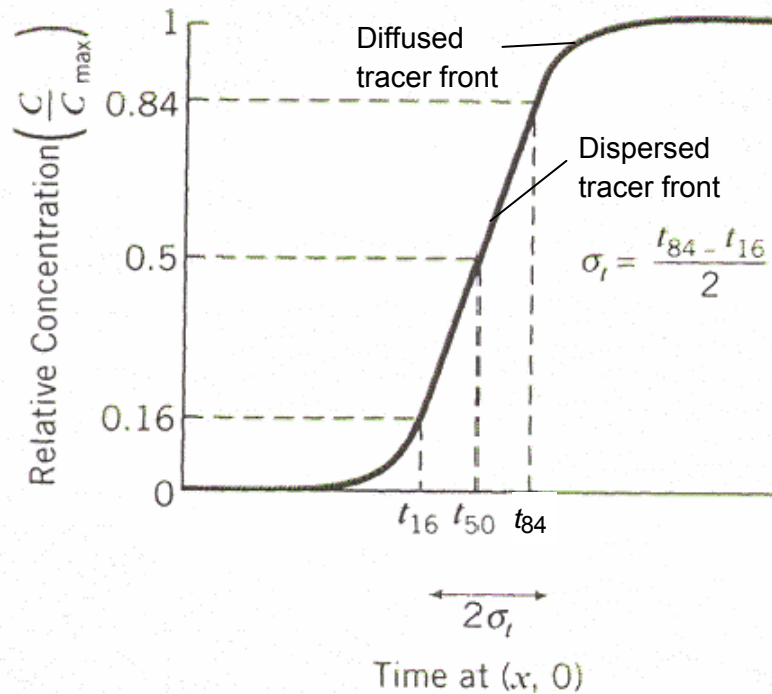


**Figure 2.12** Breakthrough curve of a contaminant from a continuous point source (Domenico and Schwartz, 1997),  $t_{50}$  is the breakthrough time of the contaminant

CXTFIT uses the advection-dispersion equation for 1-dimensional reactive solute transport, which is subjected to adsorption, first-order degradation and zero-order production (Eq. 2.32) (Toride et al., 1999).

$$\frac{\partial}{\partial t}(\theta C + \rho_b C_s) = \frac{\partial}{\partial x} \left( \theta D \frac{\partial C}{\partial x} - J_w C \right) - \theta \mu_l C - \rho_b \mu_s C_s + \theta \gamma_l(x) + \rho_b \gamma_s(x) \quad (2.32)$$

where  $C$  is the concentration of contaminant in the liquid phase,  $C_s$  is the concentration of the adsorbed phase,  $D$  is the dispersion coefficient,  $\theta$  is the volumetric water content,  $J_w$  is the volumetric water flux density,  $\rho_b$  is the soil bulk density,  $\mu_l$  and  $\mu_s$  are the first-order decay coefficients (assumed positive value) for degradation of solute in the liquid and adsorbed phases, respectively,  $t$  is time,  $\gamma_l$  and  $\gamma_s$  are zero-order production terms for the liquid and adsorbed phases, respectively, which are given as a function of the distance,  $x$ .

### 2.5.2.5 Retardation Factor

Retardation is an effect where a solute migrates slower than the groundwater flow due to numerous processes such as sorption to the surface of soil grains or organic carbon, chemical precipitation, biodegradation or chemical reaction. Retardation factor is defined as the groundwater to contaminant transport velocity ratio (Eq. 2.33), with 1.0 indicating a contaminant which migrates at the velocity of groundwater flow.

$$R = \frac{v_w}{v_c} = 1 + \frac{K_d \times \rho_b}{n} \quad (2.33)$$

where  $R$  is the retardation factor of an organic compound,  $v_w$  is the average linear velocity of groundwater,  $v_c$  is the transport velocity of an organic compound,  $K_d$  is the distribution coefficient for the solute with the soil,  $\rho_b$  is the soil bulk density and  $n$  is the total porosity.

As for organic compounds, their migration also depends on adsorption behaviour and the organic carbon content of soil. For instance, MTBE typically has a retardation factor close to 1.0 (Saponaro et al., 2009), lower than that of benzene (1.4-1.6), toluene (1.5-2.8) and o-xylene (11.3) (Da Silva and Alvarez, 2002; Saponaro et al., 2009). One of the reasons is the lighter molecular weight of MTBE than that of BTEX. However, when the carbon content of soil is high (up to 15 %) and in fine grain soil, the MTBE and benzene retardation factor can increase up to 1.86 and 2.00, respectively, for lacustrine sediments at 25 °C (Leal-Bautista and Lenczewski, 2006).

The retardation factor of an organic compound can be affected by the presence of other liquid organic compounds via the co-solvent effect. Co-solvent effect refers to the enhanced solubility of a hydrocarbon by a highly soluble organic solvent in water, resulting in the increase of concentration and migration of the more retarded hydrocarbons in water. MTBE has little effect on hydrocarbon solubility in the water phase (Groves Jr., 1988). Alberici et al. (2002) confirmed that MTBE speeds up BTEX solubilisation in water; BTEX migration at similar rate to that of MTBE but at significantly lower concentrations. Ethanol showed a greater co-solvent effect on the BTEX solubilisation than MTBE.

## CHAPTER 3

### IMMOBILISATION OF TITANIUM DIOXIDE

#### 3.0 Overview

This chapter describes the investigation for a suitable TiO<sub>2</sub> immobilisation procedure, using dip coating methods, for the in-situ photocatalytic reactor for groundwater remediation. It can be considered the foundation for this research as the immobilisation procedure determined was applied to synthesize all the immobilised TiO<sub>2</sub> for the photocatalytic reactor in this research. The process involved the selection and preparation of several coating solutions and substrates, which were then evaluated for their performance, in terms of deposition and photocatalytic activity. When the suitable combination of coating solution and substrate was determined, the suitable number of coating cycles, and calcination duration and temperature were tested to obtain the preparation conditions which yielded the best performance of the coating. The determination of preparation conditions also considered the economic aspect of the overall TiO<sub>2</sub> immobilisation procedure. The coating determined to be applied for the research was then characterised to confirm the crystal structure as well as the surface at microscopic scale. The suitable immobilisation procedure was scaled up and the samples were tested and characterised, similar to that of the small scale immobilisation procedures.

A simple light intensity measurement at various distances was conducted for both the UVA light sources for the estimation of the light intensity illuminated on the immobilised TiO<sub>2</sub> surface and also assist in the design of actual scale photocatalytic reactor for field application.

### 3.1 Introduction

The principle of the application of photocatalysis in water and wastewater treatment has been well researched, particularly in the degradation of organic compounds into simple mineral acids, carbon dioxide and water (Mills et al., 1993; Hoffmann et al., 1995). There are typically two types of reactor, i.e. slurry catalyst and immobilised catalyst. A slurry reactor refers to titanium dioxide ( $\text{TiO}_2$ ) powder which is suspended in the water to be treated, while the immobilised catalyst reactor has  $\text{TiO}_2$  powder attached to a substrate which is immersed in the water to be treated. Immobilised  $\text{TiO}_2$  has become more popular due to the complications in the  $\text{TiO}_2$  suspension systems (Wang et al., 2002). Among the complications is the post-treatment separation of  $\text{TiO}_2$  powder from the partially treated water, resulting in additional treatment cost. As a plethora of  $\text{TiO}_2$  immobilisation procedures have been developed over the past few decades, it can be quite perplexing in determining a suitable immobilisation procedure, particularly if using economical and simple equipment. The overall performance of the  $\text{TiO}_2$  coating can be affected by various factors depending on the coating methods. In addition, it is also difficult to evaluate the photocatalytic efficiencies of the coatings as the photocatalytic activity of catalysts is compound specific (Ryu and Choi, 2008). The efficiency will vary due to factors such as (i) light source: artificial light source (Peill, 1997; Wang et al., 2002) and solar energy (Alfano et al., 2000; Bahnemann, 2004), and (ii) chemical compounds: organics (Fujishima et al., 2000; Wang et al., 2002) and dyes (Mills et al., 1993; Mills and McFarlane, 2007).

There are also many alternative types of substrates used typically e.g. (i) optical fibre (Peill and Hoffman, 1996), (ii) fibreglass (Brezova et al., 1997), (iii) quartz (Peill and Hoffman, 1995) or (iv) borosilicate glass (Yu et al., 2000; Chen and Dionysiou, 2008) and (v) stainless steel (Balasubramanian et al., 2004; Chen and Dionysiou, 2006a-c). The substrate shape also can affect performance such as (i) cylinders (Chan and Lynch, 2003a), (ii) tubes (Ray and Beenackers, 1998a and b), (iii) sheets or plate (Bahnemann, 2004), and (iv) beads (Balasubramanian et al., 2004; Chan, 2005), etc.

Dip coating is a method involving the processes of dipping and withdrawing a substrate into a dip coating solution to attach  $\text{TiO}_2$  to a substrate. Dip coating solutions using either (i) commercial  $\text{TiO}_2$ : Degussa P25 (Peill and Hoffman, 1996) now known as Aeroxide  $\text{TiO}_2$  P25, Aremco (Keshmiri et al., 2004) and Ishihara ST-B01 (Balasubramanian et al., 2004), (ii) lab synthesized solutions: sol gel (Sakka, 1994; Xagas et al., 1999), reverse micelles (Yu et al., 2002a) and slurry (Chan, 2005; Rodriguez et al., 2009) or (iii) mixtures of both (Balasubramanian et al., 2004; Chen and Dionysiou, 2006b; Medina-Valtierra et al., 2006) have been reported. Nevertheless, Ryu and Choi (2008) reported that  $\text{TiO}_2$  could be

effective for degradation of certain compounds only. Therefore, there is still a level of uncertainty about which is the most appropriate method to use for a particular application.

The calcination (defined in Section 2.2.2) duration of TiO<sub>2</sub> coatings is also diverse, ranging from minutes (Sakka, 1994; Xagas et al., 1999; Fretwell and Douglas, 2001; Chen and Dionysiou, 2008) to hours (Su et al., 2004; Chen and Dionysiou, 2006b) and the calcination temperatures are also reported to vary from 200 °C in an autoclave (Kontos et al., 2005) or 450 to 700 °C (Yu et al., 2002b; Chen and Dionysiou, 2006a-c), respectively.

The more consistent aspect in the immobilisation procedures is the number of coating cycles used, in which mostly are not more than ten (Yu et al., 2002b; Balasubramanian et al., 2003; Chen and Dionysiou, 2006c; Chen and Dionysiou, 2008). The number of coating cycle refers to the number of times of dipping the substrate; one dip is one coating cycle. However, the coating thickness, which increases with the viscosity of solution in dip coating, ranges from nanometer (Sakka, 1994) to micron (Subramanian et al., 2003; Chen and Dionysiou, 2006b and c). It should be emphasized that the purpose of multiple coating is to reduce any uncoated surface of substrate, as thin TiO<sub>2</sub> film is sufficient in obtaining a favourable photocatalytic activity.

The objective of this investigation is to determine the most suitable TiO<sub>2</sub> immobilisation procedure, to be replicated using economical and simple setup of equipment usually found in the laboratory. Only dip coating was used in this research because it can coat both sides of substrate surface simultaneously, thus enabling the utilisation of both sides of the coating in the intended groundwater remediation application. In addition, dip coating can be conducted using equipment which is usually found in an environmental laboratory. The variables to be studied are type of coating solution, substrate, coating cycles, calcination duration and temperature. This work may be useful to researchers by providing the relative performance of different dip coating alternatives tested under identical conditions.

### **3.2 Methodology: TiO<sub>2</sub> Immobilisation Procedure**

The selection of coating method is important because it would affect the deposition of TiO<sub>2</sub> as well as the complexity of the immobilisation procedure. Only simple and economical coating procedures are considered in this research. Dip coating enables the utilisation of both sides of the coating during the photocatalytic reaction. In other words, this investigation intends to find the most suitable preparation method of coating, which yields the highest possible photocatalytic activity.

The coating solutions selected are: sol gel, hybrid, reverse micelles and slurry. A modified peristaltic pump, Watson-Marlow 502S (Figure 3.1), was positioned above the coating solution and used as a simple windlass to dip and withdraw the substrates vertically at a controlled rate of  $4 \text{ mm s}^{-1}$ , to obtain a uniform coating over the substrates. Room temperature was held constant  $20 \pm 2 \text{ }^{\circ}\text{C}$  (lab conditions) throughout the coating process. The number of coating cycles is specified in the respective studies.



**Figure 3.1** Modified Watson-Marlow 502S peristaltic pump for dip coating, dip coating of a  $12 \text{ cm}^2$  aluminium plate in sol gel (inset)

### 3.2.1 Preparation of Coating Solutions

#### 3.2.1.1 Sol Gel

The sol gel process refers to the generation of sol, a suspension of colloids (of  $\sim 1\text{-}1000\text{nm}$  particle size) in discrete dispersed phase, in a gel. The sols are hardly affected by gravitational forces and interactions with other materials are dominated by short-range forces, such as van der Waals and surface charges. The sol gel preparation procedures (Figure 3.2) were adopted and modified from Xagas et al. (1999). 1.1 mL titanium tetraisopropoxide was dripped to avoid agglomeration into 10 mL of a 7:10 ethanol/isopropanol mixture under vigorous stirring.  $\text{TiO}_2$  sols are formed by the decomposition of titanium isopropoxide upon the mixing with alcohol. A drop of 3 M hydrochloric acid (HCl) was added to the solution, to form a homogenous semi-transparent sol. The solution was then left standing to peptise for 1, 6 and 12 hours prior to deposition to form a clear solution. Peptisation is a process involving the dispersion of solids into a colloidal state, forming clearer sol. The coated sample was then air dried and the procedure

was repeated for the subsequent coatings. The coated substrate was dried at 105 °C for 15 minutes to remove moisture and subsequently annealed at 500 °C for 30 minutes to remove organic components.

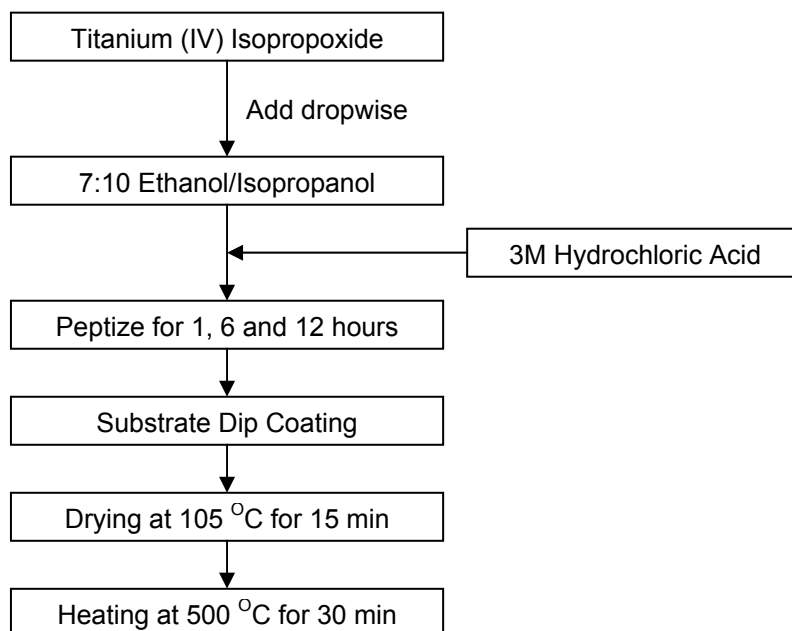


**Figure 3.2** Sol gel preparation procedure modified from Xagas et al. (1999)

### 3.2.1.2 Hybrid

Hybrid refers to the above sol gel solution enriched with Aeroxide TiO<sub>2</sub> P25 powder. Aeroxide TiO<sub>2</sub> P25 from Evonik is equivalent to Degussa P25, as Evonik recently took over the Degussa company. Degussa P25 is the most well known form of the TiO<sub>2</sub> photocatalyst (Hoffmann et al., 1995). It will be known as P25 here. The hybrid preparation procedure (Figure 3.3) used here was adopted and modified from Yu et al. (2002a) and Medina-Valtierra et al. (2006). This technique was pioneered by Balasubramanian et al. (2003). 3.0 mL titanium tetraisopropoxide were dripped, to avoid agglomeration due to local excess of precursor, into 40 mL of a 7:10 ethanol/isopropanol mixture under vigorous stirring for 1 hour. 0.5 mL 3 M hydrochloric acid (HCl) was added to the solution to form a homogenous semi-transparent sol. 15 % (w/w) of Aeroxide TiO<sub>2</sub> P25 was then added and kept stirred for 30 minutes (Medina-Valtierra et al., 2006). The solution was coated uniformly over the substrate by dipping into the solution and withdrawing at a speed of 4 mm s<sup>-1</sup>. The coated sample was air dried and the procedure was repeated for the subsequent coatings. The coated substrate was dried at 105 °C for 1 hour to remove moisture and subsequently

calcined with temperature increasing at the rate of  $4\text{ }^{\circ}\text{C min}^{-1}$  up to  $500\text{ }^{\circ}\text{C}$  and held for 3 hours to remove the organic components.

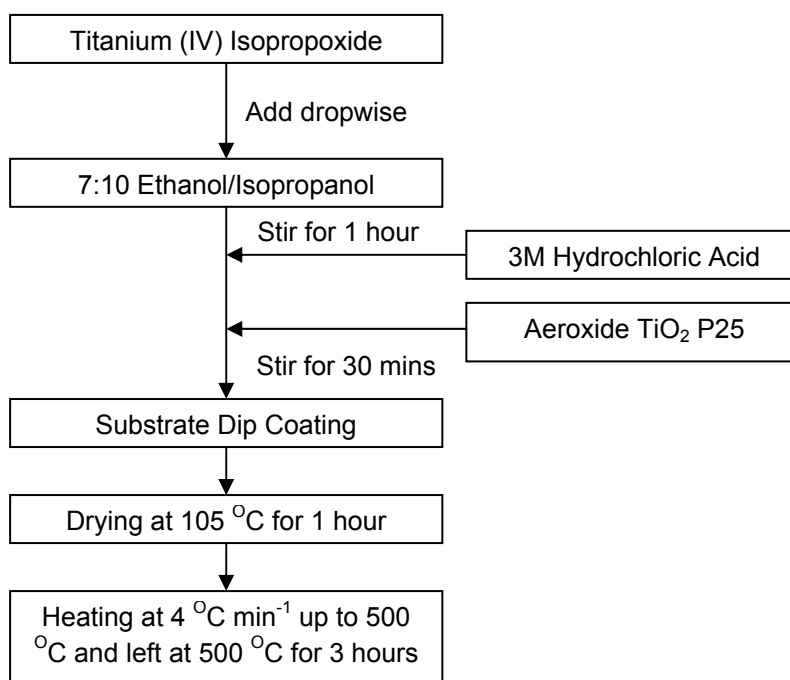


**Figure 3.3** Hybrid preparation procedure modified from Medina-Valtierra et al. (2006)

### 3.2.1.3 Reverse Micelles

A micelle is a component of an emulsion or aggregate of surfactant molecules dispersed in a liquid colloid. A reverse micelle in aqueous solution forms an aggregate with the hydrophobic tail regions in contact with surrounding solvent, sequestering the hydrophilic headgroups in the micelle centre (water-in-oil system). Surfactants improve the wettability of the film and lower the surface tension of water when present above the CMC (critical micelle concentration), thus, minimising the risk of film cracking that arises from the capillary forces of the liquid evaporating out of the pores. The reverse micelles preparation procedure (Figure 3.4) was adopted and modified from Yu et al. (2002a). 2.4 mL of Triton X-100 (a surfactant) and 15 mL of cyclohexane were mixed and stirred vigorously for 30 minutes to form an emulsion of reverse micelles. 0.1 mL of water was added creating a turbid mixture. 2.5 mL of titanium isopropoxide was added, which cleared the turbid solution. The resultant alkoxide solution was kept stirred at room temperature for 1 hour to induce a hydrolysis reaction to form a sol of titanium dioxide. The coated sample was air dried and the procedure was repeated for the subsequent coatings. The coated substrates were calcined with a temperature increase rate of  $4\text{ }^{\circ}\text{C min}^{-1}$  up to  $500\text{ }^{\circ}\text{C}$  and held for 1 hour.

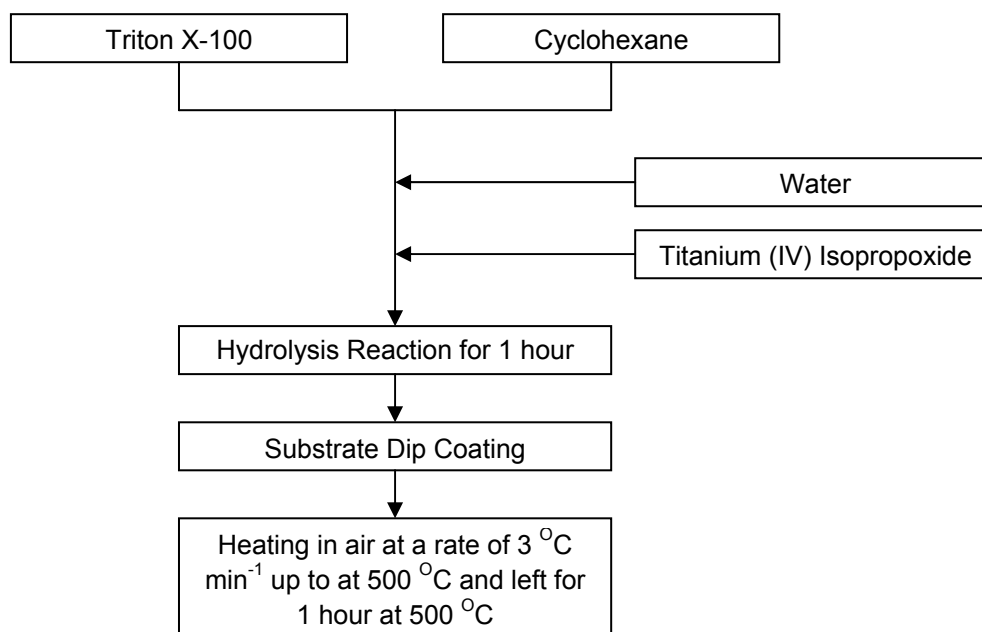


**Figure 3.4** Reverse micelles procedure modified from Yu et al. (2002a)

#### 3.2.1.4 Titanium Dioxide Powder Slurry

A slurry refers to a suspension of TiO<sub>2</sub> powder, i.e. P25 or Degussa P90, in deionised water. It will be known as P90 in this research. The slurry method (Figure 3.5) was adopted and modified from Peill (1997) and Chan (2005). 5 % (w/w) of TiO<sub>2</sub> powder (Degussa P25 or P90) was added into 50 mL deionised water to form a TiO<sub>2</sub> slurry. The substrate was dipped into the slurry for about 1 minute and withdrawn quickly to obtain sufficient deposition. The TiO<sub>2</sub> coating was dried in the oven at 105 °C for 15 minutes to remove its moisture content. The coating and drying procedure was repeated for a second coating. Unlike the other coating solutions, the slurry solutions were coated twice as the study by Chan (2005) demonstrated that there was no significant enhancement to the photocatalytic activity of the samples coated more than two times. This is because the TiO<sub>2</sub> powder does not have a binding medium when water is evaporated during the coating calcination at 500 °C. The coated substrate was then annealed at 500 °C for 1 hour, to remove any organics on the surface of the coating, and left to cool to ambient temperature overnight.

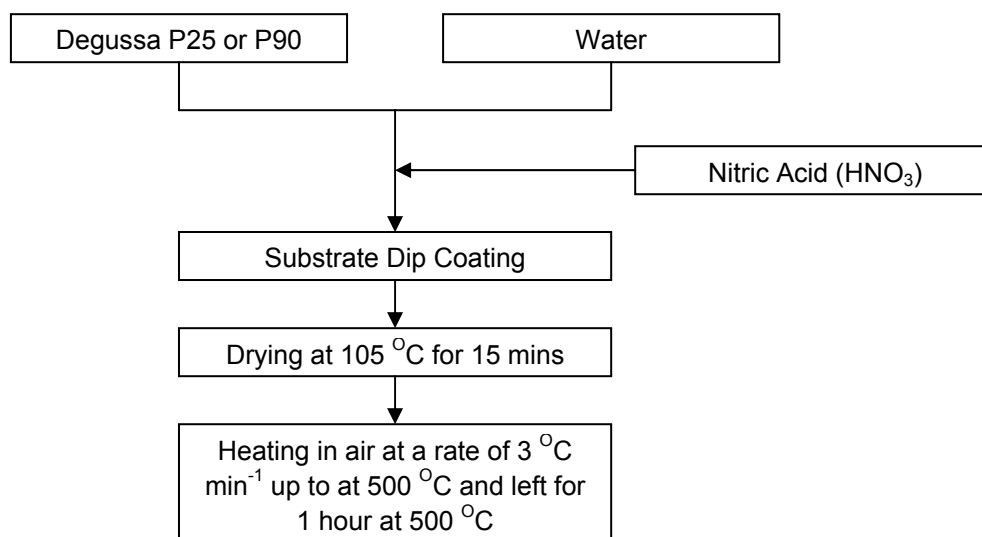


**Figure 3.5** TiO<sub>2</sub> slurry procedure modified from Chan (2005)

### 3.2.2 Preparation of Substrates

The substrate refers to the medium on to which the TiO<sub>2</sub> is to be fixed. The selection of substrate is important because TiO<sub>2</sub> does not adhere well to many types of material. In addition, the substrate should uphold a calcination temperature of 500 °C and preferably be cheap and easily available. The popular substrate applied in many studies is glass, particularly soda lime glass, because it is made of sodium silicate which has similar properties to TiO<sub>2</sub>, such as thermal expansion and contraction rate.

Four types of substrate were tested: fibreglass, woven fibreglass, aluminium plate and glass microscope slide. The sample size was 12 cm<sup>2</sup> (3 cm x 4 cm) except the glass slide of 12.5 cm<sup>2</sup> (5 cm x 2.5 cm).

#### 3.2.2.1 Fibreglass

Fibreglass material was investigated because glass is fragile, and so it may not be feasible for a field scale photocatalytic reactor due to its high tendency to break and cost. Fibreglass (Figure 3.6) and woven fibreglass (Figure 3.7), also known as woven roving (300 g m<sup>-2</sup>), were heat treated at 500 °C for 1 hour prior to coating to remove possible organic impurities on its surface (Brezova et al., 1997) and making it slightly stiffer and more manageable. The fibreglass materials used were without polymer binder to avoid formation of hazardous fumes when heated at 500 °C. In this research, fibreglass refers to the glass fibre strands (approximately 7 µm diameter) which were manually spread out from woven fibreglass. The purpose of spreading out the fibreglass is to provide a larger effective area for the coating as

well as the photocatalytic reaction. This larger effective area is suitable for dip coating into slurry ( $\text{TiO}_2$  and water) where only  $\text{TiO}_2$  remains on the fibreglass after calcination. However, it is technically not feasible to replicate the fibreglass as it is not commercially available and not viable to obtain consistent density for all the samples. It is hoped that such a form of fibreglass will be commercially available in the future as it could be used to improve the photocatalytic efficiency. Preliminary work showed a slight improvement in the amount of  $\text{TiO}_2$  deposition after calcination, if this was done.



**Figure 3.6** Fibreglass



**Figure 3.7** Woven fibreglass

### 3.2.2.2 Aluminum and Glass

Aluminum has a relatively lower melting point circa  $650^\circ\text{C}$  compared to other metals. Based on the assumption that the  $\text{TiO}_2$  could be embedded during calcination up to  $700^\circ\text{C}$ , it could then provide better immobilisation of  $\text{TiO}_2$ . Furthermore, if aluminum plate (Figure 3.8) could be used as substrate, structural support would not be required. Unlike the other types of substrate, aluminum has a greater thermal expansion and contraction rate than  $\text{TiO}_2$  which promotes substantial cracking and detachment during calcination.

Aluminum plates and microscope glass slides (Figure 3.9) were cleaned using diluted ethanol solution in an ultrasonic bath (Yu et al., 2000) for 2 hours to remove impurities from its surface and followed by 15 minutes drying in the oven at  $105^\circ\text{C}$ .



**Figure 3.8** Aluminum plate



**Figure 3.9** Glass slide

### 3.3 Methodology: Testing of Immobilised Catalysts

The study to obtain a suitable  $\text{TiO}_2$  immobilisation procedure involves the determination of a suitable combination of coating method and substrate, prior to the determination of suitable number of coating cycles, calcination duration and temperature. The coating was evaluated in terms of immobilisation efficiency and photocatalytic activity.

#### 3.3.1 Immobilisation Efficiency

$\text{TiO}_2$  does not adhere well to many substrates using simple coating methods. Excessive coating thickness results in greater detachment of  $\text{TiO}_2$ .  $\text{TiO}_2$  also detached when some of the coated sample was submerged into MB solution. Thus, it is important to study the detachment due to the substantial amount of  $\text{TiO}_2$  detached for all the coating methods examined. Immobilisation efficiency refers to the tendency of adhesion for both coating solution and substrate. It is expressed in terms of specific deposition which consists of adhesion and detachment. Specific deposition refers to the average mass of  $\text{TiO}_2$  coating per unit area. The term adhesion is defined as the mass of  $\text{TiO}_2$  remaining on the substrate after the MB test, while specific detachment refers to the mass of  $\text{TiO}_2$  detached during the MB test. Adhesion and detachment totals up to the amount of  $\text{TiO}_2$  coated on the substrate after calcination, i.e. deposition = adhesion + detachment. The adhesion of  $\text{TiO}_2$  on various substrates was studied to obtain the best combination of coating method and substrate by weighing each coated sample after calcination and MB test. Although nano scale  $\text{TiO}_2$  film thickness is sufficient for photocatalysis, the more important parameter to consider is the adhesion which exhibits how well the coating attaches to the substrate, because the micro

scale coating obtained allows for detachment. The detachment of TiO<sub>2</sub> during treatment provides a new surface for photocatalytic reaction with organic compounds.

During the coating process, the coated samples were weighed before coating, after drying at 105 °C and calcination at 500 °C, using a Mettler AE160 digital balance (Figure 3.10) to measure the amount of TiO<sub>2</sub> deposited on the surface of the substrate. It has the accuracy of ± 0.1 mg. Although many studies measure the coating thickness as part of evaluation of TiO<sub>2</sub> film (Yu et al., 2002b; Subramanian et al., 2003), there are also some which weigh the coating (Yu et al., 2000; Chan, 2005). This investigation evaluates the deposition in terms of weight per unit area of the sample. The amount of deposition is measured for the whole sample, in which the average deposition per area is more representative than measuring the thickness through SEM images, which can be localised.

The treated substrates were weighed prior to dip coating for its base weight, which is deducted from the weight of the coated sample to obtain the nett weight of the immobilised TiO<sub>2</sub>. The coated samples were dried at 105 °C for 15 minutes and weighed to obtain the dried weight of coating by deducting the weight of the substrate. After calcination, the coated samples were weighed to observe the amount of weight loss due to removal of organic compounds although it is expected that mainly TiO<sub>2</sub> is present on the coating. After the MB test, the samples were dried at 105 °C for 30 minutes and weighed to observe the amount of TiO<sub>2</sub> detached during the test. The bound water is assumed to be unaffected when the samples are dried at 105 °C. Besides the above mentioned weighing procedure, the digital balance was also used for weighing MB hydrate powder.



**Figure 3.10** Mettler AE 160 digital balance

### 3.3.2 Photocatalytic Activity

#### 3.3.2.1 Methylene Blue Dye (MB) as Photocatalytic Indicator

Although the target pollutant in this research is MTBE, methylene blue dye ( $C_{16}H_{18}N_3SCl$ ) was used as an indicator for the determination of the most suitable coating method and substrate combination tested in this study because

- i. MB is not as highly toxic and volatile as MTBE;
- ii. MB requires shorter demineralisation time compared to MTBE degradation, which shortens the duration of the experiments;
- iii. MB test has been accepted by the International Union of Pure and Applied Chemistry (IUPAC) as photocatalytic indicator besides stearic acid and resazurin test; and
- iv. MB enables visual observation as its blue colour would turn colourless when MB is completely degraded. Although some literature found that MB could recover its blue colour after the photocatalytic reaction stops, this runs counter to the observation obtained from the experiments in this research.

In any case, MB test is sufficient for the determination of a suitable coating method and substrate, among the combinations tested. Therefore, the suitable coating method and substrate combination was determined based on MB demineralisation during the experiment. The reaction effected complete mineralisation according to Mills et al. (1993) (Eq. 3.1):



Although Ryu and Choi (2008) suggested that simple spectrophotometric analysis is unsuitable due to the potential generation of coloured intermediates and hypsochromic effect, the photolysis control test (UV light without catalyst) showed negligible effect on the MB tests. This suggests that the changes of MB concentration are mainly attributed to the photocatalytic reaction. As MB is used as a photocatalytic indicator, it served the purpose of comparing the photocatalytic activity of various coatings. As Ryu and Choi (2008) confirmed that P25 is the superior photocatalyst in the degradation of most compounds, particularly chlorohydrocarbons, the comparison of coatings using MB in this investigation can still be used as a reference.

### 3.3.2.2 MB Concentration Measurement by Spectrophotometry

Prior to the MB tests, an experiment was conducted to correlate the absorbance and MB concentration to obtain the molar absorptivity,  $\zeta$  of MB. The MB solution of  $10 \text{ mg L}^{-1}$  was prepared using  $1.0 \pm 0.1 \text{ mg}$  of MB hydrate mixed in  $100 \text{ ml}$  of deionised water. The solution was subsequently diluted with deionised water to the concentrations of  $1, 2.5$  and  $5 \text{ mg L}^{-1}$ . The volume of deionised water,  $V_W$  added for dilution ( $V_W = V - V_0$ ) was calculated using  $C_0V_0 = CV$ , where  $C_0$  and  $C$  is the initial and final concentration, and  $V_0$  and  $V$  is total initial and final volume, respectively.

As the spectrometer provides the relative absorbance of solution or liquid and the ballpark MB concentration is synthesized to  $10 \text{ mg L}^{-1}$ , the spectrophotometer needs to be calibrated for measuring the concentration of MB solution. The wavelength for measuring MB needed to be determined as part of the calibration. This is because chemical compounds has specific peak wavelengths as the absorbance of a sample is proportional to its molar concentration in the sample cuvette. Choosing a wavelength where the absorbance is large gives greater accuracy in determining the concentrations. The wavelength for the measurement of MB was determined by selecting the peak absorbance in using a Varian Cary 4000 UV-Vis spectrophotometer in Cambridge University Chemistry Department (Figure 3.11) as it can measure the absorbance spectrum for each concentration. The Unicam 8620 UV-Vis spectrophotometer (Figure 3.12) can only measure the absorbance at one specified wavelength at any one time. Figure 3.13 shows the MB peak wavelength obtained for  $1, 2.5$  and  $5 \text{ mg L}^{-1}$  was  $665 \text{ nm}$ , similar to observation by Fretwell and Douglas (2001). The highest peak for  $10 \text{ mg L}^{-1}$  was obtained at  $664 \text{ nm}$ . The wavelengths for MB absorbance measurement used by Chan (2005) and Mills et al. (1993), and Chang et al. (2008) were  $660$  and  $664 \text{ nm}$ , respectively.



**Figure 3.11** Varian Cary 4000 UV/Vis spectrophotometer



**Figure 3.12** Unicam 8620 UV/Vis spectrophotometer

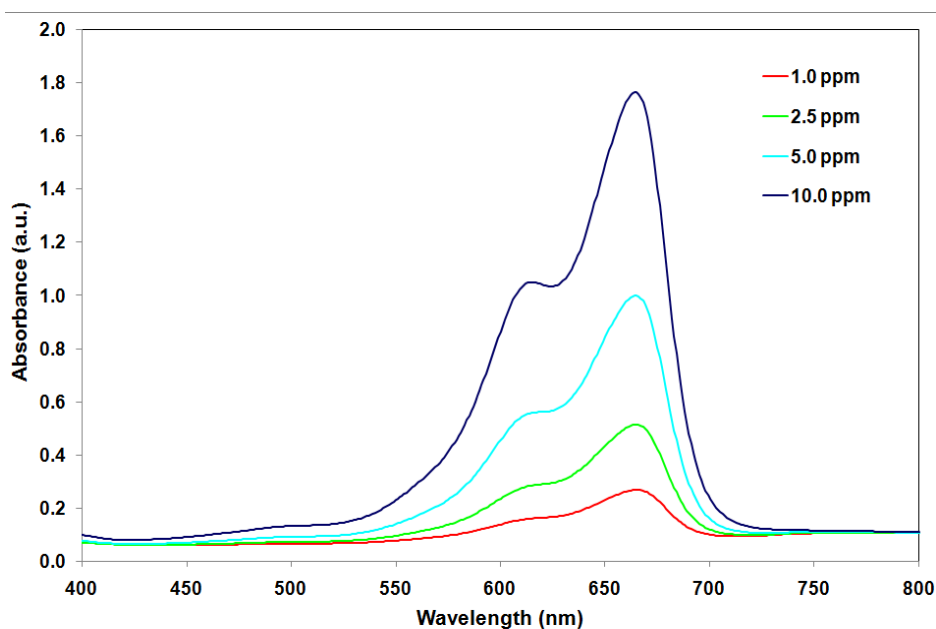


**Figure 3.13** Absorbance spectra of MB solutions at various concentrations

The determination of the absorbance value, i.e. molar absorptivity of MB,  $\xi_{\text{MB}}$ , was conducted by measuring known MB concentrations of 1, 2.5, 5 and 10 mg L<sup>-1</sup> using Unicam 8620 UV-Vis spectrophotometer at wavelength of 665 nm based on Figure 3.13. Figure 3.14 shows a strong linear correlation with regression of 0.9973 and  $\xi_{\text{MB}}$  was 48304, which yields  $A_{\text{MB}} = 0.151 \cdot c_{\text{MB}}$  from the following absorbance formula (Eq. 3.2):

$$A = \xi \cdot c \cdot l \quad (3.2)$$

where  $A$  is the absorbance unit (a.u.) measured using a spectrophotometer,  $\zeta$  is a constant, the molar absorptivity ( $\text{L mol}^{-1} \text{cm}^{-1}$ ),  $c$  is the molar concentration ( $\text{mol L}^{-1}$ ) and  $l$  is the length of light path through the cuvette, i.e. 1 cm. 0.151 is equivalent to  $\zeta_{\text{MB}}$  divided by the molecular weight of MB ( $\text{MW}_{\text{MB}}$ ) is  $319.85 \text{ g mol}^{-1}$  and  $1000 \text{ mg g}^{-1}$ .

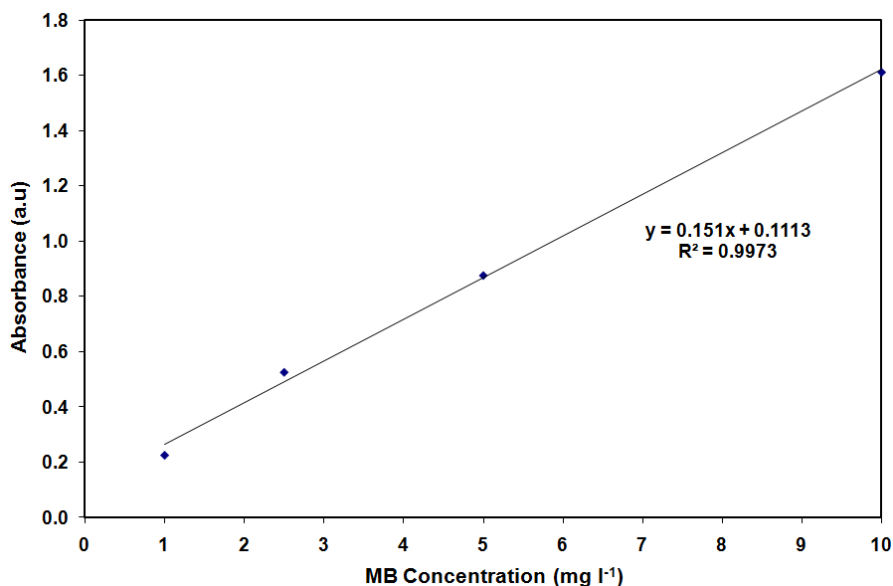


**Figure 3.14** Determination of constant for MB absorbance measurement at 665 nm

### 3.3.2.3 Turbidity Measurement

Turbidity is the indicator of cloudiness of water due to the presence of suspended foreign particles such as sediments, which could inhibit light transmissivity and possibly affect photocatalysis. Nephelometric turbidity unit (NTU) is the unit of turbidity from a calibrated nephelometer which measures the size and concentration of particles in a liquid by analysis of light scattered by the liquid. The amount of light reaching the detector varies with the amount of suspended particles scattering the source beam, indicating higher turbidity for water with more suspended particles and vice versa. Similar absorbance measurement was conducted for turbidity by diluting a standard 4000 NTU turbidity solution to several other turbidity levels to obtain the correlation graph between absorbance measurement and turbidity. Figure 3.15 will be used for studying the effect of turbidity of groundwater in the later stages of this research.

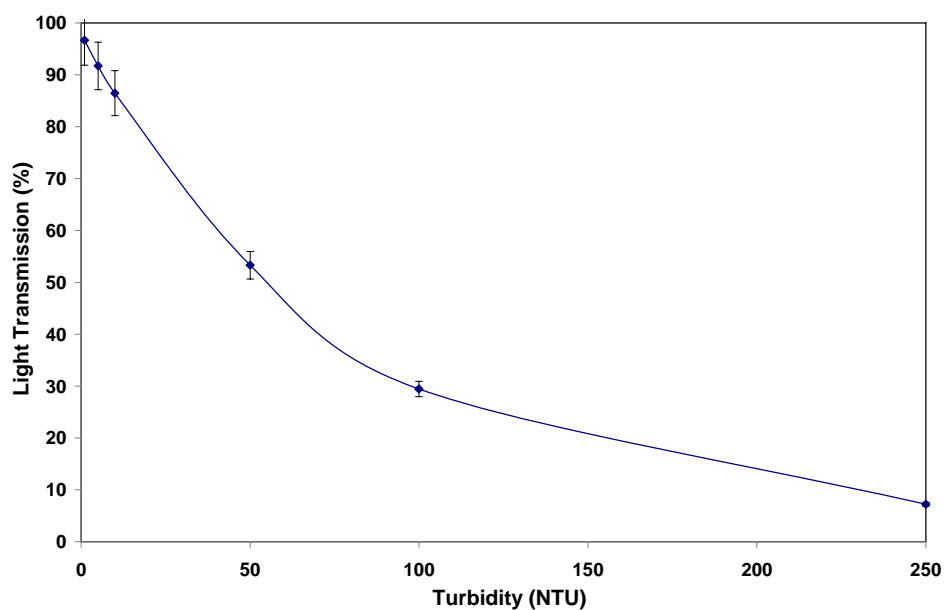


**Figure 3.15** UVA light transmission reduction with increasing turbidity

#### 3.3.2.4 2-hours MB Test

Figure 3.16 shows the experimental arrangement of the 2-hours MB test for evaluating photocatalytic activity (Mills et al., 1993) of samples in determining the suitable immobilisation procedure. The artificial UVA light source was a Blak Ray B100AP mercury lamp with a Sylvania H44GS-100M spot light bulb without filter (100 W), emitting at a peak wavelength of 365 nm. The bottom of the lamp's funnel was approximately 67 mm above the surface of MB solution. The actual distance between the lamp and the surface of MB solution was 197 mm, yielding an approximate UV irradiation of  $2.1 \text{ mW cm}^{-2}$  measured using a UVItec RX003 radiometer. The concentration of 60 mL MB solution in a Pyrex crystallising basin (70 mm dia. x 40 mm) was kept uniform throughout the test using magnetic stirrer. The initial MB concentration was  $10 \text{ mg L}^{-1}$ . The immobilised  $\text{TiO}_2$  sample was suspended in the solution by a self-made support using insulated copper wire to provide space for the magnetic stirrer. It should be noted that the photocatalytic activity was evaluated, assuming that only the side facing the light source was active. The test was initiated when the immobilised  $\text{TiO}_2$  sample was submerged into the MB solution. The 15 minutes light off period prior to switching on the lamp allows the adsorption of MB molecules onto  $\text{TiO}_2$  to achieve the equilibrium state (Su et al., 2004). The solution was sampled every 15 minutes, when the sample was transferred into a 4 mL cuvette using a pipette. The cuvette was placed into the Unicam 8620 UV/Vis Spectrophotometer for absorbance measurement. The MB sample was then returned to the solution after analysis to maintain the volume of the solution. The photocatalytic activity,  $k$ , was determined from the

exponential degradation of the MB concentration (Eq. 2.3), measured photometrically. The photocatalytic reaction conforms to the first order reaction kinetics (Eq. 2.4), in which  $k$  is the gradient obtained from  $\ln(C_0/C)$  versus time plot.

Two control tests (with and without light) were conducted without photocatalyst to observe the extent of evaporation, and thermal and photolytic effect on the MB test. However, the effect was negligible, thus, was not considered in the analysis.

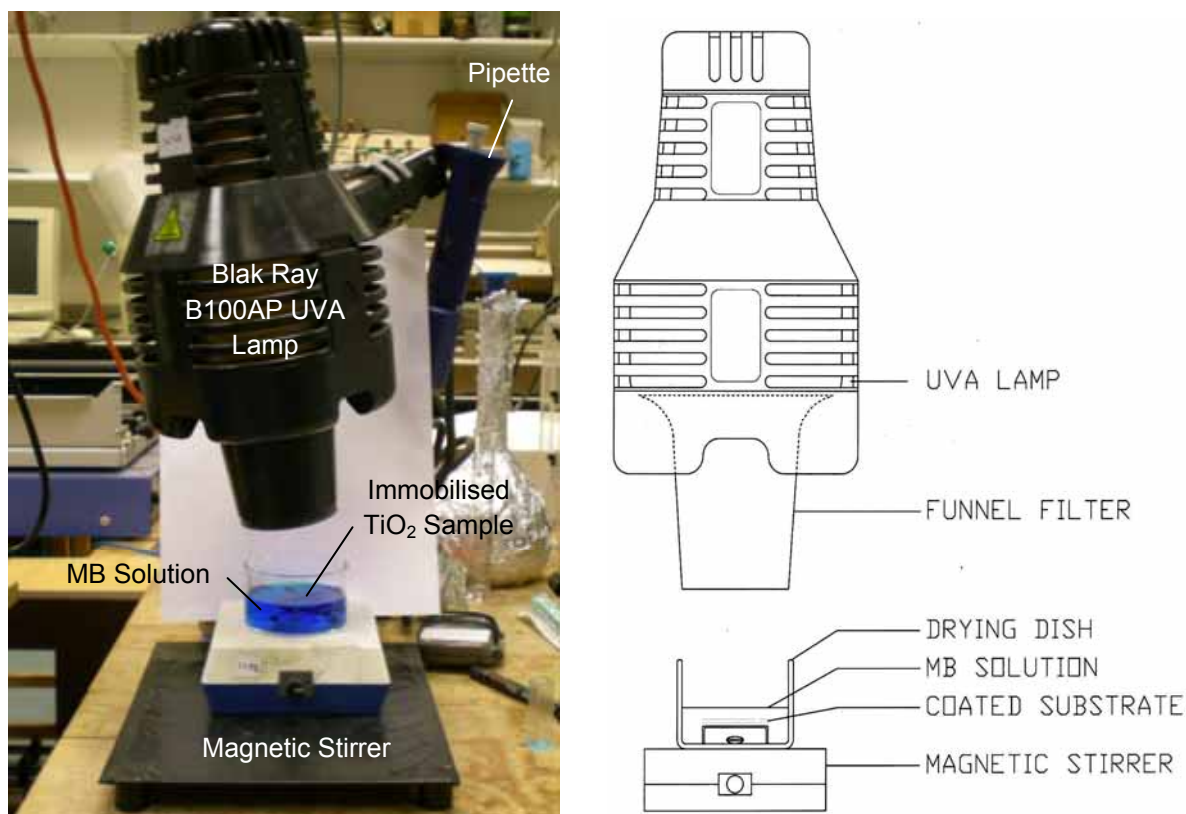


**Figure 3.16** Photo (left) and illustration (right) showing 2-hours MB test setup

10 mg L<sup>-1</sup> MB solution was prepared by dissolving the required weight of MB hydrate into the desired volume of deionised water. Although 60 mL MB solution is required for each 2-hour MB test, the solution is prepared in bulk by adding 10 mg MB hydrate powder into 1 L deionised water in a 1 L volumetric flask. The flask was manually rotated several times until the MB solution appears uniformly mixed. It is prepared in bulk for two reasons: (i) to obtain similar initial concentration for the same batch of MB solution and (ii) it is difficult to weigh trace MB hydrate accurately every time. Despite using a sensitive digital balance, the spectrophotometer showed significant differences in the absorbance measurement for different batches of MB solution prepared.

### 3.3.2.5 Light Intensity Variation with Distance

Light intensity variation with distance was experimentally conducted for estimating the sizing of field scale reactor cells. Figure 3.17 shows the variation of light intensity with distance, as the photocatalyst was moved further from light source. The light intensity for a Philips 15 W fluorescent lamp reduced with distance, which was in line with the literature. As for a Blak Ray B100AP Mercury lamp, the light intensity was measured from 118 mm below the lamp as it was covered by a funnel which function to direct the light from the lamp. It is believed that the light intensity also decays at the rate to that of fluorescent lamp as the measured distance appeared to be after the curve. The light intensity of Philips Cleo 15 W at 50 mm was about  $0.9 \text{ mW cm}^{-2}$  while the light intensity of Blak Ray B100AP 100 W at 197 mm ranged from 1.8 to  $2.1 \text{ mW cm}^{-2}$ .

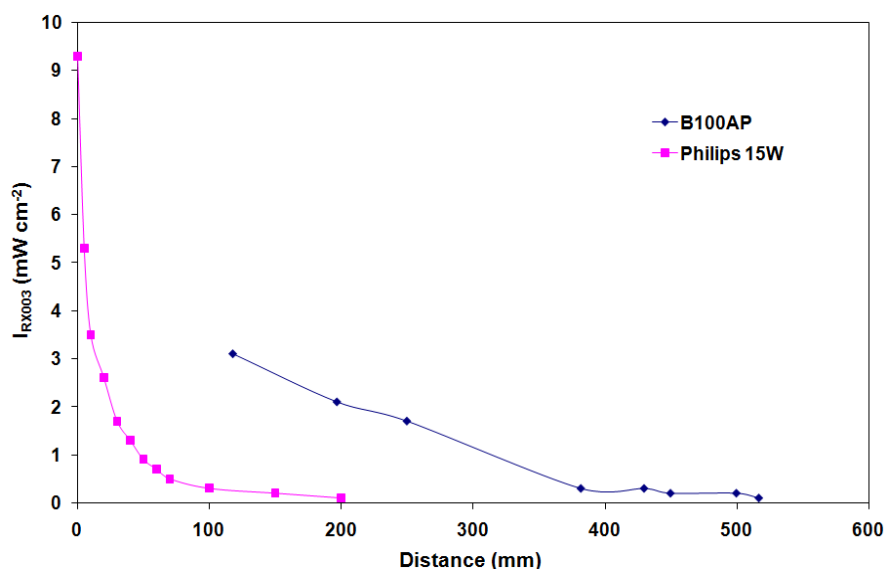


**Figure 3.17** UVA light intensity (peak wavelength of 365 nm) variation with distance

The light intensity was measured using a UVItec RX003 radiometer and light sensor using gain of 10 k $\Omega$ . The measurement of light intensity was not measured with 1 or 100 k $\Omega$  because it did not show any relationship. The light intensity measurement with 10 k $\Omega$  showed a strong linear relationship with voltage for both lamps (Figure 3.18), yielding gradient of 1.43.

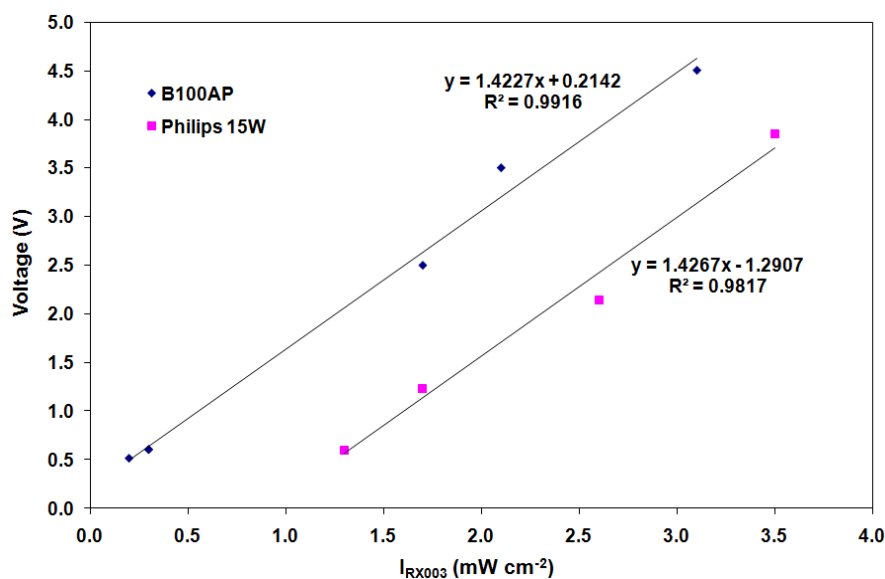


**Figure 3.18** The linear plot of voltage vs light intensity

### 3.3.2.6 Suitable Combination of Coating Method and Substrate

The test matrix combination of coating method and substrate are as summarised in Table 3.1. All coated samples had 7 coating cycles except for substrates which were dip coated only twice in P25 and P90 slurries. All the coating solutions were alcohol-based except for the slurries that were water based. It took about 5 to 10 minutes for an alcohol-based solution to air dry, while slurry  $TiO_2$  coating requires 15 minutes of drying at  $105\ ^\circ C$  in the oven. For P25 and P90 slurries, there was no significant increase in  $TiO_2$  deposition after twice dip coating (Chan, 2005) as there is no medium to hold the  $TiO_2$  powder, especially after drying and calcination.

**Table 3.1** Sample nomenclature for study of coating method and substrate

Substrate	Sol Gel (1 hour peptise)	Sol Gel (6 hour peptise)	Sol Gel (12 hour peptise)	Hybrid	Reverse Micelles	P25	P90
Fibreglass	S1FB	S6FB	STFB	HFB	RMFB	25FB	90FB
Woven fibreglass	S1WF	S6WF	STWF	HWF	RMWF	25WF	90WF
Aluminum plate	S1AP	S6AP	STAP	HAP	RMAP	25AP	90AP
Glass slide	S1GS	S6GS	STGS	HGS	RMGS	25GS	90GS

### 3.3.2.7 Coating Cycles, Calcination Duration and Temperature

When the suitable combination of coating solution and substrate was determined, the number of coating cycles as well as calcination temperature was investigated at  $500\ ^\circ C$  and  $700\ ^\circ C$  as both temperature were used for synthesizing active photocatalysts by Yu et al.

(2002b) and Su et al. (2004). The coating was calcined at 1, 2 and 3 hours to determine the suitable calcination duration. The calcination at 700 °C was limited to 1 hour because the aluminum support holding the samples was not able to withstand the temperature. Table 3.2 lists the nomenclatures for all the combinations in this investigation.

**Table 3.2** Sample nomenclature for study of calcination duration and temperature

Coating Cycles	Calcination at 500 °C			Calcination at 700 °C for 1 hour
	1 hour	2 hours	3 hours	
5	551	552	553	571
10	1051	1052	1053	1071
15	1551	1552	1553	1571
20	2051	2052	2053	2071

### 3.4 Results and Discussion: Coating Method and Substrate Combination

#### 3.4.1 Deposition of TiO<sub>2</sub>

Figure 3.19 shows the results for assessing the immobilisation efficiency, the specific deposition of TiO<sub>2</sub> for combinations of various coating solutions and substrates, before and after the MB test. All the results were normalised by area for direct comparison as the glass slide has a slightly larger area with 12.5 cm<sup>2</sup>. The combination with the highest deposition was the hybrid coating on woven fibreglass, i.e. up to 5-fold that of other combinations. This was consistent with the finding by Subramanian et al. (2003) and Chen and Dionysiou (2006a) that the P25 modified sol gel provides a thicker film than sol gel alone.

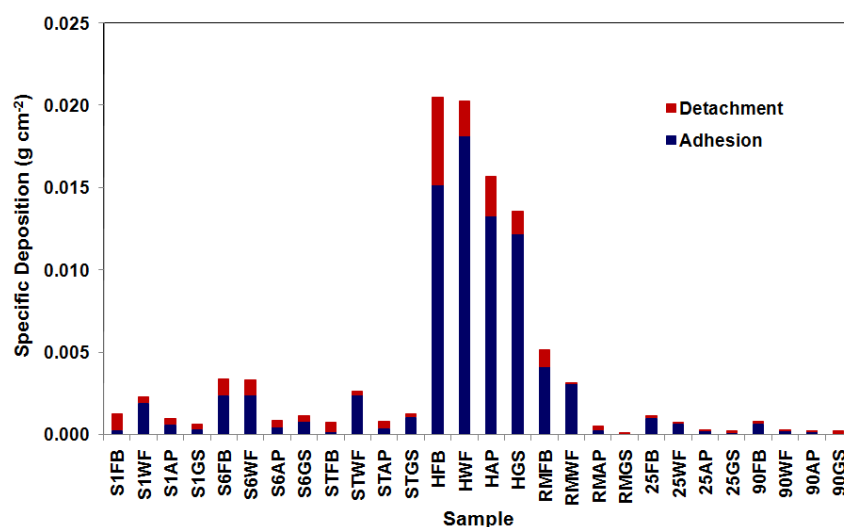


**Figure 3.19** Detachment of TiO<sub>2</sub> for various coating and substrate (refer to Table 3.1 for nomenclature)

### 3.4.1.1 Substrate

The immobilisation efficiency of substrate was observed to be in the following order: woven fibreglass = fibreglass >> aluminum plate  $\geq$  glass slide. Fibreglass materials were the best substrates for TiO<sub>2</sub> immobilisation than either aluminum or glass. Both provided more suitable surfaces for the adhesion of TiO<sub>2</sub> as fibreglass material has a relatively larger effective surface area than glass and contains a high proportion of silica (SiO<sub>2</sub>) which has similar elemental properties to TiO<sub>2</sub>. Glass slides did not have a similar outcome possibly due to their smoother surface which discourages the adhesion of TiO<sub>2</sub> coating. Besides the smooth surface, aluminum plate was not a suitable substrate particularly due to its larger thermal expansion coefficient, resulting in a higher degree of coating cracking and consequently low deposition. Figure 3.19 shows that generally viscous solutions (hybrid, sol gel and reverse micelles) adhere better to woven fibreglass than fibreglass, while fibreglass showed higher deposition for the slurry method. P25 and P90 was found to adhere better to fibreglass than the other substrates. Slightly more detachment was observed for viscous coating solutions on fibreglass than slurry solutions. Woven fibreglass was not only the most suitable substrate but has the advantages of: (i) its more economical cost compared to other materials such as stainless steel and (ii) lower density than stainless steel makes simpler handling at larger scale, and it is less fragile than glass. In addition, laminar flow groundwater can percolate slowly through the openings of the woven fibreglass.

### 3.4.1.2 Coating Solution

The immobilisation efficiency of coating solutions are in the following order: hybrid >> sol gel = reverse micelles > P25 slurry = P90 slurry. The hybrid solution showed a significantly higher deposition than other coating solutions. It was evident that the hybrid method of mixing P25 powder into sol gel solutions provide thicker coatings in terms of mass (higher deposition) for all of the substrates, in agreement with Balasubramanian et al. (2003). However, it also showed more detachment than other coating methods due to its excessive thickness. Films with excessive thickness have a higher tendency to detach when the critical thickness is exceeded (Sakka, 1994). The critical amount of hybrid coating was approximately 15 mg cm<sup>-2</sup> (Figure 3.19 and 3.23). The other possibility of the higher detachment was due to non-uniform coating where detachment occurs at a weakly adhered coating (Figure 3.21c and d), as minor detachment was observed also in sol gel and reverse micelles coatings. Nevertheless, the specific adhesion of hybrid coatings remained significantly more than the specific deposition of other coating solutions. This is because TiO<sub>2</sub> appears to adhere better to the previous coating layer than to the substrate. The

amount of deposition using the sol gel method was significantly lower than the hybrid method, mostly around  $1 \text{ mg cm}^{-2}$  (Figure 3.19). Brezova et al. (1997) also obtained an average sol gel deposition of  $0.5 \text{ mg cm}^{-2}$ , coated on  $500 \text{ g m}^{-2}$  glass fibre fabric believed to be woven fibreglass. This could be due to the rougher surface created by nano-sized Aeroxide  $\text{TiO}_2$  P25 powder, providing better anchorage for subsequent coating layers as suggested by Balasubramanian et al. (2003). Degussa P25 or P90 slurry coatings exhibited negligible amount of detachment, also due to their meager deposition (Figure 3.21b).

The detachment of the hybrid coating after calcination at  $500 \text{ }^\circ\text{C}$  for 1 hour was usually in powder form, showing that some P25 powder was weakly bound, due to insufficient sol gel. In addition, the coating was not adhered to withstand physical alteration to the coated substrate such as bending to the shape of support. Some detachment of P25 agglomerates were observed when hybrid coated samples were initially submerged into the MB solution. However, no further detachment was observed during the test. Figure 3.20 shows hybrid coating on woven fibreglass detached in the form of agglomerates, which settled at the bottom of the dish. The more intensified blue colour at the edges of coated sample indicated less active sites on the catalyst surface. The adsorption of MB was more active in loose ends of woven fibreglass due to the larger surface area, which was consistent with the photocatalytic activity of P25 and P90 slurry coating on fibreglass.

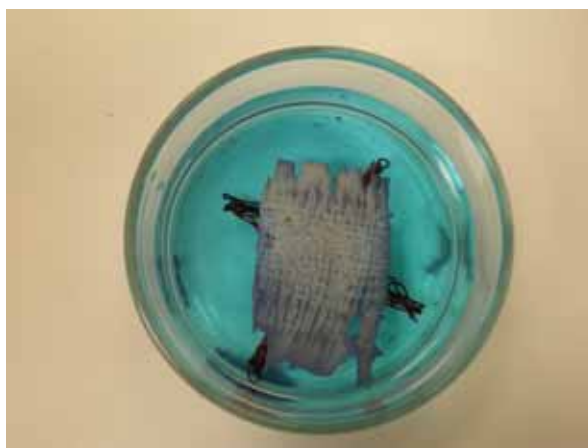


**Figure 3.20** Detachment of some hybrid coating on woven fibreglass

Sol gel was generally a better coating solution than reverse micelles as it could adhere on all types of substrates tested. Reverse micelles adhered on fibreglass material but not on aluminum or glass. P25 and P90 slurry had the least deposition as it does not adhere well on many surfaces. Although an ideal thin  $\text{TiO}_2$  film (Figure 3.21a) is preferred, it is almost impractical to obtain such film using an economical and simple dip coating method.

Nevertheless, the thicker hybrid coating could potentially have longer serviceability considering the gradual detachment of film.

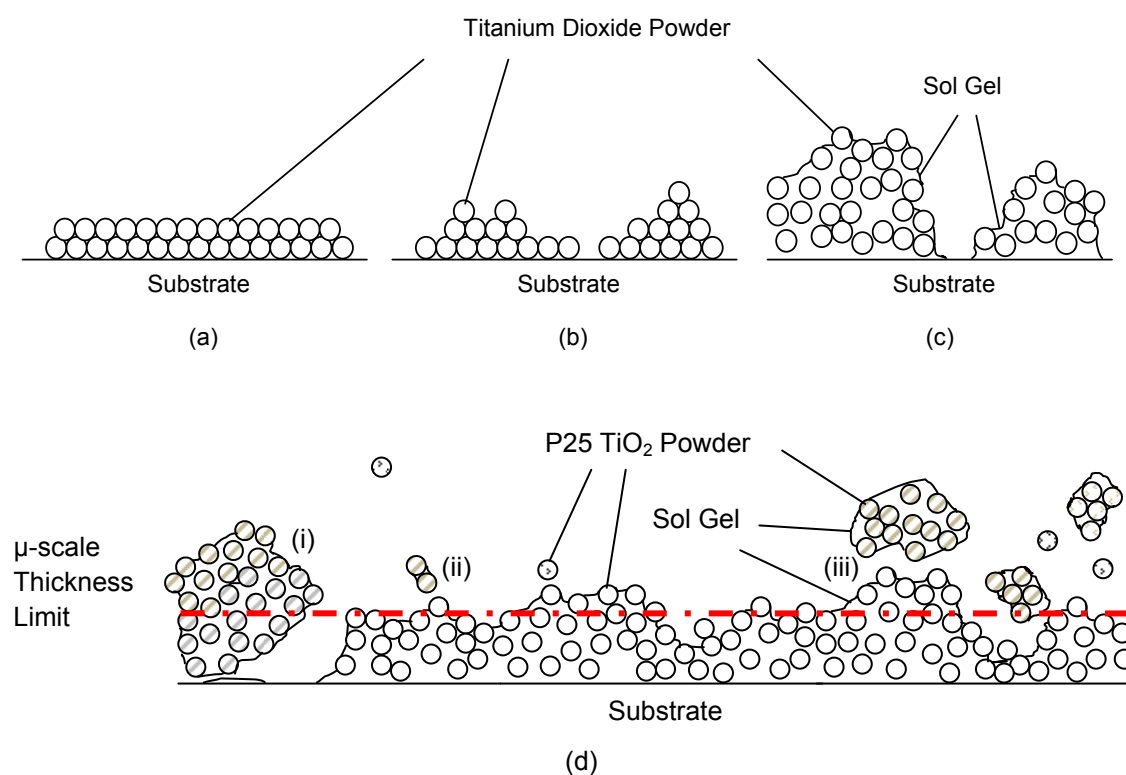


**Figure 3.21** Illustration of  $\text{TiO}_2$  coating arrangement for (a) ideal coating, (b) slurry coating, (c) hybrid coating and (d) illustration of  $\text{TiO}_2$  coating detachment (i) weak adhesion, (ii) insufficient sol gel to bind P25 and (iii) excessive coating

### 3.4.2 Photocatalytic Activity

Figure 3.22 summarises the photocatalytic activity for all combinations of coating method and substrate. Hybrid coatings on woven fibreglass had the highest photocatalytic activities followed by P90 slurries coating on fibreglass. The hybrid coating method consistently showed higher photocatalytic activity than other coating methods indicating the more reliable coating method which could work on all substrates studied. All hybrid coated substrates exhibited a more significant performance with MB removal ranging from 70 to 82 % in 2 hours.

The photocatalytic efficiency of the coating methods was in the following order: hybrid (H) > P90 Slurry (90) = P25 Slurry (25) >> reverse micelles (RM) > sol gel (S). The hybrid coating generally showed higher photocatalytic activity than other coatings for all substrates. The analogous photocatalytic activity of P25 and P90 slurries indicated that the high

photocatalytic activity of hybrid coating was mainly attributed to the addition of P25, with MB removal ranging from 43 to 70 % in both coatings.

P25 and P90 slurries coated on fibreglass yielded relatively high photocatalytic activities with lower deposition than the hybrid coating, indicating the effective surface area for photocatalytic reaction could have been larger than for hybrid coating. However, the fibreglass was manually spread out and is not manufactured in such form, and it is difficult to obtain consistent density for fibreglass if manually spread. Nevertheless, it was clear that fibreglass with lower density would be a more suitable substrate, as it provides a larger surface area for the immobilisation of TiO<sub>2</sub>. In one of the preliminary studies, hybrid coating on fibreglass yielded photocatalytic activity of  $3.3 \times 10^{-2} \text{ min}^{-1}$  in demineralising MB. In another independent study, P25 slurry coated on fibreglass tissue yielded higher photocatalytic activity than on other forms of fibreglass. However, it is not feasible to be used as substrate due to the production of fumes when the polymer binder was calcined, which resulted in the disintegration of short glass fibre strands. In addition, Warren (2006) found that the lifespan of P25 slurry coating on fibreglass was short, as the photocatalytic activity declined substantially after every batch of 2-hours experiment.

As for the viscous solutions, reverse micelles coating showed slightly higher photocatalytic activity than sol gel, but both coatings performed better when coated on woven fibreglass. The reverse micelles coated on woven fibreglass achieved about 33 % MB removal in 2 hours. As for sol gel, the photocatalytic activity varied inversely with longer peptization duration; 1 > 6 > 12 hours, achieving about 30, 27 and 24 % MB removal in 2 hours on woven fibreglass, respectively. Peptisation is a process involving the dispersion of colloids, forming a clearer sol. It was evident that the hybrid coating exhibited the advantages of both sol gel with higher deposition and higher photocatalytic activity on woven fibreglass, and P25 contributing to the high photocatalytic activity. The photocatalytic activity of slurry coatings, on the other hand, was attributed to the surface area of the TiO<sub>2</sub> powder.

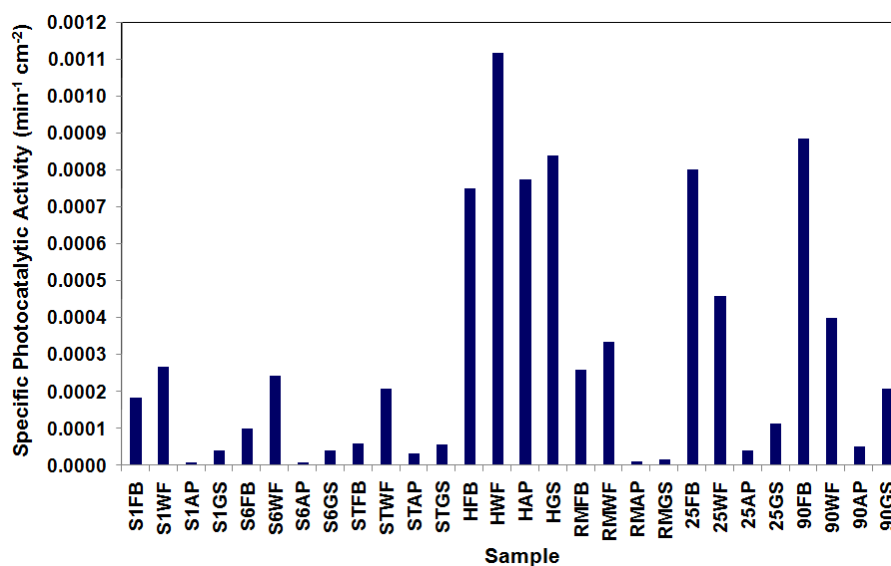


**Figure 3.22** Specific photocatalytic activity of various coating and substrate combinations (refer to Table 3.1 to for nomenclature)

The hybrid coating on woven fibreglass showed the highest deposition and photocatalytic activity among the combinations studied. Therefore, this method was used to further study the number of coating cycles, calcination duration and temperature.

### 3.5 Results and Discussion: Coating Cycles, Calcination Duration and Temperature

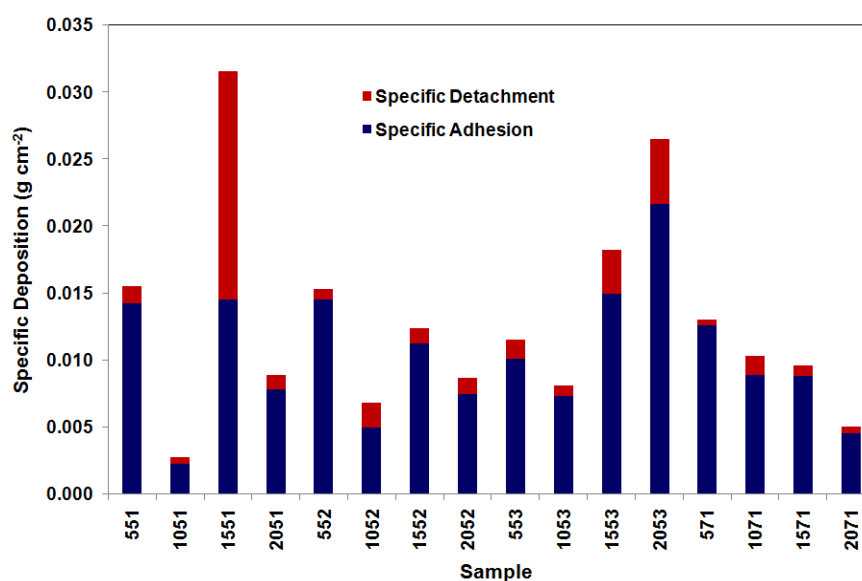
#### 3.5.1 Deposition of TiO<sub>2</sub>

Figure 3.23 shows the specific TiO<sub>2</sub> deposition of hybrid coating for the combinations of coating cycles, calcination temperature and duration, before and after MB test. It was evident that 5 coating cycles were sufficient as it was more consistent in obtaining the specific deposition between 10 to 15 mg cm<sup>-2</sup>.

There was no apparent correlation between TiO<sub>2</sub> deposition and the number of coating cycles, particularly beyond 10 coating cycles. This non-correlation could suggest that the detachment did not occur between layer of coating, as illustrated in Figure 3.21(c). It could be due to the surface morphology of the coating (Xagas et al., 1999). Although some studies showed a linear relationship between film thickness and number of coating cycles, the thickness was not more than 2 μm (Sakka, 1994; Yu et al., 2002b) and up to 10 μm (Chen and Dionysiou, 2006b and c). The thickness of the hybrid coating of five coating

cycles was measured approximately at 20  $\mu\text{m}$ , through SEM images. However, a few samples (551, 1551, 552, 1553 and 571) indicated an apparent deposition limit of about 15  $\text{mg cm}^{-2}$ . Chen and Dionysiou (2008) deposited  $\text{TiO}_2$  up to 0.1  $\text{mg cm}^{-2}$ . Therefore, it appears that the critical thickness of the coating exceeded when coated more than five times, which could explain the lack of correlation. The thick coating could have been due to the faster dip coating velocity, than that reported by Chen and Dionysiou (2008), which can yield thicker film per coating cycle. Sakka (1994) reported that immobilised films have critical thickness which could result in the cracking and peeling phenomena of films. The critical thickness varies with the processing condition. Thicker films are prone to more detachment of coating material due to the better cohesion between coating layers than adhesion to the substrate. This indicates that excessive number of coating cycles would lead to more wastage of coating material and cost. The cracking and detachment of  $\text{TiO}_2$  film could also occur during air drying between dip coating. Therefore, multiple coating cycles are mainly required for minimising the uncoated surface of substrate instead of obtaining thicker films. As a thin film of immobilised  $\text{TiO}_2$  is preferred for environmental application, the higher deposition of  $\text{TiO}_2$  provided excess  $\text{TiO}_2$  to minimise the effect of detachment on photocatalytic activity. The loss of  $\text{TiO}_2$  from the surface was not affected by calcination temperature or duration.

In terms of  $\text{TiO}_2$  deposition, 5 coating cycles calcined at 500  $^{\circ}\text{C}$  for 1 hour (551 in Figure 3.23) was sufficient, as it is better to minimise the number of coating cycles in order to optimise the  $\text{TiO}_2$  immobilisation cost (Balasubramanian et al., 2003).



**Figure 3.23** Detachment of hybrid coating of  $\text{TiO}_2$  for various coating cycles, calcination duration and temperature (refer to Table 3.2 for nomenclature)

### 3.5.2 Photocatalytic Activity

In terms of photocatalytic activity (Figure 3.24), 10 coating cycles calcined at 700 °C for 1 hour (1071) showed the highest photocatalytic activity, followed by 20 coating cycles calcined at 500 °C for 3 hours (2053) and 5 coating cycles calcined at 500 °C for 1 hour (551). However, there is not much correlation between the deposition and photocatalytic efficiency and the number of coating cycles and calcination temperature and duration. Consequently, the most probable explanation to the non-correlation is the effective surface area of TiO<sub>2</sub> coating, which is beyond control using dip coating method. Therefore, the film was studied using the SEM to observe the surface morphology of 551 (Figure 3.27a-d). The more well coated substrates appears to yield higher photocatalytic activity regardless of the number of coating cycles, calcination duration or temperature.

The calcination temperature is known to affect the relative proportions of anatase to rutile TiO<sub>2</sub> (Yu et al., 2002b; Chen and Dionysiou, 2006b). Here the calcination temperature did not have a significant impact on the photocatalytic activity of the hybrid coatings, apart from possibly higher rutile crystallite formation in the sol gel component when calcined at 700 °C (Su et al., 2004). The calcination temperature of 500 °C for 1 hour was sufficient in yielding the anatase crystal structure for the sol gel component (Xagas et al., 1999).

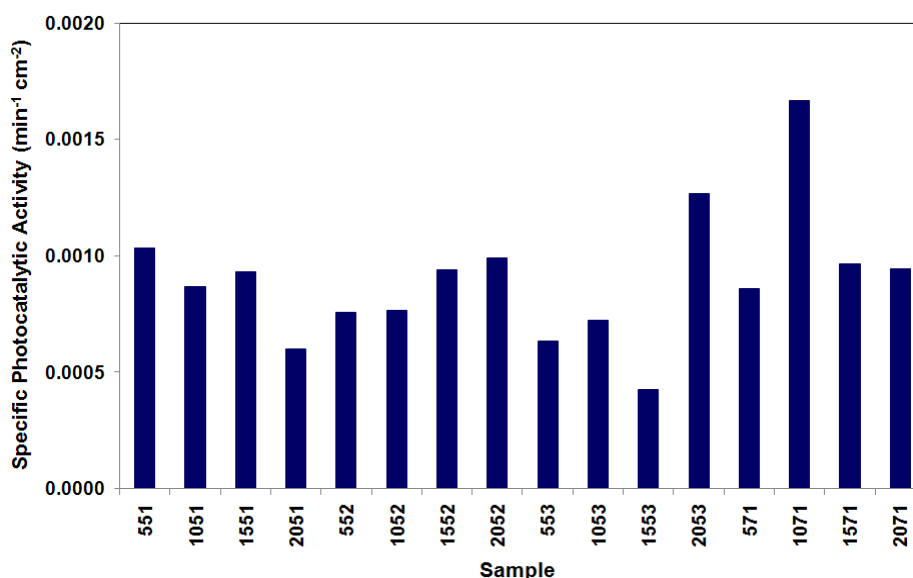


**Figure 3.24** Specific photocatalytic activity of various coating cycles, calcination duration and temperature (refer to Table 3.2 for nomenclature)

The MB removal efficiency of the coating appears to decline slightly with longer calcination duration; circa 75, 69 and 50 - 68 % for 1, 2 and 3 hours calcination, respectively. Figure

3.25 shows that the photocatalytic activity of 551 was similar to those of samples calcined at 700 °C. The difference in calcination temperature of 500 and 700 °C does not have significant impact on the photocatalytic activity of the coatings. While the apparent decline of MB removal efficiency with longer calcination duration is not understood, the similar photocatalytic activity of samples calcined at 500 and 700 °C for 1 hour indicated that it is unlikely due to the transformation of crystal phase from anatase to rutile when the samples were calcined at 500 °C longer than 1 hour.

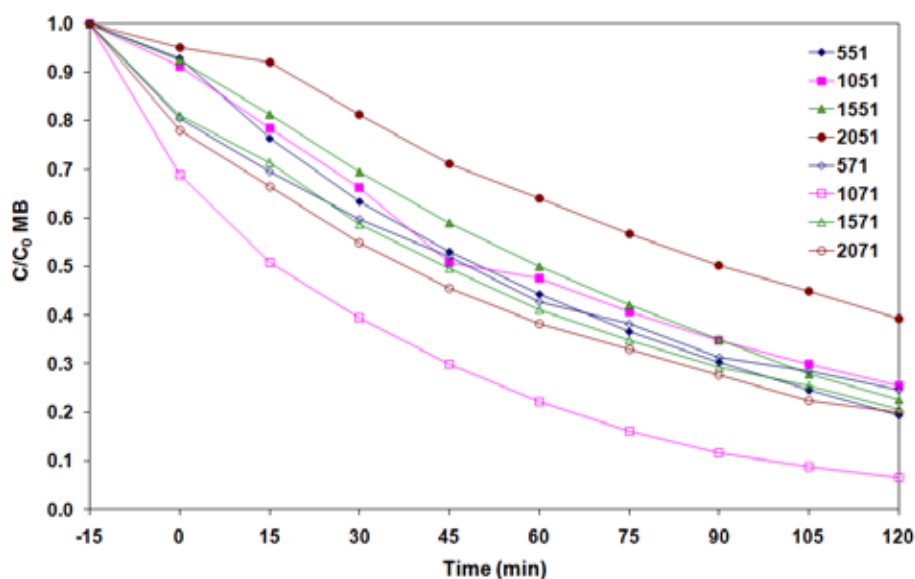


**Figure 3.25** MB decolorisation by hybrid coatings of various coating cycles, calcined at 500 and 700 °C for 1 hour (refer to Table 3.2 for nomenclature)

Five coating cycles calcined at 500 °C for 1 hour demonstrated to be sufficient in obtaining a favourable photocatalytic activity, although 10 coating cycles calcined at 700 °C for 1 hour showed slightly higher photocatalytic activity. The calcination temperature determined is consistent with the findings by Chen and Dionysiou (2006b) that the optimum calcination temperature of hybrid coating is 500 °C in order to obtain both good mechanical stability and enhanced photocatalytic activity. This was because 5 coating cycles was sufficient in saturating the substrate surface and yielding favourable photocatalytic activity. Subsequent coating cycles incur higher detachment apparently, due to the cohesive forces between the coating layers are greater than the adhering force on the substrate (Sakka, 1994). Excessive coating cycles also implies more wastage of coating material. Therefore, 5 coating cycles calcined at 500 °C for 1 hour is sufficient, based on production cost, time and energy consumption required by calcination process (Balasubramanian et al., 2003).

### 3.5.3 Characterisation of Coating

Hybrid coating on woven fibreglass was characterised based on crystal structure composition using XRD and surface morphology using SEM.

#### 3.5.3.1 Crystal Structure

The composition of TiO<sub>2</sub> crystal structure is analysed using a Philips PW1820 diffractometer from Cambridge University Chemistry Department. The sample with dimension of 1 cm<sup>2</sup> (1 cm x 1 cm) was placed into the diffractometer which measured the amount of X-ray light reflected at specific angle from the sample with the sensor. The measurements in the form of intensity unit is presented for a spectrum of angle, in which the areas below the highest peak of anatase and rutile phase of TiO<sub>2</sub> are used to obtain the composition of crystal phase. X-ray diffraction (XRD) analysis (Figure 3.26a) showed that the ratio of anatase to rutile phase of TiO<sub>2</sub> in hybrid coating was similar to Aeroxide TiO<sub>2</sub> P25, i.e. approximately 80:20. Energy dispersive X-ray (EDX) spectroscopic analysis (Figure 3.26b and c) confirmed the deposition of TiO<sub>2</sub> on the woven fibreglass surface.

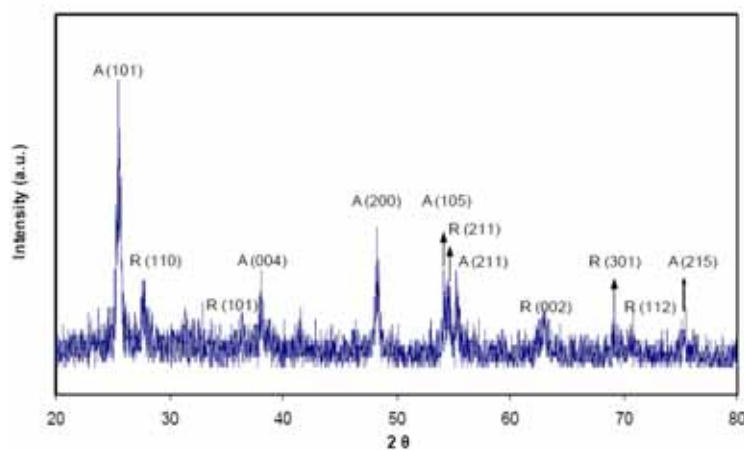


Figure 3.26a XRD analysis for hybrid coating on woven fibreglass

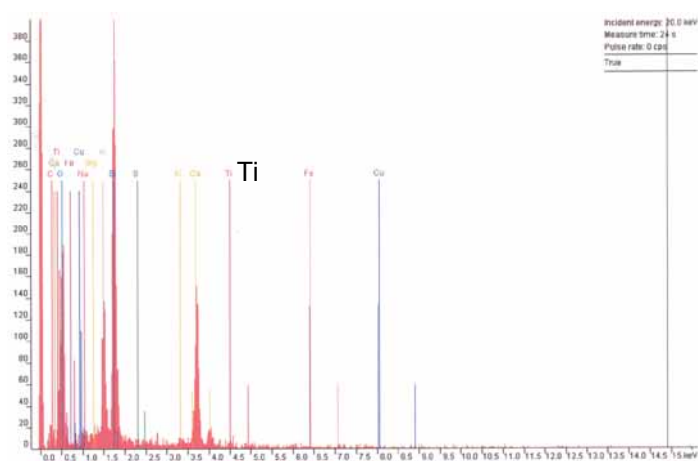


Figure 3.26b EDX spectroscopic analysis on uncoated woven fibreglass; no Ti peak at about 4.5 keV

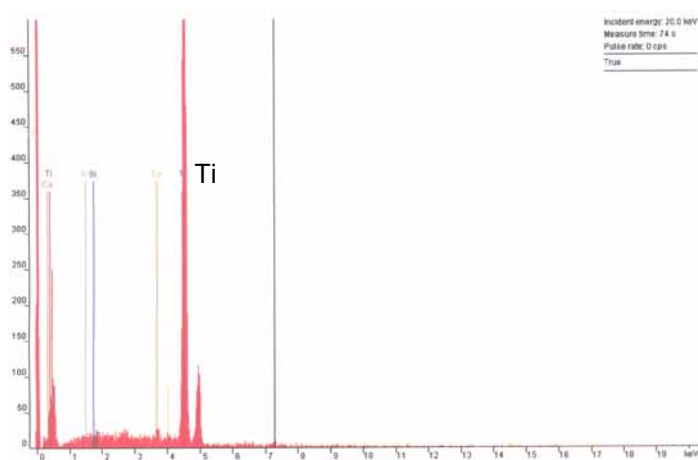
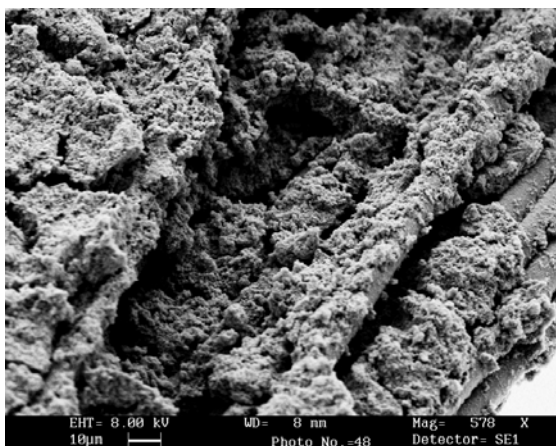


Figure 3.26c EDX spectroscopic analysis on hybrid coated woven fibreglass; Ti peak at about 4.5 keV indicate the deposition of hybrid coating

### 3.5.3.2 Surface Morphology

The surface morphology and particle size of TiO<sub>2</sub> coating was observed using a scanning electron microscope (SEM), Leica Stereoscan 430. 1 cm<sup>2</sup> (1 cm x 1 cm) pristine hybrid coatings on woven fibreglass samples were first gold-coated with a Polaron SEM Coating System. SEM images (Figure 3.27a-d) showed that the coating thickness for 5 coating cycles calcined at 500 °C for 1 hour was approximately 20 µm, which is thicker than the 10 µm sol gel coating by Xagas et al. (1999) but thinner than the 150 µm hybrid coating by Balasubramanian et al. (2003). Nevertheless, the thickness obtained is sufficient in acquiring a favourable photocatalytic activity. The hybrid coating had a fractal surface, with embedded P25 particles, which yielded larger effective surface area for photocatalysis (Figure 3.27b). This figure showed the P25 powder was anchored well by the sol gel in the form of agglomerates. The woven fibreglass was generally well coated, however, some parts of the sample had cracks and detachment (Figure 3.27c). This was consistent with the suggestion by Sakka (1994) that the cracks in films could be due to thermal expansion difference between the coating and substrate. Figure 3.27d showed the hybrid solution could not coat the openings between crossings of fibreglass, which could explain the lower deposition of a viscous solution and that there was a higher detachment of the hybrid coating on fibreglass.



**Figure 3.27a** SEM micrograph showing the hybrid coating was well attached to the fibreglass

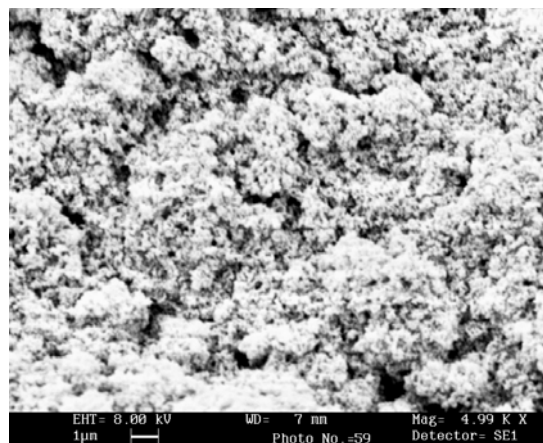


**Figure 3.27b** SEM micrograph showing fractal surface providing larger effective surface area for photocatalysis

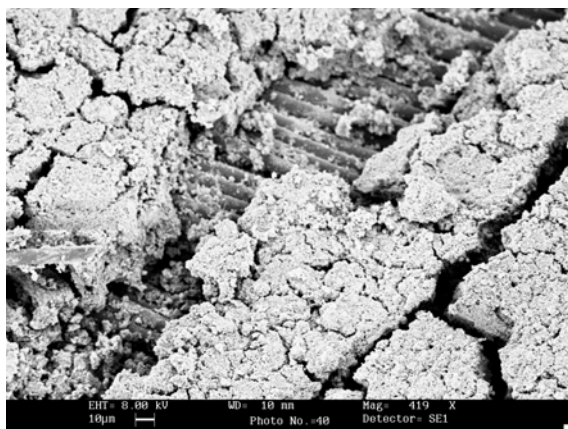


**Figure 3.27c** SEM micrograph showing some parts are not well coated and some cracking was observed to be uncoated

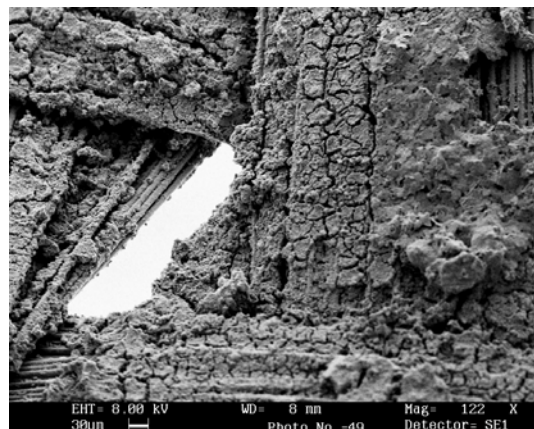


**Figure 3.27d** SEM micrograph showing some openings and crossings were uncoated

### 3.6 Scaled Up Hybrid Coating on Woven Fibreglass

The hybrid (mixture of sol gel and powder) coating on woven fibreglass showed the best performance among the immobilisation procedures studied. Therefore, this procedure was scaled up to prepare the immobilised catalyst for the subsequent studies in this research. The scale up effect on immobilisation procedure was experimentally assessed in terms of photocatalytic activity by comparing the samples coated in small and “mass production” scales using a 2-h MB test (Figure 3.16). The small and “mass production” scale coating can coat 12 and 3300 cm<sup>2</sup> woven fibreglass, respectively, which yields a scale up ratio circa 275.

### 3.6.1 Materials and Methods

The immobilisation procedure was scaled up based on the small scale hybrid dip coating on woven fibreglass. The immobilisation procedure was conducted in a larger scale (Figure 3.28) to enable simultaneous dip coating of a set of 15 pieces of 220 cm<sup>2</sup> (22 cm x 10 cm) woven fibreglass (100 g m<sup>-2</sup>). The dip coatings were conducted in two scales, i.e. 12 cm<sup>2</sup> and 3300 cm<sup>2</sup> (per set), which yields a scale up ratio of 275. Two batches of approximately 2 m<sup>2</sup> woven fibreglass (each batch) was dip coated in six sets using the scaled up immobilisation procedure; 9 January 2008 and 23 April 2008. The woven fibreglass pieces were thermally treated at 500 °C for 1 h prior to dip coating. The proportion of the chemicals used to synthesize the hybrid coating solution for mass dip coating is similar to that in the small scale (Section 3.2). The coated woven fibreglass pieces were arranged alternately between aluminium foil (to avoid adhesion of hybrid coated woven fibreglass), dried at 105 °C for 1 hour to remove moisture, and baked at 500 °C for 1 hour to transform the sol gel crystal structure from amorphous to anatase and remove organic components.

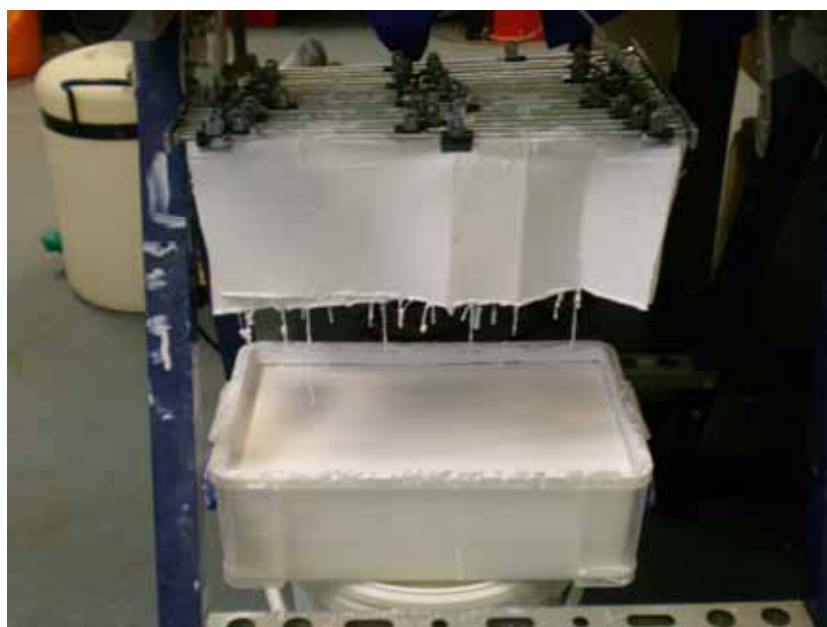


**Figure 3.28** Photo showing the scaled up hybrid coating on woven fibreglass

### 3.6.2 Results and Discussion

#### 3.6.2.1 Catalyst Performance

In order to justify the feasibility of mass coating using this simple and economical immobilisation procedure, the photocatalytic activity of 12 cm<sup>2</sup> (4 cm x 3 cm) samples from small and “mass production” coating were compared using a 2-h MB test. It is more appropriate to refer to the photocatalytic activity as MB photocatalytic oxidation (PCO) rate constant as it varies depending on the compound degraded. Figure 3.29 shows that the MB PCO rate constant and removal generally ranged from 0.6 to 0.8 h<sup>-1</sup> and 70 to 85 %, respectively. The performance of the “mass production” samples was reasonably comparable to that of samples coated in small scale, considering that the samples were made in different batches for both scales. The samples coated on 21 September 2007 and 23 November 2007 were dip coated in small scale (12 cm<sup>2</sup>) while the other samples were dip coated in “mass production” scale (3300 cm<sup>2</sup>). Catalyst ageing and immobilisation scale up did not appear to affect the photocatalytic activity significantly. This demonstrated that the immobilisation procedure is reproducible and can be applied for the “mass production” of hybrid coated woven fibreglass for larger scale photocatalytic reactor.

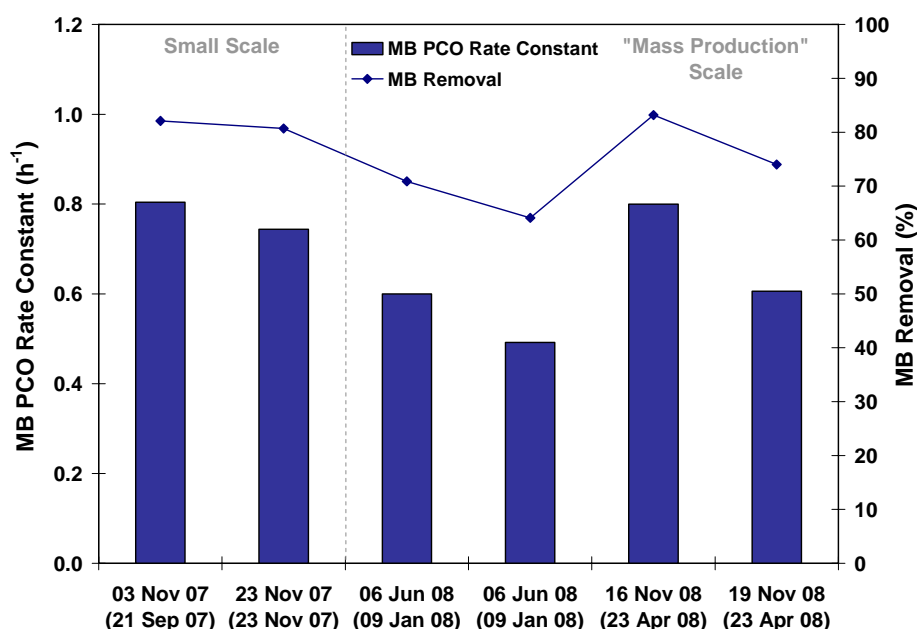


**Figure 3.29** Comparison of MB PCO rate constants and degradation efficiencies of catalysts coated in different batches and scales, obtained using the 60 mL 2-h MB test. The dates of testing and dates of coating (in brackets) are as shown. The samples tested in Nov. 07 were coated in small scale, and the others in larger, “mass production” scale.

### 3.6.2.2 Catalyst Surface Observations

SEM images did not show any visible physical change on the catalyst surface after treatment (Figure 3.30a) compared to the pristine catalyst surface (Figure 3.27 a-d). Therefore, lower magnification optical microscopic images were obtained to observe the changes on the catalyst surface. Figure 3.30b shows the immobilised catalyst surface was blue, indicating MB adsorption was confined to the catalyst surface and not fibreglass. The colour of pristine immobilised catalyst is an intense white (Figure 3.31).

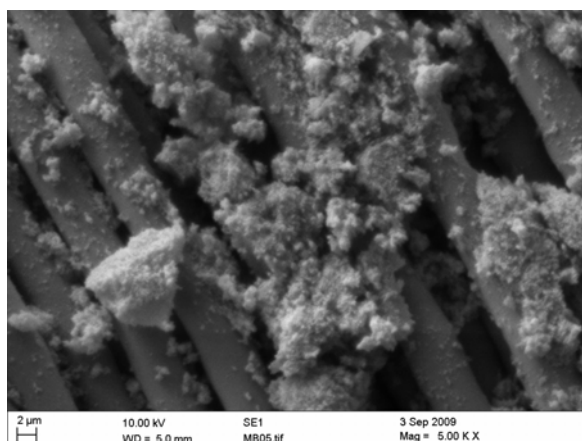


**Figure 3.30a** SEM image showing the catalyst surface after MB test

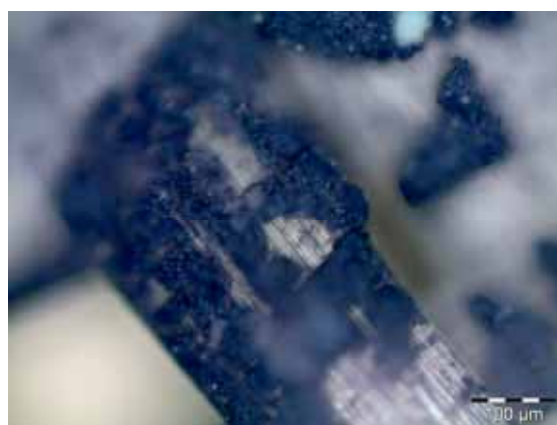


**Figure 3.30b** Microscopic image showing MB was adsorbed on the catalyst surface rather than fibreglass



**Figure 3.31** Microscopic image showing the pristine catalyst surface

### 3.7 Conclusions

This work compared the performance of various dip coating method alternatives. The hybrid coating method on woven fibreglass was found to be the best combination, with the highest photocatalytic activity and adhesion. This immobilisation procedure has several advantages such as easy replication of the literature method, a simple procedure to follow and using equipment and apparatus which are easily obtainable in an environmental laboratory. Although P25 and P90 slurry coatings on fibreglass showed relatively better photocatalytic activity, the form of fibreglass tested here is not commercially available and was manually modified, thus, making it difficult to replicate large substrate areas with consistent density of fibreglass.

Five coating cycles and calcination at 500 °C for 1 hour is sufficient to obtain a coating with reasonable TiO<sub>2</sub> deposition, yielding a photocatalytically active anatase crystal structure in the sol gel component. Calcination temperatures of 700 °C did not significantly enhance the photocatalytic activity of the hybrid coatings. This showed that more well coated substrates generally yielded higher photocatalytic activity regardless of the number of coating cycles, calcination duration and temperature. However, excess coating cycles would result in higher detachment due to better cohesion between coating layers rather than adhesion to the substrate, which also implies more wastage of coating material. The cracking and detachment of the hybrid coating could be minimised if (i) the hybrid solution was sonicated for about 3 minutes prior to dip coating, to enhance the dispersion of the P25 powder for smoother coating, (ii) slower dip coating velocity of approximately 2 mm s<sup>-1</sup> to yield better film via multiple thinner films by every coating cycle and (iii) addition of surfactant such as Tween 20 to reduce the possibility of cracking by improving the wettability of film and reducing surface tension of water (Chen and Dionysiou, 2008). Nevertheless, the required number of coating cycles is dependent on several factors such as the coating solution and the immobilisation technique used. The selection of calcination duration and temperature was also considered based on production cost and time, and energy consumption required by calcination process.

The scale up of the hybrid coating procedure showed that it is reproducible; the samples showed reasonably consistent and comparable photocatalytic activity to the samples dip coated in small scale. Therefore, this scaled up immobilisation procedure will be applied to synthesize immobilised catalyst samples for the subsequent studies in our research on removal of groundwater contaminants.

## CHAPTER 4

# EVALUATION OF A PROPOSED PHOTOCATALYTIC REACTOR

### 4.0 Overview

Existing groundwater treatment technologies typically do not degrade organic groundwater contaminants in-situ, requiring combination of technologies thus resulting in additional groundwater remediation project costs. In this chapter, a photocatalytic reactor design for in-situ groundwater remediation was proposed, which can address several issues of existing groundwater treatment technologies. Following the determination of a suitable immobilisation procedure and its successful scale up in Chapter 3, the immobilised TiO<sub>2</sub> samples were used in the proposed photocatalytic reactor design.

This chapter introduces the concept of the proposed photocatalytic reactor design, which differs from the photocatalytic reactor designs proposed in other studies for water treatment. As this is a feasibility study of a newly proposed reactor, a model of the proposed reactor design was built and evaluated for its efficiency using MB in a 4 L column reactor, to enable comparison with the 2-hours MB test in Chapter 3. Several operating conditions of the reactor was investigated, namely the experimental scale, surface area to volume (A/V) ratio, aeration and flow. The effect of experimental scale compares the MB PCO rate constants of the immobilised TiO<sub>2</sub> samples in the 2-hours MB test and in the column reactor. The effect of surface area on the reactor efficiency was investigated by comparing the proposed reactor designs, at two A/V ratios. Some of the experiments also investigated on the reliability of the immobilised TiO<sub>2</sub> via successive experiments using the same set of immobilised TiO<sub>2</sub> sample. An aeration study was conducted to observe the effect of intermittent aeration on the reactor efficiency. A flow study was conducted to observe the response of MB removal efficiency with varying flows, as groundwater flow varies depending on the natural gradient.

## 4.1 Introduction

Although photocatalysis is a relatively simple first order process, designing a photocatalytic reactor, particularly in configuration and scale up, becomes more complicated with more factors to be considered. The efficiency of the reactor can be influenced by various factors such as experimental arrangement, operating conditions, reactor scale and environment (Bisio and Kabel, 1985). This chapter is focused on immobilised catalyst reactor configurations, which can be applied in-situ and eliminate the post-treatment filtration required by slurry reactors. In the literature, photocatalytic reactors have been proposed previously as small scale reactors for water treatment at high flow, and are limited mainly by UVA light intensity and mass transfer of pollutant to the catalyst surface (Mukherjee and Ray, 1999; van Gerven et al., 2007). Therefore, designs have focused on improving efficiency of the process by using large  $A/V$  ratio: for example the fibre optic cable reactor (Figure 1.12) and multiple tube reactor (Figure 1.13) or arranging the catalyst nearer to UVA lamp for higher light intensity (Wang et al., 2002).

However, such reactor designs may not be suitable for in-situ groundwater remediation due to several reasons. Firstly, groundwater flow is significantly lower than wastewater treatment flow, which implies that the contaminants will flow through the reactor slowly resulting in long hydraulic residence times (HRTs) in the reactor. A compact reactor design can be too energy intensive for the degradation of contaminants at low flow, which may be a case of process overdesign. Overdesign of a reactor can potentially affect the cost effectiveness of the reactor and sometimes, the efficiency of the process as well. Secondly, a compact reactor design is not economically affordable for covering a large area. Covering a large area typically spanning up to meter-scale in width and depth also implies that flow through the reactor cannot simply be controlled by pumping as in wastewater treatment. Thus, recirculation is not feasible for in-situ groundwater remediation. In addition, the European Groundwater Framework Directive (European Commission, 2000; European Commission, 2006) prohibits the recharge of partially treated water into the groundwater. If a reactor is located in a trench system, the issue of groundwater recharge will not be relevant. Photocatalysis has been used to remediate groundwater as a separate process (Mehos and Turchi, 1993; Sahle-Demessie et al., 2002b; Almquist et al., 2003), but not as a groundwater remediation process underground, i.e. in-situ.

Therefore, a photocatalytic reactor with sufficient dimensions was designed for low flow and covering a treatment area larger than that of typical compact reactors. It is feasible as Fujishima et al. (2000) suggested that photocatalytic activity can be initiated at low UV light intensities. The main reactor design aims are: (i) practical design for application in the field, which enables simple installation and maintenance including catalyst replacement, (ii) robust

design where the components of the reactor can be easily modified for efficiency enhancement, especially the immobilised catalyst, (iii) cost effective reactor design with minimised mechanical components and (iv) the performance of the reactor can be evaluated at laboratory scale. A modular design approach can fulfil the above-mentioned requirements. It also enables the standardisation of reactor parts, particularly the immobilised TiO<sub>2</sub> panels, installation and maintenance; creating a potential for the commercialisation and development of the proposed reactor design.

The aim of this chapter is to introduce the concept of the Honeycomb configuration, characterise its performance and operating conditions, and demonstrate the scale up potential for a photocatalytic reactor for in-situ groundwater remediation. The term “Honeycomb” in this research is different from that in previous air purification studies, which refers to monolithic structures with small channels (Hossain et al., 1999; Singh et al., 2007). In Chapter 3, a TiO<sub>2</sub> hybrid (mixture of sol gel and powder) coating on woven fibreglass showed the best performance among the immobilisation procedures studied. Therefore, the same procedure was used to prepare the immobilised catalyst for this reactor study. The experiments were conducted using MB to characterise the performance and operating conditions, prior to investigating using MTBE in Chapter 5. MB dye was used as an indicator of reactor performance (Mills et al., 1993), since its concentration is easily monitored by its light absorbance. In addition, the photocatalytic activities obtained in this chapter can be compared with those obtained in Chapter 3.

## 4.2 Proposed Reactor Design

A photocatalytic reactor is proposed to be installed vertically in a trench, which enables in-situ clean-up of contaminated groundwater as it flows horizontally through the reactor (Figure 4.1).

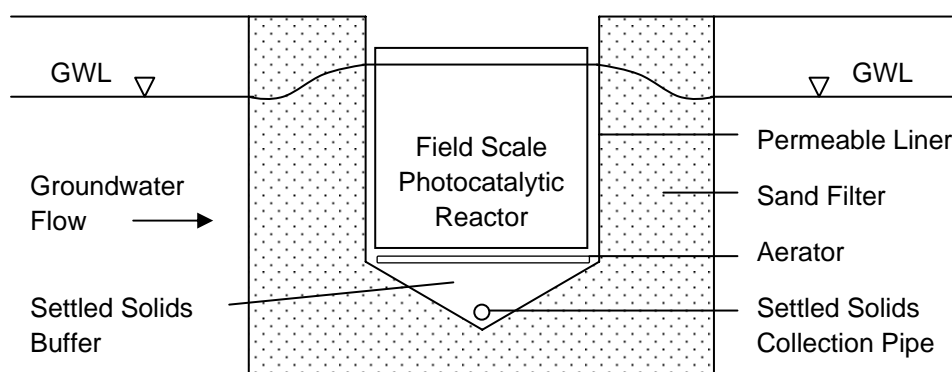


**Figure 4.1** Cross section view of the proposed photocatalytic reactor in a trench for in-situ groundwater remediation

As a photocatalytic reactor dimension is limited by UVA irradiation, the reactor will consist of modules arranged in series in order to cover a large area. Immobilised  $\text{TiO}_2$  photocatalytic reactors have been proposed using cylindrical configurations, typically tubular (Ray and Beenackers, 1998a) and column (Chan and Lynch, 2003a and b), in order to obtain uniform UV irradiation across the illuminated surface. However, gaps are present when cylinders are arranged adjacent to each another (Figure 4.2). Therefore, the hexagonal structure (Figure 4.2 and 4.3) is proposed to overcome this shortcoming. The hexagonal cells resembling the honeycomb structure is possibly the closest configuration to meet the reactor configuration criteria of modular, minimal mechanical components and simple installation.

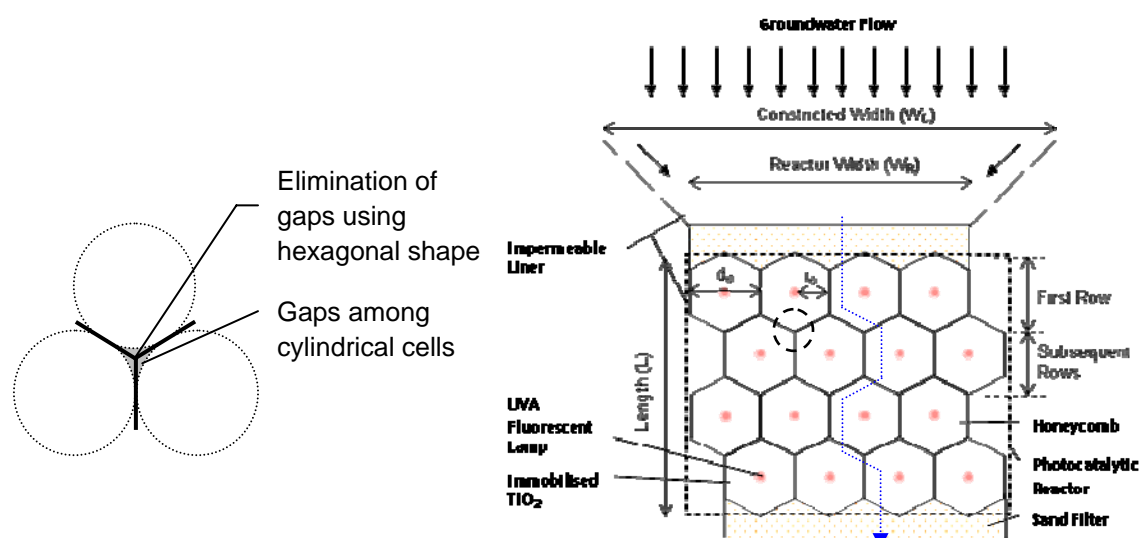


**Figure 4.2** Elimination of gaps among cylindrical cells using hexagonal structure (left; representing dotted circle on the right) and plan view of the proposed in-situ photocatalytic reactor (right); blue line indicating groundwater flow through reactor,  $r_c$ : internal radius of cell and  $d_c$ : internal diameter of cell

A hexagonal structure, which has an artificial UVA tubular light source at its axis, allows a photocatalytic reactor to be configured in arrays of photocatalytic modules without having gaps which are not irradiated (Figure 4.2). This enables a photocatalytic reactor to be arranged as a sequential pass system to improve the water quality sequentially. In addition, an array of hexagonal structures enables the utilisation of both sides of the immobilised  $TiO_2$ , optimising the usage of materials and cost. This concept was adopted from the honeycomb of bee hives, which consists of hexagonal structures, in which the walls of a cell is shared by the adjacent cells. Thus, it requires less material to create a lattice of cells with a given volume.

Another advantage of modular configuration is that the performance of the photocatalytic reactor can be evaluated by assessing a module (Hossain et al., 1999), which could be conducted in the laboratory. Although higher illumination and photocatalytic activity can be generated by arranging the immobilised  $TiO_2$  closer to the UV lamp, this will impact on the engineering requirements such as overall scale of treatment and cost. There is a compromise between reactor scale and efficiency, which sacrifices a little light intensity, but other advantages are possibly worth it. A hexagonal structure can also yield a relatively modest uniform UV irradiation across the illuminated catalyst surface when it is arranged further from the light source. A preliminary light study suggested that the distance between the immobilised  $TiO_2$  to a 15 W Philips Cleo UVA lamp should not exceed 10 cm in order to maintain a light intensity of  $0.3 \text{ mW cm}^{-2}$  (Figure 3.30). Fujishima et al. (2000) reported that photocatalysis activated at low light intensity minimises recombination losses and high

coverage of adsorbed organic compound, thus maximising the quantum yield. The Honeycomb reactor design considerations are described in the following sub-sections.

#### 4.2.1 Effect of Surface Area and Light Intensity

Surface area to volume (A/V) ratio and UV light intensity are among the principle considerations in the scale up of the photocatalytic reactor (Ray and Beenackers, 1998b; van Gerven et al., 2007). Consequently, photocatalytic reactor designs have attempted to maximise the A/V ratio (Ray and Beenackers, 1998a) as well as the UV irradiation intensity, typically by arranging the catalyst close to an artificial light source (Wang et al., 2002) or distributed light (Ray and Beenackers, 1998a). However, as mentioned earlier, a compact reactor design is not necessarily feasible for in-situ groundwater applications, which could span meters in width and depth.

A part of this section assesses the significance of additional immobilised TiO<sub>2</sub> panels fixed radially within a hexagonal module, Honeycomb I (Figure 4.3), considering it would be aligned almost parallel to the UV pathway resulting in minimal illumination. Increasing the A/V ratio of a hexagonal module enhances the mass transfer of molecules onto the catalyst surface (Ray and Beenackers, 1998a). As UVA light intensity on the radial panels is expected to be significantly lower than that on the perimeter panels, it is not known if the reactor efficiency will be proportional to the additional surface area. Therefore, additional hybrid coated woven fibreglass was retrofitted within the module, referred as Honeycomb I (Figure 4.3), to experimentally justify the significance of the radial panels. As a result, the total A/V ratio is increased by approximately 16 % to 21.5 m<sup>2</sup> m<sup>-3</sup> (Table 4.1).

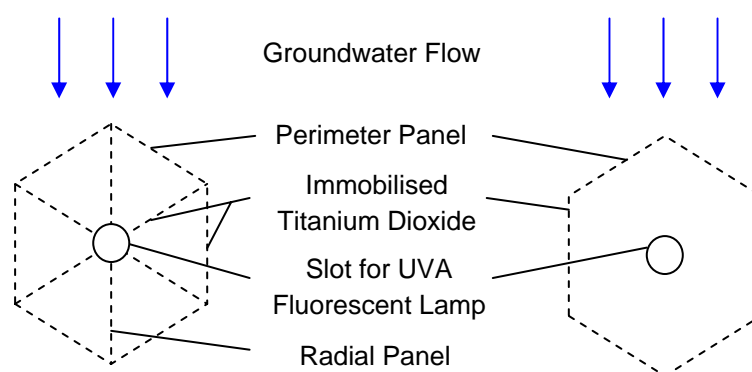


**Figure 4.3** Plan view of the proposed hexagonal structure with radial panels, Honeycomb I (left) and without radial panels, Honeycomb II (right)

### 4.2.2 Scale Effect

The scale up of reactor chemical processes can be affected by various factors, such as geometry of reactor, operating conditions and A/V ratio (Bisio and Kabel, 1985). In this chapter, the scale up involves the design of a photocatalytic reactor. It was assessed in terms of photocatalytic activity, in two experimental scales, i.e. 60 mL and 4 L column reactor, which yields a scale up ratio circa 67. Both scales have similar A/V ratio, i.e. 20.0 m<sup>2</sup> m<sup>-3</sup> (60 mL), 21.5 m<sup>2</sup> m<sup>-3</sup> (4 L, Honeycomb I) and 18.6 m<sup>2</sup> m<sup>-3</sup> (4 L, Honeycomb II) (Table 4.1).

**Table 4.1** Comparison of experimental specifications and conditions applied in a small test, Honeycomb I and II

Specifications	Small Test	Honeycomb I	Honeycomb II
Catalyst Surface Area, A (cm <sup>2</sup> )	12	866	746
Volume, V (mL)	60	4000	4000
A/V Ratio (m <sup>2</sup> m <sup>-3</sup> )	20.0	21.7	18.7
Volume Scale Up Ratio	1	66.7	66.7
UVA Light Intensity, I (mW cm <sup>-2</sup> )	2.1	0.9 <sup>a</sup>	0.9 <sup>a</sup>
MB PCO rate constant, k (h <sup>-1</sup> )	0.78	0.41 <sup>b</sup>	0.37 <sup>b</sup>

<sup>a</sup> estimated UVA light intensity on the catalyst surface perpendicular to light pathway

<sup>b</sup> average from duplicate experiments on the same catalyst

### 4.2.3 Reliability

One of the major concerns about a photocatalytic reactor is the reliability of an immobilised catalyst. Photocatalysis is a cyclic redox process, in which the catalyst is involved in promoting the redox process via excited electrons to yield radicals, but it remains photocatalytically intact (Hoffmann et al., 1995). Hence, it is anticipated that the TiO<sub>2</sub> coating has a considerable lifespan as the photocatalytic activity of TiO<sub>2</sub> itself literary remains consistent.

There have been only a handful of studies which conducted successive experiments on the same coating (Mills et al., 1993) to ascertain the reliability of the immobilised catalysts. This is because the reliability of an immobilised TiO<sub>2</sub> is also influenced by its adhesion quality and durability of the coating. The photocatalytic activity would decline if TiO<sub>2</sub> detaches substantially from the substrate, i.e. less active surface area for photocatalytic reaction. Warren (2006) observed the photocatalytic activity of a P25 slurry coating on fibreglass decreased substantially after every batch of 2-hours experiment. Therefore, there is a need to demonstrate the reliability of the immobilised catalyst synthesized in Chapter 3.

The reliability study was carried out (i) to confirm that the immobilisation procedure applied is reliable as well as (ii) to ascertain its photocatalytic activity. It is necessary to verify the

performance of immobilised TiO<sub>2</sub> as it usually varies substantially with different coating methods and materials. In this study, 9 successive experiments were conducted on the same catalyst. The second part of this study investigates the intermittent aeration (on:off) effect on the reactor efficiency. The experiments were conducted in the following order: 5 (12:0), 2 (11:1), 1 (8:4) and 1 (4:8). 5 successive experiments for continuous aeration (12:0) were assumed sufficient to validate the reliability of the catalyst, as Mills et al. (1993) reviewed a study demonstrating the performance of the immobilised catalyst remained consistent throughout 10 successive experiments.

#### 4.2.4 Effect of Aeration

The significance of oxygen on photocatalytic reactions has been studied (Turchi and Ollis, 1990; Dionysiou et al., 2002) and reviewed (Mills et al., 1993; Herrmann, 2005). The importance of oxygen in photocatalysis is evident through Eq. 2.1 and 2.2, and the photocatalytic degradation rate could be expressed for oxidants as well as reductants (Eq. 2.20).

Therefore, it is not surprising that many photocatalytic reactors were operated on continuous and excessive air supply. There are not many studies conducted to experimentally assess the effect of limiting aeration on the photocatalytic efficiency. As mentioned earlier, this aeration study was conducted at various intermittent aeration ratios to investigate the effect of intermittent aeration on the reactor efficiency. The intermittent aeration batch experiments were conducted using a 12 minute period as the maximum time ratio for aeration, for the ease of analysis.

#### 4.2.5 Effect of Flow

For any reactor design for aqueous treatment, a flow study is essential to show the response of reactor efficiency towards flow and is usually considered in the optimisation process of operating conditions. In water and wastewater treatment, the flow study is typically used to optimise flow, i.e. the fastest possible flow without compromising the reactor efficiency. Photocatalytic reactor studies have often been conducted in batch experiments, with either no flow or recirculated flow (Ray and Beenackers, 1998a; Almquist et al., 2003; Chan and Lynch, 2003a and b). Recirculation increases the contact time or treatment duration for a fraction of contaminated water by passing it through the reactor more than once, i.e. multiple pass. It is appropriate for the design of water and wastewater treatment systems to

minimise the size of reactor; treating the same volume of contaminated water and the flow can be controlled using a pump.

However, recirculation is not feasible for in-situ groundwater remediation particularly when the flow is governed by the natural gradient in a trench system. This implies that a fraction of contaminated groundwater can pass through the reactor only once, i.e. single pass. Therefore, a sequential pass system consisting of several rows of photocatalytic modules may be required to achieve the desired clean-up efficiency.

The flow study was therefore devised to evaluate the effect of flow on photocatalytic activity in a single pass system, to characterise the reactor efficiency for a range of potential groundwater flows. The groundwater flow is quantified in the form of average linear velocity as typically used in hydrogeological studies, which will be known as velocity. A range of velocities was determined which span the velocity of  $9 \text{ cm d}^{-1}$  recorded at Borden aquifer (Mackay et al., 1986).

As this is a modular reactor design, the assessment of a module can be used to estimate the performance of whole reactor (Hossain et al., 1999). As groundwater flow cannot be controlled in a trench, the response of reactor efficiency against a range of velocities can be a reasonable indicator to assess the reactor performance during monitoring by an engineer especially as the groundwater velocity typically fluctuates. Although MB was used as an indicator, it can illustrate the response of a photocatalytic reactor towards velocity variations.

### 4.3 Experimental Methodology

#### 4.3.1 Experimental Arrangement

Figure 4.4a and b shows the general arrangement of the 4 litres Perspex column reactor. The reactor dimensions are 140 mm (i.d.) x 305 mm (H), which contains approximately 4 litres at the outflow height of 282 mm. A Philips Cleo 15 W UVA fluorescent lamp emitting a peak wavelength of 365 nm is encased in a borosilicate glass tube. An internal support was used to align the lamp in the middle of the reactor and maintain the distance between the lamp and the catalyst surface. The UVA light intensity on the catalyst surface at 50 mm from the lamp was circa  $0.9 \text{ mW cm}^{-2}$ . The UVA intensity was measured using a Unitec RX003 radiometer.  $10 \text{ mg L}^{-1}$  MB solution was prepared by adding MB powder into deaired deionised water, to emulate typical low dissolved oxygen concentration of groundwater. Aeration was introduced from the bottom of the reactor using an air pump to provide oxygen for the photocatalytic degradation as well as to keep the MB concentration uniform throughout the experiments. The air flow was controlled at  $0.2 - 0.25 \text{ L}_a \text{ min}^{-1}$  using a Key Instruments air flow meter ( $0 - 0.5 \text{ L}_a \text{ min}^{-1}$ ). The immobilised  $\text{TiO}_2$  on woven fibreglass, synthesized using the scaled up hybrid coating on woven fibreglass, was fixed to a perforated stainless steel hexagonal support (100 mm (i.d) x 210 mm (H)) using insulated copper wire.

The experiment is initiated when the immobilised  $\text{TiO}_2$  sample is submerged into the MB solution. The initial MB absorbance measurement is taken before switching on the lamp 15 minutes later. The 15 minutes light off period is for the adsorption of MB molecules onto  $\text{TiO}_2$ . The first MB dye absorbance measurement taken at the beginning of the experiment was considered as the initial concentration,  $C_0$ . A sample was withdrawn using a pipette 15 minutes later and every 30 minutes thereafter in a 4 mL cuvette, and the absorbance was measured at 665 nm as used by Fretwell and Douglas (2001) using a Unicam 8632 UV/Vis Spectrophotometer. The sample was then returned into the column to be mixed with the solution, during batch experiments (no flow). It is assumed that there is no loss of solution during the experiment. The MB solution temperature typically ranged from 19 to 27 °C throughout the experiments, in which the apparent activation energy is typically small within the optimum temperature range between 20 and 80 °C (Herrmann, 2005).

Three control experiments (no light and no oxygen, no light and oxygen, and light and oxygen) were conducted without photocatalyst to distinguish the effect of oxygen supply, thermal and oxic photolysis from photocatalysis. However, the experiments showed that these effects were negligible to be considered in the analysis.

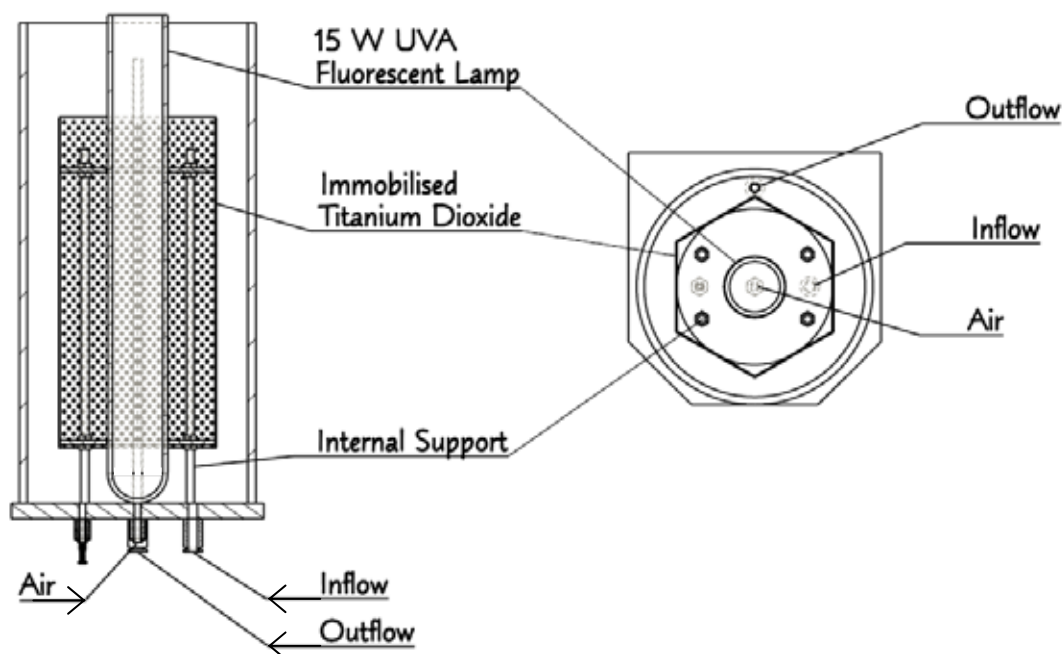


**Figure 4.4a** Cross section (left) and plan (right) view of the column reactor using Honeycomb II

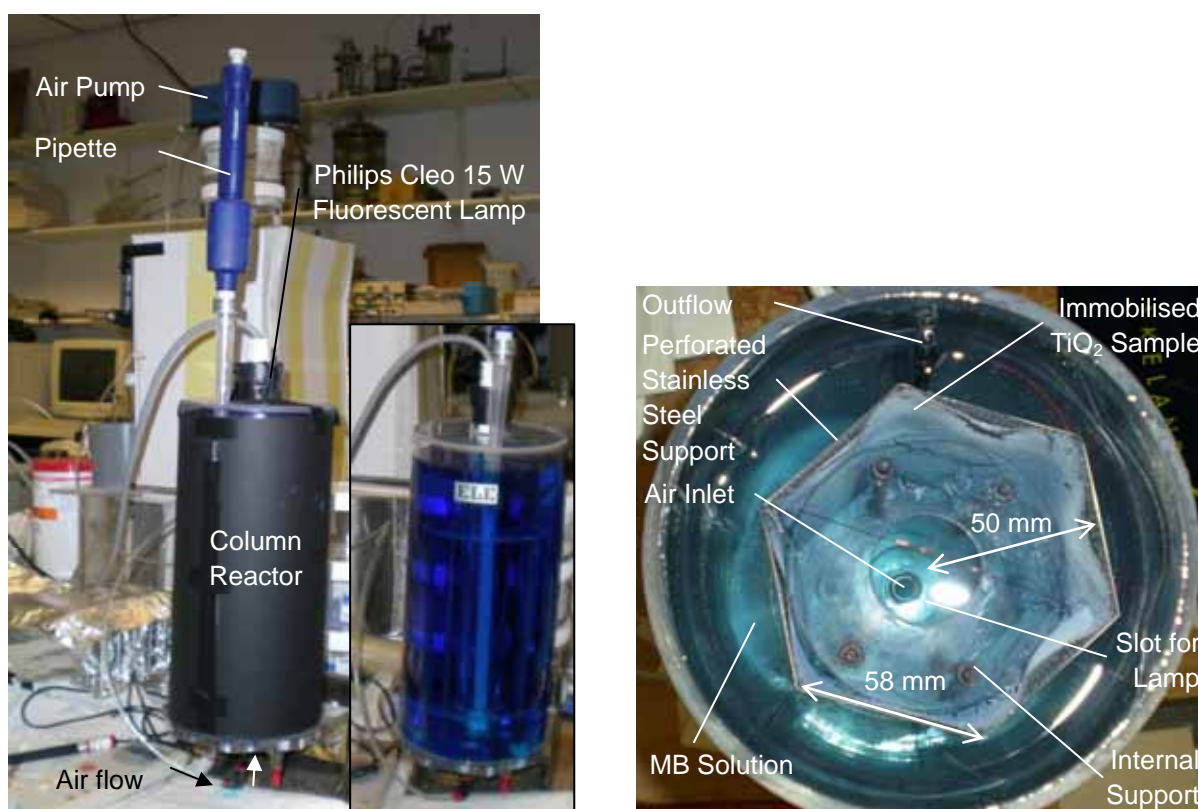


**Figure 4.4b** MB column experiment setup (inset: reactor configuration without catalyst) (left) and the plan view inside the column (right)

### 4.3.2 Single Pass Flow Study Arrangement

In the single pass flow study, the column reactor setup for the flow experiments was the same as the batch experiment except for the addition of inflow and outflow (Figure 4.4). Figure 4.5 shows the arrangement for the flow experiment. 10 mg L<sup>-1</sup> MB solution is pumped using a Watson-Marlow 323S/D peristaltic pump from a reservoir into the reactor via the inflow (bottom of the reactor) and overflows via the outflow, which also controls the water level. The effluent flows to a waste container. This is a non-recirculation experiment to simulate a single pass system. Honeycomb II, yielding a A/V ratio of approximately 18.6 m<sup>2</sup> m<sup>-3</sup> (Table 4.1), was applied in this study.

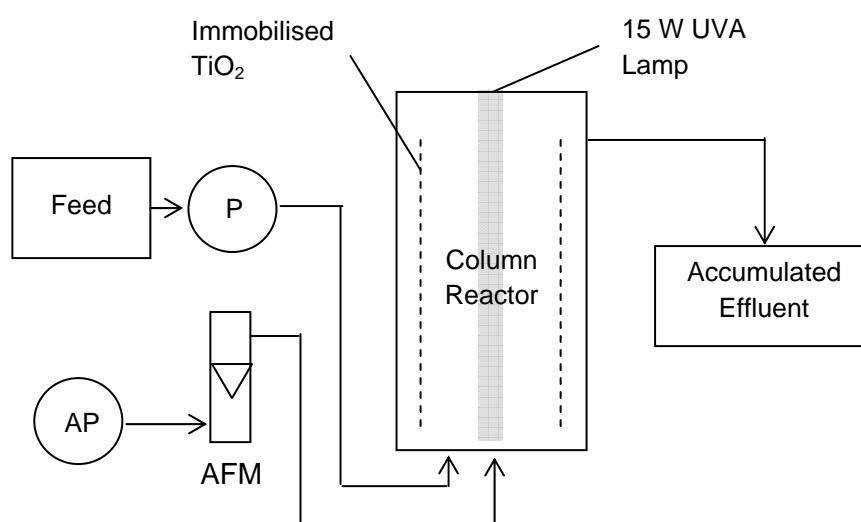


**Figure 4.5** Schematic diagram showing the experimental setup of single and double pass flow experiments; peristaltic pump (P), air pump (AP), air flow meter (AFM)

The flow was defined in terms of equivalent horizontal velocity so that the profile can be directly compared to the groundwater flow measurement on site. Six velocities including the batch experiment (0 cm d<sup>-1</sup>) were used to characterise the response of reactor efficiency towards flow. As it is expected that the photocatalytic reactor efficiency is higher at slower flow, the velocities tested were 0, 8.7, 19.4, 28.9, 64.8 and 136.1 cm d<sup>-1</sup>, in order to obtain the profile of the photocatalytic reactor efficiency. The velocities (Darcy) were calculated based on the flow per area of the section of column perpendicular to flow direction (49π cm<sup>2</sup>) (Figure 4.4a). This is to simulate the “horizontal” flow through Honeycomb II, assuming the MB solution was completely mixed in the column reactor.

## 4.4 Results and Discussion

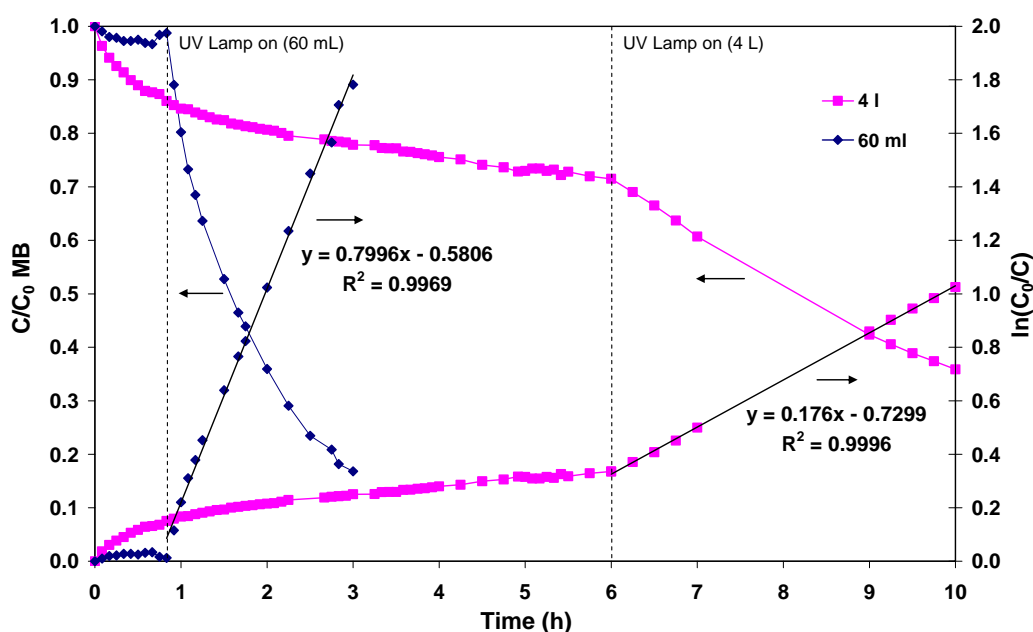
### 4.4.1 Experimental Scale Effect

Table 4.1 compares the experimental specifications and conditions in small test, Honeycomb I and II. The scale up ratio of the column reactor volume to that of the small test was 66.7. As the  $A/V$  ratio of all the experiments is similar, the MB PCO rate constant appears to vary proportionally to the UVA light intensity (Chan, 2005). The MB PCO rate constant of the 12  $\text{cm}^2$  sample in the small test was circa  $0.78 \text{ h}^{-1}$ , which was about two times higher than that of Honeycomb I,  $0.41 \text{ h}^{-1}$ . The UV irradiation in the small test (Figure 3.16) was approximately  $2.1 \text{ mW cm}^{-2}$ , from a 100 W UV spot bulb at 197 mm, which was also more than twice the  $0.9 \text{ mW cm}^{-2}$  from a 15 W fluorescent lamp at 50 mm in the column reactor. This is in agreement that the photocatalytic activity is proportional to the light intensity,  $I$ , as both UV intensities were well below  $25 \text{ mW cm}^{-2}$  (Mills et al., 1993; Herrmann, 2005). In this case, the light intensity appears to be the limiting factor affecting the MB PCO rate constant.

In the case for low flow such as groundwater flow, low photocatalytic activity does not always imply low removal efficiency,  $C/C_0$ . Unlike high flow water treatment systems, the removal efficiency can still be maintained at low flow up to the critical flow in which the photocatalytic activity varies mainly due to the duration required to achieve the specified removal efficiency. In this case, the small test, Honeycomb I and II degraded about  $8 \text{ mg L}^{-1}$  MB (80 %) in approximately 2, 4 and 4.5 hours, respectively. The corresponding MB PCO rate constants were 0.78, 0.41 and  $0.37 \text{ h}^{-1}$  (Table 4.1), showing a lower MB PCO rate constant in the column reactor. The longer time required for Honeycomb I and II to achieve 80 % MB removal than that of the small test could be due to mass transfer limitation; MB molecules require more time to reach the catalyst surface in the column reactor due to the further travel distance. The liquid layer (furthest distance from the catalyst surface) is 16 mm in the small test and 31 mm in the column reactor.

In order to observe the effect of experimental scale on the mass transfer of molecules onto the immobilised  $\text{TiO}_2$  surface, this section also includes an adsorption test conducted at two experimental scales, i.e. 60 mL (2-hours MB test -  $20.0 \text{ m}^2 \text{ m}^{-3}$ ) and 4 L column reactor (Honeycomb I -  $21.5 \text{ m}^2 \text{ m}^{-3}$ ). The  $A/V$  ratio of both experiments were assumed similar (Table 4.1). The adsorption study was devised to address the significance of liquid-surface transfer on photocatalytic activity by observing (i) the difference in the adsorption behaviour in different experimental scales and (ii) the photocatalytic activity after the liquid-surface transfer has achieved steady state. The absorbance of the solution was measured at 665 nm, typically every 5 minutes until the concentration stabilised, and typically every 15 minutes when the column reactor was switched on.

There was a significant difference in the adsorption behaviour observed in both experimental setups. Figure 4.6 shows the normalised MB concentration and  $\ln(C_0/C)$  for adsorption experiments in small test and Honeycomb I. The MB concentration in the small test stabilised in 30 minutes compared to 6 hours in the column reactor. The stabilisation of MB concentration implies that the adsorption and desorption rates on the  $\text{TiO}_2$  surface have stabilised. Although the  $A/V$  ratio was similar for both small and large scale tests, Honeycomb I showed a larger adsorption capacity but required more time for MB concentration to stabilise. It was evident that the surface area affected the MB removal, which stabilised at less than 5 % in the small test compared to 10 % in the column reactor, after 30 minutes. The column reactor adsorbed about 30 % MB after 6 hours. This could be due to (i) the larger surface area for adsorption and (ii) the further travel distance to the immobilised  $\text{TiO}_2$  surface in the column reactor, as mentioned earlier. Larger surface area in the column reactor,  $866 \text{ cm}^2$  compared to  $12 \text{ cm}^2$  in the small test, requires a longer duration to saturate.



**Figure 4.6** Variation of normalised MB concentration and  $\ln(C_0/C)$  in an adsorption study conducted in two experimental scales; 60 mL and 4 L. Adsorption only for 50 minutes (60 mL) and 6 hours (4 L).

In terms of photocatalytic activity, the small test was consistent with other batch tests (Table 4.1) at an MB PCO rate constant circa  $0.8 \text{ h}^{-1}$ , achieving about 80 % MB removal in 2 hours of photocatalytic reaction (Figure 4.6). However, the MB PCO rate constant of Honeycomb I (with 6 hours lamp-off time) was about  $0.18 \text{ h}^{-1}$  (circa 35 % MB removal), i.e. 2.3 times lower

than the Honeycomb I (Table 4.1), which only had 15 minutes adsorption time. The surface of the immobilised  $\text{TiO}_2$  in the column reactor was apparently saturated with MB. MB colour on the catalyst remained intense despite 4 hours of reaction. The catalysts are usually white with faint blue edges at the end of the experiments showing that the MB adsorbed was oxidised (Figure 3.18). This could further indicate that the adsorption process dominated the photocatalytic cycle and that the MB molecules saturated the  $\text{TiO}_2$  surface, reducing the number of active sites for adsorption and photocatalytic reaction. The extended adsorption duration could also have allowed the MB molecules to be sorbed into the interior of the catalyst (Chang et al., 2000). These phenomena could have affected the photocatalytic activity as UVA light could be inhibited from illuminating and activate the  $\text{TiO}_2$  surface. Therefore, the MB molecules on the catalyst surface might incur a longer duration to be oxidised prior to being displaced by new MB molecules (Herrmann, 2005).

The adsorption process prior to the photocatalytic process in this experiment could have dominated the overall photocatalytic process cycle. This is consistent with the review by Herrmann (2005) that the overall photocatalytic process involves the liquid-surface transfer and adsorption of reactants onto the surface, reaction in the adsorbed phase, and desorption and removal of products from the interface region, in which all the processes are required to be in steady state to obtain a favourable overall photocatalytic activity. This implies that the adsorption process ideally should not be too long and that 30 minutes should be sufficient for adsorption in order to achieve the balance of the overall photocatalytic process. This reinforces the point that photocatalysis is a cyclic process, thus, the adsorption and photocatalysis needs to occur simultaneously so that the photocatalytic activity could be maintained.

#### 4.4.2 Surface Area Study

This section encompasses two parts: (i) to obtain the relationship between the photocatalytic activity and  $A/V$  ratio for this reactor design and (ii) to assess the significance of additional immobilised  $\text{TiO}_2$  panels fixed radially within a hexagonal module, Honeycomb I.

The first part of this section involves the experiments conducted in a 4 L column reactor using various immobilised  $\text{TiO}_2$  dimensions to vary the  $A/V$  ratios. The surface areas and  $A/V$  ratios were  $0.018 \text{ m}^2$  ( $4.35 \text{ m}^2 \text{ m}^{-3}$ ),  $0.025 \text{ m}^2$  ( $6.1 \text{ m}^2 \text{ m}^{-3}$ ),  $0.075 \text{ m}^2$  ( $18.56 \text{ m}^2 \text{ m}^{-3}$ ) for Honeycomb II, and  $0.087 \text{ m}^2$  ( $21.5 \text{ m}^2 \text{ m}^{-3}$ ) for Honeycomb I. All the samples were arranged at the mid-length of the lamp to ensure maximum irradiation. Figure 4.7 shows the relationship between the photocatalytic activity (MB PCO rate constant) and  $A/V$  ratio using Honeycomb II. It appears that the MB PCO rate constant increased linearly with the surface

to volume ratio. As the distance from the UVA lamp was similar for all the ratios, the linear increment was due to a larger surface area for the photocatalytic reaction. In other words, more active sites are available for mass transfer of reactant from liquid onto the immobilised TiO<sub>2</sub> surface, resulting in faster clean-up and higher photocatalytic activity. Having said that, the increase of photocatalytic activity with increasing A/V ratio in the column reactor can be attributed to the increased opportunity for dye-surface transfer (Ray and Beenackers, 1998a). Photocatalytic activity could improve substantially if the configuration is intensified (van Gerven et al., 2007) by arranging the immobilised TiO<sub>2</sub> nearer to the UVA lamp. It does not only enhance the UV irradiation on the TiO<sub>2</sub> surface but also the mass transfer from the liquid phase onto the TiO<sub>2</sub> surface, with narrow passage between the light source and photocatalyst. Alternatively, the surface area to volume ratio can be increased by arranging the immobilised TiO<sub>2</sub> closely together, for example in distributed light systems (Figure 1.12 and 1.13). However, the modular photocatalytic reactor design also needs to consider the suitable dimensions of each module in terms of installation and cost. Therefore, the structure was designed in the form of hexagon at a relatively wider light source-catalyst passage.

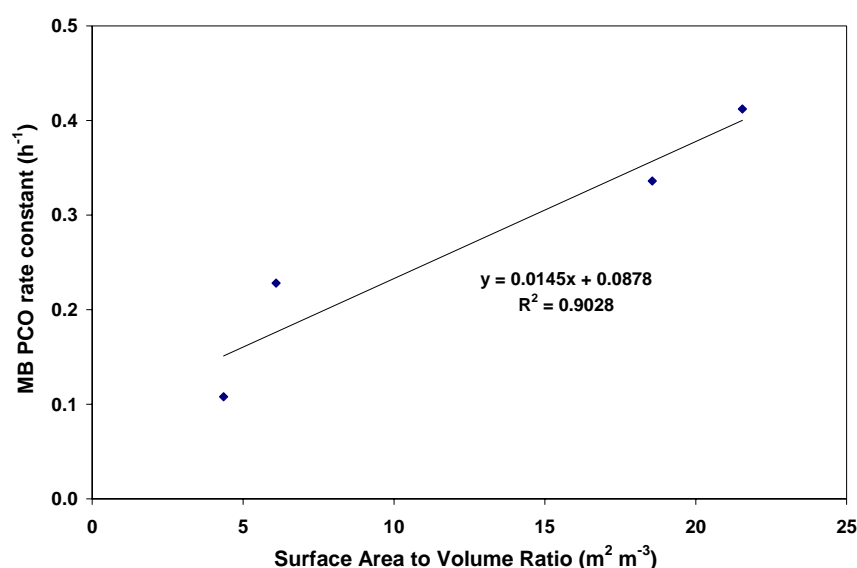


**Figure 4.7** The relationship between photocatalytic activity and A/V ratio

As the first part of this section ascertained that the significant influence of A/V ratio on a photocatalytic reactor design (Mukherjee and Ray, 1999; van Gerven et al., 2007), the second part of this section assesses the significance of additional surface area (radial panels), considering these panels are arranged pseudo parallel to the UVA light pathway, resulting in lower UVA light illumination. Figure 4.8 shows the reductions in MB

concentration for both configurations, with and without radial panels, were approximately 98 % after 10 hours of treatment. Honeycomb I consistently exhibited faster MB removal than Honeycomb II throughout the experiments. In other words, Honeycomb I exhibited higher MB PCO rates than Honeycomb II. The MB PCO rate of Honeycomb I reached a plateau at the ninth hour (Figure 4.8). This is because the MB PCO rate is defined by the MB removal efficiency, as described by the first order kinetics process (Eq. 2.3), in which the degradation of compound is typically exponential. When  $\ln(C_0/C)$  is plotted versus time,  $t$ , the gradient is the MB PCO rate constant,  $k$  (Eq. 2.4). Therefore, when MB is almost completely degraded,  $\ln(C_0/C)$  remains almost constant and  $dC/dt = 0$ , showing the plateau.

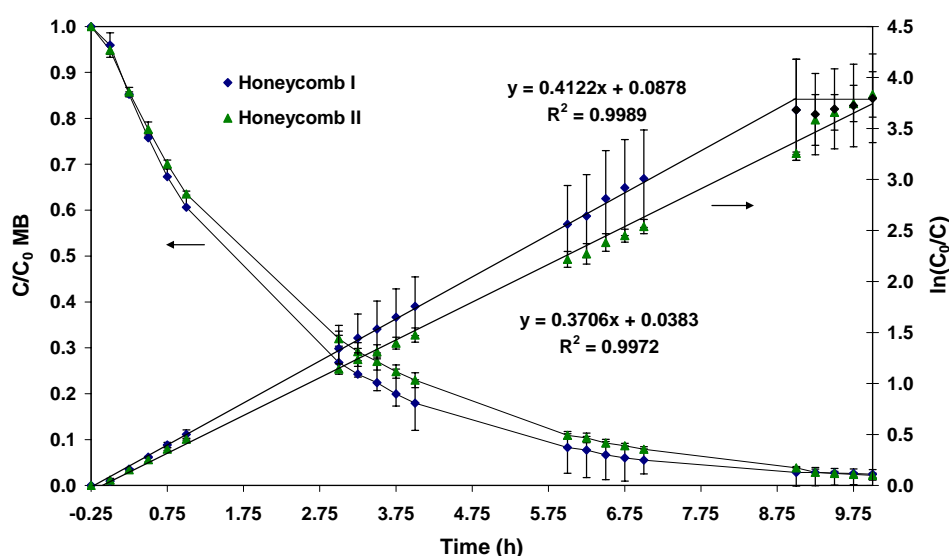


**Figure 4.8** Variation of average normalised MB concentration and  $\ln(C_0/C)$  of Honeycomb I and II (2 runs each) in the 4 L column reactor after 8 h. Error bars show the minimum and maximum values.

As the experimental conditions were similar, the difference in the MB PCO rate constant between Honeycomb I and II is attributed to the A/V ratio. This increment in MB PCO rate constant circa 11 % was proportional to the additional surface area of radial panels in Honeycomb I of about 16 %. As lower light intensity is expected on the additional surface parallel to the light path, this agrees with Fujishima et al. (2000) that a photocatalytic reaction can be initiated by low UV intensity. The radial panels expedited the MB degradation, achieving 98 % MB removal an hour faster than Honeycomb II. This implies that faster clean-up can be achieved in order to degrade more contaminants in the same duration, or the reactor can accommodate slightly higher velocity than Honeycomb II, without compromising the reactor efficiency. The enhancement of reactor efficiency by adding radial

panels suggests that Honeycomb I is the better reactor design and will be applied for in-situ groundwater remediation.

Honeycomb I showed a difference (between the minimum and maximum MB PCO rate constants obtained) of 28.6 % in the MB PCO rate constants between successive experiments, whereas Honeycomb II showed only 10.1 % (Figure 4.8). The MB PCO rate constant in the duplicate experiment for Honeycomb I was significantly slower than the first experiment, which achieved 98 % MB removal by the sixth hour. The solution became slightly cloudy with brown particles, i.e. rust, at the end of the first experiment (Figure 4.9). The precipitation of iron oxides contributed to the turbidity of the water in the reactor, which impeded the UVA light illumination on the immobilised  $\text{TiO}_2$  surface. This was not observed in MB experiments using Honeycomb II. The absorbance measurement of the solution at 365 nm using a Unicam 8632 UV/Vis Spectrophotometer ranged between 0.145 and 0.227 a.u., corresponding to 71.6 (24 NTU) and 59.3 (40 NTU) % UVA light transmission (Figure 3.15), respectively. When the reactor was switched on for 15 minutes, the absorbance measurement showed some reduction to 0.064 a.u. (10 NTU 86 % UVA light transmission). The reduction in the turbidity could be due to the reduction from ferric ( $\text{Fe}^{3+}$ ) to ferrous ( $\text{Fe}^{2+}$ ), the dissolved iron state in water, thus has less inhibiting effect on the UVA light transmission. The ferric oxides reappeared when the reactor was switched off for 5 minutes.



**Figure 4.9** Slightly cloudy MB solution after the first Honeycomb I experiment, indicating the precipitation of iron (III) oxides

The presence of iron compounds, which is known to affect the photocatalytic activity (Bhatkhande et al., 2001; Sahle-Demessie et al., 2002b; Almquist et al., 2003), is likely from the metal components for supporting radial panels because only deionised water was used here. The rust is likely generated from the corrosion of the immersed mild steel components, i.e. support and clips used to fasten the radial panels (Figure 4.10). It is feasible that oxygen and hydroxyl radicals produced from the photocatalytic reaction could have oxidised the mild steel components. Not only is this reducing available radicals but also possibly inhibiting UVA light from illuminating the catalyst surface via the precipitation of iron (III) oxides and competition between iron compounds and MB molecules for radicals in the second experiment (Bhatkhande et al., 2001; Sahle-Demessie et al., 2002b; Almquist et al., 2003). This suggests that the use of mild steel components as components immersed in the reactor should be avoided. The effect of iron on the MTBE PCO rate will be investigated in Chapter 5.

In order to prove that the corrosion was due to the oxygen radicals produced through photocatalysis, a metal clip was put in water and shaken overnight. The clip was slightly corroded but was insignificant compared to those observed after the experiment. The clip was then put into water and illuminated with UV irradiation of  $2.1 \text{ mW cm}^{-2}$  for a day but no significant corrosion was observed (Figure 4.11). This suggests that the presence of oxidising radicals generated via photocatalysis were free to oxidise the iron components.

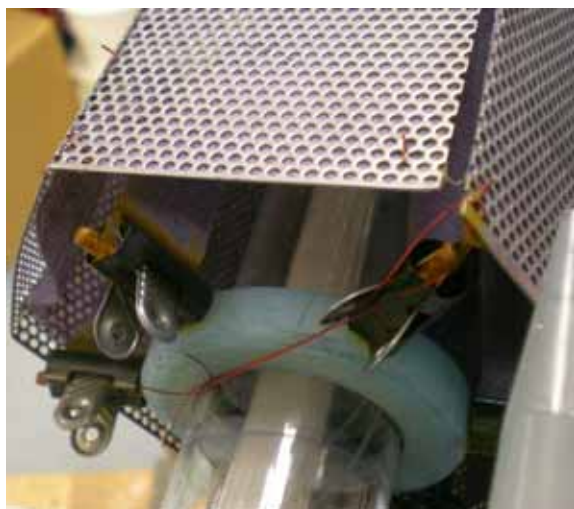


**Figure 4.10** The corrosion of radial panel support after the Honeycomb I experiments



**Figure 4.11** The metal clip from control (left) and after the Honeycomb I experiments (right)

#### 4.4.3 Reliability Study

Figure 4.12 shows the effect of variation in aeration ratio on MB removal in nine successive runs. The replicate MB degradation curves for the experiments conducted with intermittent aeration ratios (on:off) of 12:0 and 11:1 indicated that the performance of Honeycomb II was repeatable and consistent. This indicates that the immobilised  $\text{TiO}_2$  remained photocatalytically intact. The mean MB PCO rate constant and relative standard deviation (RSD) for 12:0 and 11:1 ratios were  $0.31$  ( $5\%$  RSD) and  $0.24 \text{ h}^{-1}$  ( $1\%$  RSD), respectively. This is consistent with a wear efficiency of immobilised  $\text{TiO}_2$  studies reviewed by Mills et al. (1993), demonstrating nearly identical performance over 10 successive operations. This study ascertained that photocatalysis is a cyclic redox process in which the immobilised catalyst is practically unaffected after every complete photocatalytic reaction cycle, as depicted in the photocatalytic mechanism (Hoffmann et al., 1995). The reliability shows that the immobilised  $\text{TiO}_2$  can potentially be used for a certain period of time before requiring replacement.

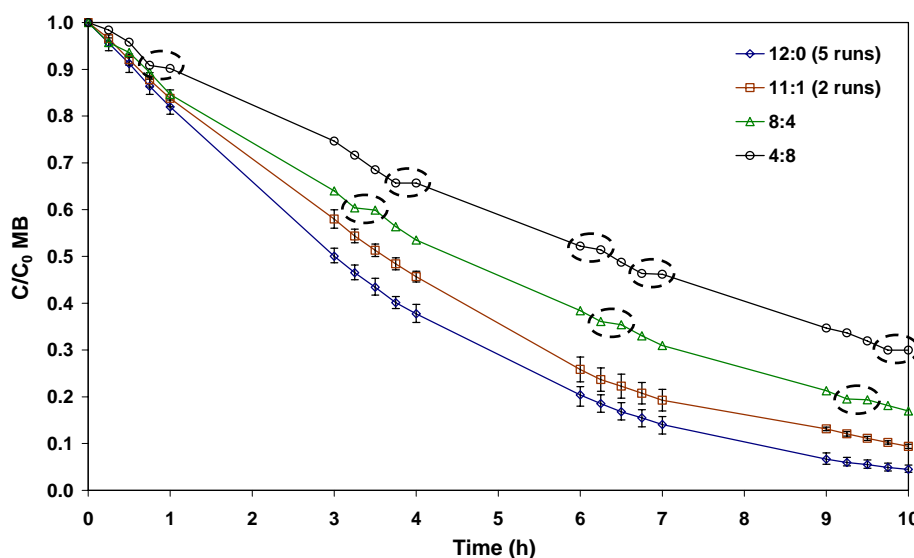


**Figure 4.12** Reduction of the average normalised MB concentrations with time in the reliability experiments at various air supply intervals (on:off). Error bars show the maxima and minima of replicate measurement.

The subsequent series of operations also implied that the performance of the sample would remain consistent had it been tested in continuous aeration mode (12:0). The sixth and seventh operation conducted with intermittent aeration ratio of 11:1 were also consistent and the eighth and ninth operation conducted in aeration ratio of 8:4 and 4:8, respectively,

showed sensible proportion in the MB removal efficiency. This will be discussed further in the aeration study.

#### 4.4.4 Aeration Study

The effect of intermittent aeration was studied using the same catalyst used for reliability study following the five successive experiments for 12:0. Figure 4.12 shows that the effect of oxygen supply on photocatalytic reaction is instantaneous as the degradation of MB is impeded when the aeration was interrupted (circled with dotted lines). This confirmed that aeration is an essential component in photocatalysis, as suggested in the photocatalytic mechanism and reaction equations (Mills et al., 1993; Hoffmann et al. 1995).

Figure 4.12 also shows that the MB removal efficiency decreased with shorter aeration duration: 95 % (12:0), 90 % (11:1), 80 % (8:4) and 67 (4:8). The half-life of MB correspondingly increased: 2.85 hr (12:0), 3.50 hrs (11:1), 4.10 hrs (8:4) and 5.85 hrs (4:8). This caused the MB PCO rate constant to decrease with shorter aeration time (Figure 4.13).

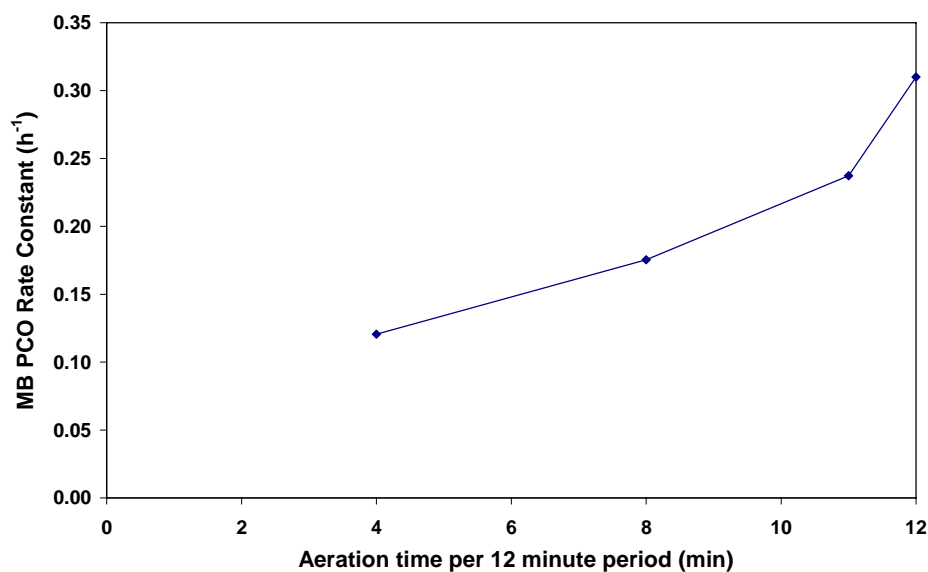


**Figure 4.13** Variation of MB PCO rate constant of Honeycomb II with aeration ratio (on:off); from left to right 4:8, 8:4, 11:1 and continuous aeration, 12:0

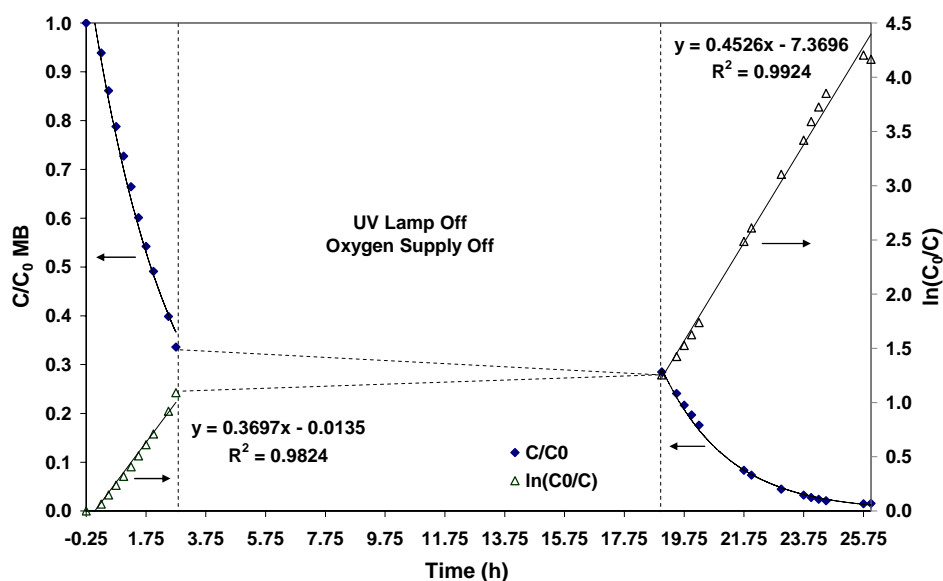
Figure 4.13 shows the effect of aeration time on the MB PCO rate constant of Honeycomb II. The MB PCO rate constant of the 4:8 ratio was less than half to that obtained via continuous aeration. There was a more significant difference between 12:0 and 11:1, indicating that the photocatalytic reactor is best operated with continuous aeration. This is consistent with the

photocatalytic mechanism that oxygen is required in the reductive pathway to scavenge the excited conduction band electrons and yield oxygen and hydroxyl radicals prior to oxidising pollutant molecules (Hoffmann et al., 1995). Despite the oxidative pathway having higher redox potential, MB was significantly not degraded in the absence of oxygen, possibly due to electron-hole recombination as the electrons are not scavenged. This reinforces that continuous aeration is an essential operating condition for a photocatalytic reactor.

In engineering works, it is common to encounter interruptions in any treatment operation, typically due to periodical maintenance or power failure. Therefore, an experiment was conducted by interrupting the reactor operation by switching off the UVA lamp and air pump; to simulate interruption to observe the variation of MB concentration. The experiment consisted of four stages: (i) 15 minutes adsorption with light and oxygen-off, (ii) light and oxygen supply for 3 hours, (iii) light and oxygen-off for 16 hours, and (iv) light and oxygen supply until MB concentration was almost depleted. Honeycomb II configuration was used in this study.

Figure 4.14 shows the variation of normalised MB concentration and  $\ln(C_0/C)$  with time. There was no significant change in the MB concentration and column reactor performance during the 16 hours interruption. There was no noticeable recovery in the colour of MB solution within 16 hours in the absence of light and oxygen supply, implying that the adsorption process could have stabilised and the degradation reaction appeared to be irreversible as found by Houas et al. (2001). This was also observed in other experiments where the colour did not recover in a discoloured MB solution, despite being kept for years.

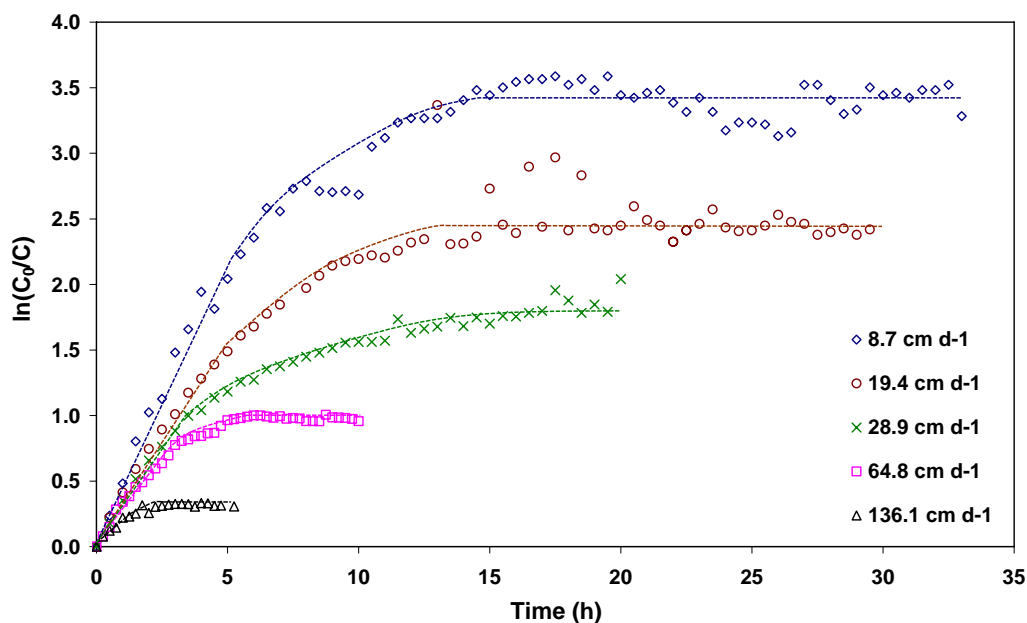
The photocatalytic activity appeared to be unaffected by the interruption as the effective treatment duration was circa 10 hours, similar to the other column experiments with continuous light and oxygen supply. This also indicated that the immobilised  $\text{TiO}_2$  remained intact throughout the experiment, which was also confirmed through observation in the column reactor. It is speculated that all the processes involved in the photocatalytic cycle needs to achieve an overall steady state condition in order to maintain and/or optimise the overall reaction rate. The overall reaction rate, i.e. photocatalytic activity, could be decelerated if one of the process involved are more dominant. This was also observed in the adsorption study and discussed under Section 4.4.1.



**Figure 4.14** Reduction of MB concentration in an experiment which had UV lamp and aeration supply interruption

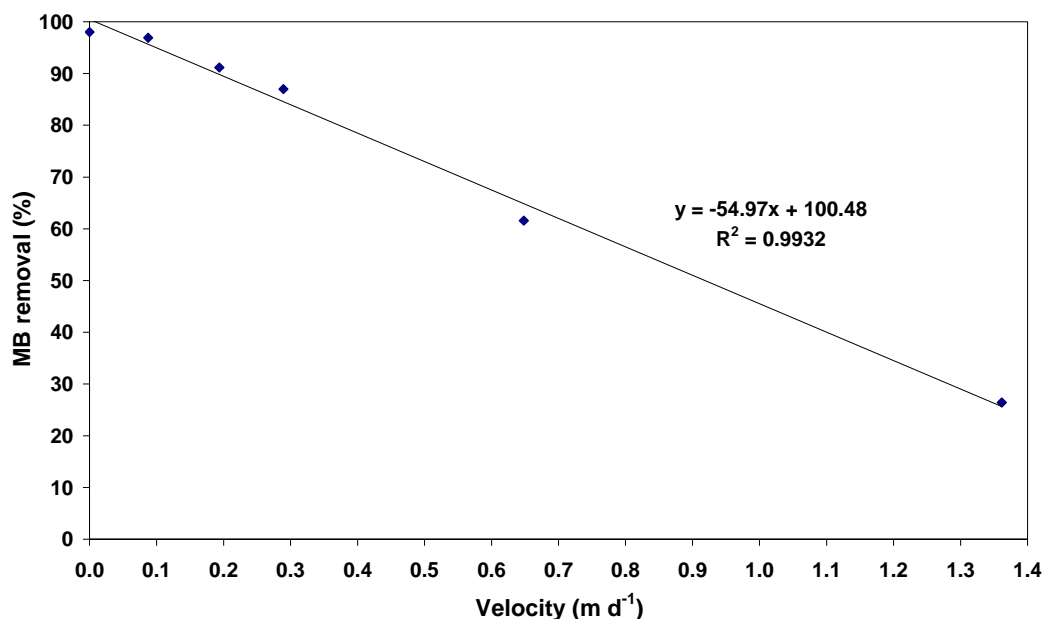
#### 4.4.5 Single Pass Flow Study

Studies conducted in batch experiments, i.e. no flow, show linear photocatalytic activity and comply with the first order reaction conditions. The  $\ln(C_0/C)$  eventually reaches a plateau when the contaminant is almost completely degraded (Figure 4.15) or the maximum  $\ln(C_0/C)$  is achieved (Herrmann, 2005). However, in the flow study, the  $\ln(C_0/C)$  reaches a plateau when the MB concentration stabilised (Figure 4.15), indicating  $dC/dt = 0$  and the rate of MB arriving equals the rate of MB removed and discharged. The MB concentration appears to level off and  $\ln(C_0/C)$  reaches a plateau at approximately half the cycle of a HRT, or about 15 hours when the HRT was 20 hours or more. The  $\ln(C_0/C)$  did not increase further when the MB concentration became constant as it is defined by the removal percentage ( $C/C_0$ ). The  $8.7 \text{ cm d}^{-1}$  experiment (68.9 h HRT) was stopped at 33 hours as the MB concentration remained constant for about 18 hours.



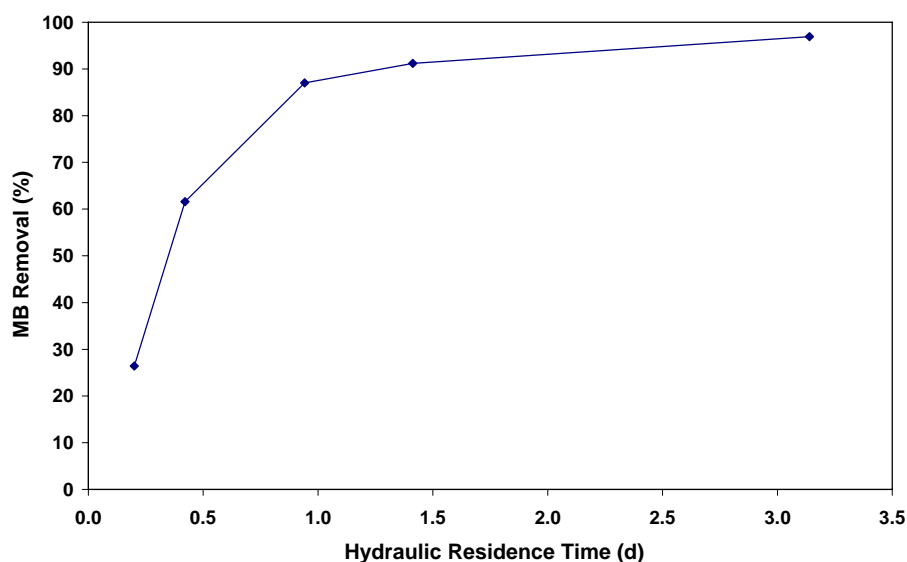
**Figure 4.15**  $\ln(C_0/C)$  plotted against time for MB degradation using Honeycomb II in the 4 L column reactor at five velocities as specified in Section 4.3.2

Figure 4.16 shows that the potential reactor efficiency decreased linearly with increasing velocity. Potential reactor efficiency refers to the removal percentage at which the MB concentration stabilises. The velocity should not exceed  $19.4 \text{ cm d}^{-1}$  in order to maintain at least 90 % MB removal in one pass and one HRT cycle. This is because, as the velocity is increased, the HRT of MB molecules in the reactor is shortened (Eq. 2.26) as it is displaced by the new batch of MB molecules prior to get adsorbed on the catalyst surface. Shorter HRT implies shorter adsorption duration, which limits the mass transfer of MB molecules onto the catalyst surface (Braham and Harris, 2009). This relationship provides useful information for the monitoring of reactor efficiency in the field from which the site average groundwater velocity can be obtained directly. However, it does not provide sufficient information to determine the optimum reactor dimensions. Therefore, there is a need to obtain the optimum HRT for the optimisation of the reactor process.



**Figure 4.16** Variation of the MB removal efficiency as a function of velocity using Honeycomb II in the 4 L column reactor

Figure 4.17 shows there was no significant enhancement in the MB removal efficiency when the HRT was more than 1 day. The MB removal efficiency decreased significantly when the HRT was less than 1 day. This indicates that the critical HRT of the reactor for the degradation of MB is approximately 1 day, which corresponds to an velocity of about 28.9 cm d<sup>-1</sup>. The critical HRT can be considered as the minimum HRT required by the reactor in order to maintain the potential removal efficiency. In terms of velocity, the critical velocity is the maximum velocity permissible in order to maintain the potential removal efficiency of the reactor. At velocities higher than the critical velocity, both the removal efficiency and HRT decreased significantly (Figure 4.17).



**Figure 4.17** MB removal efficiency in one HRT cycle using Honeycomb II in the 4 L column reactor for various velocities

The flow study demonstrated that (i) the MB removal efficiency greater than 85 % can be maintained at flows less than 1 day HRT, (ii) the critical HRT for this reactor design appears to be 1 day (corresponding to  $28.9 \text{ cm d}^{-1}$ ) and (iii) the recirculation at velocities faster than  $28.9 \text{ cm d}^{-1}$  could improve removal efficiency by increasing the HRT in the reactor. However, recirculation is not feasible as recharge of partially treated groundwater is not permitted. Therefore, an alternative approach is to apply multiple arrays of modules in a trench.

It is expected that the response of this photocatalytic reactor towards flow will be similar for other compounds but the removal efficiency and HRT are likely to vary due to the oxidative properties of the target compounds.

## 4.5 Conclusions

A photocatalytic reactor design is proposed for in-situ groundwater remediation and has been characterised in several aspects. The following inferences were made:-

(i) Scale up: The scale up of the hybrid coating procedure showed that it is reproducible. The lower MB PCO rate constants at the larger experimental scales were limited by UVA light intensity and possibly by mass transfer as well.

(ii) Surface area: The MB PCO rate constant appeared to increase linearly with increasing surface area to volume ratio. The additional radial panels in Honeycomb I enhanced the MB removal and provided higher MB PCO rate constants than Honeycomb II, which was proportional to the additional surface area.

(iii) Reliability: The immobilised catalyst demonstrated its reliability via consistent MB degradation curves, which could justify its operational and maintenance costs.

(iv) Aeration: Continuous aeration is essential to optimise the photocatalytic reactor efficiency.

(v) Flow: The MB removal efficiency decreased linearly with increasing flow. The critical HRT is 1 day, which corresponds to a velocity circa 28.9 cm d<sup>-1</sup>.

This chapter demonstrated the potential of Honeycomb for in-situ groundwater remediation and will be applied for the degradation of MTBE in Chapter 5.

## CHAPTER 5

### MTBE DEGRADATION USING HONEYCOMB II MODEL

#### 5.0 Overview

In Chapter 4, a novel hexagonal photocatalytic reactor, Honeycomb, was proposed and tested under several operating conditions using methylene blue (MB), which demonstrated its reliability and potential for in-situ groundwater remediation. In this approach, an underground reactor can intercept a pollution plume, to remove most of the harmful organic compounds. The study demonstrated that the proposed Honeycomb design, which opposes the typical intensification approaches in photocatalytic reactor design, can demineralise MB at low UVA light intensity. This chapter involves the evaluation of Honeycomb II model in the degradation of the target contaminant in this research, MTBE. This chapter consists of two major parts, i.e. effect of groundwater constituents and hydraulic performance of the reactor.

Groundwater constituents, which varies from site to site, is known to affect the efficiency of a photocatalytic reactor. Due to the diversity of groundwater composition, a systematic investigation is required, hopefully, to distinguish the effects of organic compounds and dissolved ions on the efficiency of a photocatalytic reactor. Therefore, a part of this chapter investigates the effect of organic compounds and dissolved ions on the MTBE removal efficiency of Honeycomb II model, without process optimisation such as pH adjustment or pre-treatment; to assess the reliability of the proposed reactor design in ambient conditions. The investigation was conducted separately for organic compounds and dissolved ions prior to the investigation in the presence of both types of constituents. This study also involves single and double pass flow experiments in the presence of organics and dissolved ions, for comparison with the reactor efficiencies obtained in Chapter 4.

As the reactor design considerations were evaluated in Chapter 4 and the PCO rate constant is compound specific (Ryu and Choi, 2008), this chapter focuses on the hydraulic performance of the Honeycomb II model in decomposing MTBE, using single and double

pass flow studies. The single pass flow study was conducted to obtain the reactor efficiency, at flows similar to that of MB in Chapter 4, for comparison of the response of removal efficiency with increasing velocity. As MTBE was not completely degraded in one pass, this indicated that multiple passes are required in order to achieve the desired clean-up goal. Therefore, double pass flow study was conducted to verify whether the overall reactor efficiency for multiple pass can be estimated via the sequential order of the removal efficiency obtained in the single pass flow study. This study also explored the effect of air flow to volume ratio on the MTBE vaporisation for the estimation of air flow for a larger scale photocatalytic reactor. This study is an intermediate phase of the research in developing an in-situ photocatalytic reactor for groundwater remediation.

## 5.1 Study Considerations

### 5.1.1 Hydrogeological Aspects

Unlike water treatment systems, the flow of groundwater through a barrier or trench clean-up system is typically governed by the natural gradient. Therefore, a flow study is required to measure of the reactor efficiency for a range of groundwater flows. The natural gradient constantly varies, therefore, it is necessary to measure the performance over a range of velocities. This is essential for an engineer in projecting the expected efficiency of the photocatalytic reactor on site, in either the design or operational stage. In this study, the flow is defined in terms of equivalent horizontal water velocity so that the profile can be directly correlated to the groundwater velocity measurement on site. The flows in this study were determined based on the average velocity of  $33 \text{ m yr}^{-1}$  ( $9 \text{ cm d}^{-1}$ ) recorded at a well characterised site, Borden in Canada (Mackay et al., 1986). The velocities (Darcy) were calculated based on the flow per area of the section of column perpendicular to flow direction ( $49\pi \text{ cm}^2$ ) (Figure 4.4a). This is to simulate the horizontal flow passing through a porous-walled Honeycomb II, assuming that the MTBE solution was completely mixed in the column reactor. As recirculation is not feasible for in-situ groundwater remediation and one pass is insufficient to completely eliminate a compound, the reactor efficiency can be enhanced by arranging modules in series.

### 5.1.2 Aeration

Aeration is essential for the photocatalytic degradation of MTBE, not only to provide dissolved oxygen for photocatalytic reaction but also to provide turbulence to ensure uniform concentration in the reactor. However, it can vaporise MTBE. Therefore, it is important to control the air flow so that more MTBE molecules are degraded by photocatalysis instead of transfer to the air. Thus, the effect of air flow, in terms of air flow to volume ratio, on the vaporisation of MTBE in the column reactor was explored in this study. This ratio is important for the scale up of a reactor to ensure the operating conditions are similar to that of its model. Lower air flow to volume ratio is preferred in a field scale reactor due to lower energy consumption, making it more affordable; lower capital and maintenance and operation costs.

From Eq. 1.1, the amount of dissolved oxygen required to photocatalytically degrade 320 mg MTBE (4 litres of 80 mg L<sup>-1</sup> MTBE) is 872 mg, which corresponds to approximately 3.6 L<sub>a</sub>, considering the composition of oxygen in air and the density and solubility of oxygen in water at 20 °C. L<sub>a</sub> refers to air volume to distinguish from reactor volume, L. In 3 hours, 36 L<sub>a</sub> was introduced into the column reactor at 0.2 L<sub>a</sub> min<sup>-1</sup>, so more than sufficient oxygen was provided for the photocatalytic degradation of MTBE in the experiments and can be assumed that the oxygen coverage on the catalyst surface is constant (Herrmann, 2005). The extra air flow is required for the mixing of the solution in the reactor; vertical mixing by air bubbles. The equivalent air velocity at air flow of 0.2 L<sub>a</sub> min<sup>-1</sup> in the column reactor is approximately 1870 cm d<sup>-1</sup>, which is at least one order of magnitude greater than that of the water velocities tested, so it is sufficient for complete mixing of solution in the reactor. This was confirmed by the uniform concentration of MTBE measured at two depths in the column reactor and uniform colour intensity of MB solution in the column reactor through observation. In the observation during MB experiments, a “blue jet” (more intense colour of initial MB concentration) dissipated within a short mixing zone at the base of the column reactor; indicating the complete mixing of the solution in the column reactor. Consequently, in this study, the air flow to volume ratio was limited up to 0.075 L<sub>a</sub> min<sup>-1</sup> L<sup>-1</sup> only as higher air flow would cause more MTBE vaporisation, similar to air stripping.

### 5.1.3 Groundwater Constituents

In previously reported photocatalytic processes, the removal of a target contaminant is significantly affected by the presence of groundwater constituents; for instance: MTBE using a falling film reactor (Sahle-Demessie et al., 2002b) and trichloroethylene (TCE) using a parabolic trough reactor (Mehos and Turchi, 1993), both reactors were using slurry TiO<sub>2</sub>.

Sahle-Demessie et al. (2002b) observed that the PCO rate constant of MTBE was inhibited by an order of magnitude in actual groundwater compared with deionised water and was attributed to dissolved metal ions and chlorides. Mehos and Turchi (1993) found that the PCO rate constant of TCE was enhanced 5 to 7-fold under acidic conditions compared with neutral conditions; the catalyst loading and flow effects were negligible. However, the PCO rate constant of TCE was still significantly lower when treating actual groundwater, compared to that in deionised water. Matthews (1992) reported that the reactor efficiency varied with different wastewater treated; 10 and 40 % reduction in the PCO rate for carbon dioxide formation when treating 100 mg L<sup>-1</sup> phenol spiked in wastewaters from a paint stripping operation and petroleum refinery, respectively, compared to that in deionised water. Due to the complex matrices in groundwater and wastewater, it is difficult to identify the inhibiting constituent. Some studies have investigated the effect of organics and inorganics, typically dissolved ions (Scalfani et al., 1991; Butler and Davis, 1993; Liao et al., 2001; Vamathevan et al., 2001; Wang et al., 2004; Klauson et al., 2005) on the PCO of a target contaminant. However, these studies usually scrutinise the effect of one type of constituent only, for example chloride (Liao et al., 2001) and iron (Vamathevan et al., 2001; Klauson et al., 2005).

For the organic compounds, it is likely that the more strongly adsorbed organic molecules will be degraded first and inhibit the subsequent adsorption of the other organic molecules (Sahle-Demessie et al., 2002b). The other possibility is that there is increased competition for OH radicals among the molecules (Matthews, 1992). Both phenomena can explain the reduced removal of a target contaminant in the presence of other organic compounds.

As photocatalysis involves reduction and oxidation (redox) reactions, it is also affected by the presence of dissolved ions (Mills et al., 1993; Litter, 1999). Iron, at certain concentrations (Butler and Davis, 1993; Klauson et al., 2005), is reported to have a beneficial effect on the PCO of a contaminant, thought to be due to iron (III) (Fe<sup>3+</sup>) reducing electron-hole recombination, thus increasing the OH radical generation rate. Ferrous (Fe<sup>2+</sup>) and ferric (Fe<sup>3+</sup>) ions have similar effects on the PCO rate of a contaminant possibly due to an equilibrium established between Fe<sup>2+</sup> and Fe<sup>3+</sup> in acidic aqueous solution in the presence of dissolved oxygen (Scalfani et al., 1991; Butler and Davis, 1993; Vamathevan et al., 2001; Klauson et al., 2005). Liao et al. (2001) found that chloride ion inhibited the PCO of n-chlorobutane (BuCl) by scavenging the OH radical and deactivating active sites via adsorption on the positively charged catalyst surface, especially in acidic conditions. Therefore, it would be interesting to observe the inhibition of the PCO of a contaminant in the presence of organics, dissolved ions and combination of organics and dissolved ions. As

almost all these studies were conducted in slurry reactors, there is a need for a study using an immobilised catalyst design.

#### 5.1.4 Multiple Pass Photocatalytic Reactor

A large scale photocatalytic reactor, which is suitable for underground application, will consist of modules arranged in series due to UVA irradiation and mass transfer limitations. It is necessary to investigate the efficiency of the photocatalytic reactor when contaminated groundwater flows through the modular arrays. For serially connected modules, the efficiency of every module can be assumed similar and therefore evaluated in the laboratory by testing one segment of a similar sized module (Bisio and Kabel, 1985). Therefore, a double pass flow study was conducted to simulate the attenuation of MTBE as it flows through a series of two photocatalytic modules, i.e. Honeycomb II. Double pass refers to a batch of contaminated water single-passing through two Honeycomb II modules in series. In addition, the study can experimentally verify whether the clean-up by modular arrays can be estimated by sequential order of removal efficiency in a single pass (Eq. 5.1).

$$R_N = \left[ 1 - \left( \frac{C}{C_0} \right)^N \right] \times 100 \quad (5.1)$$

where  $R_N$  is the removal efficiency after  $N$  passes in series (%),  $C$  is concentration of the contaminant after first pass ( $\text{mg L}^{-1}$ ) and  $C_0$  is the initial concentration of the contaminant ( $\text{mg L}^{-1}$ ). If verified applicable, this sequential order can be used to project the performance of a photocatalytic reactor on site by obtaining the reactor performance from a single pass flow study in the laboratory.

## 5.2 Experimental Methodology

### 5.2.1 Experimental Arrangement

The experimental arrangement of the column reactor used in this study is similar to that described in Section 4.3.1, except that the top plate was sealed to minimise MTBE vaporisation.

The initial MTBE concentration was circa  $80 \text{ mg L}^{-1}$ , similar to Barreto et al. (1995) and higher than the typical MTBE concentrations reported in the field (Schirmer et al., 1999; An et al., 2002; Ruiz-Aguilar et al., 2002). The synthesized MTBE solution was prepared by spiking  $110 \mu\text{L}$  MTBE into  $1 \text{ L}$  deionised water, using a Hamilton  $100 \mu\text{L}$  glass syringe. During sampling,  $1 \text{ mL}$  MTBE solution was transferred into a  $2 \text{ mL}$  vial using a  $10 \text{ mL}$  glass syringe from Samco, with a modified  $225 \text{ mm}$  long  $0.8 \text{ mm}$  i.d. stainless steel needle. The solution was sampled from the mid-depth outside Honeycomb II. The syringe was washed thrice after every sampling to remove MTBE residual in the syringe and needle. The samples were analysed using an Agilent 6850 Series gas chromatograph with flame ionisation detector (GC-FID) using an ambient headspace technique at  $20 \text{ }^\circ\text{C}$ . Ambient headspace technique involves the analysis of a VOC sample in vapour phase ( $50 \mu\text{L}$  gas injection) at ambient temperature, in which the concentration is assumed to be proportional to its concentration in the aqueous phase when the liquid-gas concentration equilibrium is achieved. A preliminary study indicated that the samples required about 30 minutes to achieve a liquid-gas MTBE concentration equilibrium prior to analysis (Figure 5.2). The control and aeration experiments were conducted without flow ( $0 \text{ cm d}^{-1}$ ). It is assumed that there was no loss of solution during the test.

Two control tests for photolysis (UVA only) and adsorption ( $\text{TiO}_2$  only) were conducted to distinguish the effect of thermal and photolysis, and adsorption, from photocatalysis. Both control tests showed no significant reduction in MTBE concentration, which agrees with other studies (Sahle-Demessie et al., 2002a and b; Almquist et al., 2003). MTBE is a relatively polar compound in which it does not adsorb well onto any surface (Jacobs et al., 2001). Therefore, the effect was negligible to be considered in the analysis.

### 5.2.2 Aeration Experiment

3 hour aeration experiments were carried out in the reactor, with catalyst, in the absence of UVA light at air flows of  $0.1$ ,  $0.2$  and  $0.3 \text{ L}_a \text{ min}^{-1}$ , which correspond to air flow to volume ratios of  $0.025$ ,  $0.050$  and  $0.075 \text{ L}_a \text{ min}^{-1} \text{ L}^{-1}$ , respectively. The range of air flows tested spanned the normal air flow used in the experiments at  $0.2 \text{ L}_a \text{ min}^{-1}$ . For these experiments, there was no water flow and the MTBE solution was sampled at 15 minutes interval.

### 5.2.3 Single Pass Flow Study Arrangement

The setup of single pass flow experiment and the velocities tested in this study is similar to that of MB single pass flow experiments described in Section 4.3.2. The same set of

catalyst was used throughout this series of experiments at six velocities, under similar operating conditions. The MTBE concentration in the feed container is similar to the initial concentration in the column reactor,  $80 \text{ mg L}^{-1}$ . The experiments were of 8 hours duration except at the velocity of  $136.1 \text{ cm d}^{-1}$  for 6 hours, as the HRT cycle was achieved in 4.5 hours. The sampling was conducted at 15 minutes interval during the first hour, followed by 30 minutes interval for the subsequent 7 hours. It should be noted that the photocatalytic reactor was stopped between the flow experiments.

#### 5.2.4 Double Pass Flow Study Arrangement

The operating conditions of double pass flow experiments are similar to that of single pass flow experiments. The effluent accumulated from the first pass was used as feed for the second pass at the 24<sup>th</sup> hour to simulate the same batch of water flowing through two reactors in series. This is to emulate the field scale photocatalytic reactor, in which the subsequent modules degrade the residual contaminant from the previous modules. Therefore, the solution was not recirculated in order to minimise dilution effect in the feed solution. It differed from a study by Almquist et al. (2003) (Figure 1.9), which recirculated a synthesized MTBE solution. Matthews (1989) and Almquist et al. (2003) found that the clean-up rate increased with increasing recirculation flow for MB and MTBE, respectively. This is to be expected due to the increased contact frequency of contaminants with oxidising radicals and concurrent dilution in the feed tank, with increasing recirculation flow.

The double pass flow experiment was conducted at a equivalent to the velocity of  $28.9 \text{ cm d}^{-1}$ , as it is the critical average velocity for MTBE degradation using Honeycomb II, which corresponds to 20.8 h HRT (Figure 5.13). In order to simplify the experimental procedure, the duration of each pass is assumed approximately 24 hours. In this study, the duration of the experiments was determined using HRT to distinguish when a reactor volume is completely replaced by another volume of synthesized MTBE solution (one pass).

The samples were withdrawn from the column reactor as the solution was completely mixed by aeration. The sampling frequency was every 15 minutes in the first hour, followed by 30 minutes interval for the subsequent 9 hours, of each pass. The sampling continued every 15 minutes in the first hour of each pass to observe the variation of MTBE concentration. A sample was taken at the 24<sup>th</sup> hour of each pass to obtain the concentration at which it stabilised.

Both new and used immobilised  $\text{TiO}_2$  were tested to compare their efficiencies. The used photocatalyst was continued from the single pass flow experiments, which were used for 6 experiments prior to the double pass flow experiment.

### 5.2.5 Selection of Constituents

The presence of common groundwater constituents and other contaminants affects many remediation technologies including biodegradation (Deeb et al., 2000) and photocatalysis (Matthews, 1992; Bhatkhande et al., 2001; Herrmann, 2005). As groundwater has complex matrices of constituents, only a few compounds were selected in this study in order to simplify the analysis and have a better understanding on its effect on the MTBE degradation. The compounds were determined from the common occurrence of the constituents with MTBE as reported by An et al. (2002) and Sahle-Demessie et al. (2002b). It is categorised into organic and inorganic (dissolved ion) constituents.

#### 5.2.5.1 Organic Constituents

Studies on the co-occurrence of MTBE are usually associated with BTEX since it is a fuel additive for gasoline (Schirmer et al., 1999; An et al., 2002; Ruiz-Aguilar et al., 2002). Therefore, BTEX is considered as the organic constituent in this study. Benzene was excluded from this study as a health and safety measure in the laboratory, thus the organic constituents were toluene (T), ethylbenzene (E), o-Xylene (o-X), known as TEO-X in this study. TEO-X concentrations (Table 5.1) were determined based on the respective water solubilities of gasoline components reported by An et al. (2002) as it corresponded to the formulation of oxygenated gasoline. The oxygenated gasoline typically consists of 10-11 % MTBE, 1-1.5 % benzene, 5 % toluene, 1 % ethylbenzene and 8-10 % total xylene (An et al., 2002). The concentrations of BTEX and MTBE detected in groundwater samples in other studies are typically below  $1 \text{ mg L}^{-1}$  (Squillace et al., 1999; Juhler and Felding, 2003). In this work, the initial MTBE concentration was fixed circa  $80 \text{ mg L}^{-1}$  (Barreto et al., 1995) to observe the effect of MTBE/TEO-X concentration ratio on the PCO of MTBE.

**Table 5.1** TEO-X concentrations used in the organic compound study; LO: Low Organic and HO: High Organic are used in the combination of TEO-X and dissolved ion study

Compound	Low (LO) ( $\text{mg L}^{-1}$ )	Medium ( $\text{mg L}^{-1}$ )	High (HO) ( $\text{mg L}^{-1}$ )
Toluene	10	20	30
Ethylbenzene	5	10	10
o-Xylene	5	10	20
TEO-X	20	40	60

1 mL solution was withdrawn during every sampling. The samples were analysed for MTBE/TEO-X using an Agilent 6850 Series gas chromatograph with flame ionisation detector

(GC-FID), using ambient headspace technique at 20 °C. A preliminary study indicated the samples required about 2 hours to achieve liquid-gas TEO-X concentration equilibrium prior to analysis (Figure 5.1). The sampling frequency is once every 30 minutes for the first two hours of experiment and once hourly thereafter.

#### 5.2.5.2 Inorganic Constituents

Calcium, iron, nitrate and chloride ions, typically found in groundwater, were chosen to represent inorganic compounds. Iron was chosen because it is often found in groundwater samples and the field installation of this reactor is likely to consist of metal components. Calcium was selected because it is commonly found in groundwater samples and used to represent hardness and alkalinity in the form of calcium carbonate ( $\text{CaCO}_3$ ) (Eq. 5.2) (An et al., 2002).  $100 \text{ mg L}^{-1}$  calcium chloride yields an approximate hardness of  $250 \text{ mg L}^{-1}$   $\text{CaCO}_3$  (Eq. 5.2) and  $177.5 \text{ mg L}^{-1}$  chloride.  $250 \text{ mg L}^{-1}$   $\text{CaCO}_3$  is considered as hard in some parts in the United Kingdom (DWI, 2009). Magnesium (Mg) is not considered in this study.

$$\text{mg L}^{-1} \text{ CaCO}_3 = [(\text{mg L}^{-1} \text{ Ca} \times 2.50) + (\text{mg L}^{-1} \text{ Mg} \times 4.12)] \quad (5.2)$$

Chloride is an anion of concern as it can actively compete for valence band holes (Mills et al., 1993; Bhatkhande et al., 2001; Liao et al., 2001) on the immobilised  $\text{TiO}_2$  surface. Nitrate ion ( $\text{NO}_3^-$ ) was selected as nitrate fertilisers are used in agricultural activities. Therefore, iron (III) nitrate ( $\text{Fe}(\text{NO}_3)_3$ ) and calcium chloride ( $\text{CaCl}_2$ ) was used in this study. The dissolved ion concentrations were selected based on the iron concentration reported by Sahle-Demessie et al. (2002b) and calcium concentrations in the hardness standards (DWI, 2009) (Table 5.2).

**Table 5.2** Dissolved ion concentrations used in the dissolved ion study, LI: Low Ion and HI: High Ion is used in the combination of TEO-X/dissolved ion study

Dissolved Ion	Ion Concentration ( $\text{mg L}^{-1}$ )				
	15 (LI)	30	50	100	200 (HI)
$\text{Fe}^{3+}$	15	30	50	100	200
$\text{NO}_3^-$	35	69	155	230	460
$\text{Ca}^{2+}$	15	30	50	100	200
$\text{Cl}^-$	27	54	90	180	360

The synthesized solution in the presence of dissolved ions was acidic due to a co-hydrolysis of calcium chloride and iron nitrate, in which among the insoluble product formed is the iron hydroxide.

The sampling procedures are similar to that of organic constituents. 5 mL solution was withdrawn for every sampling. A total of approximately 60 mL sample was withdrawn from the 4 L solution, which is 1.5 % and considered an insignificant amount to affect the 8 hour batch experiment. The samples were diluted to ion concentrations of not more than 5 mg L<sup>-1</sup> for analysis of cations and anions using the atomic absorption spectrophotometer (AAS) and ion chromatograph (IC), respectively. Although the samples withdrawn were clear, the samples were filtered using a 0.20 µm syringe filter to ensure no particles can plug the column of the ion chromatograph.

### 5.2.5.3 Combination of Organic and Inorganic Compounds

The combination of organic compounds and dissolved ions were tested to investigate whether the presence of both organic compounds and dissolved ions could cause further inhibition to the PCO of MTBE than in the presence of organic compounds or dissolved ions only. It could also indicate whether organic compounds or dissolved ions have more effect on the PCO of MTBE, via the MTBE removal efficiency. The respective nomenclatures and concentrations of organic compounds and dissolved ions and variations in the composition are shown in Table 5.3. As the medium concentrations of respective constituents were tested individually in the earlier stages in this study, only the extreme concentrations were tested in this stage.

**Table 5.3** Concentrations of dissolved ion and organic compounds in the four solutions used in combined study

Component	LILO	LIHO	HILO	HIHO
Fe <sup>3+</sup>	15	15	200	200
NO <sub>3</sub> <sup>-</sup>	35	35	460	460
Ca <sup>2+</sup>	15	15	200	200
Cl <sup>-</sup>	27	27	360	360
Toluene	10	30	10	30
Ethylbenzene	5	10	5	10
o-Xylene	5	20	5	20

Note: all units in mg L<sup>-1</sup>.

Single pass flow experiments were conducted to obtain the reactor efficiency and compare with the efficiency obtained in treating synthesized MTBE solution. The single pass flow

experiment is detailed in Section 4.3.2. The average velocities tested in this study were 28.9, 64.8 and 136.1 cm d<sup>-1</sup>.

## 5.2.6 Gas Chromatograph

### 5.2.6.1 Preparation of Standard MTBE Solution

1000 mg L<sup>-1</sup> MTBE solution was prepared by spiking 135 µL MTBE into 100 mL deionised water (Table 5.4). The solution was prepared in bulk by adding 135 µL MTBE into 100 mL deionised water in a 100 mL volumetric flask, using a Hamilton 100 µL glass syringe. The flask was manually rotated several times until the MTBE solution appears uniformly mixed. It is prepared in bulk to obtain similar uniform concentration for the same batch of MTBE solution. The concentrated solution was then diluted to a total fraction of 30 mL using a pipette into 40 mL vials for the respective MTBE concentration (Table 5.4). The MTBE concentration of the samples was measured at various analysis times to determine the optimum analysis time for the samples. The cycle time for the analysis of MTBE is 4 minutes per sample. There are 27 vial slots in the gas chromatograph autosampler. This calibration procedure needs to be repeated prior to every experimental analysis.

**Table 5.4** Preparation of standard MTBE solutions for GC calibration

Vial Number	Deionised Water Volume (mL)	MTBE		MTBE Concentration (mg L <sup>-1</sup> )
		Volume (mL)	Concentration (mg L <sup>-1</sup> )	
100 mL Volumetric Flask	100	0.135	-	1000
1	27	3	1000	100
2	27.6	2.4	1000	80
3	28.2	1.8	1000	60
4	28.8	1.2	1000	40
5	29.4	0.6	1000	20

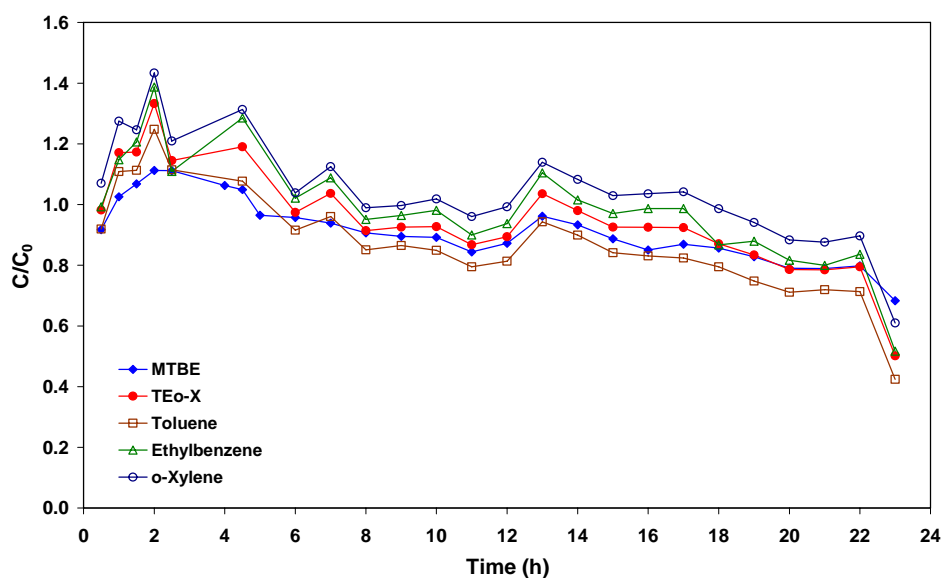
### 5.2.6.2 Configuration of Gas Chromatograph

1. Check syringe is 100 µL:
  - Put needle of syringe through the hole
  - Lock the syringe in place with black holder
  - Lock syringe handle and make sure it is fastened
  - Close the autosampler
2. Check the "Method": Emily1.m.

3. Check "Sequence Parameters": Operator Name, Folder and Prefix (file name).
4. Check "Sequence Table": Check vial number then save sequence.
5. Check the baseline signal before start. Sometimes the baseline signal might not be horizontal yet though it indicated ready (green light).
6. Check drain vials if there is residue.
7. Press "Start".

### 5.2.6.3 Determination of Equilibration Time between Preparation and Analysis for MTBE and TEO-X

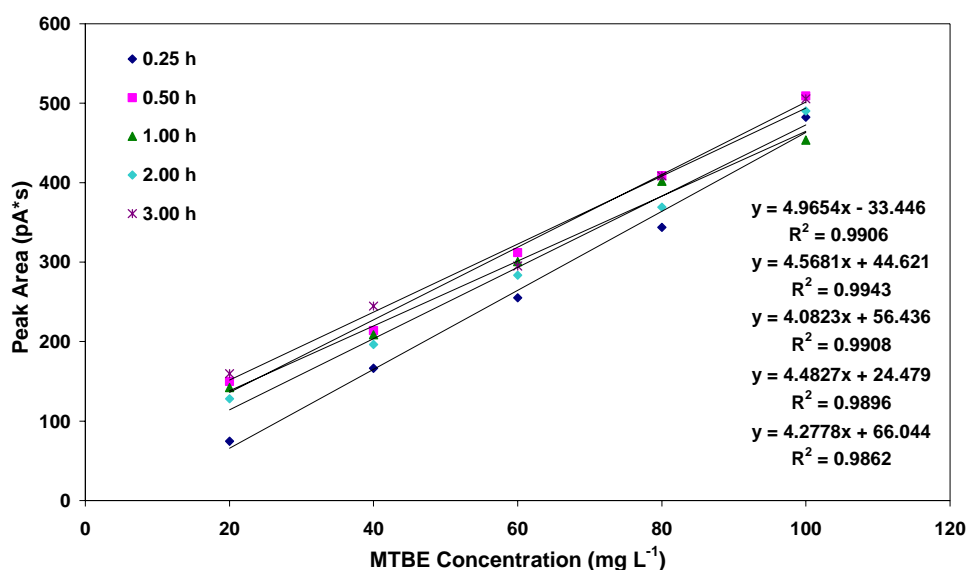
Figure 5.1 shows the normalised concentrations of MTBE and TEO-X measured at specific times, in order to determine the optimum equilibration time for the MTBE/TEO-X samples prior to analysis. The MTBE and TEO-X concentrations peaked between the 2<sup>nd</sup> and 4<sup>th</sup> hour of equilibration time, which also indicate the optimum analysis time for MTBE and TEO-X after sampling during experiments. Although some of the concentrations measured during the analysis for all compounds exceeded 1.0, the fluctuation of concentration was the indicator for the determination of analysis time for MTBE and TEO-X.



**Figure 5.1** Normalised concentrations of a mixture containing MTBE and TEO-X, measured by the GC at the specified times. The concentrations of MTBE, toluene, ethylbenzene and o-xylene are 100, 30, 10 and 20 mg L<sup>-1</sup>, respectively. The concentration of all the compounds appeared to peak between the 2<sup>nd</sup> and 4<sup>th</sup> hour, which indicated the analysis time of the samples.

## 5.2.6.4 Calibration of Gas Chromatograph

Figure 5.2 shows the linear plot of peak area against MTBE concentration for standard MTBE solutions (Table 5.4), analysed between 15 minutes to 3 hours equilibration time, in order to determine the equilibration time of MTBE prior to analysis. The gradient of the linear plots appeared to be consistent (within acceptable range) for measurements after 30 minutes.



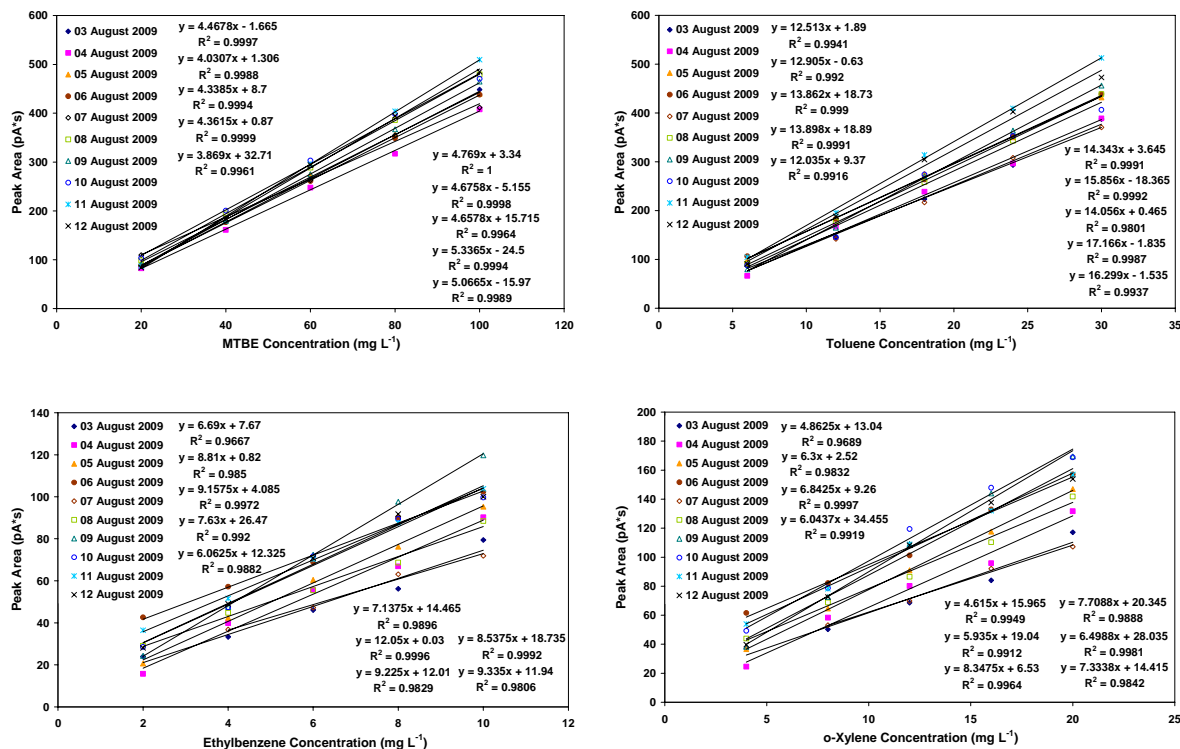
**Figure 5.2** Peak area to MTBE concentration, analysed at various MTBE equilibration times

Figure 5.3 shows the calibration of gas chromatograph for MTBE and TEO-X, analysed after 2 hours of equilibration time (Figure 5.1). These calibrations, conducted using known MTBE and TEO-X concentrations (Table 5.4), provide the conversion ratio of the respective organic compound for the analysis of samples during experiments (Eq. 5.3).

$$C = a.A_p \quad (5.3)$$

where  $C$  is the concentration of sample in aqueous phase ( $\text{mg L}^{-1}$ ),  $a$  is the conversion ratio of concentration over peak area ( $\text{mg L}^{-1}/(\text{pA}\cdot\text{S})$ ) and  $A_p$  is the peak area obtained from the

GC analysis performed by the Agilent 6850 GC-FID in units designated as pA\*s. The conversion ratio,  $\alpha$ , is the inverse of the gradient obtained in the GC calibration (Figure 5.3).



**Figure 5.3** Calibrations of gas chromatograph for MTBE (top left), toluene (top right), ethylbenzene (bottom left) and o-xylene (bottom right), analysed after 2 hours of liquid-gas equilibration time

## 5.3 Results and Discussion

### 5.3.1 Considerations Affecting MTBE Vaporisation

MTBE vaporisation will be affected by its properties and the reactor operation. In this study, the effect of air flow to volume ratio and average width (cell diameter) to height (D/H) ratio of the reactor on MTBE vaporisation was explored.

#### 5.3.4.1 Aeration

Without light and catalyst, the MTBE vaporisation appeared to increase proportionally with the air flow to volume ratio; 11.3, 20.6 and 32.5 % MTBE reduction at 0.025, 0.050 and 0.075 L<sub>a</sub> min<sup>-1</sup> L<sup>-1</sup>, respectively. The aeration study demonstrated 20.6 % MTBE removal

over 3 hours at  $0.2 \text{ L}_a \text{ min}^{-1}$ . Nevertheless, it should be considered as part of the photocatalytic efficiency in degrading MTBE as aeration is an essential component of a photocatalytic process. Warren obtained higher MTBE reduction of about 95 % when aerated at about  $0.25 \text{ L}_a \text{ min}^{-1}$  in a 1.4 L beaker for 4 hours, corresponding to the air flow to volume ratio of  $0.18 \text{ L}_a \text{ min}^{-1} \text{ L}^{-1}$ .

#### 5.3.4.2 Cell Diameter to Height (D/H) Ratio

The MTBE vaporisation can also vary with the geometry of the reactor, i.e. D/H ratio. For the same air flow to volume ratio, the vaporisation would increase with increasing D/H ratio, and vice versa. Similar to evaporation, higher D/H ratio would have relatively larger surface area for vaporisation to the atmosphere. The D/H ratio in this study was 0.50, compared to 0.85 by Warren. This section suggests that the effect of air flow to volume ratio on MTBE vaporisation would be less significant in a field scale reactor than a laboratory scale reactor as the air flow to volume ratio applied would not be more than  $0.05 \text{ L}_a \text{ min}^{-1} \text{ L}^{-1}$ . In addition, the D/H ratio will be significantly smaller as the internal diameter of the reactor will be limited to circa 20 cm due to UVA irradiation and mass transfer limitations, and the reactor can be 2 m deep.

#### 5.3.4.3 Contaminant Properties

Besides the air flow to volume and D/H ratios, the MTBE vaporisation is also affected by the ambient air pressure and temperature, which varies the Henry's law constant. Warren obtained about 90 and 95 % MTBE reduction when aerated at temperatures of 12 and 25 °C, respectively. The Henry's law constant (vapour/aqueous concentrations) of MTBE ranges from 0.012 to 0.029 at temperatures between 10 and 25 °C, respectively (Eq. 5.4) (Fischer et al., 2003).

$$\frac{H}{RT} = \frac{C_v}{C} \quad (5.4)$$

where  $H$  is the Henry's law constant (dimensionless),  $R$  is the gas constant ( $8.2 \times 10^{-5} \text{ atm m}^3 \text{ mol}^{-1} \text{ K}^{-1}$ ),  $T$  is the temperature (K),  $C_v$  is the concentration of compound in vapour phase ( $\text{mg L}^{-1}$ ),  $C$  is the concentration of compound in aqueous phase ( $\text{mg L}^{-1}$ ).

Volatile organic compounds with Henry's law constants below 0.05 typically tend to be very soluble and remain in water (Jacobs et al., 2001). Therefore, modest aeration in a field scale photocatalytic reactor is not expected to induce significantly the vaporisation of such VOCs due to the physical design and lower Henry's law constant of the target VOC (Sahle-Demessie et al., 2002b), especially with a groundwater temperature typically circa 10 °C.

A control experiment with aeration is essentially to distinguish the vaporisation of the compounds from the photocatalytic degradation. The experiment was conducted by introducing 0.2 L<sub>a</sub> min<sup>-1</sup> air flow with UVA lamp off. Figure 5.4 shows that more TEo-X was removed than MTBE during the control experiment with aeration. The aeration at 0.2 L<sub>a</sub> min<sup>-1</sup> removed circa 22 % MTBE, which is in agreement with Section 5.4.4.1 of about 20.6 %. The 8 hours aeration removed approximately 92, 100 and 80 % toluene, ethylbenzene and o-xylene, respectively, totalling circa 89 % TEo-X. This is expected due to their higher Henry's law constants and lower solubility than that of MTBE (An et al., 2002; Sahle-Demessie et al., 2002b).

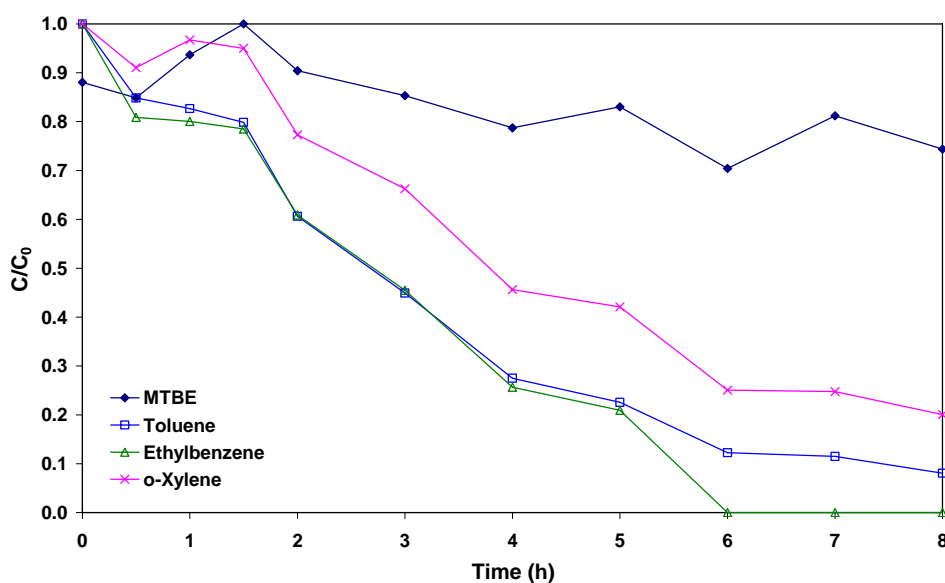


**Figure 5.4** Normalised concentration of MTBE and TEo-X vaporisation during the control batch experiment for aeration, with concentrations of MTBE, toluene, ethylbenzene and o-xylene of approximately 80, 30, 10 and 20 mg L<sup>-1</sup>, respectively. The data was plotted with  $C_0$  being the maximum concentration, not necessarily at  $t = 0$ .

A control experiment to observe the effect of photolysis (UVA only - no air) was also conducted to distinguish the effect of thermal and photolysis from photocatalysis. Procedure was identical to the control experiment for aeration in the presence of catalyst (Section 5.2.2). Less than 5 % reduction in MTBE and TEO-X concentrations was observed. MTBE does not adsorb on the catalyst surface (Sahle-Demessie et al., 2002a). MTBE is a slightly polar compound, which does not adsorb well onto any inorganic surface (Jacobs et al., 2001).

These control experiments demonstrated that aeration contributes to the reduction of TEO-X concentration while the effect of thermal, photolysis and adsorption is negligible.

### 5.3.2 Effect of Groundwater Constituents on MTBE Degradation

The effect of the presence of groundwater constituents on MTBE degradation is described under the respective parts (TEO-X, dissolved ions and a combination of both) followed by the discussions. Figure 5.5a-d shows the MTBE removal efficiency using Honeycomb II at various TEO-X and dissolved ion concentrations. The duration of every experiment was 8 hours except for a single pass flow study at HIHO ( $136.1 \text{ cm d}^{-1}$ ) of 5 hours; equivalent to one hydraulic residence time (HRT) cycle. It should be noted that one set of catalyst was used for each series of experiments: (i) organic, (ii) dissolved ion and (iii) a combination of these. The experiments were conducted as per the sequence in Figure 5.5d, starting from left to right. A reference test with MTBE only was conducted in the organic and dissolved ion series of experiments for comparison with the subsequent experiments in the respective series, as well as to demonstrate the reliability of different sets of catalyst.

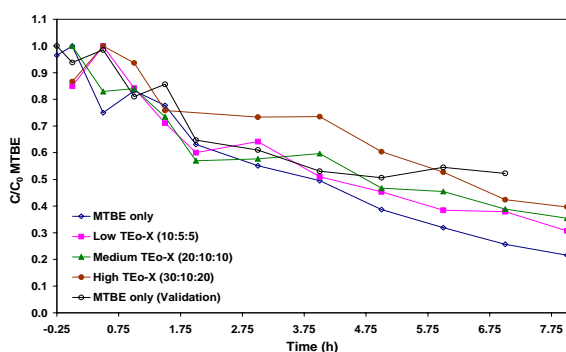


**Figure 5.5a** Variation of normalised MTBE concentration in the presence of TEO-X (refer to Table 5.1 for TEO-X concentrations)

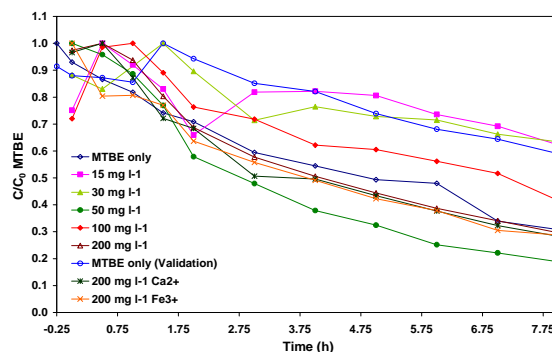


**Figure 5.5b** Variation of normalised MTBE concentration in the presence of dissolved ions (refer to Table 5.2 for ion concentrations)

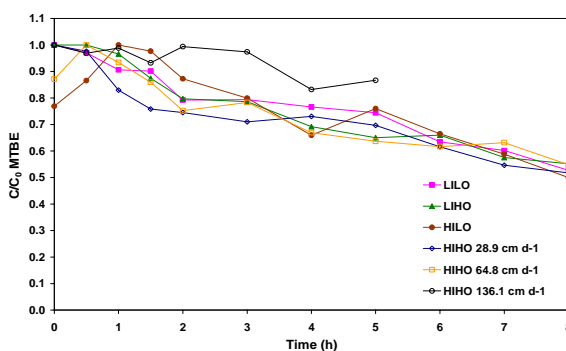


**Figure 5.5c** Variation of normalised MTBE concentration in the presence of both TEO-X and dissolved ions (refer to Table 5.3 for concentrations)

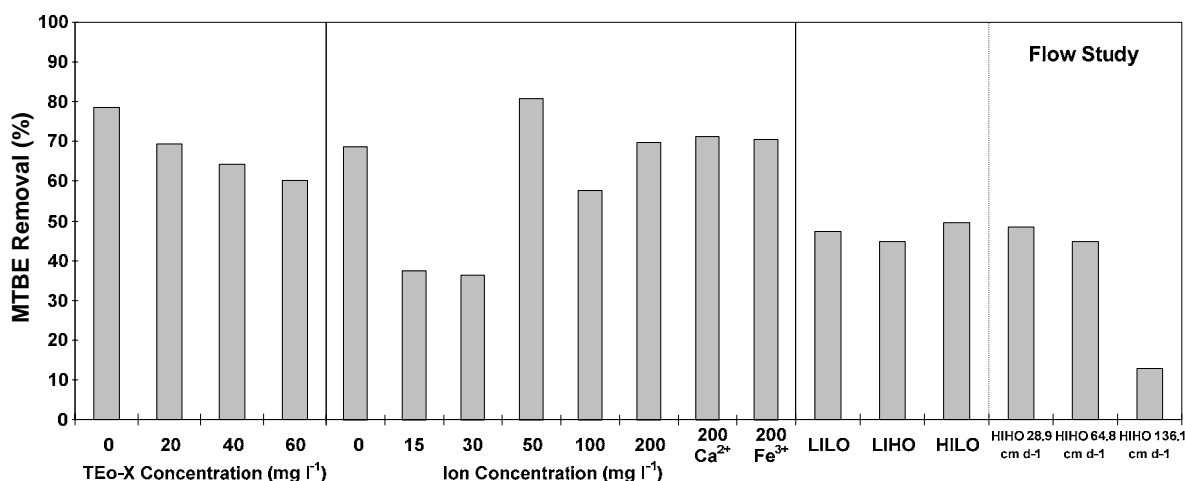


**Figure 5.5d** MTBE removal efficiency of Honeycomb II reactor in 8 hours batch ( $0 \text{ m d}^{-1}$ ) experiments (except for the last three are single pass flow experiments) at various TEO-X and dissolved ions concentrations. Low dissolved ions, low TEO-X (LILO), Low dissolved ions, high TEO-X (LIHO), High dissolved ions, low TEO-X (HILO), High dissolved ions, high TEO-X (HIHO).

### 5.3.2.1 Toluene, Ethylbenzene and o-Xylene (TEo-X)

Figure 5.5a shows that the MTBE removal efficiency decreased with decreasing MTBE:TEo-X ratio: 78.4 (80:0), 69.3 (80:20), 64.5 (80:40) and 60.3 (80:60) %. Higher TEo-X concentrations have more TEo-X molecules to compete with MTBE molecules for radicals (Sahle-Demessie et al., 2002b). The more strongly adsorbed TEo-X was degraded prior to MTBE, which agrees with Sahle-Demessie et al. (2002b); inhibiting the MTBE degradation (Figure 5.5d). Figure 5.6 confirmed that TEo-X up to a total of  $60 \text{ mg L}^{-1}$  was completely removed within 6 hours. Aeration alone removed about 89 % TEo-X ( $C_0 = 60 \text{ mg L}^{-1}$ ) in 8 hours (Figure 5.4). The difference in the TEo-X concentration between the control and photocatalytic experiment was attributed to photocatalytic degradation.

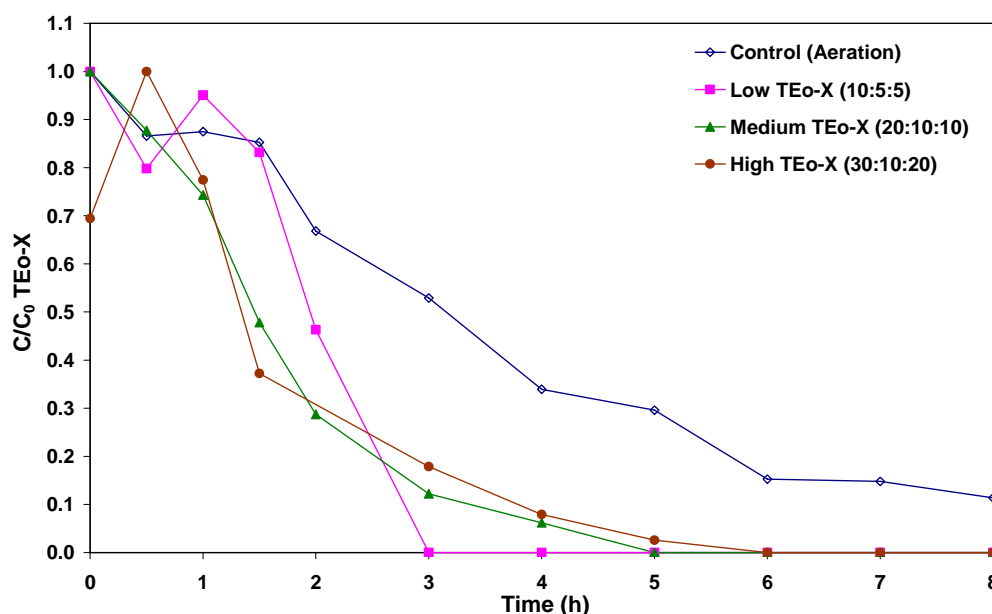


**Figure 5.6** Normalised TEo-X concentration during the control experiment for aeration and the PCO of MTBE at various TEo-X concentrations. The data was plotted with  $C_0$  being the maximum concentration, not necessarily at  $t = 0$ .

### 5.3.2.2 Cations and Anions

Figure 5.5b shows that the MTBE removal efficiency was significantly affected by dissolved ions at lower ion concentrations (up to  $30 \text{ mg L}^{-1}$ ). The MTBE removal efficiency decreased significantly to circa 35 % at ion concentrations of 15 and  $30 \text{ mg L}^{-1}$ . This is possibly because the effect of chloride ion on the PCO of MTBE appeared to be more dominant than that of iron. Chloride ion is known to reduce the number of OH radicals by blocking some of

the active sites on the catalyst surface (Sahle-Demessie et al., 2002b) and scavenging the OH radicals, in acidic conditions (Liao et al., 2001). Concurrently, there may be relatively insufficient  $Fe^{3+}$  for electron trapping on the catalyst surface to minimise electron-hole recombination in order to increase the rate of OH radical formation (Butler and Davis, 1993; Kabra et al., 2004).

At ion concentrations of  $50 \text{ mg L}^{-1}$  or greater, the MTBE removal efficiency remained between 58 and 81 %, which was comparable to that of the reference experiment ( $0 \text{ mg L}^{-1}$  ion) of about 70 %. The peaking of MTBE removal efficiency at ion concentration of  $50 \text{ mg L}^{-1}$  and the trend with increasing  $Fe^{3+}$  ion is consistent with Klauson et al. (2005), who found that the efficiency peaked at about  $55 \text{ mg L}^{-1}$ . A possible explanation is that sufficient  $Fe^{3+}$  was available for electron trapping at this concentration, minimising electron hole recombination and increasing the number of holes for the formation of hydroxyl radicals (Vamathevan et al., 2001). The catalyst surface appeared slightly yellowish brown, perhaps indicating some deposition of iron. The precipitation of  $Fe^{3+}$  in the reactor was minimal. Further increase in the ion concentration demonstrated a slight decrease in the MTBE removal efficiency than that at  $50 \text{ mg L}^{-1}$  (Figure 5.5d). This could be due to excessive  $Fe^{3+}$  ions, which could adsorb onto the  $TiO_2$  surface and scavenge photogenerated electrons to form  $Fe^{2+}$  (Eq. 5.5), which then competes for photogenerated holes (Eq. 5.6) resulting in a “short-circuit” phenomenon (Vamathevan et al., 2001; Klauson et al., 2005) and reducing OH radical formation.  $Fe^{2+}$  ion is not expected to be present as it tends to achieve its highest oxidation state,  $Fe^{3+}$ . Butler and Davis did not detect  $Fe^{2+}$  ion in their reactor.



Also iron can deposit on the catalyst (Figure 5.7a) and precipitate out of the bulk solution (Figure 5.7b), as  $Fe(OH)_3$  probably decreased the rate of PCO by reflecting UV illumination through increased solution opacity (Butler and Davis, 1993; Litter, 1999; Vamathevan et al., 2001). Figure 5.7a shows the deposition of iron on the catalyst surface after treatment of MTBE and  $200 \text{ mg L}^{-1} Fe^{3+}$ , contributing to the yellowish brown surface. The more intense yellowish brown “line” (Figure 5.7a) indicates mainly the adsorption of iron and minimal photocatalytic reaction as UVA light was blocked by the internal support from illuminating this part of the catalyst surface, showing the significance of UVA light in initiating the

photocatalytic reaction. The white catalyst surface indicates the active sites (Figure 5.7a). An energy-dispersive X-ray (EDX) spectroscopy analysis confirmed the presence of iron on the catalyst surface, while calcium was not detected. Figure 5.7b shows some yellowish brown particles in the column reactor, indicating precipitation of iron during the photocatalytic reaction. Both deposition and precipitation at  $200 \text{ mg L}^{-1} \text{ Fe}^{3+}$  were more significant than that observed at concentration of  $50 \text{ mg L}^{-1}$ , as may be expected. It should be noted that the deposition of  $\text{Fe}^{3+}$  was accumulated over seven experiments (Figure 5.5d).



**Figure 5.7a** Photo of catalyst after double pass flow experiment with HIHO. The yellowish brown area indicates the adsorption of iron on the catalyst while the white surface indicates active sites on the catalyst.



**Figure 5.7b** Plan view of the bottom of the reactor showing yellowish brown particles in the reactor, indicating precipitation of iron during the photocatalytic reaction

Figure 5.8 shows the variation of normalised iron concentration in the respective MTBE/dissolved ion experiments. Figure 5.8 indicates that the iron concentration is reduced during the experiments. Brown iron (III) hydroxide was also found deposited on the catalyst (Figure 5.7a) and deposited on the bottom of the reactor (Figure 5.7b). The iron concentration reduction typically ranged from 10 to 20 % after 8 hours except for the experiments with initial concentrations of 50 and  $200 \text{ mg L}^{-1} \text{ Fe}^{3+}$ , reduced by 40 %. No clear correlation between the reduction of iron concentration and the initial iron concentration (Figure 5.8) was observed possibly due to the reuse of catalyst, which had some iron adsorbed on the catalyst surface from preceding experiments (Figure 5.7a). This could possibly explain the steady MTBE removal efficiency in the subsequent dissolved ion experiments.

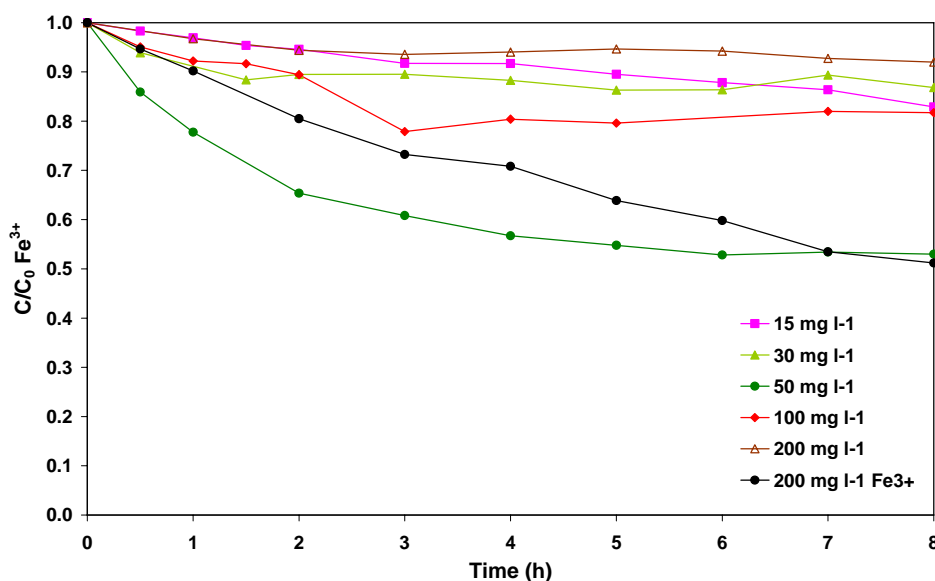


**Figure 5.8** Normalised iron concentration at various initial dissolved ion concentrations (refer to Table 5.2 for initial ion concentrations)

There was no significant change observed in the calcium, chloride and nitrate ions concentrations. Under these conditions, these ions are unlikely to undergo an oxidative or reductive process, owing to their high stability in terms of oxidation and reduction potential. In addition, the positively charged calcium ion is repelled from the catalyst surface, as the catalyst surface was positively charged at acidic pH (Wang et al., 2004; Herrmann et al., 2005). However, the negatively charged chloride ion is attracted to the surface and can screen the valence band holes generated on the catalyst surface, thus competing with the other oxidisable molecules.  $\text{NO}_3^-$  has little effect on photocatalysis (Kabra et al., 2004) as it is not hydrolysed as it is a strong acid and the central element, i.e. nitrogen, is at its maximum oxidation state (Herrmann, 2005).

Although the formation of radicals is not dependent on the pH, pH affects the adsorption of dissolved ions on the catalyst surface and OH scavenging for cations and anions, respectively. In other words, a photocatalytic reactor is not pH sensitive and can still operate without pH adjustment or chemical addition. However, its efficiency can be optimised with pH adjustment (Mehos and Turchi, 1993) and addition of certain transition metals. Mehos and Turchi (1993) found more than 5-fold increase in the TCE PCO rate constant when the pH of contaminated groundwater was adjusted from 7 to 5. Liao et al. (2001) suggested that the adjustment of pH is more effective than the removal of chloride ion in order to optimise the reactor efficiency. This indicates that pH adjustment and presence of transition metals can enhance the efficiency of the photocatalytic reactor proposed in this research.

Nevertheless, process optimisation of the reactor is not among the scope of this research as it is still in the initial development phase, in which evidence to demonstrate the feasibility of the proposed reactor for in-situ groundwater remediation is essential. The process optimisation operation incurs additional costs and requires careful control of pH level and/or metal ion concentration to avoid inhibition.

### 5.3.2.3 Combination of TEO-X and Dissolved Ions

Figure 5.5d showed that there was no significant change in the MTBE removal efficiency, which maintained circa 50 % MTBE removal, despite the variation of TEO-X and dissolved ion concentrations in the 8 hours batch experiments, and 28.9 and 64.8 cm d<sup>-1</sup> single pass flow experiments.

The effect of chloride ion in LILO and LIHO and beneficial effect of iron in HILO and HIHO could have been dampened by the presence of TEO-X molecules to compete for the radicals. Figure 5.9 shows the normalised concentration of TEO-X during the PCO of MTBE at various organic compound and dissolved ion concentrations. The presence of dissolved ions also inhibited TEO-X degradation as it typically achieved more than 90 % after 8 hours of experiment compared to complete removal in 6 hours (Figure 5.4). The removal efficiency of TEO-X was rapid in HILO, which could be due to both low TEO-X concentration and the beneficial effect of iron. The higher TEO-X removal efficiency in HILO than that of HIHO was due to the high initial concentration of organic compound (Mills et al., 1993).

Dissolved ions appears to have greater impact on the MTBE degradation than TEO-X because (i) ionic concentration is not affected by aeration, (ii) they can adsorb on the catalyst surface and deactivate the active sites (Butler and Davis, 1993; Sahle-Demessie et al., 2002b) and (iii) they are able to scavenge OH radicals (Litter, 1999; Liao et al., 2001).

Although the photocatalytic mechanism (Section 2.1.1) has been well accepted, there are, however, some exceptions such as (i) a contaminant molecule, i.e. MTBE, can be oxidised by OH radicals on the catalyst surface or its vicinity, thus, does not necessarily appear to be adsorbed on the catalyst surface prior to oxidation by valance band holes with oxidation potential about 1.15 times greater than that of OH radical (Klauson et al., 2005), and (ii) some products do not necessarily desorb after the reaction, as observed in the case of iron and methylene blue (MB). The adsorption of contaminants onto the catalyst surface deactivates some active sites, which can deteriorate the efficiency of the catalyst in the long term. In the case of MTBE, the MTBE molecules can be oxidised in the vicinity of the catalyst surface, where the concentration of radicals is likely to be greater. This could also explain the precipitation of iron oxides at the bottom of the reactor at the end of the

experiments in this study and rapid corrosion of metal components in Honeycomb I in Section 4.4.2. The PCO rate of a contaminant depends on the contact frequency of contaminant molecules and radicals, which is governed by the agitation from aeration. In the case of iron and MB, some adsorption on the catalyst did not desorb due to the strong adsorption of the molecules. In short, while many suggested that adsorption process occurs prior to degradation of contaminant molecules, the possibility of contaminant molecules being degraded by radicals in the vicinity of the catalyst surface should not be ruled out.

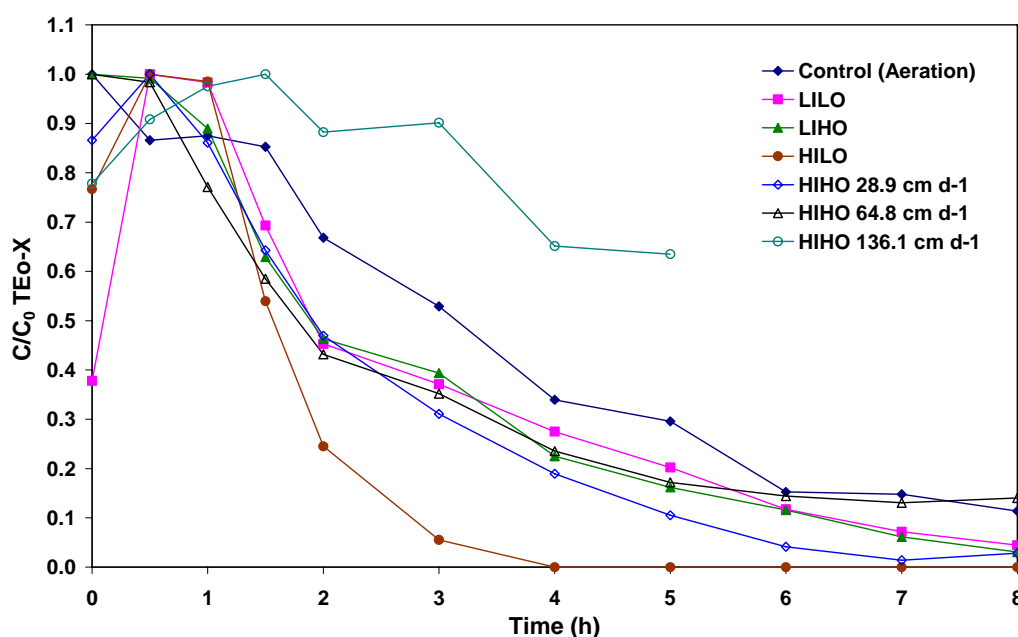


**Figure 5.9** Normalised concentration of TEO-X during the photocatalytic degradation of MTBE at various organic compound and dissolved ion concentrations. The data was plotted with  $C_0$  being the maximum concentration, not necessarily at  $t = 0$ .

### 5.3.3 Single Pass Flow Study

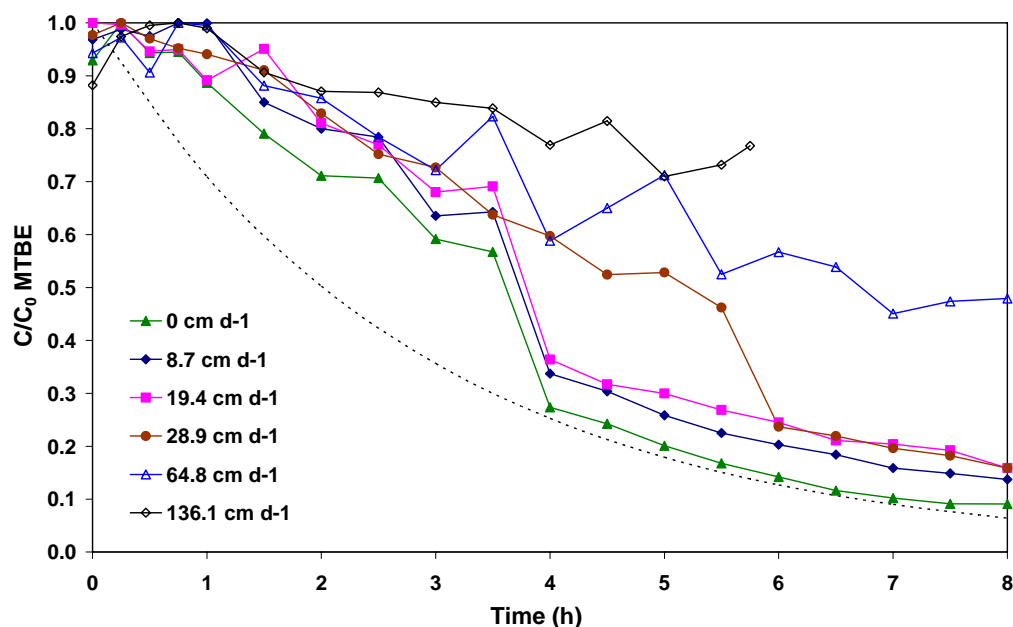
#### 5.3.3.1 MTBE only

Figure 5.10 shows the MTBE degradation by Honeycomb II with the solution flowing once through the reactor at various velocities up to  $136.1 \text{ cm d}^{-1}$ . The MTBE removal at velocities below  $28.9 \text{ cm d}^{-1}$  was higher than 84 % while the efficiency declined significantly at velocities of  $64.8$  and  $136.1 \text{ cm d}^{-1}$ , showing 52 and 27 % MTBE removal, respectively. It required about 8 hours to degrade 91 % MTBE in the batch experiment. It was more than the 67 % removal obtained at 8<sup>th</sup> hour using a 15 W UVA lamp and  $\text{TiO}_2$  coated on inner wall of a 48 mm diameter glass cylinder (Chan, 2005). Sahle-Demessie et al. (2002a) obtained about 99.8, 75.9 and 59.2 % MTBE removal for initial MTBE concentrations of 100, 500 and

925  $\mu\text{g L}^{-1}$ , after 5 hours solar illumination ( $1.6\text{-}2.9 \text{ mW cm}^{-2}$ ) on a 500 mL Pyrex flask filled with  $0.05 \text{ g L}^{-1}$   $\text{TiO}_2$  slurry. This is comparable to the 79.9 % removal at the 5<sup>th</sup> hour in the batch experiment using Honeycomb II, illuminated at  $0.9 \text{ mW cm}^{-2}$ . This is to show that the efficiency of Honeycomb II was relatively comparable to that of a slurry reactor.

Unlike MB degradation, the MTBE degradation exhibited a sudden dip in the concentration especially at velocities below  $28.9 \text{ cm d}^{-1}$ . The drop was observed at the 4<sup>th</sup> and 6<sup>th</sup> hour of experiments conducted at velocities below  $19.4 \text{ cm d}^{-1}$  and at  $28.9 \text{ cm d}^{-1}$ , respectively (Figure 5.10). This phenomenon was also observed in the MTBE degradation using  $0.05 \text{ g L}^{-1}$   $\text{TiO}_2$  slurry (Sahle-Demessie et al., 2002a). The reason for this sudden dip is unknown, nevertheless, the photocatalytic degradation of MTBE still conforms well to the pseudo first order kinetics with  $R^2$  typically beyond 0.9 (Table 5.5).

The single pass flow study also demonstrated that the MTBE concentration in the column reactor stabilised within a residence time cycle, similar to MB degradation. The MTBE concentration stabilised at the 7<sup>th</sup> and 4<sup>th</sup> hour of the experiments conducted at velocities of  $64.8$  and  $136.1 \text{ cm d}^{-1}$ , respectively. It should also be noted that the solution flows through the reactor once, which makes it different from other studies (Almquist et al., 2003; Chan and Lynch, 2003a and b).



**Figure 5.10** MTBE degradation by Honeycomb II at various velocities. The data was plotted with  $C_0$  being the maximum concentration, not necessarily at  $t = 0$ . The dotted exponential decay curve was calculated using Eq. 2.3, with  $k$  of  $0.344 \text{ h}^{-1}$  (Table 5.5), fitted to the experimental data ( $0 \text{ cm d}^{-1}$ ), confirming the PCO of MTBE is a pseudo first order process.

### 5.3.3.2 MTBE, TEO-X and Dissolved Ions

Figure 5.5c shows that the MTBE removal efficiency remained circa 50 % in 8 hour batch experiments despite the variation of TEO-X and dissolved ion concentrations. There was not much decrease in the reactor efficiency in the presence of both TEO-X and dissolved ions at 28.9 and 64.8 cm d<sup>-1</sup>, showing about 50 and 45 % MTBE removal, respectively. When the velocity was increased to 136.1 cm d<sup>-1</sup>, the efficiency decreased significantly to about 13 % (Figure 5.5d).

### 5.3.4 Relationship between Reactor Efficiency and Flow

From the engineers' perspective, a plot showing the relationship between the reactor efficiency and flow will be useful especially during the maintenance of reactor on site; to check if the reactor is performing well. This is because groundwater flow can be obtained instantaneously on site and the geochemistry on site would be relatively consistent. In hydrogeological studies, the groundwater flow is obtained on site in terms of average velocity. Therefore, the reactor efficiency is reported with respect to the equivalent "groundwater" velocity and HRT.

#### 5.3.4.1 Velocity

Figure 5.11 shows the effect of groundwater velocity on the MTBE removal efficiency of the column reactor. The percentage removal for MTBE refers to the MTBE concentration at the end of the respective experiments (Figure 5.10). In the case of MB, the percentage removal refers to the MB concentration removed at which MB concentration stabilised in the respective experiments (Figure 4.15). MTBE concentration declined linearly with increasing velocities. A similar trend was found with MB. Despite having different adsorption behaviour, the removal efficiencies of both compounds decreased linearly at similar rate (Figure 5.11).

The removal efficiency of MB was consistently slightly higher than that of MTBE. This is mainly due to the longer experimental duration for MB flow experiments (typically one HRT cycle) than that for MTBE flow experiments (limited up to 8 hours only – before MTBE concentration stabilised). The reactor efficiency for both compounds decreased to circa 25 % removal when the velocity was increased to 136.1 cm d<sup>-1</sup> (Figure 5.11). In view of this, photocatalytic reactor designs for water treatment are typically intensified to accommodate high flows, which are of several orders of magnitude higher than that of groundwater (Ray and Beenackers, 1998a; van Gerven et al., 2007). However, it should be noted that this

reactor is configured for in-situ remediation of groundwater, which typically has flows in the lower range of velocities tested in this study.

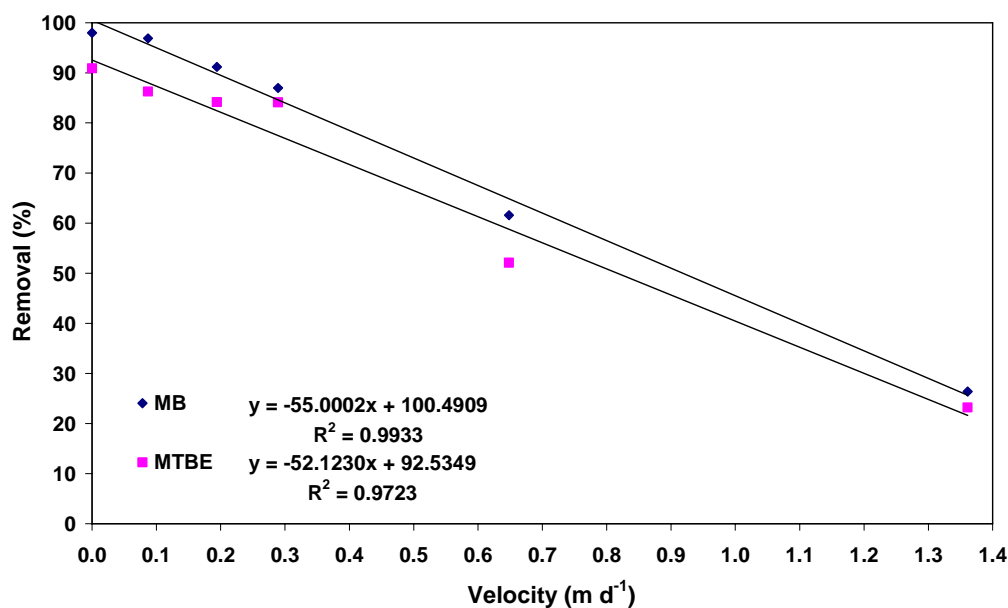


**Figure 5.11** Effect of flow on the column reactor efficiency in degrading MB and MTBE at various velocities

Table 5.5 shows the PCO rate constants of MB and MTBE during the linear phase of every experiment at various velocities. All the experiments were conducted using the same set of catalyst in the order of the velocities listed in Table 5.5, except for the double pass flow experiment using new catalyst. The initial concentrations of MB and MTBE were 10 and 80 mg L<sup>-1</sup>, respectively. MB PCO rate constants were slightly higher than that of MTBE at the same velocity. The MTBE PCO rate constants of Honeycomb II were higher than 0.24 h<sup>-1</sup> at velocities slower than 28.9 cm d<sup>-1</sup> but were significantly lower at velocities of 64.8 and 136.1 cm d<sup>-1</sup>, yielding 0.101 and 0.051 h<sup>-1</sup>, respectively. The batch experiment (0 cm d<sup>-1</sup>) yielded a MTBE rate constant of 0.344 h<sup>-1</sup> which was more than 3-fold that of 0.107 h<sup>-1</sup> obtained by Chan (2005).

**Table 5.5** PCO rate constants of MB and MTBE using column reactor at various velocities in 8 hours experiments, except for 64.8 and 136.1 cm d<sup>-1</sup>

Average Velocity, $v_D$ (cm d <sup>-1</sup> )	MB PCO Rate Constant, $k_{MB}$ (h <sup>-1</sup> ) (Section 4.4.5)	R <sup>2</sup>	MTBE PCO Rate Constant, $k_{MTBE}$ (h <sup>-1</sup> )	R <sup>2</sup>	MTBE/MB PCO rate constants ratio
0	0.388	0.994	0.344	0.962	0.887
8.7	0.360	0.973	0.285	0.958	0.792
19.4	0.285	0.987	0.253	0.953	0.888
28.9	0.251	0.979	0.237	0.915	0.944
64.8	0.224	0.977	0.101	0.918	0.451
136.1	0.166	0.970	0.051	0.822	0.307
28.9 (1 <sup>st</sup> Pass of Double Pass - Used Catalyst)			0.102	0.978	-
28.9 (2 <sup>nd</sup> Pass of Double Pass - Used Catalyst)			0.137	0.906	-
28.9 (1 <sup>st</sup> Pass of Double Pass - New Catalyst)			0.235	0.949	-
28.9 (2 <sup>nd</sup> Pass of Double Pass - New Catalyst)			0.247	0.899	-

The MTBE/MB PCO rate constants ratios were reasonably consistent at velocities up to 28.9 cm d<sup>-1</sup>, but were significantly lower at velocities of 64.8 and 136.1 cm d<sup>-1</sup>. This is expected due to the shorter HRT with increasing velocity. As the MB PCO rate constant is affected by the adsorption coefficient of MB molecules on the catalyst surface (Matthews, 1989; Mills et al., 1993; Herrmann, 2005), the decrease in the MTBE/MB PCO rate constant ratios at higher velocities may indicate that the PCO of MTBE is dependent on the contact time of MTBE molecules with the radicals in the vicinity of the catalyst surface. This is because MTBE does not adsorb onto the catalyst surface, therefore, it is probably that the MTBE molecules are oxidised by radicals in the vicinity of the catalyst surface. The presence of highly reactive free radicals is also a possible reason for the corrosion of mild steel in Honeycomb I.

The fourth single pass flow experiment with used catalyst and the first pass of the double pass flow experiment using new catalyst at 28.9 cm d<sup>-1</sup> (lines 4 and 9 in Table 5.5) yielded similar MTBE PCO rate constants. This increases confidence in the reliability of the catalyst immobilisation procedure and reproducibility of the catalyst performance.

#### 5.3.4.2 Hydraulic Residence Time (HRT)

It is apparent in Figure 5.10 that there was a significant reduction in MTBE removal efficiency above a certain velocity. As it is not possible to determine the critical flow from Figure 5.11, there is a need to determine the critical flow using the HRT (Eq. 2.26). Figure 5.12 shows the response of column reactor efficiency in degrading MB and MTBE with increasing HRT. Both showed similar response and a critical HRT of 1 day. There was no significant improvement in the removal efficiency for MB and MTBE beyond 1 day HRT. In the presence of both TEO-X and dissolved ions, the variation of MTBE removal efficiency of

Honeycomb II at various HRT was similar to that obtained with MTBE only, only at lower removal efficiencies. The critical HRT is likely to be 1 day. This indicates that the response of MTBE removal efficiency towards HRT is generic. Similar to MTBE, the increased groundwater velocity showed detrimental effects on the TEO-X removal efficiency.

It appears that the removal efficiency of the reactor for MB and MTBE is similar despite the different adsorption behaviour of both compounds on  $\text{TiO}_2$  surface. This implies that the photocatalytic reaction does not necessarily occur on the catalyst surface only and that the radicals generated can oxidise compounds away from the catalyst surface, in the case of MTBE. This is also a possible explanation for the corrosion of mild steel components of Honeycomb I observed in Figure 4.10 and 4.11. It is believed that the relationship of removal efficiency and HRT (Figure 5.12) is generic for the degradation of organic compounds and can assist in the reactor design process by indicating a maximum practical linear velocity.

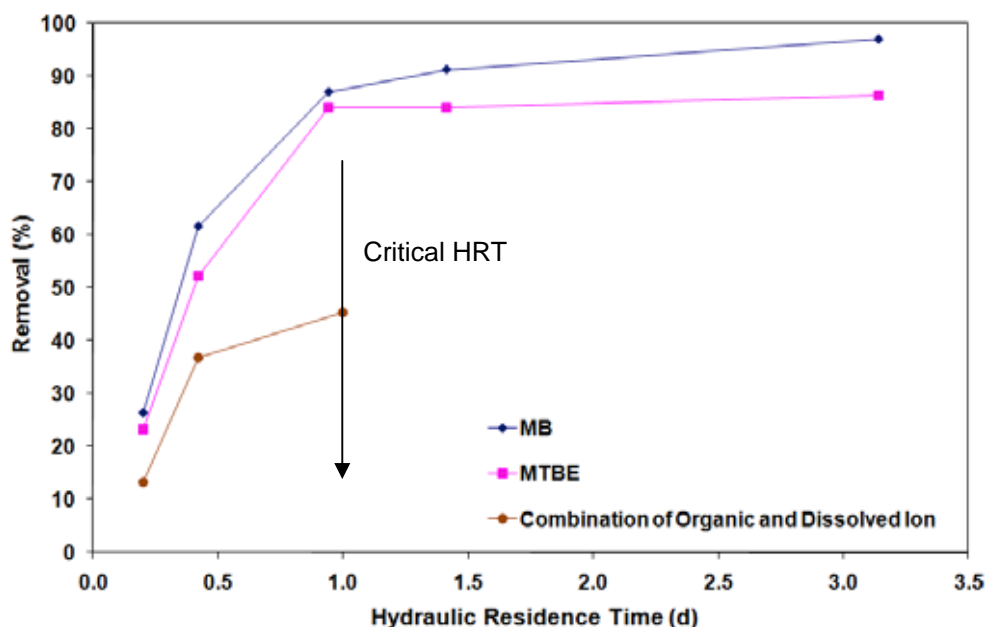


**Figure 5.12** The variation of Honeycomb II reactor efficiency in degrading MB, MTBE only and MTBE in the presence of TEO-X and dissolved ions at various HRT

As the critical HRT was 1 day, the corresponding velocity of  $28.9 \text{ cm d}^{-1}$  was used in the double pass flow study.

### 5.3.5 Double Pass Flow Study

Figure 5.13 shows the normalised MTBE concentration results for all the double pass flow experiments conducted in this study. Figure 5.13 shows the reduction in MTBE concentration using new and old catalysts in the double pass flow experiment conducted at a velocity of  $28.9 \text{ cm d}^{-1}$ , which is assumed equivalent to 1 day HRT per pass. Both new and used catalyst achieved more than 95 % MTBE removal after flowing through a series of two Honeycomb II modules in 48 hours. Table 5.5 shows that the MTBE PCO rate constants in the second pass were higher than in the first pass for both catalysts. This agrees with the fact that the PCO rate constant of a contaminant increases with decreasing initial concentrations (Matthews, 1989). The used catalyst removed 63 and 70 % MTBE in the first and second pass, respectively. The overall MTBE degradation estimated using sequential order (Eq. 5.1) was 89 %, which was lower than the experimental measurement of 95.7 %. The new catalyst removed 84 % MTBE in both passes, yielding an estimate of 97.4 %, which was similar to the experimental measurement of 97.6 %. This indicates the efficiency of a series of the modules can be estimated using sequential order (Eq. 5.1).

The new catalyst exhibited a steeper exponential curve, implying faster MTBE degradation for the specific times, compared to that of the used catalyst. The MTBE concentration stabilised faster using the new photocatalyst (Figure 5.13). Although the MTBE PCO rate constant of the used photocatalyst was less than half to that of the new catalyst (Table 5.5), its MTBE removal was only about 19 % less than that of the new catalyst at the end of first pass. This agrees with the previous suggestion that it is more important to look at the removal efficiency below the critical HRT rather than only the PCO rate constant.

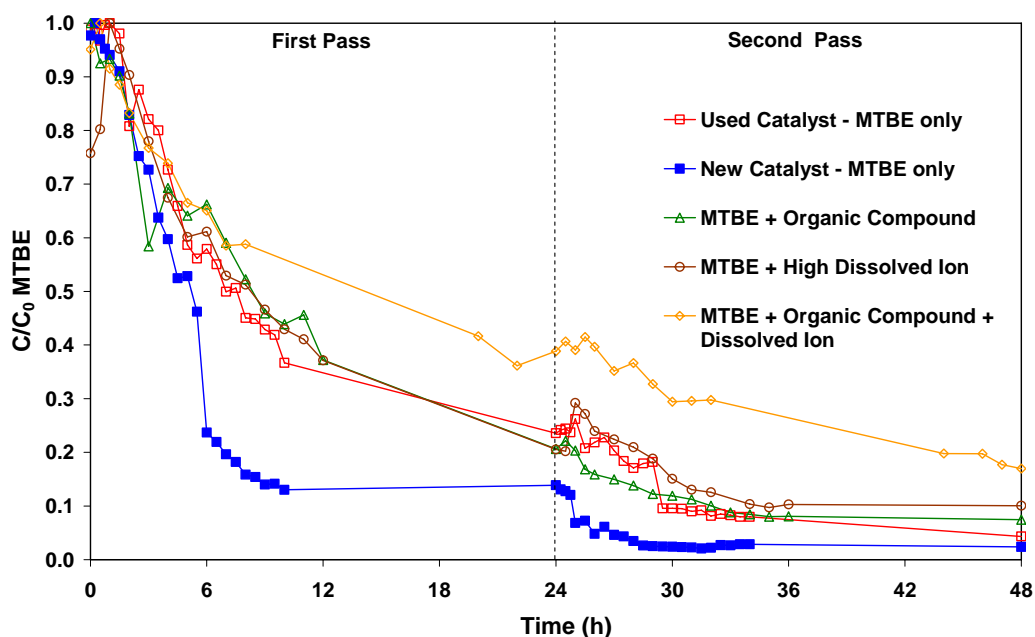


**Figure 5.13** Normalised MTBE concentration in all the double pass flow experiments, with two (new and used catalyst) in the presence of MTBE only. All the catalysts used in the double pass flow experiments are used catalysts except for the one specified new catalyst.

The MTBE removal efficiency in the presence of TEO-X or dissolved ion was comparable to that of the used catalyst in degrading MTBE only, showing more than 90 % MTBE removal after two passes in 48 hours. In all the experiments with TEO-X, the TEO-X concentration was depleted by the ninth hour in each pass (Figure 5.14). There was no decline in all the dissolved ion concentrations except for iron of about 9 and 24 % for dissolved ion and combined TEO-X and dissolved ions, respectively. In the presence of both TEO-X and dissolved ions, the reactor efficiency decreased to 80 % after two passes (Figure 5.13). This demonstrated that the reactor can still function in the presence of both organic compounds and dissolved ions, although the reactor efficiency was slightly inhibited. Perhaps the performance can be enhanced via process optimisation or pre-treatment by removing ions prior to the reactor.

Figure 5.14 shows the normalised concentrations of MTBE and TEO-X in the MTBE/TEO-X double pass flow experiment. The toluene:ethylbenzene:o-xylene concentrations used were 30:10:20 mg L<sup>-1</sup>. It appears that the TEO-X was completely depleted by the ninth hour in the first pass and fifth hour in the second pass. The TEO-X concentration depleted faster in the second pass due to the significantly lower concentration and dilution in the reactor. The MTBE removal efficiency at the 12<sup>th</sup> hour of first and second pass was approximately 62.8 and 63.5 (of about 0.2  $C/C_0$  MTBE at the beginning of second pass) %, respectively. This

indicated that the efficiency of the immobilised  $\text{TiO}_2$  was consistent, after 6 consecutive days of application. The total MTBE removal efficiency after two passes was circa 92.5 %, which is slightly higher than the estimated 87 % from sequential order.

In the presence of dissolved ions, about 90 % MTBE removal was achieved in the double pass flow experiment. The pH shifted from 2.8 to 4.5 within the 48 hours.

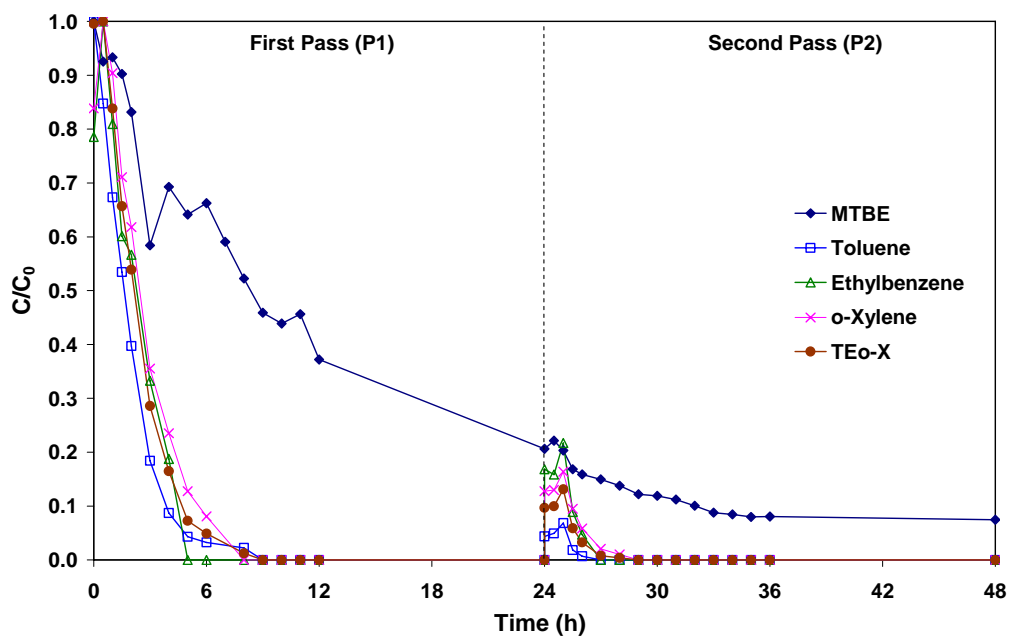


**Figure 5.14** Normalised concentrations of MTBE and TEO-X in the double pass flow experiment for organic study. The MTBE:toluene:ethylbenzene:o-xylene concentrations applied were 80:30:10:20  $\text{mg L}^{-1}$ .

### 5.3.6 Catalyst Surface Observation

Similar to the MB experiments, scanning electron microscope (SEM) images did not show any visible physical change on the catalyst surface after treatment (Figure 5.15b) compared to the pristine catalyst surface (Figure 3.27c). Therefore, lower magnification optical microscopic images were obtained to observe the changes on the catalyst surface. Unlike the immobilised catalyst surface after MB treatment (Figure 3.30b), there was no colour change on the immobilised catalyst surface after MTBE treatment (Figure 5.15a) because MTBE is colourless and does not adsorb to the catalyst surface. Figure 3.31 shows the white pristine immobilised catalyst surface.



**Figure 5.15a** Microscopic image of catalyst surface after MTBE degradation

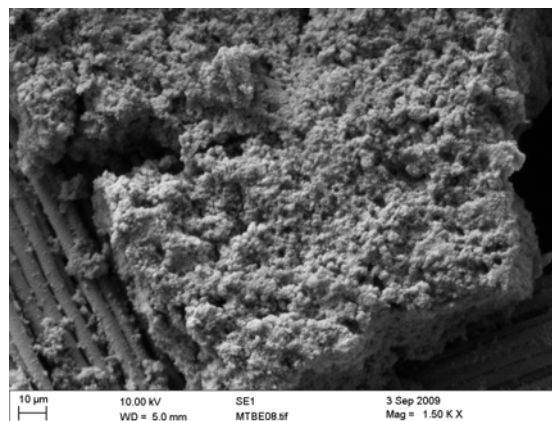


**Figure 5.15b** SEM image of catalyst surface after MTBE degradation

The microscopic image did not show any colour change on the catalyst surface after the series of MTBE/TEo-X treatment (Figure 5.16). Similar to experiments using MB, iron adsorbed onto the catalyst surface, contributed to the yellowish brown on the catalyst surface (Figure 5.17 and 5.18a). EDX spectroscopy analysis detected only iron on the catalyst surface for the catalysts used in the dissolved ion and combined organic and dissolved ion studies. SEM image (Figure 5.18b) did not show any visible physical changes on the catalyst surface after MTBE degradation in the presence of TEO-X and dissolved ions, compared to the pristine catalyst surface. This was the same case for all the other used catalysts.



**Figure 5.16** Microscopic image showing the catalyst surface after degradation of organic compounds, i.e. MTBE and TEO-X

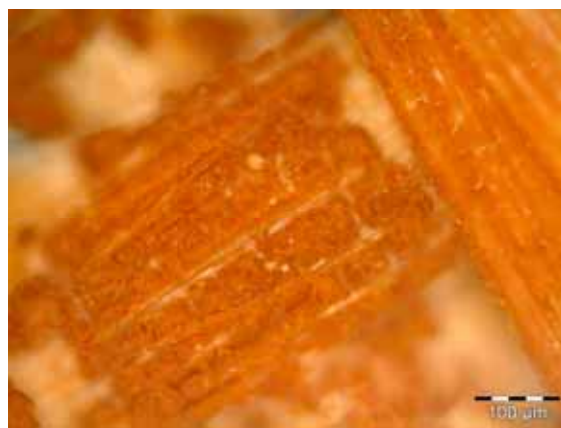


**Figure 5.17** Microscopic image showing the catalyst surface was yellowish brown, indicating iron was concentrated on the catalyst surface instead of the fibreglass, after the PCO of MTBE in the presence of dissolved ions.



**Figure 5.18a** Microscopic image showing that the catalyst surface was yellowish brown after HIHO experiments

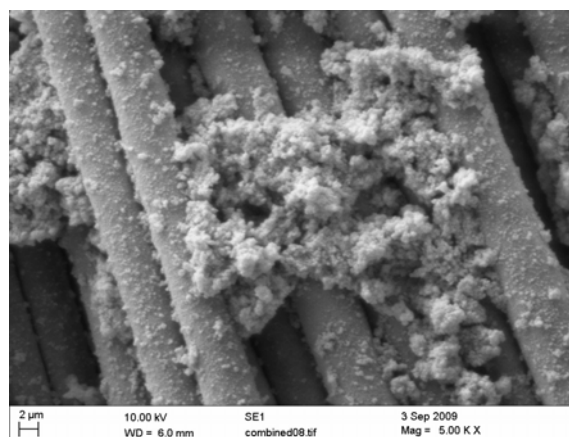


**Figure 5.18b** SEM image of the catalyst surface after double pass flow experiment with HIHO

## 5.4 Conclusions

The proposed photocatalytic reactor design removed MTBE effectively, achieving more than 84 % removal within 8 hours of experiment at velocities slower than  $28.9 \text{ cm d}^{-1}$ . The inferences were made as follows:

(i) MTBE vapourisation appears to vary proportionally to the air flow to volume ratio tested. Nevertheless, it is also affected by the D/H ratio of the reactor as well as the ambient air pressure and temperature.

(ii) Flow variation showed that the MTBE removal efficiency decreased linearly with increasing velocity. The critical HRT for both MTBE and MB is 1 day. The response of MTBE and MB removal efficiency of the reactor towards flow variations were similar despite the contrasting properties of both compounds.

(iii) Both new and used catalysts achieved more than 95 % MTBE removal after two passes in 48 hours. The double pass flow study showed that the clean-up by a series of modules can be estimated via sequential order of the removal efficiency of one pass obtained in the laboratory. This reinforces its potential for in-situ groundwater remediation of MTBE.

In the presence of TEO-X and dissolved ions, Honeycomb II generally demonstrated acceptable MTBE removal efficiencies without any process optimisation measures. In general, the MTBE PCO rate was inhibited by the OH radical scavenging by chloride ion, competition for OH radical and deactivation of active sites by other constituents. The inferences were made as follows:

(i) Organics: The MTBE removal efficiency decreased with increasing TEO-X concentration, due to the competition for OH radicals between MTBE and TEO-X molecules. The PCO of the more strongly adsorbed TEO-X inhibited the PCO of MTBE.

(ii) Dissolved ions: The MTBE removal efficiency was significantly affected by the effect of chloride ion at ion concentrations of 15 and  $30 \text{ mg L}^{-1}$ . The MTBE PCO removal efficiency peaked at iron concentration of  $50 \text{ mg L}^{-1}$ . The concentrations of calcium, chloride and nitrate ions did not change due to their high stability in terms of oxidation and reduction potential. Iron concentration reduced due to the deposition on the catalyst surface and precipitation in the solution as  $\text{Fe}(\text{OH})_3$ .

(iii) Combined organics and inorganics: It is believed that the presence of dissolved ions has more significant impact on the PCO of MTBE than that of organic constituents, as ions are more active in OH radical scavenging and deactivation of active sites, besides remaining unaffected by aeration.

(iv) Single pass flow study: The single pass flow study showed that the variation of MTBE removal efficiency of Honeycomb II with flow, in the presence of TEO-X and dissolved ions, was similar to that obtained in degrading MTBE only, except that the reactor efficiencies were lower.

(v) Double pass flow study: Passing contaminated water twice through the reactor can still degrade MTBE in the presence of TEO-X and dissolved ions, without process optimisation measures such as pH adjustment or chemical addition. This reinforces the potential of Honeycomb reactor design for in-situ groundwater remediation of MTBE.

The promising results in this chapter demonstrated the feasibility of the proposed photocatalytic reactor design for in-situ groundwater remediation. This led to the testing of the reactor at the proposed actual scale in sand tank experiments in the laboratory, simulating the clean-up of a MTBE plume in groundwater, presented in Chapter 6.

## **CHAPTER 6**

# **EVALUATION OF HONEYCOMB I PROTOTYPE IN A SAND TANK**

### **6.0 Overview**

Chapter 5 demonstrated the feasibility of using a Honeycomb I model for the in-situ attenuation of MTBE in a column reactor. In this chapter, a scaled up Honeycomb I prototype (a 22 cm horizontal segment of the proposed field scale diameter) was fabricated and evaluated for its performance in attenuating a MTBE plume, simulated at various migration velocities in a laboratory sand tank. The results and discussions in the sand tank experiments were presented based on the experimental phases, which includes observations on the plume migration in the sand chamber, effect of aeration and the MTBE removal by photocatalysis. It also involves a sand tank experiment in the presence of organic compounds; to observe its effect on the attenuation of MTBE by Honeycomb I. The later sections of this chapter encompasses the comparison of the reactor performance of different scales, as well as the discussion on the cumulative performance and observations of Honeycomb I prototype.

## 6.1 Introduction

A model of the proposed photocatalytic reactor design, Honeycomb I, has demonstrated its potential for in-situ MTBE attenuation in Chapter 5. In this study, Honeycomb I was scaled up from 100 mm i.d. to 200 mm i.d. (field scale dimension) in longitudinal direction. The depth of the tank, 0.3 m, is much less than the expected field scale depth (2 m). This modular scale up study is intended to validate the efficiency of an actual field scale photocatalytic reactor design in an emulated field condition by testing an individual (horizontal) segment of a photocatalytic reactor system in a sand tank.

The study was designed to emulate field conditions and simulate the in-situ clean-up of MTBE plume using an immobilised  $\text{TiO}_2$  reactor (Figure 6.1a), under controlled conditions. The concept of the sand tank experiment is similar to transferring a section of homogeneous soil from a site to a sand tank and testing in the laboratory. The sand tank represents a horizontal (22 cm) slice of the full scale reactor, which can be as deep as 2 m. This is useful for testing a new reactor design because it is (i) more economical to evaluate in smaller experimental dimension (a horizontal segment of the full scale module), (ii) difficult to obtain a well characterised site in terms of hydrogeology, and (iii) manageable experimental parameters and shorter experimental duration allows variation of experiments. In this study, the MTBE plume is simulated by injecting MTBE into the tank to emulate a leakage from underground storage tank. The objective of generating an MTBE plume is to test the clean-up process, rather than to examine the plume itself in detail. The plume behaviour in the sand tank is constricted by the tank, but it still provides a reasonably realistic clean-up test. The velocities applied in this study were based on an extensive hydrogeological study at Borden Air Force Base, Canada, which yielded an average linear groundwater velocity of  $9 \text{ cm d}^{-1}$  (Mackay et al., 1986).

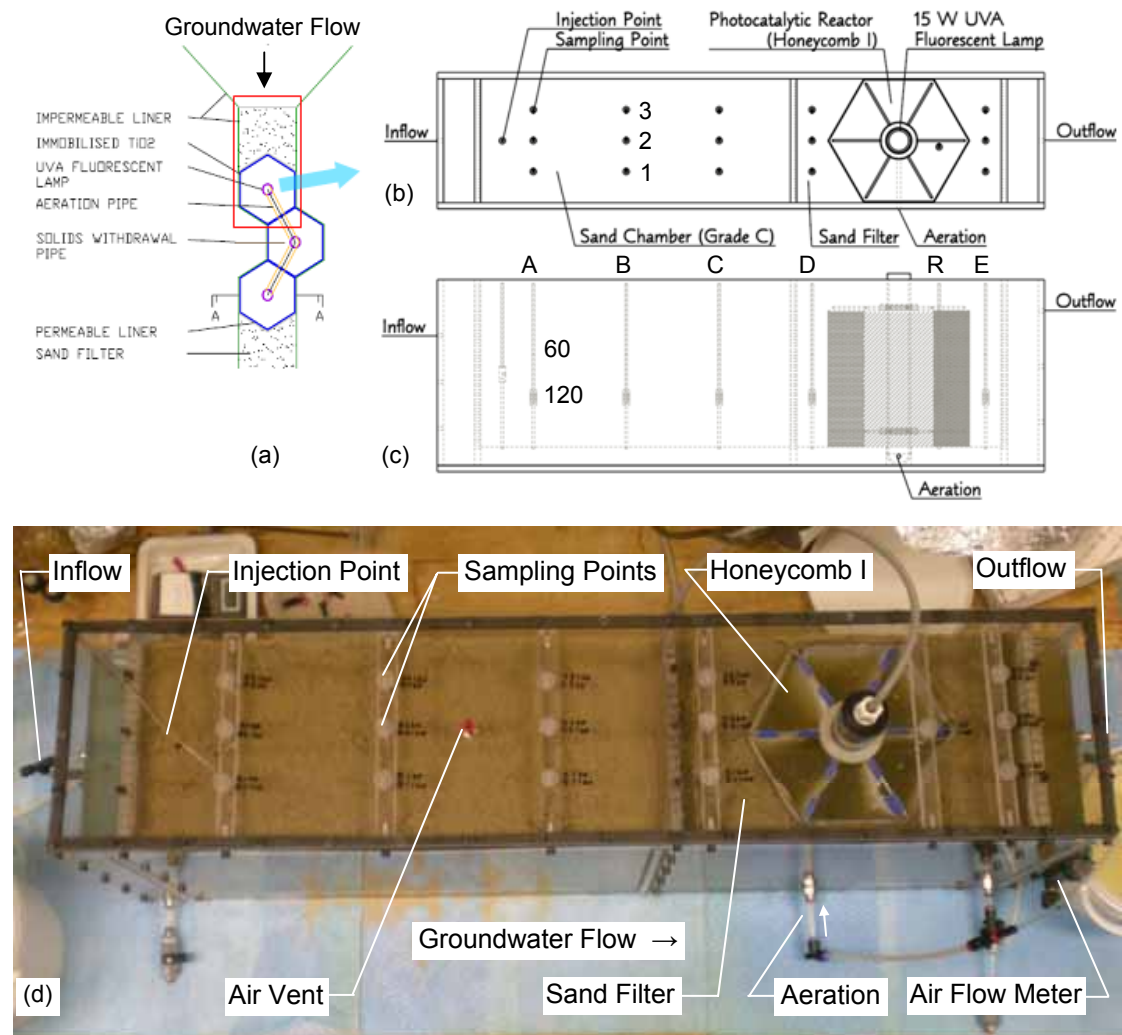


**Figure 6.1** (a) Plan view of intended application on site showing how hexagonal units can be linked together in series to achieve the required clean-up level, (b) plan view of the sand tank, which examines the clean-up using a single hexagonal unit (Honeycomb I), (c) side view of the sand tank showing the inflow and outflow chambers, sampling points and reactor, and (d) photo showing the plan view of the sand tank after installation and the location of sampling points.

## 6.2 Experimental Arrangement

### 6.2.1 Setup of Sand Tank Experiment

The laboratory scale sand tank (Figure 6.1b-d) has a dimension of 980 mm (L) x 200 mm (W) x 305 mm (H), where the effective lengths are 500 mm and 330 mm for sand and reactor chambers, respectively. The groundwater depth is about 220 mm. The tank width of 200 mm is the same as the photocatalytic reactor width. The sand tank consists of an inlet chamber, sand chamber, reactor chamber and outlet chamber. The chambers are partitioned by 10 mm thick Perspex drilled with 5 mm diameter holes at 10 mm (c/c) spacing

and lined with 60  $\mu\text{m}$  stainless steel mesh on the side facing the sand. The inflow chamber was filled with only deaired deionised water to (i) provide uniform flow across the section area of the tank, (ii) prevent possible air trapped in the inlet tube from entering and trapped in the sand chamber and (iii) allow settlement of any particles which might clog the screen or mesh partition. The sand chamber allows the plume to develop in a leaking tank simulation. The reactor chamber, with partitions acting as the walls of a trench, contains sheets of woven fibreglass impregnated with titanium dioxide (Section 3.2.1.2), illuminated by a 15 W Philips Cleo UVA fluorescent lamp (Honeycomb I). The space around Honeycomb I was filled with Grade 'C' sand (Table 6.2), which functions as a sand filter to minimise turbidity in the reactor by preventing fine particles from entering the reactor. The outlet chamber maintains the groundwater level and equalises the flow. The flow through the tank is controlled by the difference in hydraulic head between inlet and outlet chambers. When used for MTBE removal, the tank was covered by a 10 mm thick Perspex lid and the sampling points were sealed using PTFE sheets to prevent emission of MTBE via vaporisation. There is a vent leading to a fume cupboard to release vaporised MTBE.

The tank has a total of 32 sampling points spaced out at 16 locations (Figure 6.1b) at two depths of 60 and 120 mm for each location (Figure 6.1c), with two sampling points are located in the photocatalytic reactor (Figure 6.1b). The sampling ports are made of 3 mm i.d. stainless steel tubes; the withdrawal point of sample in the sand was covered with 60  $\mu\text{m}$  stainless steel mesh to minimise intrusion of sand particles, which can affect the sampling. The samples were withdrawn from the sampling ports using a modified 10 mL glass syringe, with a 220 mm long 0.8 mm i.d. stainless steel tube. Stainless steel and a glass syringe were used to minimise corrosion and prevent adsorption of MTBE during sampling, respectively. MTBE concentrations were measured using an Agilent 6850 series gas chromatograph with flame ionisation detector (GC-FID).

**Table 6.1** The coordinates and nomenclatures of sampling points

Width, y (mm)	Depth, z (mm)	Distance from injection point, x (mm)					
		50	200	350	500	715	780
50	60	A160	B160	C160	D160		E160
	120	A1120	B1120	C1120	D1120		E1120
100	60	A260	B260	C260	D260	R60	E260
	120	A2120	B2120	C2120	D2120	R120	E2120
150	60	A360	B360	C360	D360		E360
	120	A3120	B3120	C3120	D3120		E3120

Note: Injection point coordinate: x, y, z = 35, 100, 90 mm

### 6.2.2 Scaled Up Photocatalytic Reactor

This Honeycomb I prototype, with an internal hexagonal cross section of 200 mm, was scaled up from the 100 mm i.d model (Section 4.2.1). This prototype is the proposed full scale in plan view (horizontal slice) but not in the vertical section. It was determined from a preliminary study that 100 mm between the UVA lamp and immobilised catalyst can still obtain a favourable photocatalytic activity. The UVA light intensity at 100 mm away from a 15 W Philips Cleo UVA fluorescent lamp is approximately  $0.3 \text{ mW cm}^{-2}$ , measured at a peak wavelength of 365 nm using a UVItec RX-003 radiometer (Figure 3.30). The perimeter immobilised catalyst (Section 4.2.1) was tied to the perforated stainless steel hexagonal frame using insulated copper wire. The radial immobilised catalyst sheets were held by plastic paper clips, which were supported by two holders. The catalyst support was arranged around a 50 mm i.d. borosilicate glass sleeve, which encloses the UVA lamp. It should be noted that only a single set of catalyst sheets, coated 14 months previously, was used throughout this study. The total catalyst surface area is about  $0.252 \text{ m}^2$ , yielding a surface area to volume ratio of approximately  $33.1 \text{ m}^2 \text{ m}^{-3}$ . The perforated hexagonal stainless steel structure was wrapped with a layer of  $60 \mu\text{m}$  stainless steel mesh to prevent intrusion of sand particles into the photocatalytic reactor. Honeycomb I was submerged in the reactor chamber for approximately 10 months throughout this study.

In the modular scale up of Honeycomb I, the air flow was maintained at  $0.2 \text{ L}_a \text{ min}^{-1}$  ( $\text{L}_a$  for litres of air), similar to that in the column reactor (Chapter 5). Consequently, the air flow to volume ratio was halved to  $0.025 \text{ L}_a \text{ min}^{-1} \text{ L}^{-1}$ , also to compensate for the larger width (cell diameter) to height (D/H) ratio in the larger scale reactor. Sufficient air is provided at this ratio as the complete photocatalytic oxidation (PCO) of  $1 \text{ mg L}^{-1}$  MTBE requires approximately  $2.7 \text{ mg L}^{-1}$  dissolved oxygen. The agitation in the reactor by aeration was assumed to be similar for both scales, achieving complete mixing of solution. The flow into the tank is not a parameter of concern as it is typically laminar in both scales (without aeration) due to the slow groundwater flow. The main reactor dimensions, which have significant impact on chemical reaction and mass transfer, are reactor volume and width to height ratio (Bisio and Kabel, 1985), respectively. The scaled up reactor (cell diameter doubled; reactor volume approximately 7.6 L) has a larger surface area to volume ratio, which affects the mass transfer of contaminants, due to the relatively wider radial panels than that of its model ( $21.5 \text{ m}^2 \text{ m}^{-3}$  – Honeycomb I, Table 4.1).

### 6.2.3 Preparation of Homogeneous Aquifer

The deionised water was deaired (synthetic groundwater) as the ambient dissolved oxygen concentration in groundwater is typically below  $2 \text{ mg L}^{-1}$  (McCarty et al., 1998) and to minimise air trapped among the sand grains, which can hinder the passage of groundwater. Deaired deionised water was used as groundwater and to make the MTBE solution.

Grade 'C' sand, from David Ball Ltd., with grain size from 125 to 500  $\mu\text{m}$ , determined using sieve analysis (Figure 6.2), was used due to its (i) grain size within the range between 70 and 690  $\mu\text{m}$  at Borden aquifer (Mackay et al., 1986), (ii) permeability closer to that of Borden aquifer (Mackay et al., 1986), and (iii) lower transverse dispersion to the sides of the tank to avoid the contaminant to flow from the sides of the tank. The Grade 'C' sand in this study was characterised and is tabulated in Table 6.2. The permeability of the aquifer in the sand tank is the gradient of the slopes (Figure 6.3), measured 10 months apart.

**Table 6.2** Characteristics of Grade 'C' sand used in this study

Characteristic	Value
Grain size ( $\mu\text{m}$ )	125 to 500
Density ( $\text{g cm}^{-3}$ )	1.5*
Permeability ( $\text{m s}^{-1}$ )	$2 \times 10^{-3}$ (initial); $5 \times 10^{-5}$ (after 10 months)
Porosity, $n_e$	0.42
$d_{10}$ ( $\mu\text{m}$ )	240
$d_{50}$ ( $\mu\text{m}$ )	390
$d_{85}$ ( $\mu\text{m}$ )	450

\* from David Ball Ltd.

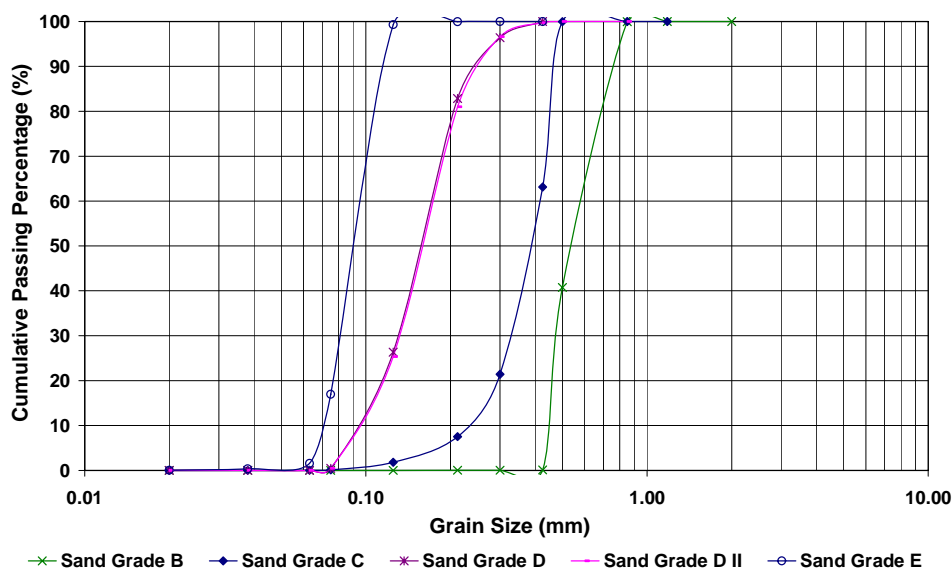


**Figure 6.2** Particle size distribution (PSD) of various sand grades using sieve analysis

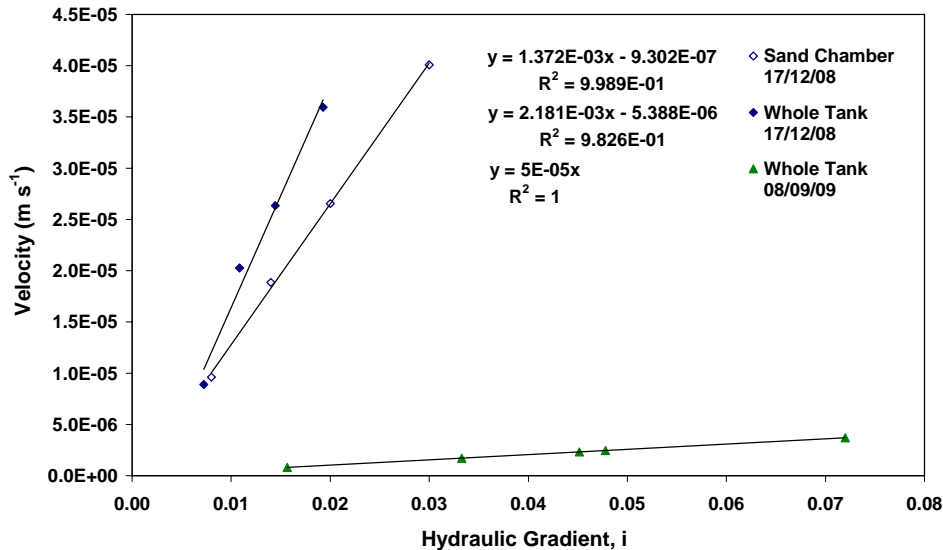


**Figure 6.3** Permeability of sand tank obtained before and after the sand tank experiments. Velocity was calculated by dividing flow by the area perpendicular to the flow direction, 0.2 m (W) x 0.22 m (H). Flow, induced using constant head device, was obtained by measuring the volume of water overflowed and time.

Grade 'C' sand was filled using the wet method, whereby the deaired deionised water was filled up to the outflow level prior to filling with sand. The main reasons for using this method are to (i) ensure no air bubbles trapped among sand grains, which would affect permeability, and (ii) enable water displacement test to obtain the sand volume. The tank volume is approximately 42 litres when filled up to the outflow at the height of 220 mm. It requires between 55 to 60 kg of sand to fill up to 240 mm, to model an unconfined aquifer. The photocatalytic reactor was of course not filled with sand. The sand volume was estimated at circa 12.7 litres through water displacement, which yields a porosity of about 0.42. The mean aquifer porosity at the Borden aquifer was 0.33 (Mackay et al., 1986). A permeability test was conducted using a constant head control device and measuring the flow. The sand permeability was initially about  $2 \times 10^{-3} \text{ m s}^{-1}$  (1 day after filling the tank) but after 10 months, it decreased to about  $5 \times 10^{-5} \text{ m s}^{-1}$  (Figure 6.3), which is similar to the mean permeability of  $7 \times 10^{-5} \text{ m s}^{-1}$  obtained at Borden aquifer (Mackay et al., 1986). It remains in the range of medium to coarse sand, i.e. from  $9 \times 10^{-7}$  to  $5 \times 10^{-3} \text{ m s}^{-1}$  (Domenico and Schwartz, 1997). It is worth noting the change in the permeability of sand, however, this does not affect this study significantly as the velocity is controlled using peristaltic pumps (variable hydraulic gradient) and the main purpose of this study is to clean-up a MTBE plume.

The flows for the experiments were selected based on the average linear velocity of approximately  $9 \text{ cm d}^{-1}$  at Borden aquifer (Mackay et al., 1986). The groundwater flow and MTBE injection were controlled using Watson Marlow 323S/D peristaltic pumps (with 1.6 mm

i.d. silicone tubing) because the simulated flow were too slow to be controlled using a head control device. The velocity of MTBE injection,  $v_{\text{MTBE}}$ , was calculated (similar to groundwater velocity,  $v_{\text{gw}}$ ) by assuming the plume conveyed through the whole cross section area of the saturated sand,  $A$  (0.2 m (W) x 0.22 m (H)), for simple estimation of plume migration and a reasonable ratio to simulate leakage from underground storage tank ( $v_{\text{MTBE}} = Q/A$ ). The average velocities used are summarised in Table 6.3.

**Table 6.3** Flow profile applied in the sand tank experiments. Velocity refers to Darcy's velocity except for total average linear velocity and porosity is 0.42

Exp	Groundwater Flow		MTBE injection		Total		Total Average Linear Velocity (cm d <sup>-1</sup> )
	Flow (mL min <sup>-1</sup> )	Velocity (cm d <sup>-1</sup> )	Flow (mL min <sup>-1</sup> )	Velocity (cm d <sup>-1</sup> )	Flow (mL min <sup>-1</sup> )	Velocity (cm d <sup>-1</sup> )	
7.3:7.3	2.23	7.3	2.23	7.3	4.46	14.6	34.8
7.8:7.8	2.38	7.8	2.38	7.8	4.76	15.6	37.1
20:9	6.11	20.0	2.75	9.0	8.86	29.0	69.0
30:7.3	9.17	30.0	2.23	7.3	11.40	37.3	88.8

#### 6.2.4 Determination and Preparation of Contaminants

Groundwater consists of a complex matrices of constituents, thus, it is difficult to identify the inhibiting constituent if cleaning up actual groundwater. Therefore, a systematic study was conducted to evaluate the effect of organic compounds in the migration and PCO of MTBE, prior to treating actual contaminated groundwater in future studies. Toluene, ethylbenzene and o-xylene (TEo-X) were chosen to represent organic compounds in this study due to their co-occurrence with MTBE (Da Silva and Alvarez, 2002; Ruiz-Aguilar et al., 2002). The TEo-X concentrations were determined from the highest concentrations (toluene: 30, ethylbenzene: 10 and o-xylene: 20 mg L<sup>-1</sup>) used in Chapter 5. MTBE concentration was 100 mg L<sup>-1</sup>. The contaminant solution was prepared by adding MTBE (135  $\mu\text{L}$ ), toluene (35  $\mu\text{L}$ ), ethylbenzene (12  $\mu\text{L}$ ) and o-xylene (23  $\mu\text{L}$ ) into 1 L deaired deionised water. The contaminant solution was injected into the sand tank until the flushing phase.

#### 6.2.5 Experimental Phases

The groundwater is pumped into the tank via the inflow (Figure 6.1b) throughout the experiment. MTBE is injected continuously until the flushing phase. The sand tank experiment consists of four phases (Table 6.4):

**Table 6.4** The initiation times (hours) of experimental phases for the three sand tank experiments

Experimental Phase	Sand Tank Experiments				
	14.6	15.6 V <sup>a</sup>	15.6 TEO-X <sup>b</sup>	29.0	37.3
MTBE Migration	0	0	0	0	0
Aeration	96	72	93	120	72
Photocatalytic Reaction	102	78	99	127	79
Flushing	121	120	120	150	96

<sup>a</sup> 15.6 V is the fifth sand tank experiment (MTBE only) conducted at total water velocity of 15.6 cm d<sup>-1</sup> to compare the reactor efficiency with 14.6 (for validation) and 15.6 TEO-X.

<sup>b</sup> 15.6 TEO-X is the sixth sand tank experiment (MTBE/TEO-X) conducted at total water velocity of 15.6 cm d<sup>-1</sup> to compare the reactor efficiency with 14.6 and 15.6 V, to observe the effect of TEO-X on the PCO of MTBE.

(i) MTBE migration: The MTBE migration phase was conducted in the sand chamber to observe and characterise the MTBE migration in homogeneous sand, to simulate a plume from an underground storage tank or pipeline leakage. This includes obtaining the advection and dispersion coefficients via the breakthrough curves and plotting the MTBE plume, in plan view. This phase involves continuous injection of 100 mg L<sup>-1</sup> MTBE solution into the tank horizontally via the injection point at 90 mm depth (Figure 6.1b), using a Watson Marlow 323S/D peristaltic pump. 100 mg L<sup>-1</sup> MTBE solution was prepared by spiking MTBE into deaired deionised water. The sampling in this phase is focused in the sand chamber to obtain the breakthrough curve of MTBE at various sampling points. When the MTBE injection was initiated, the sampling was conducted every half hourly for 3 hours at rows where MTBE is likely to be detected in order to obtain the breakthrough curve of MTBE migration. After 24 hours, the sampling frequency was reduced to once daily when there was no significant change in the MTBE concentration at all the sampling points. To obtain data for the breakthrough curves, the sampling times for the specific rows were estimated using the average linear velocity equation (Eq. 2.31) as MTBE literally migrates at the groundwater flow (Schirmer et al., 1999; Jacobs et al., 2001; Saponaro et al., 2009). The average linear water velocity,  $v_w$ , is the ratio of Darcy's velocity to soil porosity (Eq. 2.31).

The MTBE migration phase was continued until the MTBE concentration in row E (Figure 6.1b) reaches a constant value; indicating that the MTBE concentration in reactor has also stabilised. The reactor can be assumed as a "well" when no treatment was applied.

(ii) Aeration: The purpose of this phase is to completely mix the MTBE plume to obtain a uniform MTBE concentration in the reactor ( $C_{0 \text{ MTBE}}$ ) and also to observe the percentage removal of MTBE by aeration only. The air flow is fixed at 0.2 L<sub>a</sub> min<sup>-1</sup>, which yields air flow to volume ratio of approximately 0.025 L<sub>a</sub> min<sup>-1</sup> L<sup>-1</sup>. The sampling is focused on the photocatalytic reactor. Nevertheless, a batch of sampling for the whole tank was conducted daily.

(iii) Photocatalytic Reaction: When the MTBE concentration in the photocatalytic reactor stabilised (approximately 6 to 8 hours after aeration started), this phase is initiated by switching on the 15 W Philips Cleo UVA lamp. The purpose of this phase is to observe the attenuation of MTBE plume by photocatalysis. The dissolved oxygen for the photocatalytic reaction was supplied through aeration in the reactor at the air flow of  $0.2 \text{ L}_a \text{ min}^{-1}$ . Again, the sampling is focused on the photocatalytic reactor. Nevertheless, a batch of sampling for the whole tank was conducted daily.

(iv) Flushing: When the MTBE concentration in the photocatalytic reactor stabilised, the MTBE injection was stopped. The groundwater flow is continued to observe the clearing of MTBE in the sand chamber. The sampling in this phase is focused in the sand chamber to obtain the breakthrough curve of MTBE at various sampling points. The aeration and UVA light illumination is continued to degrade MTBE.

### 6.3 Results and Discussion

Similar to the experimental section, the results and discussion is categorised into the four phases of the sand tank experiment.

#### 6.3.1 MTBE Migration Phase

Figure 6.4 shows the MTBE concentration plotted against time at a row of sampling points on the centre line of the tank with the same  $y$  (width) and  $z$  (height) coordinates (Table 6.1) in the sand tank experiment at a total Darcy's velocity of  $14.6 (7.3:7.3) \text{ cm d}^{-1}$ ; indicating the experimental phases. Figures 6.5, 6.6 and 6.7 show the complete set of MTBE concentrations plotted against time at a row of sampling points for experiments at velocities of  $14.6, 29.0$  and  $37.3 \text{ cm d}^{-1}$ , respectively. The data from each sampling point consists of a breakthrough curve, concentration stabilisation phase and flushing phase. Only the initial breakthrough curve (Figure 6.8) was analysed for migration velocity (advection) and dispersion coefficients using a software program known as CXTFIT (Toride et al., 1999). The MTBE concentration at all the sampling points upgradient of the reactor stabilised prior to the aeration phase. MTBE concentrations obtained in the reactor and in row E were in most cases similar, indicating that the MTBE plume migrated through the more permeable reactor instead of flowing around it. With regular sampling for the whole tank during the experiments (Figure 6.5 to 6.7), the data was used to plot the MTBE migration at the 60 and 120 mm planes (below groundwater level) in the tank with time (Figure 6.12 to 6.16).

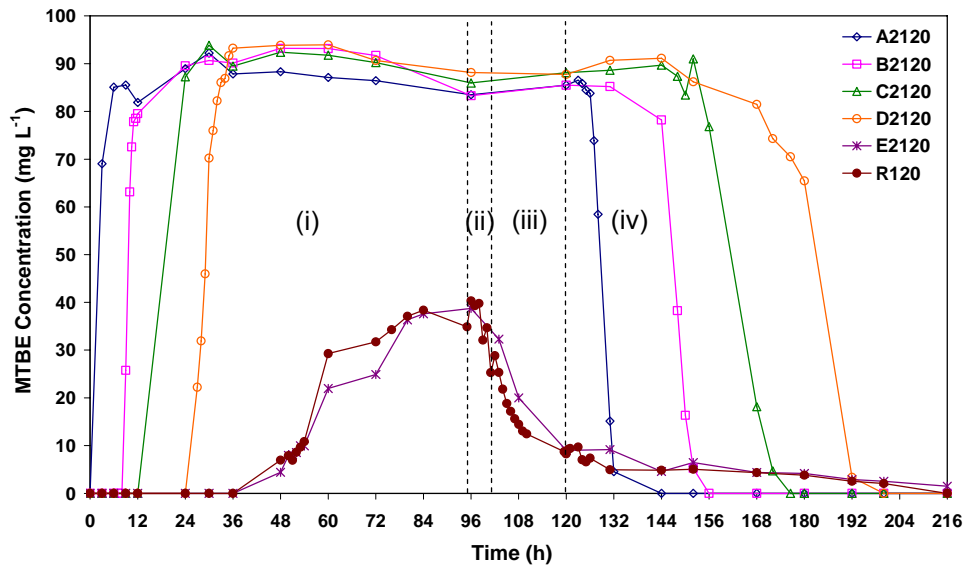


**Figure 6.4** Plot of MTBE concentration with time for six sampling points along  $y = 100$  cm (on the tank centre line) and  $z = 120$  mm (depth) during 7.3:7.3 experiment. Every series consists of a breakthrough curve, stabilisation phase and flushing phase, except for R120 having aeration and reaction phase between stabilisation and flushing phase; E2120 follows R120; (i) MTBE migration (air and light off), (ii) aeration (air on, light off), (iii) photocatalytic reaction (air and light on) and (iv) flushing phase (air and light on) (refer to Table 6.1 for sampling point identification).

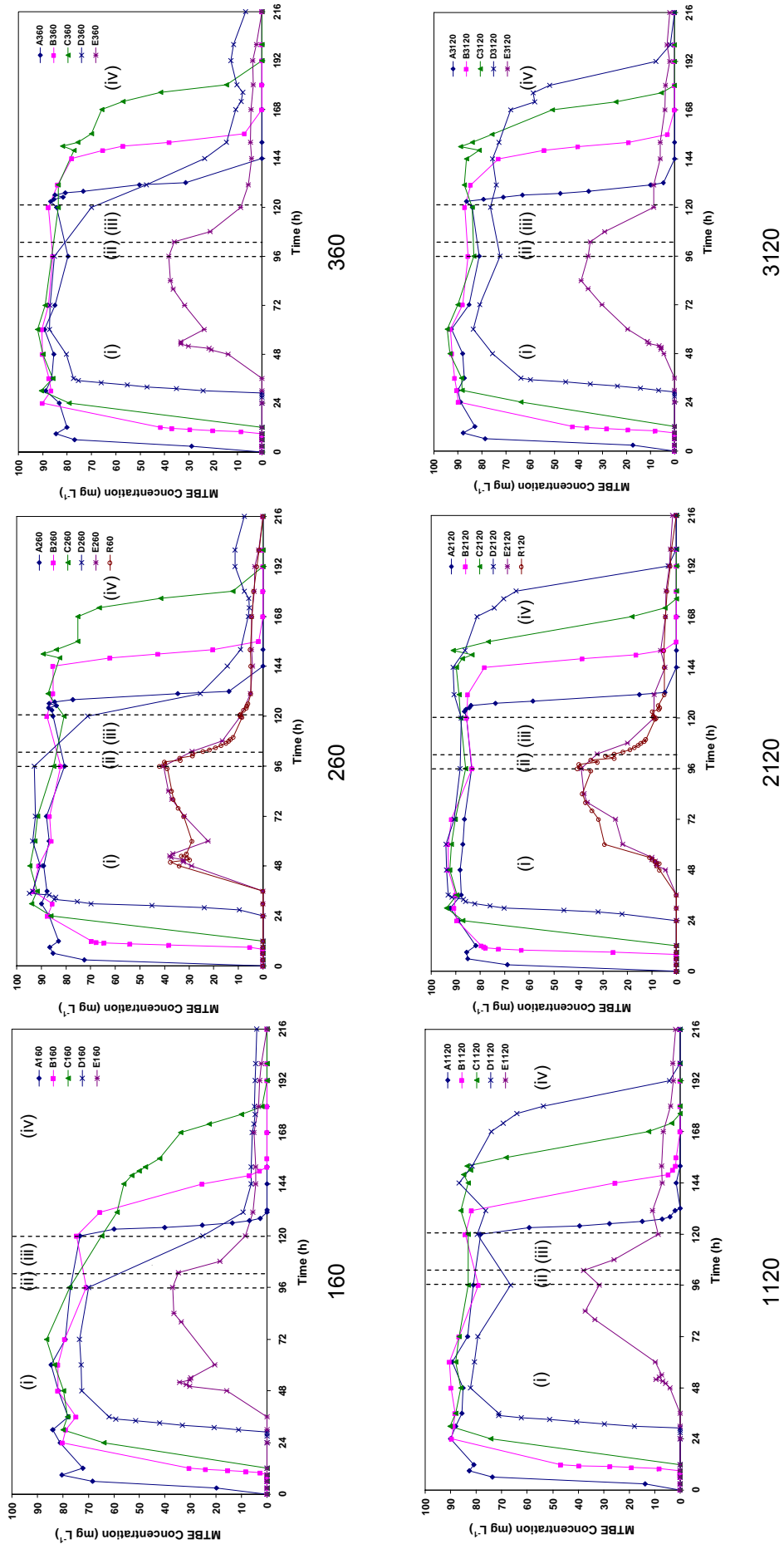


**Figure 6.5** Plot of MTBE concentration with time for sampling points at 50, 100 and 150 mm across the 200 mm tank width at depths of 60 and 120 mm (refer to Table 6.1 for coordinates) during the 14.6 (7.3:7.3) experiment (refer to Table 6.3 for flow details)

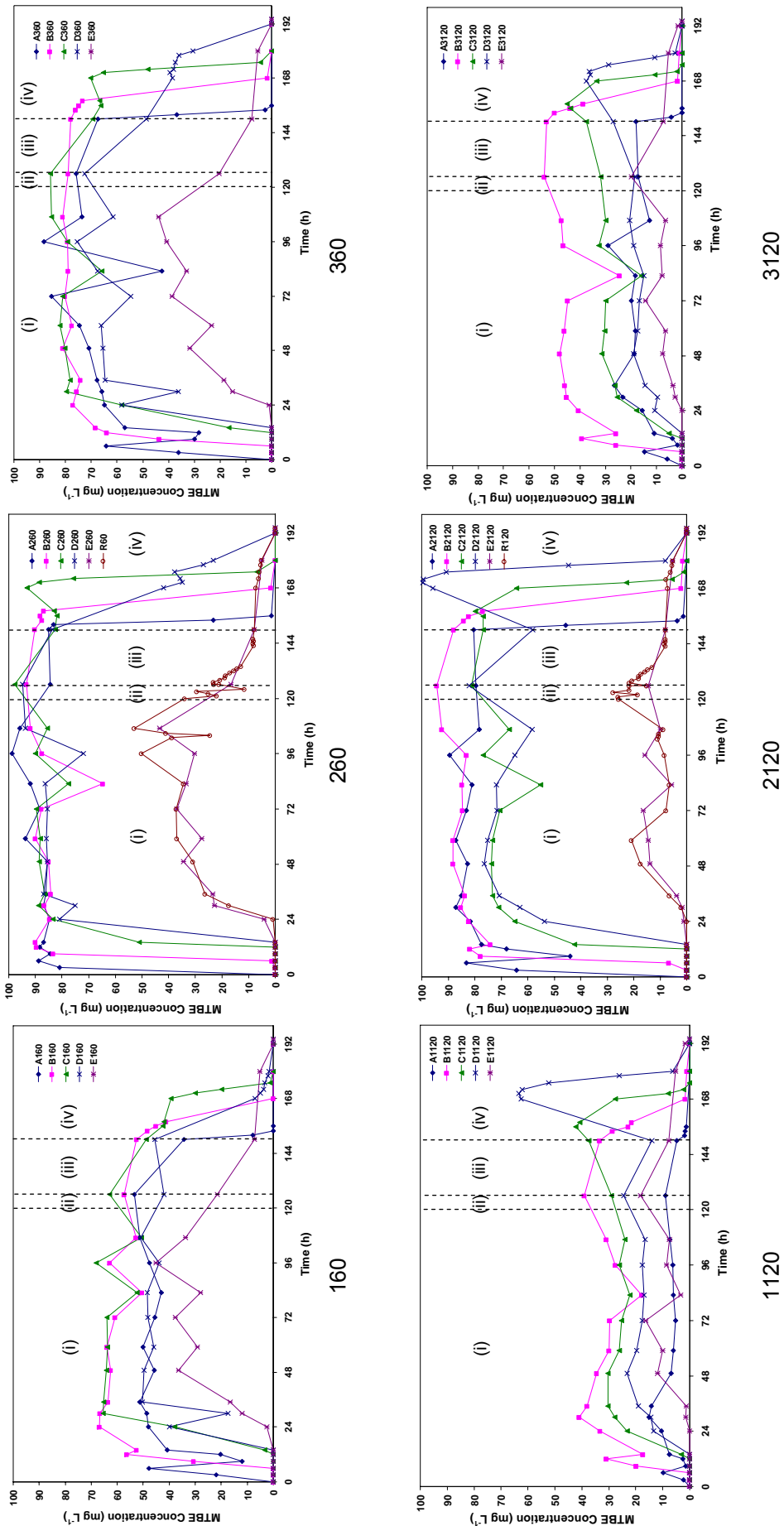


**Figure 6.6** Plot of MTBE concentration with time for sampling points at 50, 100 and 150 mm across the 200 mm tank width at depths of 60 and 120 mm (refer to Table 6.1 for coordinates) during the 29.0 (20.0:9.0) experiment (refer to Table 6.3 for flow details)

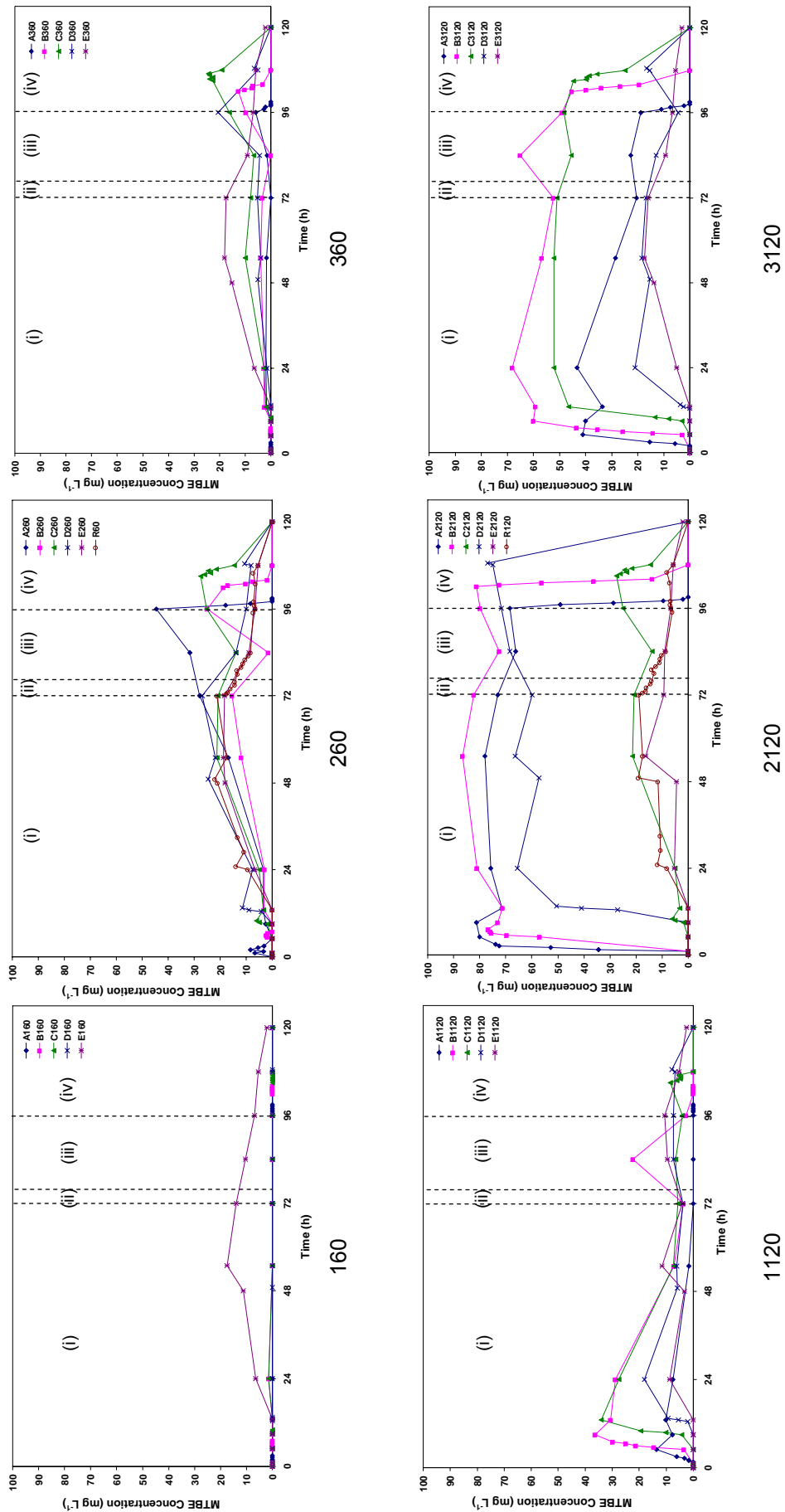


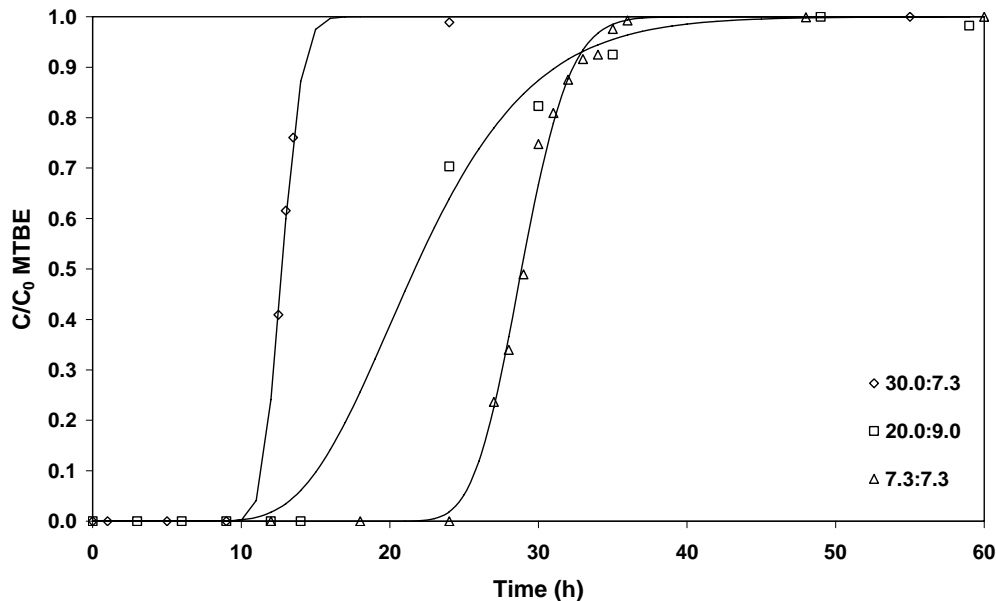
**Figure 6.7** Plot of MTBE concentration with time for sampling points at 50, 100 and 150 mm across the 200 mm tank width at depths of 60 and 120 mm (refer to Table 6.1 for coordinates) during the 37.3 (30.0:7.3) experiment (refer to Table 6.3 for flow details)

### 6.3.1.1 Advection, Dispersion and Retardation Factor

The breakthrough data obtained in the sand tank experiment were used as input for CXTFIT version 2.0 to obtain the advection, dispersion coefficient and retardation factor of MTBE. It should be noted that it is difficult to estimate these values, therefore it is briefly mentioned in this study. CXTFIT is a software program which uses the advection-dispersion equation to model the transport during steady 1-dimensional flow by fitting parameters to the experimental data iteratively. In this study, the advection and dispersion coefficients were obtained from the CXTFIT model, which was then used to obtain the retardation factor by dividing the design average velocity of groundwater.

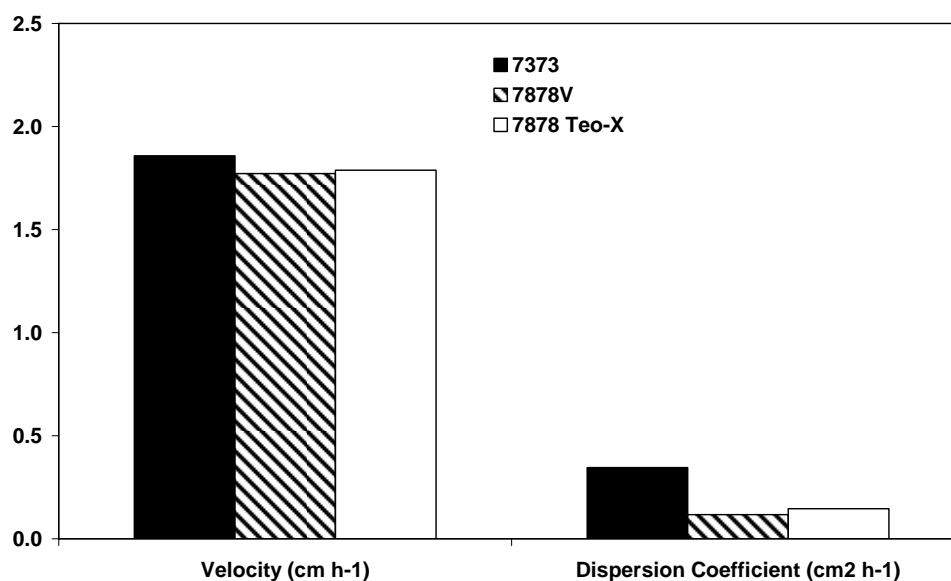
Figure 6.8 shows an example of CXTFIT models fitted to the experimental MTBE concentrations obtained at D2120 at three average velocities. The correlation coefficients ( $R^2$ ) are typically more than 0.97, indicating that the CXTFIT model fitted well to the experimental data. MTBE was detected earlier with increasing velocities. The main MTBE plume ( $0.5 C/C_0$ ) reached row D at the 13<sup>th</sup>, 22<sup>nd</sup> and 29<sup>th</sup> hour when the average velocities were 37.3, 29.0 and 14.6 cm d<sup>-1</sup>, respectively (Figure 6.8). It should be noted that the velocity obtained through the CXTFIT model is the average linear velocity, i.e. the true contaminant transport velocity,  $v_c$ . The dispersion coefficients at D2120 were 0.70, 4.90 and 0.35 cm<sup>2</sup> h<sup>-1</sup>, respectively (Figure 6.8). The second value did not comply with the descending dispersion coefficient with decreasing velocity because the MTBE plume appeared to migrate upwards (Figure 6.6 (R60 and R120) and 6.12), which could explain the greater dispersion at D2120. This could be because the 29.0 cm d<sup>-1</sup> experiment was conducted first, within the first month after the filling of the tank, in which the sand grains have yet to consolidate. There was about 1 cm settlement of the sand surface over 6 months, indicating sand consolidation. The dispersion coefficient at D260 (29.0 cm d<sup>-1</sup>), which is 60 mm above D2120, was about 0.50 cm<sup>2</sup> h<sup>-1</sup> (data not shown), which is in between the coefficients obtained in the other two experiments. Higher dispersion coefficients were obtained at the sampling points nearest to the injection point (A260 and A2120) due to the higher MTBE flow. The dispersion coefficients at A260 and A2120 (data not shown) decrease with increasing  $v_{gw}:v_{MTBE}$  ratio, which agrees with the narrower plume width with increasing  $v_{gw}:v_{MTBE}$  ratio (Figure 6.12). The retardation factor ranged from 1.00 to 1.12, averaging circa 1.07 in all the experiments, which indicates negligible MTBE sorption in agreement with Schirmer et al. (1999). This is also consistent with an MTBE retardation factor of 1.06, flowing through a column with sand porosity of 0.40, obtained by Saponaro et al. (2009). The retardation factor is the ratio of transport velocity of groundwater to the transport velocity of an organic compound (Eq. 2.33) (Odermatt, 1994). There is no significant retardation because MTBE has very low adsorptivity. It has been suggested that low molecular weight hydrocarbons,

below  $150 \text{ g mol}^{-1}$ , have low adsorptivity, and MTBE is no exception (Jacobs et al., 2001). An adsorption test, using 1 L containers (a control without sand and duplicates with 100 g sand) filled with  $100 \text{ mg L}^{-1}$  MTBE solution, showed no significant reduction of MTBE concentration in all the tests. This verifies that MTBE does not adsorb to sand. Retardation is linked to adsorption by Eq. 2.33, which assumes a linear relation between adsorption and the equilibrium concentration.



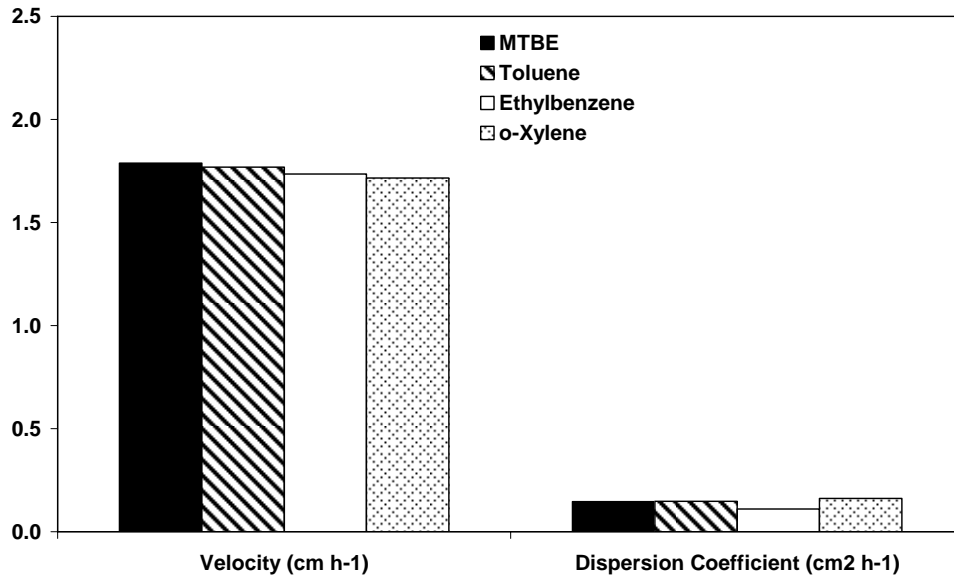
**Figure 6.8** Breakthrough curves modelled using CXTFIT (full line) fitted well to experimental data from sampling point D2120 at various average velocities (refer to Table 6.3 for flow details).

The breakthrough curves modelled using a 1-dimensional advection-dispersion model, CXTFIT, fitted well to the experimental data (Figure 6.8). Therefore, it was also used to estimate the advection and dispersion coefficient of contaminants for every sampling point in the sand tank in this study. As Figure 6.16 showed that TEO-X migration followed the MTBE migration pattern, the retardation factor for TEO-X were assumed 1.07 in modelling the breakthrough curves using CXTFIT. The CXTFIT model for all the contaminants fitted well to the experimental data, with  $R^2$  typically greater than 0.95. Figure 6.9 shows the MTBE advection and dispersion coefficient at sampling point, D2120, in the three sand tank experiments conducted at similar velocities. The similar MTBE advection and dispersion coefficients indicated the MTBE migration in all these three experiments were consistent.



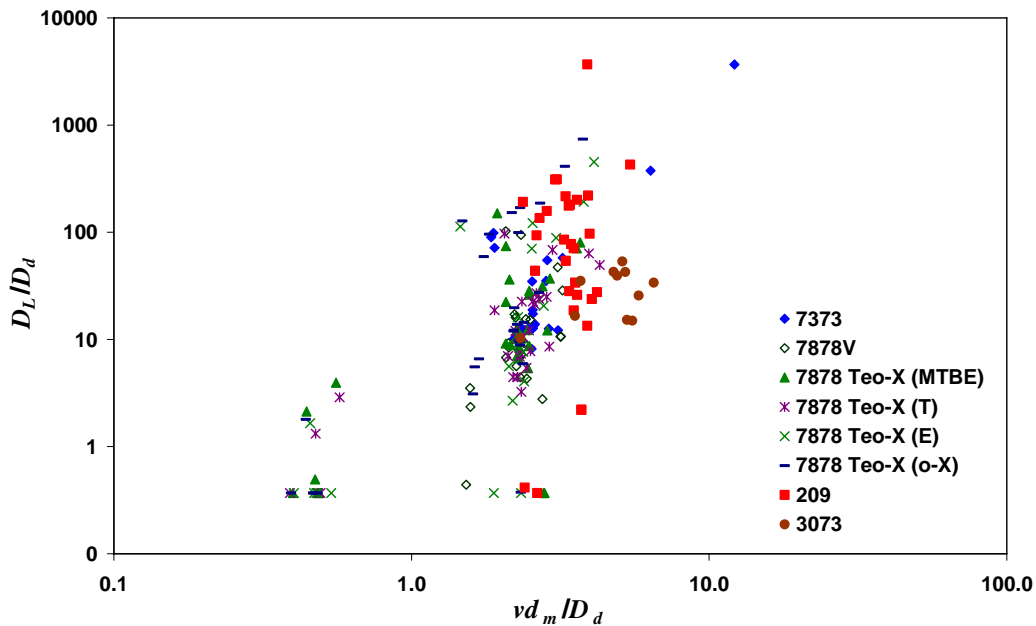
**Figure 6.9** Comparison of MTBE velocity and dispersion coefficients, obtained using CXTFIT, from three sand tank experiments (7.3:7.3, 7.8:7.8V and 7.8:7.8 TEO-X, refer to Table 6.3 for flow details) conducted at similar groundwater velocities indicating similar migration pattern

Figure 6.10 shows the velocity and dispersion coefficient of MTBE and TEO-X at D2120. The similar velocity and dispersion coefficient among the contaminants showed that MTBE and TEO-X migrated at similar pattern. Despite the retardation factor of TEO-X being higher than that of MTBE (Squillace et al., 1996; Da Silva and Alvarez, 2002; Saponaro et al., 2009), TEO-X migration was assisted by MTBE due to the co-solvent effect (Alberici et al., 2002).



**Figure 6.10** The velocity and dispersion coefficient of MTBE and TEo-X, obtained through CXTFIT, at D2120 during sand tank experiment at velocity of  $15.6 \text{ cm d}^{-1}$  in the presence of TEo-X

Figure 6.11 shows the plot of dimensionless dispersion coefficients against Peclet number in all the sand tank experiments, in order to show the relative contribution of dispersion and diffusion to solute transport. A Peclet number is a dimensionless number, which is a ratio of transport rate by advection ( $v$ ) and the average grain diameter ( $d_m$ ) to the transport rate of molecular diffusion ( $D_d$ ),  $vd_m/D_d$ . The Peclet number typically increases with higher velocities and/or longer travel distance (Fetter, 1999). In this study, the higher Peclet number was obtained in experiments conducted with higher flows and at sampling points located further from the injection points. The plot is within the Class 2 region (Figure 2.9), indicating that the contaminant migration is influenced by both diffusion and dispersion. As the groundwater velocity is assumed evenly distributed across the perpendicular tank area, the dispersion is assumed to be longitudinal dispersion. It is possible that occasional high values of  $D_L/D_d$  were caused by the main plume migrating away from the sampling point.



**Figure 6.11** Peclet distribution in all the sand tank experiments showing the plume migration was influenced by diffusion and dispersion ( $v d_m/D_d$  is within Class 2 - Figure 2.11)

### 6.3.1.2 Concentration Distribution Plots

Figure 6.12 shows some MTBE concentration distribution plots at 60 and 120 mm sampling depths in the sand tank experiments at various times and water velocities. A more detailed plots for experiments conducted at velocities of 14.6, 29.0 and 37.3  $\text{cm d}^{-1}$  are shown in Figure 6.13, 6.14 and 6.15, respectively. Figure 6.12 shows that MTBE migration was faster, longer plume length and narrower plume width, with increasing  $v_{\text{gw}}:v_{\text{MTBE}}$  ratio. After 24 hours of MTBE injection, MTBE was detected in row C, D and reactor at velocities of 14.6, 29.0 and 37.3  $\text{cm d}^{-1}$ , respectively. The MTBE plume width was narrower with increasing  $v_{\text{gw}}:v_{\text{MTBE}}$  ratio (Figure 6.12), indicating less transverse dispersion, which is the usual case (Fetter, 1999). The MTBE plume width was broader at lower  $v_{\text{gw}}:v_{\text{MTBE}}$  ratio because the injected MTBE would disperse “radially”, prior to being transported by the regional groundwater. The MTBE concentration especially along the midline ( $y = 100 \text{ mm}$ ) stabilised at circa  $90 \text{ mg L}^{-1}$  (90 %  $C/C_0$ ), in all the sand tank experiments, which indicated that advection was dominant. The time at which MTBE concentration was first detected, was predicted using the average linear water velocity equation (Eq. 2.31), which assisted the determination of the sampling times. This also indicates that MTBE migration is not significantly retarded.

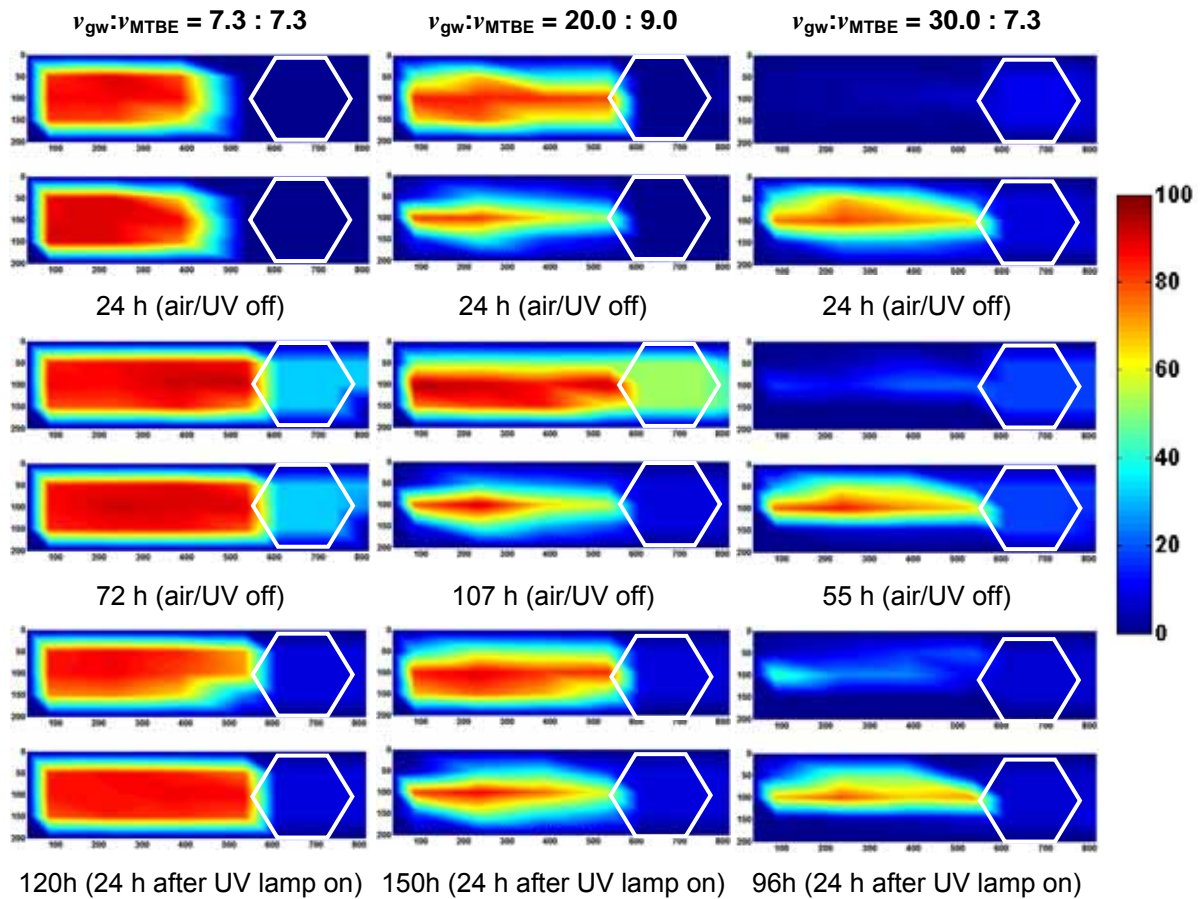


**Figure 6.12** Plan views of MTBE plume migration at increasing water velocities at depths of 60 mm (top) and 120 mm (bottom) in the sand tank plotted using Matlab. The velocities ( $v_{gw}:v_{MTBE}$ ,  $\text{cm d}^{-1}$ ) applied were 7.3:7.3 (left column), 20:9 (centre column) and 30:7.3 (right column). The first, second and third rows of plan views show the similar stages of every experiment.

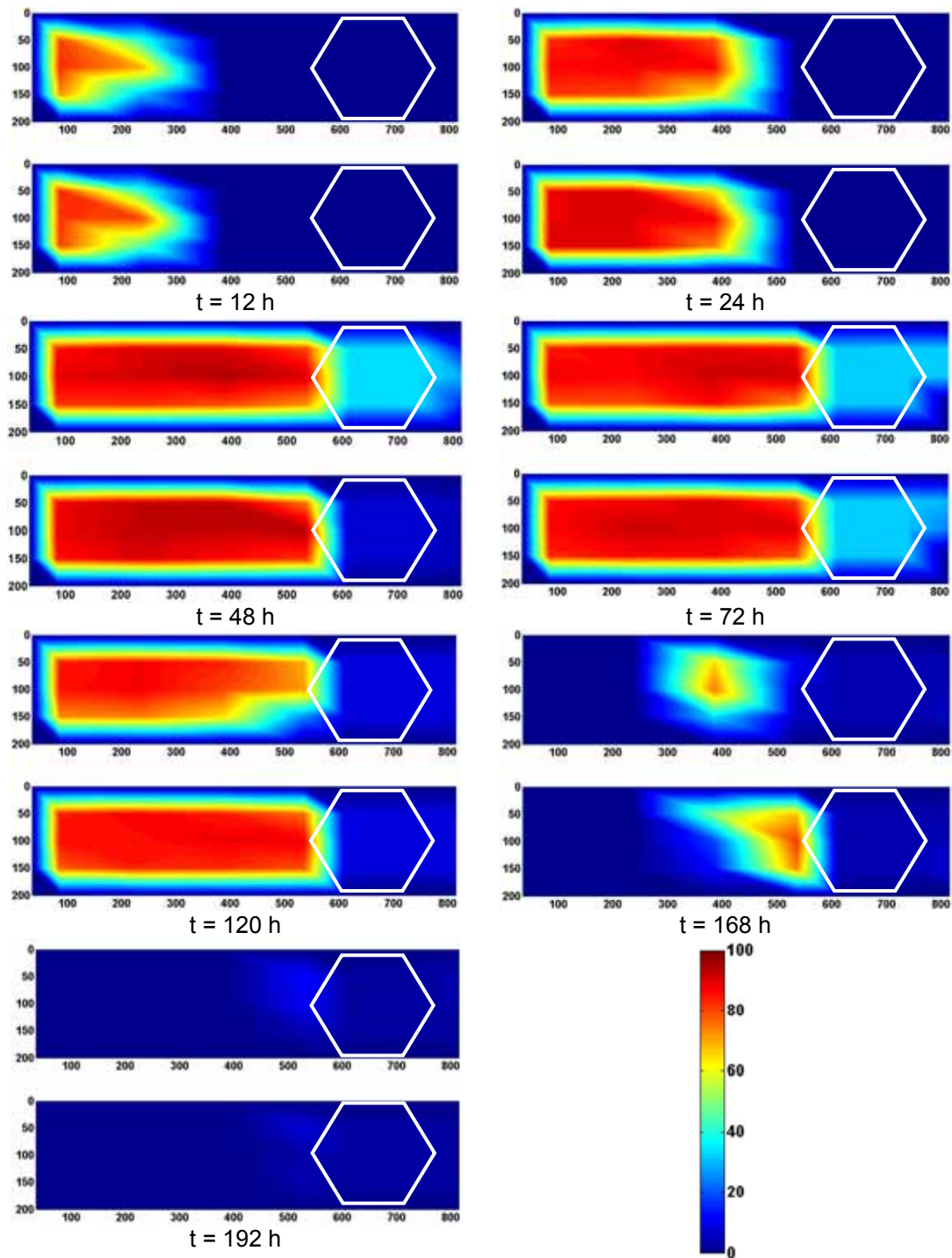


**Figure 6.13** Concentration plots at specified times showing MTBE plume migration at depths of 60 and 120 mm in the sand tank at velocity of  $14.6 \text{ cm d}^{-1}$  ( $v_{\text{gw}}:v_{\text{MTBE}} = 7.3:7.3$ )

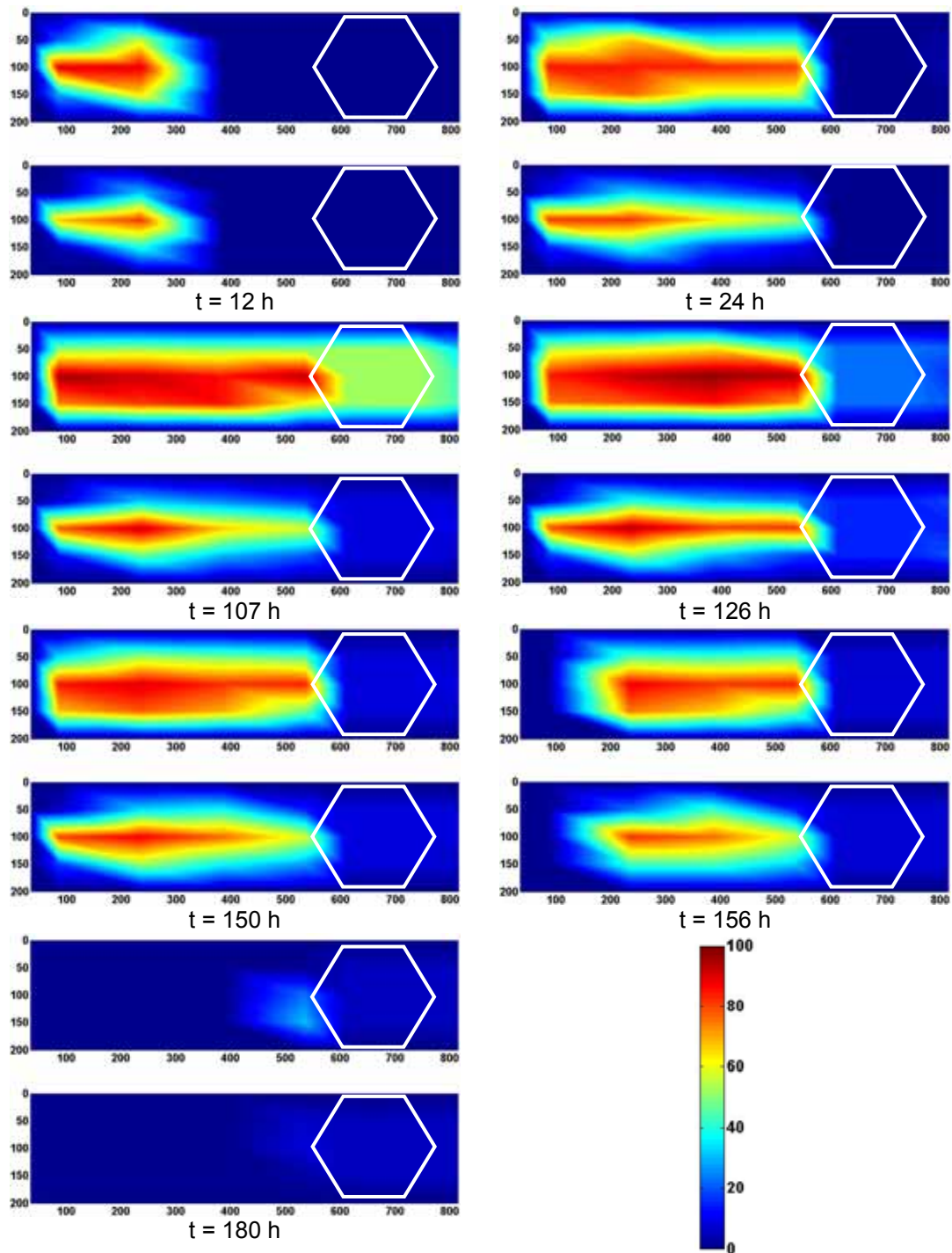


**Figure 6.14** Concentration plots at specified times showing MTBE plume migration at depths of 60 and 120 mm in the sand tank at velocity of  $29.0 \text{ cm d}^{-1}$  ( $v_{\text{gw}}:v_{\text{MTBE}} = 20.0:9.0$ )

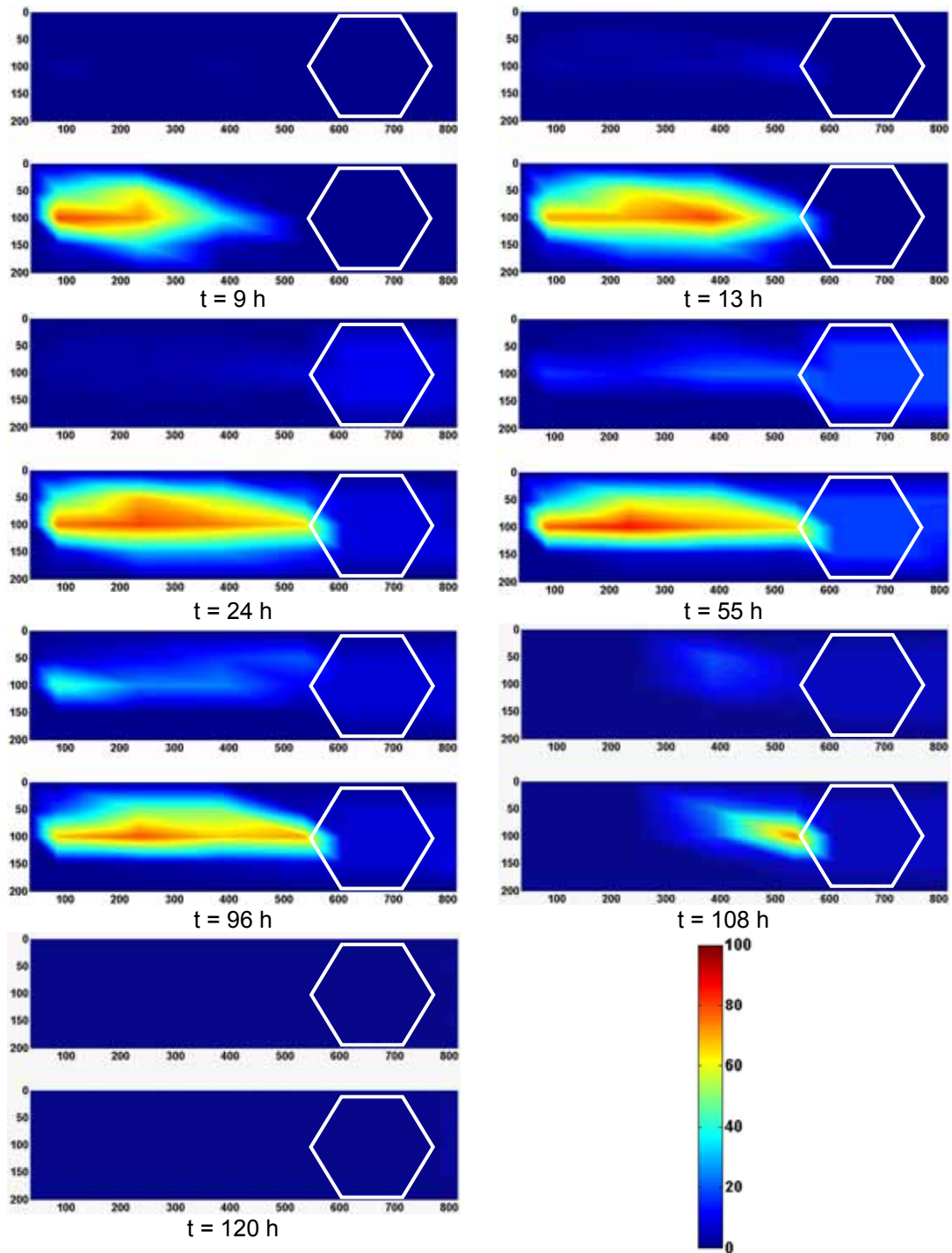


**Figure 6.15** Concentration plots at specified times showing MTBE plume migration at depths of 60 and 120 mm in the sand tank at velocity of  $37.3 \text{ cm d}^{-1}$  ( $v_{\text{gw}}:v_{\text{MTBE}} = 30.0:7.3$ )

Figure 6.16 shows the surface plot of the plume of contaminants at real time in the sand tank. The plots showed that TEO-X migration was similar to that of MTBE, indicating that the TEO-X migration was assisted by MTBE via the co-solvent effect (Alberici et al., 2002). Co-solvent effect is the increase of hydrocarbon solubility by a highly soluble organic solvent in water, resulting in the increase of concentration and migration of the more retarded hydrocarbons in water. Nevertheless, the maximum toluene, ethylbenzene and o-xylene concentrations obtained in the sand chamber were about 4, 1.5 and 3 mg L<sup>-1</sup>, i.e. about 15 % of the initial concentrations of the respective contaminants. This could explain the TEO-X migration at similar rates to that of MTBE but at significantly lower concentrations. This agrees with Groves Jr. (1988) that MTBE has little effect on hydrocarbon solubility in the water phase. The TEO-X concentrations obtained at the sampling points were significantly lower than their respective initial concentrations, indicating the limited transverse dispersion of the main TEO-X plume.

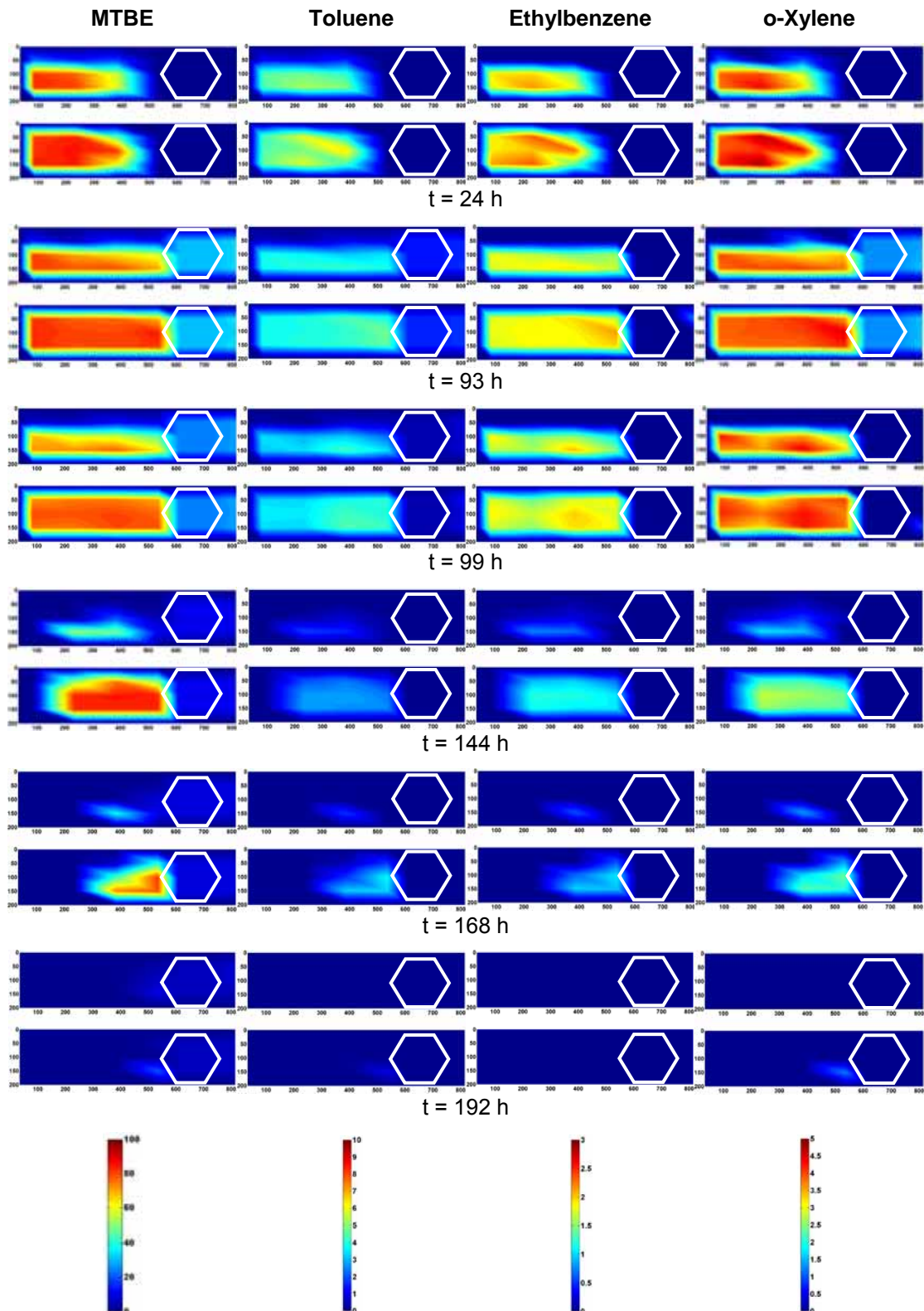


**Figure 6.16** Surface plot of concentration showing the migration of the organic compounds in the sand tank at a velocity of  $15.6 \text{ cm d}^{-1}$ . The migration of toluene, ethylbenzene and o-xylene is similar to that of MTBE, implying that the migration of toluene, ethylbenzene and o-xylene in the tank is assisted by MTBE via the co-solvent effect. TEo-X concentrations obtained at the sampling points were about 10 - 15 % of the initial concentration injected into the sand tank.

The contour mapping of the MTBE concentrations between sampling points in Figure 6.12 to 6.16 was obtained by interpolation using a Matlab programme, due to the considerably sparse sampling coordinates. The limited number of sampling points was mainly due to the concern that excessive withdrawal of samples may affect the flow pattern in the tank. Moreover, it was practically not feasible to sample and analyse more samples (due to MTBE equilibration time and GC-FID capacity) particularly during frequent sampling periods.

### 6.3.1.3 Within the Photocatalytic Reactor

The second row in Figure 6.12 shows the MTBE migration into the reactor before aeration and the UVA lamp was switched on, simulating a typical trench or well without treatment. In the 29.0 cm d<sup>-1</sup> experiment, the upper level concentrations are greater than that of the lower level, both in the sand and in the reactor. The upper layer could have been slightly more permeable because this experiment was conducted shortly after the sand tank was filled. The sand was likely to have consolidated after 6 months. In the 14.6 cm d<sup>-1</sup> experiment, this difference was not observed due to the potential “radial” spread of MTBE prior to transport by water, resulting in more evenly distributed concentration across the incoming flow area. Similarly for 15.6 V and 15.6 TEO-X experiments, the respective concentrations of MTBE and TEO-X at both sampling depths in the reactor appeared similar (Figure 6.16). The maximum toluene, ethylbenzene and o-xylene concentrations recorded in the reactor were 1.5, 0.5 and 1.5 mg L<sup>-1</sup>, respectively. This is similar to the percentage reduction of MTBE concentration, of about 50 to 60 %, in the reactor, prior to aeration phase.

### 6.3.2 Aeration Phase

The aeration phase was conducted to observe and distinguish between the vaporisation and the PCO of MTBE. When the reactor was aerated, MTBE concentrations at both depths were similar, indicating complete mixing by aeration. Figure 6.17 shows the reductions of normalised MTBE concentration in the aeration and reaction phase in Honeycomb I at four average velocities. Immediately after the aeration phase started, the initial MTBE concentration in the reactor ( $C_{0\text{ MTBE}}$ ) at total groundwater velocities of 14.6, 15.6 V, 15.6 TEO-X, 29.0 and 37.3 cm d<sup>-1</sup> was approximately 41, 32, 30, 30 and 20 mg L<sup>-1</sup>, respectively. The initial MTBE concentration in the reactor reduces with the increasing  $v_{\text{gw}}:v_{\text{MTBE}}$  ratios (Table 6.3) of approximately 1:1, 2:1 and 4:1. A higher  $v_{\text{gw}}:v_{\text{MTBE}}$  ratio resulted in more dilution in the reactor as a greater fraction of water flows through the reactor. This is also shown by the narrower MTBE plume width at the higher  $v_{\text{gw}}:v_{\text{MTBE}}$  ratio (Figure 6.12).

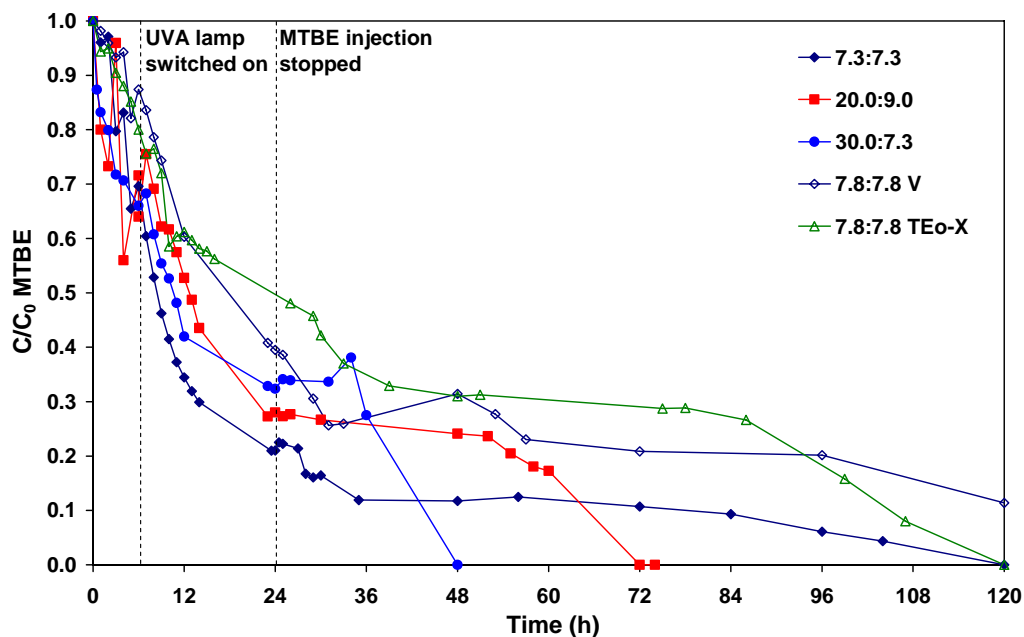


**Figure 6.17** Reduction of MTBE concentration in Honeycomb I from the initiation of the aeration phase. The aeration and UVA lamp was switched on at 96 h, 102 h (7.3:7.3); 120 h, 127 h (20.0:9.0); 72 h, 79 h (30.0:7.3); 72 h, 78 h (7.8:7.8 V); 93 h, 99 h (7.8:7.8 TEO-X), respectively, after MTBE injection started (refer to Table 6.3 for flow details).

During the aeration phase, the reduction of MTBE concentration fluctuated, which differed from the steady exponential reduction observed when the UVA lamp was switched on. Vaporisation by aeration appeared to be independent of the total velocity. The percentages of MTBE removed by  $0.2 L_a \text{ min}^{-1}$  air flow at velocities of 14.6, 29.0 and 37.3  $\text{cm d}^{-1}$  were approximately 30 (6 h), 25 (7 h) and 33 (7 h) %, respectively (Figure 6.17). They are slightly higher than approximately 20 % MTBE removal observed at  $0.2 L_a \text{ min}^{-1}$  ( $0.05 L_a \text{ min}^{-1} L^{-1}$ ) in the 4 L column reactor (Section 5.3.1.1), which has a relatively smaller D/H ratio. The effect of aeration on the MTBE vaporisation in the reactor increased with increasing air flow to volume ratio and D/H ratio (Section 5.3.1). Vaporisation via aeration should be considered as part of the overall photocatalytic reactor efficiency, as aeration is an essential component of a photocatalytic reactor system.

In the 7.8:7.8 TEO-X experiment, the initial TEO-X concentration in the reactor was  $3.2 \text{ mg L}^{-1}$ , mainly consisted of toluene and o-xylene. Ethylbenzene concentration was below detectable limit within the first hour of aeration possibly due to its low initial concentration, followed by o-xylene after 4 hours. About 29.5 % toluene remained after 6 hours of aeration.

### 6.3.3 Photocatalytic Reaction Phase

The third phase of the sand tank experiment, i.e. the reaction phase, was initiated when the UVA lamp was switched on. The clean-up using Honeycomb I appeared to be localised and did not affect the MTBE or TEO-X concentration prior to the reactor (third row in Figure 6.12 – MTBE only and  $t = 99$  h in Figure 6.16 – MTBE/TEO-X). This indicated that the photocatalytic reaction is contained within the reactor in the presence of UVA light, air and titanium dioxide. This can be an advantage particularly when groundwater remediation is required in environmentally sensitive areas, for instance aquifer preservation, and agricultural lands.

Figure 6.17 shows the reduction of MTBE concentration in Honeycomb I from the initiation of the aeration phase. It should be noted that the time of reactor operation in Figure 6.17 was reset to the time when aeration was initiated in the reactor for comparison purposes. The UVA lamp was switched on after 6, 6, 6, 7 and 7 hours of aeration for the sand tank experiment at velocities of 14.6, 15.6 V, 15.6 TEO-X, 29.0 and 37.3  $\text{cm d}^{-1}$ , respectively (Table 6.4). Table 6.5 summarises the experimental details and performance of Honeycomb I in all the sand tank experiments for comparison purposes, as well as providing the cumulative performance of the reactor. The MTBE removal efficiency was 88.1, 79.2, 71.3, 72.3 and 61.9 % at total velocities of 14.6, 15.6 V, 15.6 TEO-X, 29.0 and 37.3  $\text{cm d}^{-1}$ , respectively (Table 6.5). As found previously in Section 5.3.4.2, higher MTBE removal was achieved at lower velocities due to the longer hydraulic residence time (HRT) for the PCO of MTBE molecules in the reactor. Despite the lower initial MTBE concentration in the reactor at higher  $v_{\text{gw}}:v_{\text{MTBE}}$  ratios, the MTBE removal efficiency can be compared directly because the PCO of MTBE is a pseudo first order reaction (Eq. 2.3).

**Table 6.5** Sand tank experimental details and performance of Honeycomb I

Total Velocity (cm d <sup>-1</sup> )	HRT (d)	Total duration (h)	Reaction Duration <sup>a</sup> (h)	Volume treated (L)	$C_{0, \text{MTBE}}$ <sup>b</sup> (mg L <sup>-1</sup> )	MTBE removal (%)	MTBE removed (mg)	$k_{\text{MTBE}}$ (h <sup>-1</sup> )	R <sup>2</sup>
14.2 <sup>c</sup>	1.00	8	8	8	~ 80	84.0	538	0.253	0.95
29.0 <sup>d</sup>	0.60	69	45	23.9	-	-	-	-	-
14.6	1.18	216	120	32.1	~ 41	88.1	1160	0.106	0.98
29.0	0.60	194	74	39.3	~ 30	72.3	853	0.073	0.98
37.3	0.46	120	48	32.8	~ 20	61.9	406	0.091	0.98
15.6 V	1.11	220	148	42.3	~ 32	79.2	1072	0.045	0.99
15.6 TEo-X	1.11	240	147	42.0	~ 30	71.3	898	0.040	0.95
<b>Total</b>		1039	582	212.4		76.2	4389 <sup>e</sup>		

<sup>a</sup> reaction duration include aeration phase as aeration is an essential component of photocatalysis

<sup>b</sup> the initial MTBE concentration in Honeycomb I reactor after aeration phase was initiated (assumed completely mixed).

<sup>c</sup> data from batch experiment using 100 mm (i. d.) Honeycomb II in a 4 L column reactor (Figure 5.11 and Table 4.1) for comparison with sand tank experiment at total velocity of 14.6 cm d<sup>-1</sup>; not included in the total for sand tank experiments.

<sup>d</sup> trial sand tank experiment, the MTBE removal efficiency was not known as the reactor was switched on when the MTBE plume just reached the reactor. The final concentration stabilised at about 6 mg L<sup>-1</sup>.

<sup>e</sup> the total amount of MTBE removed did not include the amount removed in the trial experiment as it was unknown.

The lower MTBE removal efficiency in the 15.6 V experiment compared to that of 14.6 was possibly due to the gradual wearing of the catalyst performance, which could be due to gradual deactivation of active sites on the catalyst surface by adsorbed compound molecules and some catalyst detachment; considering Honeycomb I was submerged in the tank for 10 months. There was some adsorption on the catalyst surface as the catalyst surface was slightly brownish like the sand colour when Honeycomb I was not operated for approximately 4 months after the second sand tank experiment, which was similar to the catalyst in Honeycomb I after completing all the sand tank experiments (Figure 6.18). The slightly higher velocity in the 15.6 V experiment was unlikely to have significant impact on the MTBE removal efficiency of Honeycomb I as the HRT was 1.1 day, which was more than the critical HRT of 1 day. The catalyst performance can be recovered via UVA light irradiation in clean water or baking the catalyst at 500 °C (Bhatkhande et al., 2001).



**Figure 6.18** The catalyst surface was slightly brown like the sand colour 10 months after the reactor was installed and including six sand tank experiments

In the presence of TEO-X, the MTBE removal efficiency decreased about 7.9 % to 71.3 %, which was consistent with the decrease of about 9.1 % in the presence of 20 mg L<sup>-1</sup> TEO-X using Honeycomb II (Figure 5.6). The MTBE removal efficiency of Honeycomb I was not affected as significantly as Honeycomb II due to the significantly lower TEO-X concentrations, mainly toluene and o-xylene, and the absence of dissolved ions. Nevertheless, the presence of TEO-X affected the performance of Honeycomb I due to the competition of radicals among the contaminant molecules and the adsorption of the more strongly adsorbed TEO-X molecules on the catalyst surface, leading to its degradation prior to MTBE molecules and inhibiting the degradation of MTBE (Sahle-Demessie et al., 2002b).

#### 6.3.3.1 Reliability

Honeycomb I was submerged in the reactor chamber for 10 months. Two experiments at 29.0 cm d<sup>-1</sup> were conducted within a month after the installation, achieving 72.3 % MTBE removal (Table 6.5). A subsequent experiment at 14.6 cm d<sup>-1</sup>, which was conducted 5 months later, achieved 88.1 % MTBE removal which compared well with the 84 % MTBE removal achieved using a new set of catalyst in the 4 L column reactor (Table 6.5). This indicates that Honeycomb I still performed similar to a new catalyst after 6 months of submersion. This may be because the number of active sites available for photocatalytic reaction did not reduce significantly, due to negligible MTBE adsorption. Only deaired deionised water passed through the sand tank at 3 cm d<sup>-1</sup> in between sand tank experiments. Conversely, there was a five-fold decline in the photocatalytic activity of Honeycomb I model following 6 hours of methylene blue (MB) adsorption (Figure 4.6), probably because MB

adsorbed on the TiO<sub>2</sub> surface, reducing the number of active sites for the photocatalytic reaction. This implies that, in order to minimise the reduction in the number of active sites with time, (i) the immobilised TiO<sub>2</sub> needs to be continuously illuminated during a treatment to maintain the cyclic photocatalytic reaction at all times to sustain the balance of the overall photocatalytic process and (ii) the long term performance of an immobilised TiO<sub>2</sub> can be affected by the presence of strongly adsorbed groundwater constituents.

### 6.3.3.2 Scale Up

The performance of the two reactor scales tested at similar velocity and HRT (about 1 day) can be compared to evaluate the scale up of the reactor. Table 6.5 shows that the MTBE removal efficiency is maintained by the scaled up Honeycomb I because sufficient time was provided for the MTBE molecules to be in contact with hydroxyl radicals or holes for degradation. Despite both reactor scales having similar MTBE removal efficiency, the 200 mm i.d. Honeycomb I had a lower PCO rate constant of 0.106 h<sup>-1</sup> at a water velocity of 14.6 cm d<sup>-1</sup>, which is about 40 % of that of 100 mm (i. d.) Honeycomb II in the column reactor (0.253 h<sup>-1</sup> at a similar water velocity of 14.2 cm d<sup>-1</sup>) (Table 6.5). Honeycomb I and II both have similar hexagonal structures, with and without radial panels, respectively (Figure 4.3). The lower PCO rate constant in the 200 mm i.d. Honeycomb I, was probably due to the lower UVA illumination (0.3 mW cm<sup>-2</sup>) than that in the column reactor, Honeycomb II (0.9 mW cm<sup>-2</sup>). It should be noted that the latter result is after 8 hours of photocatalytic reaction, thus its potential MTBE removal efficiency is likely to be slightly higher than that of the former (after 30 hours - Figure 6.17). The correlation coefficient R<sup>2</sup> of at least 0.95 indicated that the photocatalytic reaction was of pseudo first order kinetics (Herrmann, 2005). It should be noted that only the initial linear plot of the photocatalytic reaction was considered for measuring the MTBE PCO rate constant, excluding the aeration phase.

As the PCO rate depends on the contact frequency of a contaminant with oxidising/reducing agents, a lower MTBE PCO rate constant in a larger scale reactor is expected due to the longer travel distance to the catalyst. This implies that a larger scale reactor requires longer time to achieve the specific clean-up level, compared to smaller scale reactor. This indicates that a lower MTBE PCO rate constant in a larger scale reactor does not necessarily mean lower MTBE removal efficiency (Section 5.3.4), therefore the rate constant alone is not the main parameter for comparing the performance of reactors without specifying the reactor scale. In addition, during the monitoring of a reactor applied in the field, it is practically simpler to evaluate the reactor efficiency based on the clean-up level, considering the constant fluctuation of groundwater flow and contaminant concentration.

#### 6.3.4 Flushing Phase

The flushing phase was initiated when MTBE injection was stopped about almost 1 day after the aeration was initiated in all the sand tank experiments. It was shown previously (Figure 5.15) in a 4 L column reactor that the MTBE concentration stabilised after about 20 hours of photocatalytic reaction. The MTBE concentration in row D (just before the reactor) only begins to decrease at least 12 hours after MTBE injection was stopped, depending on the groundwater velocity applied. Thus, it does not have immediate effect on the MTBE concentration in the reactor. The MTBE plume eventually cleared up in all the sand tank experiments after 1 to 4 days (about 1 pore volume) from the stopping of MTBE injection depending on the average groundwater velocity applied.

When the MTBE concentration in the reactor stabilised, the flushing phase was initiated by stopping the MTBE injection. The clear up of MTBE plume in both the 15.6 V and 15.6 TEO-X experiments was similar to that of the 14.6 experiment. The second last row in Figure 6.16 ( $t = 168$  h) shows that MTBE and TEO-X migrated at similar rates, which is in agreement with the earlier mentioned co-solvent effect. All the contaminants were cleared out at the end of the sand tank experiments (last row in Figure 6.16).

#### 6.3.5 Cumulative Performance of Honeycomb I

Table 6.5 summarises the details of all the sand tank experiments and performance of Honeycomb I throughout this study. The total effective experimental duration was 1039 hours. Honeycomb I was operated up to 582 hours, removing about 4389 mg MTBE (overall 76.2 % MTBE removal) from the 212.4 L of contaminated groundwater treated.  $R^2$  was more than 0.95 in all the experiments, confirming the PCO of MTBE was a pseudo first order reaction.

The MTBE removal efficiencies in 15.6 V and 15.6 TEO-X were less than 20 % lower than that of 14.6, despite the MTBE PCO rate constant in both experiments was less than half to that of 14.6. This agrees with the double pass flow study (Section 5.3.5) that the MTBE PCO rate constant does not necessarily represent the MTBE removal efficiency of a photocatalytic reactor, especially at slow groundwater flows.

Despite the Honeycomb I efficiency decrease after being submerged for 10 months, Honeycomb I still achieved 71.3 % MTBE removal in the presence of TEO-X. This also demonstrated the reliability of the immobilised catalyst in terms of adhesion to the woven fibreglass and the durability of its performance. Therefore, this can be considered as among the success in the development of Honeycomb I for in-situ groundwater remediation. Nevertheless, the efficiency of this novel reactor design can still be further improved,

especially in terms of the quality of immobilised catalyst and the fine tuning of the UVA light irradiation and dimensions of Honeycomb I via pilot studies in the field.

### 6.3.6 Honeycomb I Observation

Figure 6.19a shows the water in Honeycomb I was slightly turbid after its installation. However, the turbidity in Honeycomb I reduced (Figure 6.19b) as more water was flowed through the tank, indicating the sand filter and 60  $\mu\text{m}$  stainless steel mesh is adequate in separating bigger particles from entering Honeycomb I and minimising the turbidity in Honeycomb I, which can affect the efficiency by inhibiting UVA light from illuminating the catalyst surface. The turbidity and UVA light transmission in Honeycomb I after all the sand tank experiments was below 10 NTU and more than 85%, respectively.

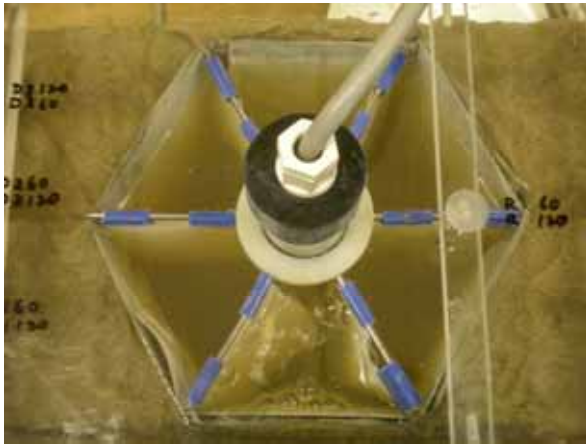


**Figure 6.19a** Honeycomb I after installation



**Figure 6.19b** Honeycomb I after two sand tank experiments

### 6.3.7 Comparison of Reactor Performance

Figure 6.20 shows the MTBE removal efficiency of Honeycomb configurations at various HRTs tested in the flow study in a column reactor (100 mm i.d.) and sand tank (200 mm i.d.). The MTBE removal efficiencies in the column reactor were achieved after 8 hours, while the ones in the sand tank experiments were achieved after 24 hours. The HRT obtained in the scaled up reactor was within the range to that conducted in a column reactor (Section 5.3.4) to validate the trend. HRT refers to the average duration for a contaminant molecule to remain in the reactor. The MTBE removal percentage increased with the HRT, which the trend varies inversely with velocity. The critical HRT appears to be 1 day for both reactor

scales. The scale up of Honeycomb I appeared to be successful as it achieved similar MTBE removal percentage than that of in the column reactor when only MTBE was present.

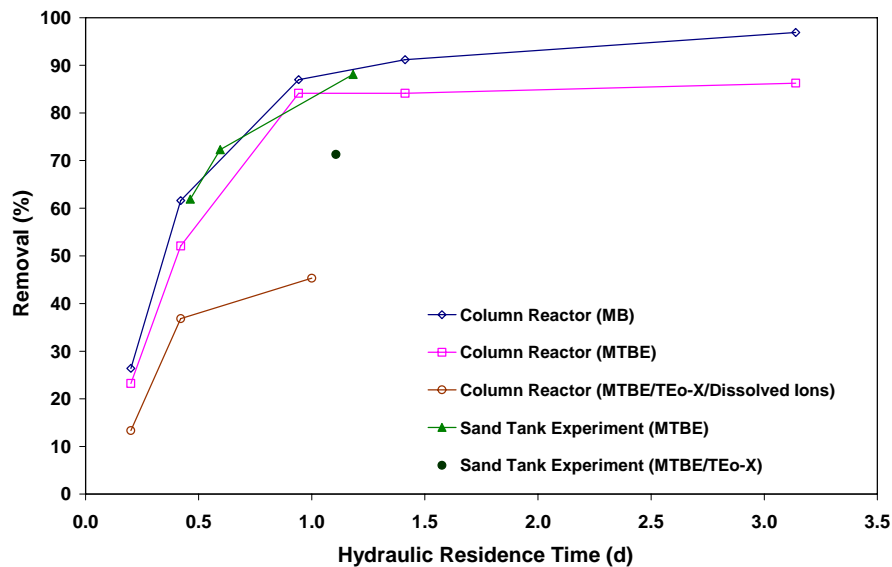


**Figure 6.20** MTBE removal efficiency of the column reactor and sand tank reactor at various HRTs are in agreement, in both cases of MTBE only and MTBE with TEo-X

The generic trends obtained for both scales (Figure 6.20) imply that the performance of Honeycomb I obtained in the sand tank can be applied in monitoring the performance of the photocatalytic reactor in the field. The efficiency of an actual scale module can be tested in the laboratory in order to estimate the efficiency of the photocatalytic reactor system in the field via Eq. 5.1. As the groundwater velocity in a trench system is governed by natural gradient, such plot is a useful reference in monitoring the performance of the reactor in the field. The efficiency of the photocatalytic reactor can be estimated from the trend by obtaining the groundwater velocity on site during the monitoring. Since the area perpendicular to the groundwater flow and the photocatalytic reactor volume is known, the groundwater velocity can be converted to HRT (Eq. 2.26).

In the presence of organic compounds and dissolved ions (Section 5.3.2), a similar trend between the MTBE removal efficiency and HRT was obtained, except with lower MTBE removal efficiencies. The lower MTBE removal efficiency is expected because the presence of other water constituents is likely to compete with MTBE for oxidising agents (radicals and holes on the catalyst surface) generated via activation of catalyst surface by UVA light illumination, which inhibits the PCO of MTBE (Bhatkhande et al., 2001; Sahle-Demessie et al., 2002b; Klauson et al., 2005). The reduction in MTBE removal efficiency in the presence

of organic compounds and dissolved ions at shorter HRTs (higher flows) was not as significant as that at HRT longer than 1 day (Figure 6.20), compared to that of MTBE only. The reduction rate of MTBE removal efficiencies at HRTs of 0.20 and 0.42 day for MTBE only and MTBE with other constituents appeared similar.

As the trend appeared consistent from three flow studies, a sand tank experiment was conducted in the presence of TEO-X at the critical HRT of 1 day. The reduction of Honeycomb I efficiency in the sand tank was not as significant as that of Honeycomb II in the column reactor due to the lower initial TEO-X concentration and also the absence of dissolved ions in Honeycomb I.

## 6.4 Conclusions

The sand tank experiment simulated the MTBE clean-up of an underground storage tank leakage using the Honeycomb I prototype and was tested its efficiency in a relatively long term. From the MTBE migration phase, regular samplings enabled the plotting and measurement of breakthrough curves, which were used to determine the advection, dispersion coefficient and retardation factor using CXTFIT, and MTBE migration in the tank. The ratio of the initial concentration of contaminants in the reactor to that of maximum concentrations in the sand chamber (Figure 6.1b) was proportional to the  $v_{gw}:v_{MTBE}$  ratio. The MTBE plume width became narrower with increasing  $v_{gw}:v_{MTBE}$  ratio. TEO-X migrated through the sand chamber at similar rates to that of MTBE but at significantly lower concentrations via co-solvent effect.

Measurements from two depths showed that aeration completely mixed MTBE in the reactor. Although 25 to 33 % MTBE was vaporised due to aeration in the sand tank, aeration is not expected to pose a significant vaporisation effect in the field due to the lower D/H ratio.

The Honeycomb I prototype achieved up to 88 % MTBE removal when the HRT was slightly more than 1 day. The trend of Honeycomb I efficiency at various HRTs appeared to be generic, based on three flow studies. The similar trend of reactor efficiency against HRT indicated that the reactor performance in the field can be simulated in a column reactor. The PCO of MTBE was inhibited by the presence of TEO-X in the sand tank. The reduction in the turbidity of water in Honeycomb I indicated that the sand filter and 60  $\mu\text{m}$  stainless steel mesh filtered the solids from flowing through Honeycomb I.

Honeycomb I was operated in the sand tank for 10 months throughout this study, using one set of catalyst for 582 h (~ 24 days) and achieved an overall 76.2 % MTBE removal, treating

212.4 L contaminated water. Some reduction in the efficiency of Honeycomb I was observed after being submerged in the sand tank for 10 months, possibly due to gradual deactivation of active sites on the catalyst surface by adsorbed compound molecules and some catalyst detachment. The reliability of the immobilised catalyst and reasonable Honeycomb I efficiency over a 10-month period can be considered among the successes in the development of Honeycomb I for in-situ groundwater remediation.

The scale up of this photocatalytic reactor design was considered successful and demonstrated the potential of Honeycomb I for in-situ groundwater remediation. Nevertheless, the efficiency of this novel reactor design can still be further improved, especially in terms of the quality of immobilised catalyst and the fine tuning of the UVA light irradiation and dimensions of Honeycomb I via pilot studies in the field. The proposed installation options in the field are described in Chapter 7.

## **CHAPTER 7**

# **PROPOSED FIELD SCALE IN-SITU PHOTOCATALYTIC REACTOR INSTALLATION**

### **7.0 Overview**

This chapter is intended to propose an in-situ photocatalytic reactor design based on the photocatalytic efficiency obtained in the experiments in this research. There are not many studies which involve the scaling up of a photocatalytic reactor design for field application. As there is a plethora of design considerations involved and time constraints for this research, only the aspects believed to be amongst the key design considerations were studied. The other important design considerations not studied in this research is recommended as future work in Chapter 8.

This chapter can be divided into 3 parts: design parameters from the experimental data, specifications of material for the field application of in-situ photocatalytic reactor and installation approach of the photocatalytic reactor. The last part involves more consideration for its application on site, dependent on site conditions such as location and concentration of target contaminants.

### **7.1 Introduction**

Many studies do not scale up photocatalytic reactors and it is claimed that they are difficult to scale up due to particularly UVA illumination and mass transfer limitations. Therefore, this research was conducted to study several key design considerations by obtaining data via series of experiments. In designing an in-situ groundwater remediation system, it does not only depend on the reactor design but also the site conditions such as chemical and physical characteristics of groundwater and the type of target contaminant.

## 7.2 Design Parameters and Material Specifications

The design parameters were determined from the experimental results and operating conditions fixed in this research. From these findings, it is clear that materials prone to corrosion should not be used, to minimise the formation of iron oxides, which can affect the turbidity of water in the reactor and inhibit the UVA illumination on the catalyst surface. Therefore, the utilisation of metals should be avoided as much as possible; inert materials which do not corrode and withstand UVA light, such as stainless steel or polymers, is encouraged. It is also recommended to use light weight materials, such as polymers or stainless steel tubes instead of rods.

### 7.2.1 UVA Lamp and Shield Tube

In the literature, many immobilised catalyst and reactor designs were developed but not continued to application in the field. Most of the photocatalytic reactors being scaled up for field application are operated using solar energy. However, in the case of in-situ groundwater remediation, it is difficult to convey sunlight into several meters water depth. Therefore, artificial light sources, i.e. UVA fluorescent lamps emitting a peak wavelength of 365 nm are proposed. As this research is focused on developing a low light intensity photocatalytic reactor for in-situ groundwater remediation and all the experiments in the laboratory have used 15 W UVA Philips Cleo lamps, the field scale photocatalytic reactor will be utilising 1.5 m 100 W UVA fluorescent lamps without reflector. It should be noted that the UVA light intensity of at least  $0.3 \text{ mW cm}^{-2}$  on the catalyst surface is maintained, as used in the sand tank experiments. This implies that the internal diameter of Honeycomb I modules can be greater than the recommended 20 cm as long as the UVA intensity on the catalyst surface is maintained at least  $0.3 \text{ mW cm}^{-2}$ , when a 100 W UVA fluorescent lamp is used. Nevertheless, if the internal diameter is maintained at the recommended 20 cm, higher UVA light intensity on the catalyst surface will enhance the reactor efficiency. It is economical (approximately £10 per unit) and easily available as it is typically used for artificial sun tanning. Low intensity also implies low energy consumption. Solar panels could also be used to operate the reactor, depending on the project and environment. A 100 W UVA Philips Cleo lamp has a length of approximately 1.5 m, which limits the depth of the photocatalytic reactor in the field. It is important for every lamp to be equipped with a safety cut-off device, which automatically switches off the lamp if groundwater gets into the shield tube encasing the lamp, such a device has already been produced by the Electronics Development Group. A 50 mm i.d. borosilicate waterproof shield tube is recommended to be used to protect the lamp from being in contact with water. The shield tube was developed

for Photocat I, which was used in a preliminary groundwater clean-up test in Canada (Chan et al., 2006). Borosilicate glass is proposed instead of quartz because it can transmit a high proportion of UVA light and is more economical than the latter. The shield tube can be used to support the radial panels of Honeycomb I (Figure 7.1). Field testing is required to determine the average lifespan of a UVA fluorescent lamp in order to estimate the replacement interval.

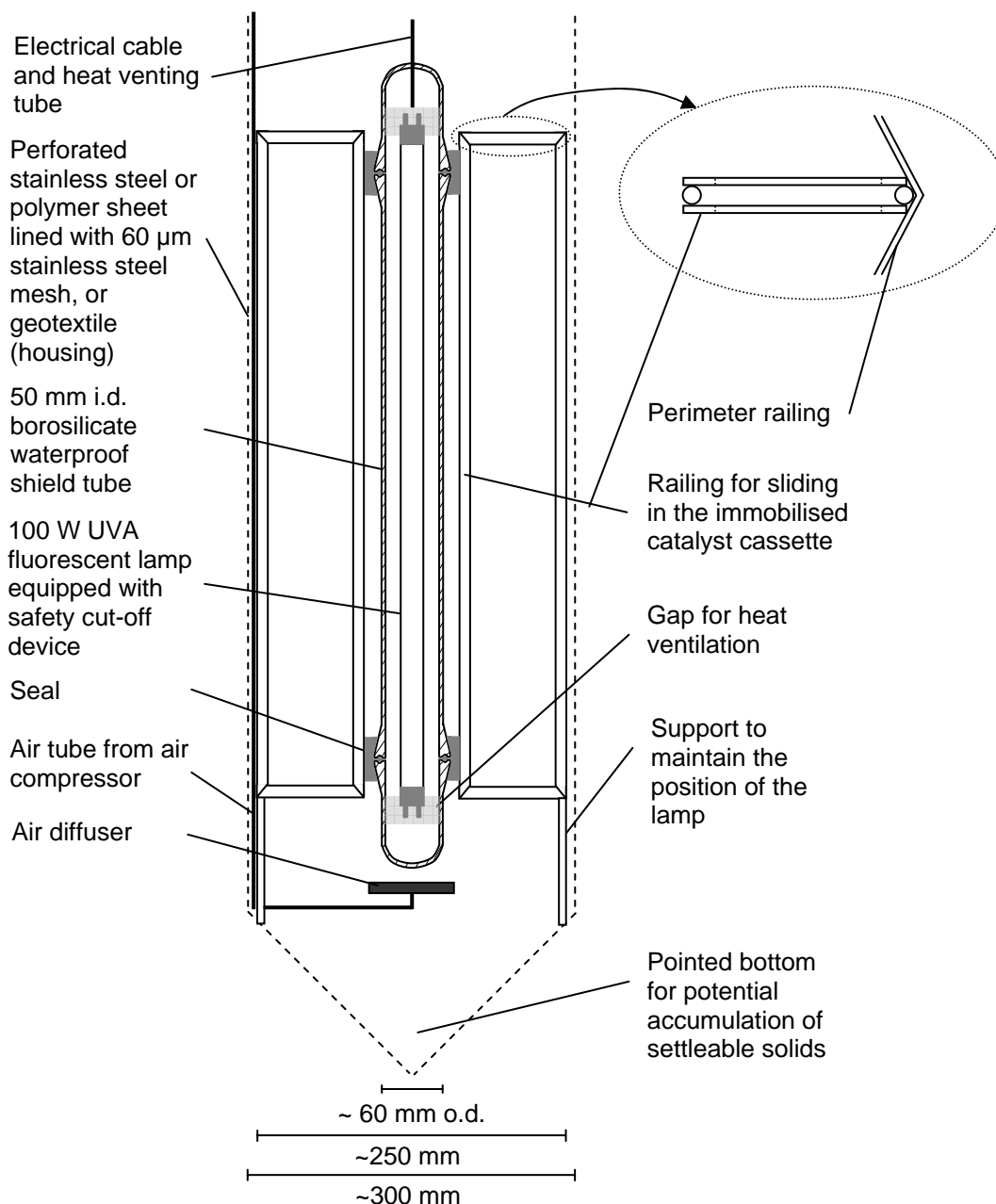


**Figure 7.1** Cross section view of the proposed internal component of Honeycomb I, which is assembled ex-situ prior to installation by lowering into the housing on site. The housing functions as a secondary filter, in addition to the sand filter, to separate solids from entering the reactor and inhibit UVA light illumination on the catalyst surface. The pointed bottom of the housing is for the accumulation of potential settleable solids in the reactor; allows water to flow through and simple maintenance. Inset: Plan view of the railing for sliding in the immobilised catalyst cassettes. The estimated height of Honeycomb I with housing is 2.0 m, yielding D/H ratio of approximately 0.15. Drawing not to scale.

### 7.2.2 Aerator

The air flow to volume ratio recommended for the design of the field scale photocatalytic reactor is  $0.05 \text{ L}_a \text{ min}^{-1} \text{ L}^{-1}$ , equivalent to  $0.05 \text{ m}_a^3 \text{ min}^{-1} \text{ m}^{-3}$ . This implies that a 52 L Honeycomb I module with a depth of 1.5 m (horizontal section of  $0.035 \text{ m}^2$ ) requires air flow of  $2.6 \text{ L}_a \text{ min}^{-1}$ , which is significantly smaller than  $400 \text{ L}_a \text{ min}^{-1}$  using air stripping (US EPA, 2004). Therefore, if a photocatalytic reactor has a horizontal area of  $1 \text{ m}^2$ , a total air flow of  $75 \text{ L}_a \text{ min}^{-1}$  (equivalent air velocity:  $10800 \text{ cm d}^{-1}$ ) is required for the reactor with 1.5 m depth ( $1.5 \text{ m}^3$ ). Chapter 5 demonstrated the importance to control the vaporisation of volatile organic compounds (VOCs). Nevertheless, the air flow to volume ratio in the field scale photocatalytic reactor can be increased if the bubbling does not provide sufficient turbulence to completely mix the contaminant concentrations in the reactor. This is because the aeration is not expected to have significant impact on the vaporisation of VOCs, such as MTBE, due to the significantly smaller D/H ratio in the field scale reactor than that in the laboratory experiments (Section 5.3.1.2).

An air tube is attached along one of the edges of Honeycomb I to the bottom of the reactor (Figure 7.1). The aeration system, which is fixed with the internal components (Figure 7.1), is designed to be connected to the air supply system at the top of the reactor for ease of maintenance, i.e. by detaching the connection prior to withdrawing the internal components. The air compressor to be used should be able to produce greater pressure than the groundwater pressure at the cell. For instance, if the air diffuser is located about 3 m below groundwater level, where the water pressure is about 29.4 kPa or 0.3 bar, the compressor should produce pressure greater than 0.3 bar.

### 7.2.3 Photocatalyst

Similar to the immobilised photocatalyst applied in this research, a hybrid coating of sol gel and Aeroxide  $\text{TiO}_2$  P25 will be dip coated to the  $100 \text{ g m}^{-2}$  woven fibreglass. Hybrid coating has also been used by other researchers in their reactor designs (Balasubramanian et al., 2004; Antoniou and Dionysiou, 2007). Among the advantages of woven fibreglass, it is worth highlighting that woven fibreglass has the structural stability to remain intact after the immobilisation procedure and reliable for application in larger scale reactor, and yet remain porous. Nevertheless, the efficiency of the photocatalytic reactor can be enhanced by using a better coated immobilised photocatalyst.

Based on the sand tank experiments, the total surface area of a 200 mm (i. d.) Honeycomb I is approximately  $1.15 \text{ m}^2 \text{ m}^{-1}$ . At a reactor depth of 1.5 m, the total surface area of catalyst is about  $1.72 \text{ m}^2$ . The average surface area to volume ratio of Honeycomb I is about  $33 \text{ m}^2 \text{ m}^{-3}$ ,

if the depth of the trench is only slightly deeper than the reactor. In terms of reliability, the catalyst is expected to have a reasonable lifespan prior to replacement of catalyst, which can only be known through field testing.

The proposed installation recommends ex-situ assembly of components for quick installation on site. The application of immobilised catalyst cassettes, i.e. hybrid coated  $100 \text{ g m}^{-2}$  woven fibreglass fastened using rectangular frames, enables simple installation and maintenance by slotting it into the railings for radial panels (Figure 7.1), and perimeter panels. There are only two different dimensions of panels, i.e. radial and perimeter panels, used in this proposed field scale reactor design for standard manufacturing and simple installation and maintenance. Perimeter panel refers to the panels arranged around the internal components. The railings for radial panels are attached to the shield tube via the seal. The attachment of railing for perimeter panels to the internal component is optional and dependent on the installation approaches, which will be described in Section 7.4.

#### 7.2.4 Permeable and Impermeable Liner

Two types of liner are required for the field scale photocatalytic reactor, i.e. permeable and impermeable liner. A permeable liner is used as an additional mitigating measure in separating solids as groundwater flows through the reactor, to reduce the turbidity in the reactor and maintain an effective UVA light illumination on the catalyst surface. It is only used for areas perpendicular to groundwater flow (Figure 7.4). An impermeable liner is used to prevent groundwater from flowing into the reactor, typically on the sides of the reactor and parallel to groundwater flow (Figure 7.4). A “trench” sheet pile by Giken can be used as permeable (need to be perforated ex-situ) and impermeable liner, as it also provides geotechnical support by holding the soil from collapsing into the trench. The application of sheet piles for both the proposed approaches is described in Section 7.3.

Alternatively, geosynthetic liners such as geotextiles and geomembranes can be used as permeable and impermeable liners, respectively. Geotextile, a permeable fabric made from polypropylene or polyester, is used in association with soil as filter, reinforcement or protection. With the advancement in technology, the permeability of geotextiles can be controlled during its manufacturing. Although  $60 \mu\text{m}$  stainless steel mesh was used in this research (Section 6.2.2), it would probably be more economical to use geosynthetic liner in the large scale, instead of piles lined with  $60 \mu\text{m}$  stainless steel mesh. Geomembranes, impermeable membranes made from synthetic polymers, are used in association with soil and prevent the migration of fluid.

### 7.2.5 Sand Filter

Grade 'C' sand, with typical sand grains between 300 and 600  $\mu\text{m}$ , is recommended to be used as the sand filter to separate the bigger particles in the groundwater from entering the photocatalytic reactor. In other words, it is required to minimise the turbidity in the photocatalytic reactor, which can inhibit the UVA light from illuminating the immobilised  $\text{TiO}_2$  surface. Grade 'C' sand was selected over Grade 'D' and 'E' sands due to its larger pore size (less clogging) and higher permeability. Nevertheless, the selection of sand filter is dependent on the permeability of soil on site, as the sand filter must be more permeable than the soil on site to encourage groundwater to flow through.

## 7.3 Estimating the Number of Cells Required in Series

The application of in-situ photocatalytic reactor can be economised by constricting the flow through the reactor (Figure 7.4). Fewer units of photocatalytic cells are then required for a narrowed treatment area, if the groundwater flow is slow. Based on the sand tank experiment results, the groundwater velocity can be increased to about 35  $\text{cm d}^{-1}$ , while maintaining the potential contaminant removal efficiency. Alternatively, if groundwater flow is slow and not constricted, the number of rows of photocatalytic cells to achieve the desired clean-up level can be reduced. The number of cells required in series,  $N$ , in order to achieve the required clean-up level can be estimated as follows.

The overall removal efficiency of the reactor with  $N$  units of cell in series,  $R_N$ , can be written as Eq. 7.1. Since the operation of the reactor involves flow, the time,  $t$  in Eq. 2.3 is regarded as the hydraulic residence time (HRT),  $\tau$  in any one cell (Eq. 7.2).

$$R_N = \frac{C_0 - C_N}{C_0} \quad (7.1)$$

$$\frac{C}{C_0} = e^{-k\tau} \quad (7.2)$$

where  $C_0$  is the initial contaminant concentration ( $\text{mg L}^{-1}$ ),  $C_N$  is the regulated or required clean-up concentration ( $\text{mg L}^{-1}$ ),  $\tau$  is the hydraulic residence time ( $\text{d}^{-1}$ ), and  $k$  is the photocatalytic degradation rate of contaminant (refer to Table 5.5 for typical values) ( $\text{d}^{-1}$ ). As

$k$  may vary considerably depending on the target contaminant and composition of groundwater constituents, it is best obtained via laboratory experiments treating the actual groundwater. For example, the  $k_{\text{MTBE}}$  of  $4.8 \text{ d}^{-1}$ , obtained in Chapter 5, can be used in the case of MTBE.

The HRT refers to the average duration,  $\tau$  for a contaminant molecule to remain in a single photocatalytic cell. As groundwater flow is reported in velocity due to the infinite area of a site in hydrogeological studies, there is a need to express the HRT independently. In this case, it is assumed that the area of incoming groundwater flow is the same as the area of the reactor, with reactor volume,  $V = d_c A$ . By substituting Eq. 2.31 into Eq. 2.26,  $\tau$  becomes

$$\tau = \frac{nd_c}{v_D} \quad (7.3)$$

where  $\tau$  is the hydraulic residence time ( $\text{d}^{-1}$ ),  $v_D$  is the Darcy velocity of water ( $\text{m d}^{-1}$ ),  $n$  is the soil porosity and  $d_c$  is the lateral dimension of a single photocatalytic cell (m). Therefore, by substituting Eq. 7.1, 7.2 and 7.3 into Eq. 5.1 becomes

$$\frac{C_0 - C_N}{C_0} = 1 - \left[ e^{-k \left( \frac{nd_c}{v_D} \right)} \right]^N \quad (7.4)$$

$$\frac{Nknd_c}{v_D} = \ln \left( \frac{C_0}{C_N} \right) \quad (7.5)$$

Finally, Eq. 7.6 is obtained by rearranging Eq. 7.5

$$N = \left[ \ln \left( \frac{C_0}{C_N} \right) \right] \times \frac{v_D}{knd_c} \quad (7.6)$$

Eq. 7.6 enables the estimation of the number of cells required in series using the typical information available in a project, such as the initial concentration on site, the regulated concentration for a contaminant, dimension of a modular photocatalytic cell, groundwater

velocity and soil porosity. For example, the estimated numbers of cells required in series to attenuate an initial concentration of 1 or 100 mg L<sup>-1</sup> to a regulated 0.04 mg L<sup>-1</sup> are 3.2 (rounded up to 4) or 5.8 (rounded up to 6), respectively, which appears reasonable and practicable. This estimate assists in estimating the amount and cost of materials required for a photocatalytic reactor in a groundwater remediation project. Eq. 7.6 is therefore useful for indicating the feasibility of in-situ photocatalytic remediation of groundwater for a specific site.

#### 7.4 Installation Approaches

The installation approaches can differ, dependent on the aims of the groundwater remediation project and site conditions, such as the distance of the photocatalytic reactor from the source of pollution, contaminant concentration and the chemical and physical characteristics of groundwater. Although MTBE was used as the target contaminant in this research, photocatalysis can be used for groundwater remediation of other organic contaminant as it is effective in degrading a wide range of organic compounds (Mills et al., 1993; Hoffmann et al., 1995; Herrmann, 2005).

The clean-up level of a groundwater remediation project is typically determined by the regulated limit of target contaminant concentration in groundwater. The regulated limit for MTBE concentration in groundwater is typically 40 µg L<sup>-1</sup> and can be as low as 20 µg L<sup>-1</sup> (Sahle-Demessie et al., 2002b). Therefore, the extent of MTBE clean-up is likely to be dependent on the concentration of the target contaminant at the proposed location of the reactor. MTBE pollution is typically point source pollution as it gets into groundwater via underground storage tank or pipeline leakages. In point source pollution, the concentration of contaminants is the highest within a relatively narrow plume near the source, and reduces as the contaminants migrate further from the source. The MTBE concentration in groundwater can be below 1 mg L<sup>-1</sup> (Sahle-Demessie et al., 2002b) and as high as 830 mg L<sup>-1</sup> (Schmidt et al., 2003). The concentrations of contaminants decrease and the plume widen due to dispersion. The extent of the dispersion depends on the soil characteristics; a contaminant plume is likely to disperse more in soils with finer grain size. In short, a preliminary site characterisation or hydrogeological study is required prior to the reactor design so that contaminant concentrations can be estimated in terms of the width of the plume, and the average velocity and direction of groundwater flow.

In view of the above mentioned nature of point source pollution, two types of design approach are proposed for the installation of the photocatalytic reactor, i.e. sheet pile and intensive clean-up approach. It should be noted that as the arrangement can differ

considerably depending on the site conditions, the descriptions are just guidelines to be considered during the planning stages of a groundwater remediation project.

#### 7.4.1 Sheet Pile Approach

As the name suggests, the sheet pile approach involves the installation of sheet piles into the ground. This approach was suggested by Bolton (2009). Such an approach has the photocatalytic cells spaced across the site like a fence, slightly wider than the plume width of the target contaminant. The sheet pile approach is suitable for cleaning up plumes with low contaminant concentrations, for example below  $1 \text{ mg L}^{-1}$  for MTBE, as the reactors are spaced out to cover a wider plume width, typical at locations further from pollution source. For serial clean-up, several fences of piles can be installed. The conceptual illustration of the sheet pile approach is as shown in Figure 7.2.

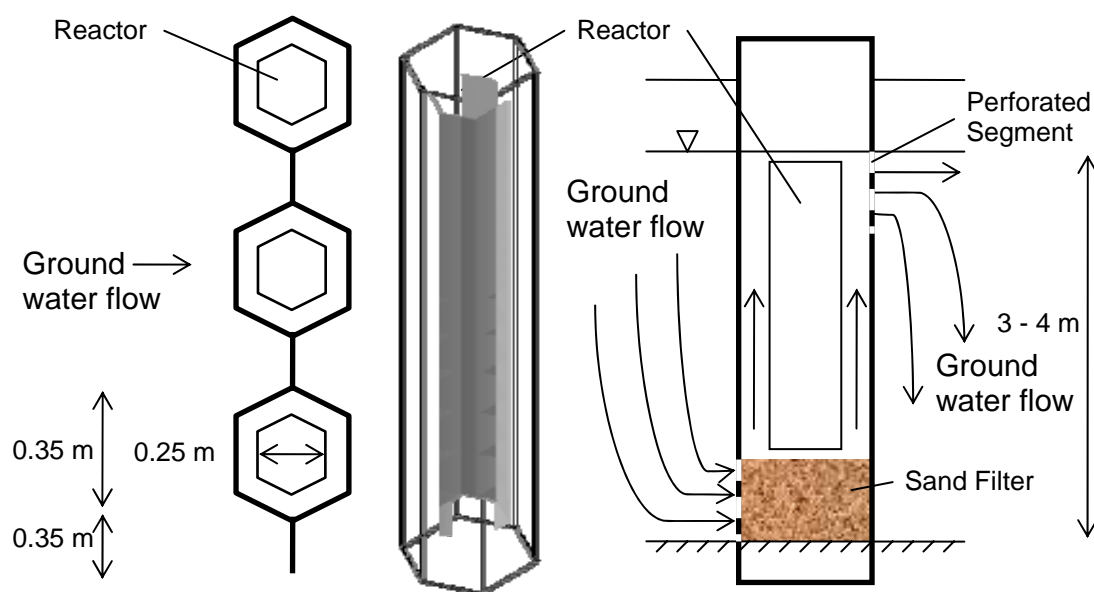


**Figure 7.2** Plan (left), 3-dimensional (centre) and cross section (right) view of the sheet pile approach. Plan and 3-dimensional views show the arrangement of Honeycomb I in a trench made using “zero” sheet pile by Giken. Drawing not to scale.

There are two ways of installation in this case (Figure 7.3), (i) direct piling using a closed end “tubular” pile and (ii) excavation of a trench prior to installation, which is similar to, and will be described under the intensive clean-up approach. For the second way of installation, a trench needs to be excavated to prevent soil in between two “zero” sheet piles (Figure 7.2). Nevertheless, the installation of Honeycomb I using this approach requires a housing, which

consists of perforated polymer or stainless steel sheet lined with 60  $\mu\text{m}$  stainless steel mesh on the outside (Figure 7.1). Housing refers to the structure encasing the internal component. The housing is designed with a pointed bottom for the accumulation of potential settleable solids; allowing water to flow through and for the ease of cleaning during maintenance. The installation methods are dependent on the site conditions, as shown in Figure 7.3. The direct piling method is suitable in the case of plume diving, where the perforation of the pile for groundwater flow can be focused on the postulated elevation of the main plume (Figure 7.2). Plume diving refers to a plume migrating deeper into the aquifer; could be due to geological formation or density of contaminant greater than that of water. The other installation method is suitable for clean-up of a shallow plume. This implies the importance of site characterisation prior to the planning of remediation project and reactor design.

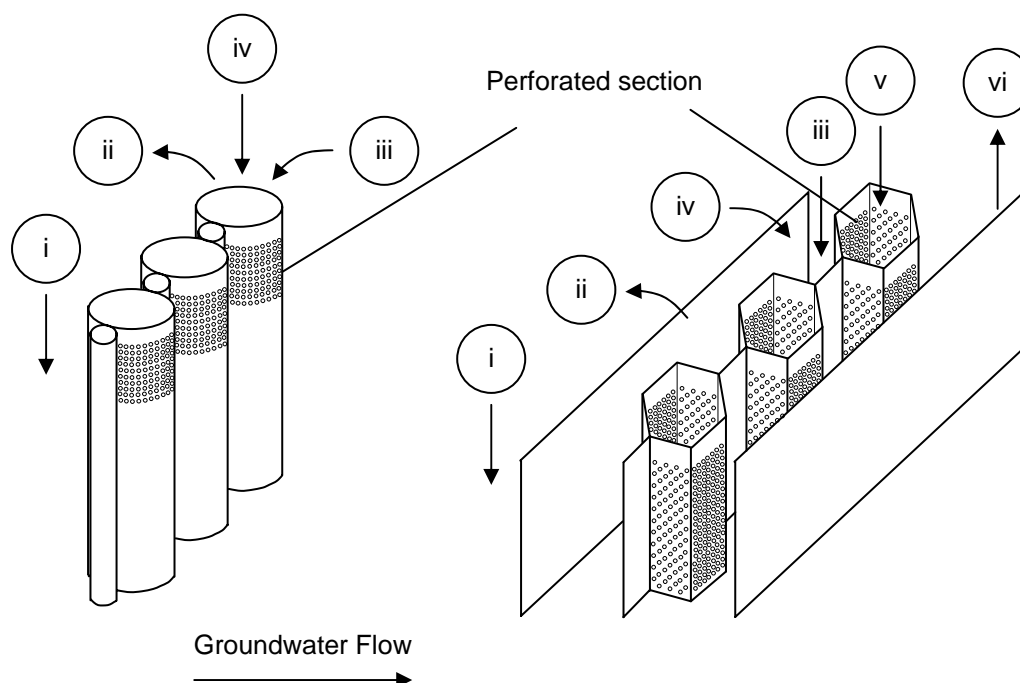


**Figure 7.3** Proposed installation options using the sheet pile approach: closed end “tubular” pile with “P-P” connection (left) and “zero” sheet pile (right). Closed end “tubular” pile: (i) driving in “tubular” piles (ii) purging of groundwater in the pile (iii) filling in sand into “tubular” pile as sand filter, and (iv) installation of housing and Honeycomb I. “Zero” sheet pile: (i) driving in “trench” sheet pile, (ii) excavation of soil (iii) filling in sand as base and installation of “zero” sheet pile, (iv) filling in sand at the vicinity of “zero” sheet piles, (v) installation of housing and Honeycomb I, and (vi) removal of “trench” sheet pile. Drawing not to scale.

This section describes the direct piling method using a closed end “tubular” pile. Using this method, site characterisation is required in order to estimate the depth of the main plume so that the piles can be perforated at the required depth for more effective clean-up of groundwater. A 60  $\mu\text{m}$  stainless steel mesh is to be lined on the inner wall of the perforated sections of the “tubular” pile. The piles are perforated ex-situ, prior to installation. This installation method involves the piling of a closed end 500 mm o.d. “tubular” pile with “P-P” connection by Giken using a silent piling technology, i.e. “tubular” press-in method. One of the advantages of this piling method is its quiet and quick installation. The “P-P” connection is preferred to that of “P-T” connection as it provides wider interlock connection. When the piles are driven into the specified locations, grade ‘C’ sand is filled to about 300 mm above the perforated section at the bottom of the pile (Figure 7.2) to form a filter. This is followed by the installation of the internal components (Figure 7.1) into the “tubular” piles. This method enables quick installation of the reactor on site, estimated to be several days in ideal situations with proper project planning. Although this photocatalytic reactor design is meant for shallow aquifer applications, with careful design, it can also be used for the clean-up of plumes in deep aquifers as the “tubular” pile can be at least 13 m long (Figure 7.2). In view of the spaced out arrangement, the use of individual solar power supplies can be a long term option, considering the low energy requirement by 100 W UVA lamps. The capital cost of a solar power supply may be more expensive, but it eases the maintenance effort and avoids the wiring which can span meters wide.

#### 7.4.2 Intensive Clean-up Approach

The intensive clean-up approach is suitable for cleaning up plumes with high contaminant concentrations as the reactors are arranged adjacent to each other (Figure 7.4). Typically, the plume width is narrower at locations near the pollution source. In contrast to sheet pile installation, the photocatalytic cells are interlocked to enable intensive groundwater remediation. Such an approach can be useful as it offers economic of scale, since the immobilised  $\text{TiO}_2$  can be shared by two adjacent cells, as shown in Figure 7.4. Using this method, site characterisation is required in order to identify a strategic location based on the migration direction of the main plume.

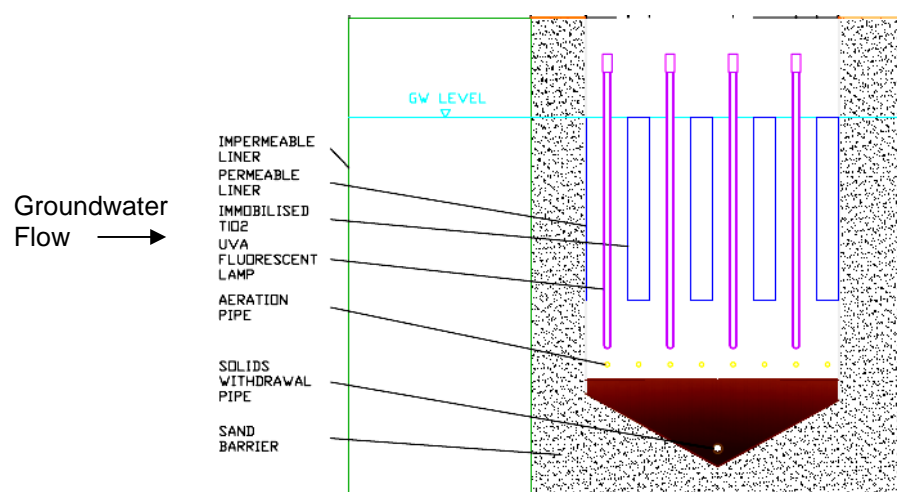
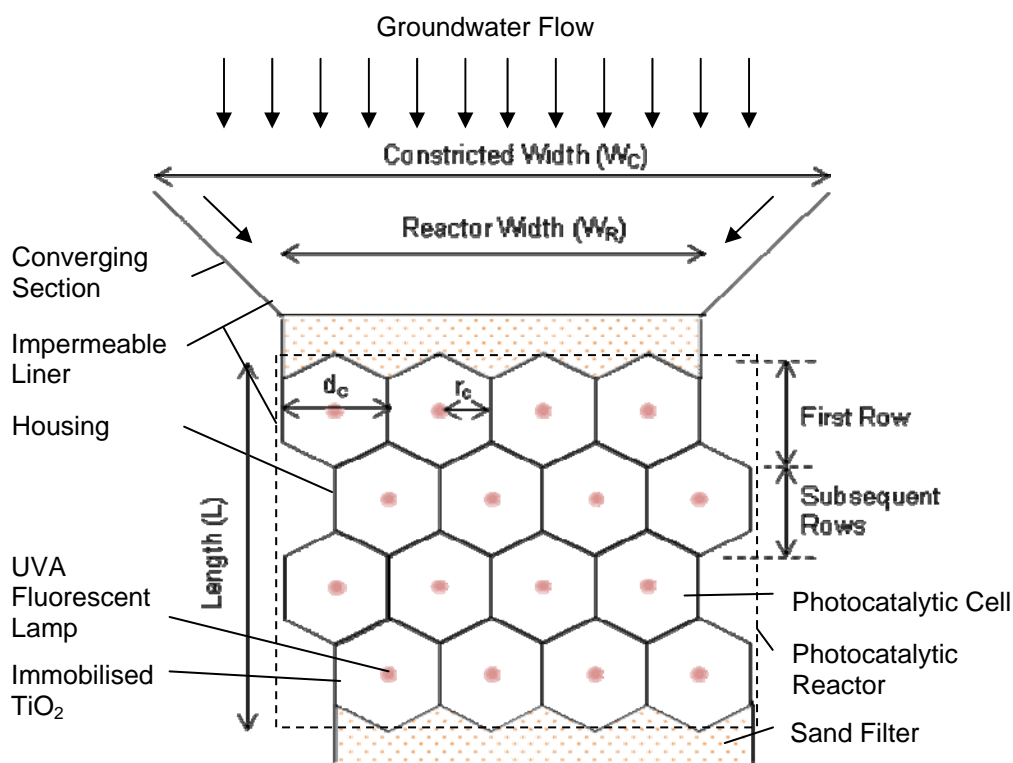


**Figure 7.4** Plan (top) and cross section (bottom) view of the interlocking modules arrangement for intensive groundwater remediation. This arrangement is suitable for the remediation of groundwater with high contamination, typically located near the pollution source. The plan view shows that both sides of the catalyst can be used or shared by adjacent modules, thus maximising the utilisation and cost effectiveness of material. Drawing not to scale.

The proposed installation method requires the excavation of a trench prior to the installation of the reactors. Unlike the direct piling method, this approach is initiated with the installation of “trench” sheet piles at the perimeter of the trench to be excavated to prevent the collapse of soil during the installation works, as well as the converging structure to concentrate groundwater flow into the reactor (Figure 7.4). Perforated “trench” sheet pile, which is perforated ex-situ prior to installation, can be installed for areas perpendicular to groundwater flow to allow passage. As mentioned earlier, a “trench” sheet pile can be used as a geotechnical support structure and liner. When the sheet piles are in place, a trench where the reactor is to be installed is excavated, followed by purging of groundwater. After that, the base of the trench is filled with grade ‘C’ sand, and sloped (for solids withdrawal pipe) (Figure 7.4) and lined with geotextile to maintain the slope. This is followed by the installation of a solids withdrawal pipe (Figure 7.4), with the connection to a pump at ground level to ease maintenance. A submersible pump is not recommended to avoid the removal of pump for maintenance during the operation of the reactor. When the solids withdrawal pipe is installed, the housing can then be installed. Unlike the sheet pile approach, the housing for this approach comprises a frame of interlocking railings, with the housing perimeter covered with liners (Figure 7.5): perforated sheets (stainless steel or polymer) lined with 60  $\mu\text{m}$  stainless steel mesh for areas perpendicular to groundwater flow and sheets (stainless steel or polymer) for areas parallel to the groundwater flow. Similar to the rails for radial panels, interlocking rails are used to slot in perimeter panels. When the housing is in place, grade ‘C’ sand is filled at the vicinity of the housing (Figure 7.4) as sand filter. This is followed by the installation of the internal components (Figure 7.1) and perimeter panels into the housing. The internal components including an air tube, similar to that illustrated in Figure 7.1, except without housing.

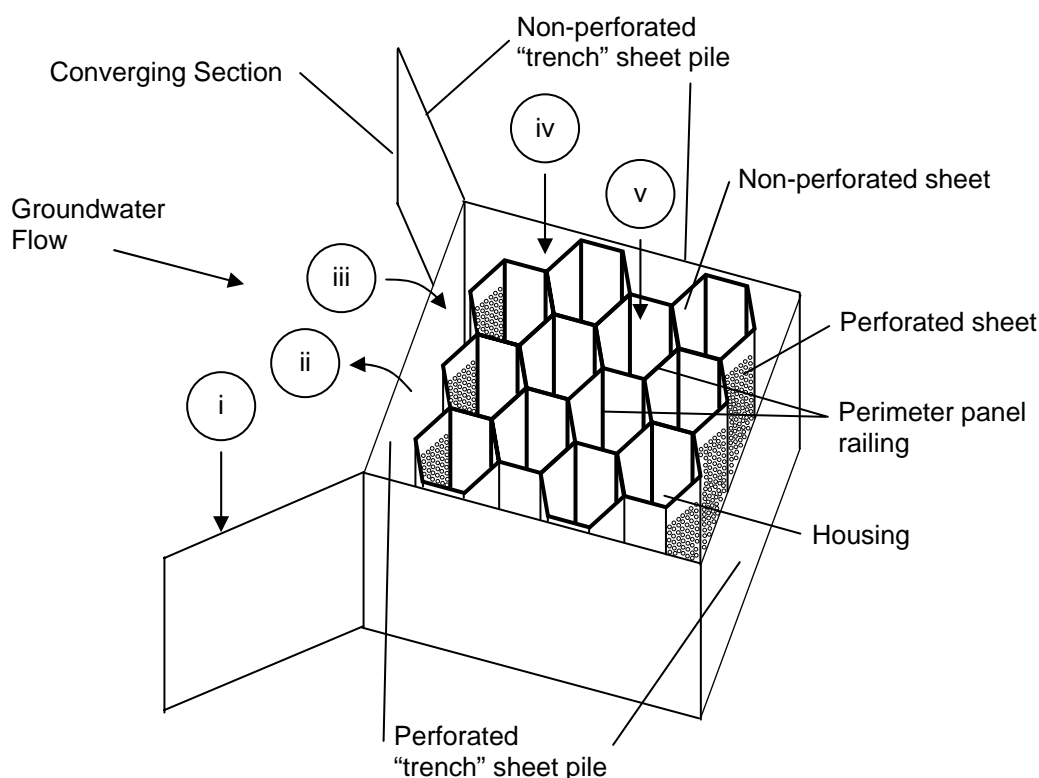


**Figure 7.5** Proposed installation option for intensive clean-up approach: (i) driving in “trench” sheet pile, (ii) excavation of soil and purging of groundwater, (iii) filling in sand as base and installation of housing, (iv) filling in sand at the vicinity of the housing, and (v) installation of Honeycomb I. Non-perforated sheets for housing perimeter are only areas parallel to groundwater flow. There is nothing between the interlocking reactors as perimeter panels are slotted into the perimeter panel railing. Drawing not to scale.

Three differences between the sheet pile approach using “zero” sheet pile and the intensive clean-up approach are that the former requires (i) the non-perforated “trench” sheet pile for the area perpendicular to groundwater flow (step (i) for “zero” sheet pile in Figure 7.3), (ii) the perforated “zero” sheet pile to be lined with 60  $\mu\text{m}$  stainless steel mesh on the outside (step (iii) for “zero” sheet pile in Figure 7.3) and (iii) the “trench” sheet pile needs to be removed upon completing the reactor installation (step (vi) for “zero” sheet pile in Figure 7.3).

Similar to the direct piling method, this method also enables quick installation of the reactor on site. This reactor design is meant for shallow aquifer application. Similar to sheet pile approach, the use of individual solar power supply can be a long term option. In order to prevent mounding, a collection trench at the converging section can be an option (Bowles et al., 2000).

## 7.5 Monitoring Programme

Monitoring of the reactor performance in the field is essential to evaluate efficiency, control maintenance, and keeping a chronological record of the reactor performance. The essential sampling locations in assessing the performance of the reactor are (i) prior to the reactor, (ii) in the reactor and (iii) after the reactor, in order to obtain the removal efficiency of the target contaminant by the reactor. In the initial stages of the operation, it is recommended to conduct multi-level sampling in order to (i) monitor the location of the main plume, (ii) ensure sufficient air flow to achieve complete mix in the reactor and (iii) ensure the target contaminant concentration is reasonably comparable to that in the reactor to indicate the groundwater flow through the reactor. In order to maintain an affordable monitoring cost, the sampling locations can be focused on the sections of significance, typically with higher target contaminant concentration, instead of at every sampling location at pre-determined intervals. The frequency of sampling should be more frequent in the initial stages of the reactor operation in order to obtain the changes in target contaminant concentration. When the target contaminant concentration in the reactor has stabilised, indicating the operation is in its steady state, the sampling frequency and points can be reduced depending on the purpose of the sampling.

## 7.6 Material Cost Estimate

Costs is not mentioned because the series of studies were conducted in the laboratory, thus, does not provide sufficient information to estimate the cost of the reactor including installation. Nevertheless, the total cost for material is estimated about £5,000 m<sup>-3</sup> reactor, in the case of intensive clean-up approach.

The cost estimate for the 1 m width photocatalytic reactor design with 3 arrays encompasses the reactor components only as other cost estimate such as trenching and installation is not available. The cost does not include groundwater monitoring and labour cost.

**Table 7.1** Material cost estimate for 1 m width photocatalytic reactor (2 m deep) with 3 arrays (Figure 7.4)

Description	Units	Unit Cost (£)	Total Cost (£)
<b>Reactor Component</b>			
<b>Lighting</b>			
Glass sleeve	16 pcs	200 /pc	3 200
100 W UVA lamp (5 ft)	16 pcs	10 /pc	160
Power/Main switch	-	-	
Electrical works	-	-	500
		Sub total	3 910
<b>Catalyst</b>			
TiO <sub>2</sub>	0.15 kg L <sup>-1</sup>	46 /kg	373
Chemicals*	3 L m <sup>-2</sup>	30.5 /L	1 647
Woven fibreglass	18 m <sup>2</sup>	4 /m <sup>2</sup>	72
Perforated stainless steel	7 m <sup>2</sup>	33.9 /m <sup>2</sup>	237.30
Internal radial panels	90 sets	2 /set	180
60 µm stainless steel mesh	7 m <sup>2</sup>	85 /m <sup>2</sup>	595
50 mm hollow ss rod for structural support	130 m	5 /m	650
		Sub total	3754.30
<b>Aeration</b>			
Aerator disc	15 pcs	35 /pc	525
Air compressor (120 L min <sup>-1</sup> )	1 unit	100 /unit	100
Air flow meter (0 – 100 L min <sup>-1</sup> )	1 pc	85 /pc	85
Piping or tubing and connectors	-	-	300
		Sub total	1 010
Sand filter (Grade C)	51 bags	30 /25 kg bag	1 530
		<b>Total</b>	<b>10204.30</b>

\* Chemicals: ethanol, isopropanol, titanium (IV) isopropoxide, hydrochloric acid

## 7.7 Conclusions

The field scale in-situ photocatalytic reactor design was proposed to a general extent, to allow modifications for specific site installation. Nevertheless, field testing is required to obtain more information for developing this photocatalytic reactor design. It is hoped that this research, which can be considered to have scaled up the photocatalytic reactor design, can be applied successfully in the field.

## CHAPTER 8

### CONCLUSIONS AND RECOMMENDATIONS

#### 8.1 Conclusions

In this research, a novel photocatalytic reactor design for in-situ groundwater remediation was proposed and developed, from the determination of suitable catalyst immobilisation procedure to the simulation of plume clean-up using a Honeycomb I prototype in a sand tank. All the objectives specified in Section 1.6 are fulfilled. The summary of the main achievements in this research are as follows.

##### *8.1.1 Catalyst Immobilisation*

A suitable catalyst immobilisation procedure, which is simple and economical, was determined prior to the photocatalytic reactor design.

1. Hybrid TiO<sub>2</sub> coating on woven fibreglass demonstrated the best performance, in terms of photocatalytic activity and coating adhesion, among the combinations of coating solution and substrate tested.
2. 5 coating cycles of hybrid coating on woven fibreglass calcined at 500 °C for 1 hour was sufficient to obtain a reliable immobilised catalyst, in terms of photocatalytic activity and durability.
3. The coated samples produced from the scaled up immobilisation procedure exhibited reasonably comparable photocatalytic activity to that of the small scale coating, demonstrating the reproducibility and reliability of the immobilisation procedure.

### 8.1.2 Evaluation of Honeycomb Reactor Model in a Column Reactor

A photocatalytic reactor design, Honeycomb, was proposed for in-situ groundwater remediation. The performance of Honeycomb was assessed and the optimum operating conditions was determined using MB and MTBE.

1. The performance of the photocatalytic reactor appeared to increase proportionally to the increase of surface area to volume ratio, despite that the radially arranged catalyst was receiving lower light intensity compared to that of the catalyst surface arranged perpendicular to the UVA lamp.
2. Continuous aeration is essential for optimising the performance of reactor.
3. The MTBE removal efficiency of the photocatalytic reactor was affected by other constituents.
  - i. Organics: The MTBE removal efficiency of the photocatalytic reactor decreased with increasing TEO-X concentration. The more strongly adsorbed compounds are degraded prior to the less strongly adsorbed compounds.
  - ii. Inorganics: The performance of a photocatalytic reactor is affected by the effect of the dominant ion species, which can suppress the effect of other inhibiting compounds. At low concentrations of dissolved ions, the inhibiting effect of chloride ions appeared to be more pronounced on the MTBE removal efficiency than the beneficial effect of iron. However, the detrimental effect of chloride appeared to be suppressed by the benefits of iron, when sufficient iron is present.
  - iii. Combined: The presence of dissolved ions is believed to have a more significant impact on the PCO of MTBE than that of organic constituents, as ions are more active in OH radical scavenging and deactivation of active sites, besides remaining unaffected by aeration.
4. The single pass flow study on the PCO of MB and MTBE showed that the removal efficiencies of both compounds can be maintained with increasing velocities up to a certain HRT, which the removal efficiency will decrease thereafter. Despite the different adsorption behaviour, the critical HRT for both MB and MTBE degradation was 1 day.
5. A double pass flow study was conducted in the PCO of MTBE, which verified that the photocatalytic reactor performance in the field can be estimated via the sequential order of contaminant removal efficiency in a single pass flow experiment in the laboratory.

### 8.1.3 Simulation of MTBE Plume Clean-up in a Sand Tank

The sand tank experiment simulated the MTBE plume clean-up using a 200 mm i.d. Honeycomb I prototype.

1. The MTBE removal efficiency decreased with increasing flow, i.e. shorter HRT, and also in the presence of other organic compounds, i.e. TEO-X.
2. The study demonstrated the potential of Honeycomb I for in-situ remediation of organics in groundwater as the same set of catalyst and a 15 W Philips Cleo UVA lamp was used over 10 months, with total reactor operation time of 582 hours of the total 1039 hours of sand tank experiments. The overall MTBE removal efficiency of Honeycomb I was 76.2 %.

This research demonstrated the potential of Honeycomb, without process optimisation, for in-situ groundwater remediation, particularly the reliability of the immobilised catalyst through numerous series of experiments.

## 8.2 Recommendations

As this is an initial research phase of a novel photocatalytic reactor design, there are many aspects of the reactor design which needs to be scrutinised for better understanding and development of the reactor design for field application. This research involved somewhat a direct development of a field scale design from laboratory experimental data, with some technical decisions and compromises, due to time constraint resulting limited information for more precise scientific and engineering judgements. There are several recommendations from this research as follows.

### 8.2.1 Field Testing

This research has been studied up to the pilot scale. There is a need to conduct a case study on the remediation of actual MTBE contaminated groundwater using a field scale reactor. The case study could comprise: (i) the field scale reactor construction, (ii) long term reactor efficiency monitoring and (iii) identification of limitations of the field scale reactor and the required maintenance during the operation. The identification of the shortcomings could help to improve or rectify the field scale reactor design proposed in Chapter 7. This is important because some treatment technologies became ineffective after operating for a certain period of time, such as pump-and-treat system (Mackay and Cherry, 1989). The

purpose of this case study is also to obtain a more detailed costing of the field scale photocatalytic reactor encompassing the capital, maintenance and operational costs. The capital cost includes the construction cost and reactor components such as aeration, lighting and power supply systems. The maintenance and operational costs includes energy consumption, replacement or repair of reactor components, monitoring and other costs such as labour cost.

### 8.2.2 Enhancement of Immobilisation Procedure

This research has been emphasized on the configuration of immobilised TiO<sub>2</sub> to obtain a good MTBE clean-up efficiency, particularly by improving the liquid-film transfer of MTBE molecules onto the immobilised TiO<sub>2</sub> surface. Though the hybrid coating is reliable and has a considerable lifespan, there is still some detachment. Therefore, the hybrid coating method in this research needs to be improved particularly in terms of adhesion and stability of coating. Prof Mills suggested, in his email correspondence, the addition of polyethylene glycol (PEG) during the preparation of sol gel solution, prior to addition of Aeroxide TiO<sub>2</sub> P25, can produce a mesoporous film and improve the stability and adhesion of coating. The cracking and detachment of the hybrid coating could be minimised if (i) the hybrid solution was sonicated for about 3 minutes prior to dip coating, to enhance the dispersion of the P25 powder for smoother coating, (ii) slower dip coating velocity of approximately 2 mm s<sup>-1</sup> to yield better film via multiple thinner films by every coating cycle and (iii) addition of surfactant such as Tween 20 to reduce the possibility of cracking by improving the wettability of film and reducing surface tension of water (Chen and Dionysiou, 2008).

As this research demonstrated that the presence of 50 mg L<sup>-1</sup> iron enhanced the reactor performance despite of competition with other groundwater constituents, the performance of the catalyst could be enhanced by doping with metal, which minimises the electron-hole recombination.

The woven fibreglass have been used in this study mainly because (i) of its compatible chemical and physical properties for immobilisation of TiO<sub>2</sub> sol gel, (ii) it could withstand calcination temperature of 500 °C during immobilisation procedure, (iii) easily obtainable and affordable and (iv) structurally stable and manageable, and not fragile. However, some detachment of immobilised TiO<sub>2</sub> was due to its flexibility, in which the coating would crack and detach when the coated woven fibreglass was bent. Therefore, the woven fibreglass was cut into small pieces to avoid bending during its installation onto the perforated reactor wall. Although woven fibreglass is a suitable substrate particularly dip coating of viscous

solution, it can be replaced by other substrate deemed more suitable based on the coating method.

### 8.2.3 Process Optimisation

If the extensive studies for building a formal numerical model have been conducted, the depth of understanding on the interferences of groundwater constituents on the PCO rate constant of a target contaminant should be sufficient for optimising the reactor efficiency. Many studies have demonstrated the effect of dissolved ions, both cation and anion, on the photocatalytic oxidation of a target contaminant (Butler and Davis, 1993; Mills et al., 1993; Bhatkhande et al., 2001; Liao et al., 2001; Klauson et al., 2005). However, these studies have tested only one type of dissolved ion in their experiments. It is important to test in the presence of more than one type of groundwater constituent, as groundwater consists of complex matrices of constituents, which vary significantly from site to site; some with high organic content while others might contain high dissolved ions.

In this research, a systematic study was conducted to observe the effects of organic compounds, dissolved ions and combination of both organic compounds and dissolved ions on the PCO of MTBE. While the PCO of MTBE decreased with increasing TEO-X concentration, the effect of dissolved ions was somewhat more complicated. The degradation of organic compounds could be expedited by adding oxidising agents. As for dissolved ions, it is probably true that pH adjustment is more effective than removal of chloride ion, as pH adjustment also affects other dissolved ions. However, the complication of pH adjustment comes in when the optimum pH is narrowed by ions which require the other extreme pH for minimised effect on the scavenging of electrons, for example the optimum pH is between 5 and 7 in the presence of both bicarbonate and chloride ions (Liao et al., 2001). Mehos and Turchi (1993) observed about 5-fold increase in the photocatalytic degradation rate constants of TCE in groundwater when the groundwater pH was adjusted from 7 to 5.

Therefore, a comprehensive study is required for further understanding on these interferences for enhancement and better projection of the photocatalytic reactor efficiency in the field, based on the characterisation of groundwater constituents. Some experiments treating actual groundwater from several sites needs to be conducted for validation of understanding obtained from the comprehensive study.

#### 8.2.4 *Combination with Electrokinetics*

In the case of groundwater with high concentration of dissolved ions, another alternative to pH adjustment is to combine photocatalysis with electrokinetics, which separates the dissolved ions from the groundwater prior to the photocatalytic reactor using electric potentials. The application of electrokinetics, which can be powered using solar panels, can help to avoid continual chemical addition for pH adjustment, thus minimise operation and maintenance activities and costs. It should be noted that there will be opposite extreme pH on both electrodes.

#### 8.2.5 *Study on the Effect of Ethanol*

It is strongly recommended for the next research to investigate the reactor efficiency in degrading ethanol, in the synthesized groundwater with known constituents and actual groundwater. Ethanol is chosen as the next target contaminant as it is widely used in reformulated gasoline, following the ban of MTBE due to its detrimental effects in groundwater. Although ethanol is biodegradable, there is no concrete evidence to support this claim in the case of a large amount of ethanol release into groundwater through leakages of underground storage tanks and transfer pipelines. Unlike benzene, toluene, ethylbenzene and xylene (BTEX), ethanol has lower Henry's law constant than that of MTBE (US EPA, 2004), thus, remediation technologies such as air stripping might not be effective in removing ethanol from groundwater.

Ethanol significantly inhibits the biodegradation of the less readily biodegradable BTEX, which is the reverse effect in the presence of MTBE, implying BTEX plume would be extended (Da Silva and Alvarez, 2002). In addition, ethanol has a significantly greater co-solvent effect than MTBE (Groves, Jr., 1988), resulting in the reduction of the retardation factor and enhancing the mobility of organic contaminants (Alberici et al., 2002; Da Silva and Alvarez, 2002). Both of these phenomena are likely to increase the concentration of organic contaminants in the leading plume. Therefore, it is essential for this study to be conducted in order to reinforce this reactor design as an alternative to the existing groundwater remediation technologies. It may be interesting to observe the effect of ethanol on the existing organic contaminant plumes. This can be simulated in a sand tank experiment by injecting MTBE/TEo-X into the sand chamber, followed by ethanol; using the similar sand tank experiment procedure.

### 8.2.6 Numerical Modelling

As this is the initial research proposing a new reactor design, this research was focused on obtaining concrete evidence through experimental data to validate the potential of photocatalytic reactor design for in-situ groundwater remediation. Consequently, this research did not involve numerical modelling of this photocatalytic reactor design because the experimental data obtained was not sufficient for a formal numerical modelling of this reactor design. It is important to understand how the presence of groundwater constituents affect the PCO rate constant of a target contaminant, whether organic compounds can be accumulated as total organic carbon for the analysis. In terms of the catalyst efficiency, many extensive studies may be required to obtain the specific constants for an equation or coefficients, for instance adsorption, as the degradation rates of compounds vary significantly (Ryu and Choi, 2008). The photocatalytic reactor efficiency is significantly affected by the presence of groundwater constituents, which varies diversely from site to site. Therefore, an extensive experimental study needs to be conducted at various known concentrations of organic and inorganic compounds in order to, hopefully, provide sufficient information for building a formal numerical model. The modelling of this reactor would be useful for the understanding of the reactor and prediction of reactor efficiency, without experiments.

## References

- Agustina, T. E., Ang, H. M., Vareek, V. K. (2005) A Review of Synergistic Effect of Photocatalysis and Ozonation on Wastewater Treatment. *Journal of Photochemistry and Photobiology C: Photochemistry Reviews*, 6 (4), 264-273.
- Alberici, R. M., Zampronio, C. G., Poppi, R. J., Eberlin, M. N. (2002) Water Solubilisation of Ethanol and BTEX from Gasoline: On-line Monitoring by Membrane Introduction Mass Spectrometry. *Analyst*, 127, 230-234.
- Alfano, O. M., Bahnemann, D., Cassano, A. E., Dillert, R., Goslich, R. (2000) Photocatalysis in Water Environments using Artificial and Solar Light. *Catalysis Today*, 58, 199-230.
- Almquist, C. B., Sahle-Demessie, E., Enriquez, J., Biswas, P. (2003) The Photocatalytic Oxidation of Low Concentration MTBE on Titanium Dioxide from Groundwater in a Falling Film Reactor. *Environmental Progress*, 22 (1), 14-23.
- An, Y.-J., Kampbell, D. H., Cook, M. L. (2002) Co-Occurrence of MTBE and Benzene, Toluene, Ethylbenzene, and Xylene Compounds at Marinas in Large Reservoir. *Journal of Environmental Engineering*, 128 (9), 902-906.
- Antoniou, M. G., Dionysiou, D. D. (2007) Application of Immobilized Titanium Dioxide Photocatalysts for the Degradation of Creatinine and Phenol, Model Organic Contaminants Found in NASA's Spacecrafts Wastewater Streams. *Catalysis Today*, 124 (3-4), 215-223.
- Bahnemann, D. (2004) Photocatalytic Water Treatment: Solar Energy Applications. *Solar Energy*, 77, 445-459.
- Balasubramanian, G., Dionysiou, D. D., Suidan, M. T., Baudin, I., Laine, J.-M. (2004) Evaluating the Activities of Immobilized TiO<sub>2</sub> Powder Films for the Photocatalytic Degradation of Organic Contaminants in Water. *Applied Catalysis B: Environmental*, 47(2), 73-84.
- Balasubramanian, G., Dionysiou, D. D., Suidan, M. T., Subramanian, V., Baudin, I., Laine, J.-M. (2003) Titania Powder Modified Sol-gel Process for Photocatalytic Applications. *Journal of Material Science*, 38, 823-831.
- Barreto, R. D., Gray, K. A., Anders K. (1995) Photocatalytic Degradation of Methyl-tert-butyl Ether in TiO<sub>2</sub> Slurries: A Proposed Reaction Scheme. *Water Research*, 29 (5), 1243-1248.
- Bhatkhande, D. S., Pangarkar, V. G., Beenackers, A. A. C. M. (2001) Photocatalytic Degradation for Environmental Applications – A Review. *Journal of Chemical Technology & Biotechnology*, 77 (1), 102-116.

- Bisio, A., Kabel, R. L. (1985) Scale up of Chemical Processes: Conversion from Laboratory Scale Tests to Successful Commercial Size Design. John Wiley and Sons. Inc., U. S. A.
- Bolton, M. D. (1979) A Guide to Soil Mechanics, Macmillan Education, Ltd, London.
- Bolton, M. D. (2009) Personal communication.
- Boulding, J. R. (1995) Practical Handbook of Soil, Vadose Zone and Groundwater Contamination: Assessment, Prevention and Remediation. CRC Press LLC, U. S. A.
- Bowles, M. W., Bentley, L. R., Hoyne, B., Thomas, D. A. (2000) In Situ Ground Water Remediation Using the Trench and Gate System. *Ground Water*, 38 (2), 172-181.
- Braham, R. J., Harris, A. T. (2009) Review of Major Design and Scale-up Considerations for Solar Photocatalytic Reactors. *Industrial & Engineering Chemistry Research*, 48 (19), 8890-8905.
- Brezova, V., Blazkova, A., Karpinsky, L., Groskova, J., Havlinova, B., Jorik, V., Ceppan, M. (1997) Phenol Decomposition using  $M^{n+}/TiO_2$  Photocatalysts Supported by the Sol-gel Technique on Glass Fibers. *Journal of Photochemistry and Photobiology A: Chemistry*, 109, 177-183.
- Butler, E. C., Davis, A. P. (1993) Photocatalytic Oxidation in Aqueous Titanium Dioxide in Suspensions: The Influence of Dissolved Transition Metals. *Journal of Photochemistry and Photobiology A: Chemistry*, 70 (3), 273-283.
- Chan, M. S. M. (2005) Photocatalytic Remediation of Organics in Groundwater, PhD Thesis, University of Cambridge, U. K.
- Chan, M. S. M., Lynch, R. J. (2003a) Photocatalytic Degradation of Aqueous Methyl-tert-butyl-ether (MTBE) in a Supported-catalyst Reactor. *Environmental Chemistry Letters*, 1 (3), 157-160.
- Chan, M. S. M., Lynch, R. J. (2003b) Photocatalytic Remediation of MTBE in Groundwater. *Proceedings of the 8th International FZK/TNO Conference on Contaminated Soil (ConSoil)*, ICC Gent, Belgium, 12-16 May.
- Chan, M. S. M., Lynch, R. J., Rolt, S. (2006) Design of Underground Photocatalytic Reactor for Borden Test, University of Cambridge, U. K. (unpublished work).
- Chang, C.-C., Chen, J.-Y., Hsu, T.-L., Lin, C.-K., Chan, C.-C. (2008) Photocatalytic Properties of Porous  $TiO_2/Ag$  Thin Films. *Thin Solid Films*, 516, 1743-1747.
- Chang, H. T., Wu, N.-M., Zhu, F. (2000) A Kinetic Model for Photocatalytic Degradation of Organic Contaminants in a Thin-film  $TiO_2$  Catalyst. *Water Research*, 34 (2), 407-416.

- Chen, Y. J., Dionysiou, D. D. (2006a) TiO<sub>2</sub> Photocatalytic Films on Stainless Steel: The Role of Degussa P-25 in Modified Sol-gel Methods. *Applied Catalysis B: Environmental*, 62, 255-264.
- Chen, Y. J., Dionysiou, D. D. (2006b) Effect of Calcination Temperature on the Photocatalytic Activity and Adhesion of TiO<sub>2</sub> Films Prepared by the P-25 Powder-modified Sol-gel Method. *Journal of Molecular Catalysis A: General*, 244 (1-2), 73-82.
- Chen, Y. J., Dionysiou, D. D. (2006c) Correlation of Structural Properties and Film Thickness to Photocatalytic Activity of Thick TiO<sub>2</sub> Films Coated on Stainless Steel. *Applied Catalysis B: Environmental*, 69 (1-2), 24-33.
- Chen, Y. J., Dionysiou, D. D. (2008) Bimodal Mesoporous TiO<sub>2</sub>-P25 Composite Thick Films with High Photocatalytic Activity and Improved Structural Integrity. *Applied Catalysis B: Environmental*, 80, 147-155.
- Chisala, B. N., Tait, N. G., Lerner, D. N. (2007) Evaluating Risks of Methyl Tertiary Butyl Ether (MTBE) Pollution of Urban Groundwater. *Journal of Contaminant Hydrology*, 91, 128-145.
- Da Silva, M. L. B., Alvarez P. J. J. (2002) Effects of Ethanol Versus MTBE on Benzene, Toluene, Ethylbenzene, and Xylene Natural Attenuation in Aquifer Columns. *Journal of Environmental Engineering*, 128 (9), 862-867.
- Davis, L. C., Erickson, L. E. (2004) A Review of Bioremediation and Natural Attenuation of MTBE. *Environmental Progress*, 23 (3), 243-252.
- de Lasa, H., Serrano, B., Salaiques, M. (2005) Photocatalytic Reaction Engineering, Springer, U. S. A.
- Deeb, R. A., Scow, K. M., Alvarez-Cohen, L. (2000) Aerobic MTBE Biodegradation: An Examination of Past Studies, Current Challenges and Future Research Directions. *Biodegradation*, 11 (2-3), 171-186.
- Dionysiou, D. D., Balasubramanian, G., Suidan, M. T., Khodadoust, A. P., Baudin, I., Laine, J.-M. (2000a) Rotating Disk Photocatalytic Reactor: Development, Characterization, and Evaluation for the Destruction of Organic Pollutants in Water. *Water Research*, 34 (11), 2927-2940.
- Dionysiou, D. D., Khodadoust, A. P., Kern, A. M., Suidan, M. T., Baudin, I., Laine, J.-M. (2000b) Continuous-mode Photocatalytic Degradation of Chlorinated Phenols and Pesticides in Water using a Bench-scale TiO<sub>2</sub> Rotating Disk Reactor. *Applied Catalysis B: Environmental*, 24 (3-4), 139-155.

- Dionysiou, D. D., Suidan, M. T., Bekou, E., Baudin, I., Laine, J.-M. (2000c) Effect of Ionic Strength and Hydrogen Peroxide on the Photocatalytic Degradation of 4-Chlorobenzoic Acid in Water. *Applied Catalysis B: Environmental*, 26 (3), 153-171.
- Dionysiou, D. D., Burbano, A. A., Suidan, M. T., Baudin I., Laine, J.-M. (2002) Effect of Oxygen in a Thin-film Rotating Disk Photocatalytic Reactor. *Environmental Science & Technology*, 36 (17), 3834-3843.
- Domenico, P. A., Schwartz, F. W. (1997) Physical and Chemical Hydrogeology, Second Edition. John Wiley and Sons, Inc. U. S. A.
- Drinking Water Inspectorate (DWI) (2009) DWI Water Hardness, <http://www.dwi.gov.uk/consumer/faq/hardness.htm>. Accessed on 21 July 2009.
- Dutta, P. K., Pehkonen, O., Sharma, V. K., Ray, A. K. (2005) Photocatalytic Oxidation of Arsenic (III): Evidence of Hydroxyl Radicals. *Environmental Science & Technology*, 39, 1827-1834.
- Egerton, T. A., King, C. J. (1979) The Influence of Light Intensity on Photoactivity in TiO<sub>2</sub> Pigmented Systems. *Journal of the Oil and Colour Chemists Association*, 62 (10), 386-391.
- Energy Information Administration (EIA) (2010) Eliminating MTBE in Gasoline in 2006, [http://www.eia.doe.gov/pub/oil\\_gas/petroleum/feature\\_articles/2006/mtbe2006/mtbe2006.pdf](http://www.eia.doe.gov/pub/oil_gas/petroleum/feature_articles/2006/mtbe2006/mtbe2006.pdf), assessed on 10 January 2010.
- Energy Information Administration (EIA) (2010) Status and Impact of State MTBE Bans, [www.eia.doe.gov/oiaf/servicerpt/mtbeban/pdf/mtbe.pdf](http://www.eia.doe.gov/oiaf/servicerpt/mtbeban/pdf/mtbe.pdf), assessed on 10 January 2010.
- European Commission (2000) Directive 2000/60/EC: Establishing a Framework for Community Action in the Field of Water Policy (OJ L327).
- European Commission (2006) Directive 2006/118/EC: On the Protection of Groundwater against Pollution and Deterioration (OJ L372).
- Fetter, C. W. (1999) Contaminant Hydrogeology, Second Edition. Wiley and Sons. Inc., the U. S. A.
- Fischer, A., Müller, M., Klasmeier, J. (2003) Determination of Henry's Law Constant for Methyl Tert-butyl Ether (MTBE) at Groundwater Temperatures. *Chemosphere*, 54, 689-694.
- Fox, M. A., Dulay, M. T. (1993) Heterogeneous Photocatalysis. *Chemical Reviews*, 93, 341-357.
- Freeze, R. A., Cherry, J. A. (1979) Groundwater. Prentice Hall, Inc., U. S. A.

- Fretwell, R., Douglas, P. (2001) An Active, Robust and Transparent Nanocrystalline Anatase TiO<sub>2</sub> Thin Film - Preparation, Characterisation and the Kinetics of Photodegradation of Model Pollutants. *Journal of Photochemistry and Photobiology A: Chemistry*, 143 (2-3), 229-240.
- Fujishima, A., Rao, T. N., Tryk, D. A. (2000) Titanium Dioxide Photocatalysis. *Journal of Photochemistry and Photobiology C: Photochemistry Reviews*, 1 (1), 1-21.
- Garoma, T., Gurol, M. D., Osibodu, O., Thotakura, L. (2008) Treatment of Groundwater Contaminated with Gasoline Components by an Ozone/UV Process. *Chemosphere*, 73 (5), 825-831.
- Garoma, T., Gurol, M. T. (2006) Oxidation of Methyl *tert*-butyl Ether in Aqueous Solution by an Ozone/UV Process. *Journal of Environmental Engineering*, 132 (11), 1404-1412.
- Gibbs, J. T., Williamson, T. K. J., Naber, S. J., Macchiarella, T. L. (2002) Multiple Methods for Determining Stability of Attenuating MTBE Groundwater Plume. *Journal of Environmental Engineering*, 128 (9), 891-901.
- Groves Jr., F. R. (1988) Effect of Cosolvents on the Solubility of Hydrocarbons in Water. *Environmental Science & Technology*, 22(3), 282-286.
- Guerin, T. F., Horner, S., McGovern, T., Davey, B. (2002) An Application of Permeable Reactive Barrier Technology to Petroleum Hydrocarbon Contaminated Groundwater. *Water Research*, 36, 15-24.
- Gurol, M. D., Akata, A. (1996) Kinetics of Ozone Photolysis in Aqueous Solution. *AIChE Journal*, 42 (11), 3283-3292.
- Herrmann, J.-M. (2005) Heterogeneous Photocatalysis: State of the Art and Present Applications. *Topics in Catalysis*, 34 (1-4), 49-65.
- Hoffmann, M. R., Martin, S. T., Choi, W. Y., Bahnemann D. W. (1995) Environmental Applications of Semiconductor Photocatalysis. *Chemical Reviews*, 95, 69-96.
- Hossain, M. M., Raupp, G. B., Hay, S. O., Obee, T. N. (1999) Three-dimensional Developing Flow Model for Photocatalytic Monolith Reactors. *AIChE Journal*, 45 (6), 1309-1321.
- Houas, A., Lachheb, H., Ksibi, M., Elaloui, E., Guillard, C., Herrmann, J.-M. (2001) Photocatalytic Degradation Pathway of Methylene Blue in Water. *Applied Catalysis B: Environmental*, 31 (2), 145-157.
- Jacobs, J., Guertin, J., Herron, C. (2001) MTBE: Effects on Soil and Groundwater Resources, CRC Press, Inc., Florida, U. S. A..

- Johnson, R., Pankow, J., Bender, D., Price, C., Zogorski, J. (2000) MTBE to What Extent Will Past Releases Contaminate Community Water Supply Wells? *Environmental Science & Technology*, 34 (9), 2A-9A.
- Juhler, R. K., Felding, G. (2003) Monitoring methyl tertiary butyl ether (MTBE) and other organic micropollutants in groundwater: Results from the Danish National Monitoring Program. *Water, Air and Soil Pollution*, 149 (1-4), 145-161.
- Kabra, K., Chaudhary, R., Sawhney, R. L. (2004) Treatment of Hazardous Organic and Inorganic Compounds through Aqueous-Phase Photocatalysis: A Review. *Industrial & Engineering Chemistry Research*, 43 (24), 7683-7696.
- Kane, S. R., Beller, H. R., Legler, T. C., Koester, C. J., Pinkart, H. C., Halden, R. U., Happel, A. M. (2001) Aerobic Biodegradation of Methyl Tert-butyl Ether by Aquifer Bacteria from Leaking Underground Storage Tank Sites. *Applied Environmental Microbiology*, 67 (12), 5824-5829.
- Keshmiri, M., Mohseni, M., Troczynski, T. (2004) Development of Novel TiO<sub>2</sub> Sol-gel-derived Composite and its Photocatalytic Activities for Trichloroethylene Oxidation. *Applied Catalysis B: Environmental*, 53, 209-219.
- Kiriakidou, F., Kondarides, D. I., Verykios, X. E. (1999) The Effect of Operational Parameters and TiO<sub>2</sub>-doping on the Photocatalytic Degradation of Azo-dyes. *Catalysis Today*, 54, 119-130.
- Klauson, D., Preis, S., Portjanskaja, E., Kachina, A., Krichevskaya, M., Kallas, J. (2005) The Influence of Ferrous/Ferric Ions on the Efficiency of Photocatalytic Oxidation of Pollutants in Groundwater. *Environmental Technology*, 26 (6), 653-661.
- Kontos, A. I., Arabatzis, I. M., Tsoukleris, D. S., Kontos, A. G., Bernard, M. C., Petrakis, D. E., Falaras, P. (2005) Efficient Photocatalyst by Hydrothermal Treatment of TiO<sub>2</sub>. *Catalysis Today*, 101, 275-281.
- Kostarelos, K., Pope, G. A., Rouse, B. A., Shook, G. M. (1998) A New Concept: The Use of Buoyant Micro-emulsions for DNAPL Remediation. *Journal of Contaminant Hydrology*, 34, 383-397.
- Kuburovic, N., Todorovic, M., Raicevic, V., Orlovic, A., Jovanovic, L., Nikolic, J., Kuburovic, V., Drmanic, S., Solevic, T. (2007) Removal of Methyl Tertiary Butyl Ether from Wastewaters using Photolytic, Photocatalytic and Microbiological Degradation Processes. *Desalination*, 213, 123-128.

- Lambert, J. M., Yang, T., Thomson, N. R., Barker, J. F. (2009) Pulsed Biosparging of a Residual Fuel Source Emplaced at CFB Borden. *International Journal of Soil, Sediment and Water*, 2 (3), Article 6.
- Leal-Bautista, R. M., Lenczewski, M. E. (2006) Sorption of Methyl Tert-butyl Ether and Benzene in Fine-grained Materials from Northern Illinois and the Chalco Basin, Mexico. *Environmental Geosciences*, 13 (1), 31-41.
- Legrini, O., Oliveros, E., Braun, A. M. (1993) Photochemical Processes for Water Treatment. *Chemical Reviews*, 93, 671-698.
- Li Puma, G., Yue, P. L. (2001) A Novel Fountain Photocatalytic Reactor: Model Development and Experimental Validation. *Chemical Engineering Science*, 56, 2733—2744.
- Liao, C.-H., Kang, S.-F., Wu, F.-A. (2001) Hydroxyl Radical Scavenging Role of Chloride and Bicarbonate Ions in the H<sub>2</sub>O<sub>2</sub>/UV Process. *Chemosphere*, 44 (5), 1193-1200.
- Linsebigler, A. L., Lu, G. Q., Yates Jr., J. T. (1995) Photocatalysis on TiO<sub>2</sub> Surfaces: Principles, Mechanisms, and Selected Results. *Chemical Reviews*, 95, 735-758.
- Litter, M. I. (1999) Heterogeneous Photocatalysis: Transition Metal Ions in Photocatalytic Systems. *Applied Catalysis B: Environmental*, 23 (2), 89-114.
- Liu, S.-J., Jiang, B., Huang, G.-Q., Li, X.-G. (2006) Laboratory Column Study for Remediation of MTBE-contaminated Groundwater using a Biological Two-layer Permeable Barrier. *Water Research*, 40, 3401-3408.
- Loveland, J. P., Bhattacharjee, S., Ryan, J. N., Elimelech, M. (2003) Colloid Transport in a Geochemically Heterogeneous Porous Medium: Aquifer Tank Experiment and Modelling. *Journal of Contaminant Hydrology*, 65, 161-182.
- Mackay, D. M., Cherry, J. A. (1989) Groundwater Contamination: Pump-and-Treat Remediation. *Environmental Science & Technology*, 23 (6), 630-636.
- Mackay, D. M., Freyberg, D. L., Roberts, P. V., Cherry, J. A. (1986) A Natural Gradient Experiment on Solute Transport in a Sand Aquifer: 1. Approach and Overview of Plume Movement. *Water Resources Research*, 22 (13), 2017-2029.
- Matthews, R. W. (1989) Photocatalytic Oxidation and Adsorption of Methylene Blue on Thin Films of Near-ultraviolet-illuminated TiO<sub>2</sub>. *Faraday Transactions 1*, 85 (6), 1291-1200.
- Matthews, R. W. (1992) Photocatalytic Oxidation of Organic Contaminants in Water: An Acid to Environmental Preservation. *Pure and Applied Chemistry*, 64 (9) 1285-1290.

- McCarty, P. L., Goltz, M. N., Hopkins, G. D., Dolan, M. E., Allan, J. P., Kawakami, B. T., Carrothers, T. J. (1998) Full-scale Evaluation of In Situ Cometabolic Degradation of Trichloroethylene in Groundwater through Toluene Injection. *Environmental Science & Technology*, 32, 88-100.
- Medina-Valtierra, J., Garcia-Servin, J., Frausto-Reyes, C., Calixto, S. (2006) The Photocatalytic Application and Regeneration of Anatase Thin Films with Embedded Commercial TiO<sub>2</sub> Particles Deposited on Glass Microrods. *Applied Surface Science*, 252 (10), 3600-3608.
- Mehos, M. S., Turchi, C. S. (1993) Field Testing Solar Photocatalytic Detoxification on TCE-contaminated Groundwater. *Environmental Progress*, 12 (3), 194-199.
- Mills, A., Davies, R. H., Worsley, D. (1993) Water Purification by Semiconductor Photocatalysis. *Chemical Society Reviews*, 22 (6), 417-425.
- Mills, A., McFarlane, M. (2007) Current and Possible Future Methods of Assessing the Activities of Photocatalyst Films. *Catalysis Today*, 129, 22-28.
- Minero, C., Pelizzetti, E., Malato, S., Blanco, J. (1996) Large Solar Plant Photocatalytic Water Decontamination: Effect of Operational Parameters. *Solar Energy*, 56 (5), 421-428.
- Moran, M. J., Zogorski, J. S., Squillace, P. J. (2005) MTBE and Gasoline Hydrocarbons in Ground Water of the United States. *Ground Water*, 43 (4), 615-627.
- Mukherjee, P. S., Ray, A. K. (1999) Major Challenges in the Design of a Large-scale Photocatalytic Reactor for Water Treatment. *Chemical Engineering & Technology*, 22 (3), 253-260.
- Odermatt, J. R. (1994) Natural Chromatographic Separation of Benzene, Toluene, Ethylbenzene and Xylenes (BTEX Compounds) in a Gasoline Contaminated Ground Water Aquifer. *Organic Geochemistry*, 21 (10/11), 1141-1150.
- Orlov, A. (2004) Environmental Aspects of Heterogeneous Photocatalysis: Studies with Practical Catalysts and Model Systems. PhD Thesis, University of Cambridge, UK.
- Peill, N. J. (1996) Fiber-Optic Bundled Array Cable Reactors for Heterogenous Photocatalysis and Waste Stream Remediation, PhD Thesis, California Institute of Technology, U. S. A.
- Peill, N. J., Hoffmann, M. R. (1995) Development and Optimization of a TiO<sub>2</sub>-coated Fiber-optic Cable Reactor: Photocatalytic degradation of 4-Chlorophenol. *Environmental Science & Technology*, 29, 2974-2981.

- Peill, N. J., Hoffmann, M. R. (1996) Chemical and Physical Characterization of a TiO<sub>2</sub>-coated Fiber Optic Cable Reactor. *Environmental Science & Technology*, 30, 2806-2812.
- Peill, N. J., Hoffmann, M. R. (2000) TiO<sub>2</sub>-coated Fibre Optic Cable Reactor, US Patent 6051194.
- Preis, S., Krichevskaja, M., Kharchenko, A. (1997) Photocatalytic Oxidation of Aromatic Aminocompounds in Aqueous Solutions and Groundwater from Abandoned Military Bases. *Water Science & Technology*, 35 (4), 265-272.
- Prince, R. C. (2000) Biodegradation of Methyl Tertiary-butyl Ether (MTBE) and Other Fuel Oxygenates. *Critical Reviews in Microbiology*, 26 (3), 168-178.
- Puig-Grajales, L., Tan, N. G., van der Zee, F., Razo-Flores, E., Field, J. A., 2000. Anaerobic Biodegradability of Alkylphenols and Fuel Oxygenates in the Presence of Alternative Electron Acceptors. *Applied Microbiology and Biotechnology*, 54, 692-697.
- Rajeshwar, K., Chenthamarakshan, C. R., Goeringer, S., Djukic, M. (2001) Titania-based Heterogeneous Photocatalysis. Materials, Mechanistic Issues, and Implications for Environmental Remediation. *Pure and Applied Chemistry*, 73 (12), 1849-1860.
- Ray, A. K., Beenackers, A. A. C. M. (1998a) Development of a New Photocatalytic Reactor for Water Purification. *Catalysis Today*, 40, 73-83.
- Ray, A. K., Beenackers, A. A. C. M. (1998b) Novel Photocatalytic Reactor for Water Purification. *AIChE Journal*, 44 (2), 477-483.
- Robert, D., Malato, S. (2002) Solar Photocatalysis: A Clean Process for Water Detoxification. *The Science of the Total Environment*, 291, 85-97.
- Rodriguez, P., Mellie, V., Pallier, S., Sawah, M. A. A. (2009) Deposition and Characterisation of TiO<sub>2</sub> Coatings on Various Supports for Structured (photo)Catalytic Reactors. *Applied Catalysis A: General*, 360 (2), 154-162.
- Rubin, E., Ramaswami, A. (2001) The Potential for Phytoremediation of MTBE. *Water Research*, 35 (5), 1348-1353.
- Ruiz-Aguilar, G. M. L., Fernandez-Sanchez, J. M., Kane, S. R., Kim, D., Alvarez, P. J. J. (2002) Effect of Ethanol and Methyl-tert-butyl Ether on Monoaromatic Hydrocarbon Biodegradation: Response Variability for Different Aquifer Materials under Various Electron-Accepting Conditions. *Environmental Toxicology and Chemistry*, 21 (12), 2631-2639.
- Ryu J. H., Choi, W. Y. (2008) Substrate-specific Photocatalytic Activities of TiO<sub>2</sub> and Multiactivity Test for Water Treatment Application. *Environmental Science & Technology*, 42 (1), 294-300.

- Sahle-Demessie, E., Enriquez, J., Gupta, G. (2002a) Attenuation of Methyl Tert-butyl Ether in Water using Sunlight and a Photocatalyst. *Water Environmental Resources*, 74 (2), 122-130.
- Sahle-Demessie, E., Richardson, T., Almquist, C. B., Pillai, U. R. (2002b) Comparison of Liquid and Gas-phase Photooxidation of MTBE: Synthetic and Field Samples. *Journal of Environmental Engineering*, 128 (9), 782-790.
- Sakka, S. (1994) Preparation and Properties of Sol-gel Coating Films. *Journal of Sol-Gel Science and Technology*, 2, 451-455.
- Saponaro, S., Negri, M., Sezenna, E., Bonomo, L., Sorlini, C. (2009) Groundwater Remediation by an In Situ Biobarrier: A Bench Scale Feasibility Test for Methyl Tert-butyl Ether and Other Gasoline Compounds. *Journal of Hazardous Materials*, 167, 545-552.
- Scalfani, A., Palmisano, L., Davi, E. (1991) Photocatalytic Degradation of Phenol in Aqueous Polycrystalline TiO<sub>2</sub> Dispersions : The Influence of Fe<sup>3+</sup>, Fe<sup>2+</sup> and Ag<sup>+</sup> on the Reaction Rate. *Journal of Photochemistry and Photobiology A: Chemistry*, 56 (1), 113-123.
- Schirmer, M., Butler, B. J., Barker, J. F., Church, C. D., Schirmer, K. (1999) Evaluation of Biodegradation and Dispersion as Natural Attenuation Processes of MTBE and Benzene at the Borden Field Site. *Physics and Chemistry of the Earth B: Hydrology, Oceans and Atmosphere*, 24 (6), 557-560.
- Schmidt, T. C., Bittens, M., Arp, H. P., Haderlein, S. (2003) Transfer Pathways of MTBE into Groundwater: The Role of Diffuse vs. Point Sources. *First European Conference on MTBE*. Dresden University of Technology, Germany. 8-9 September.
- Serpone, N. (2007) Some Remarks on So-called Heterogeneous Photocatalysis and on the Mechanical Application of the Langmuir-Hinshelwood Kinetic Model. *Journal of Advanced Oxidation Technology*, 10(1), 111-115.
- Shang, J., Li, W., Zhu, Y. F. (2003) Structure and Photocatalytic Characteristics of TiO<sub>2</sub> Film Photocatalyst Coated on Stainless Steel Webnet. *Journal of Molecular Catalysis*, 202, 187-195.
- Shih, T., Wangpaichitr, M., Suffet, M. (2003) Evaluation of Granular Activated Carbon Technology for the Removal of Methyl Tertiary Butyl Ether (MTBE) from Drinking Water. *Water Research*, 37, 375-385.
- Singh, M., Salvado-Estivill, I., Li Puma, G. (2007) Radiation Field Optimization in Photocatalytic Monolith Reactors for Air Treatment. *AIChE Journal*, 53 (3), 678-686.

Squillace, P. J., Moran, M. J., Lapham, W. W., Price, C. V., Clawges, R. M., Zogorski, J. S. (1999) Volatile Organic Compounds in Untreated Ambient Groundwater of the United States, 1985–1995. *Environmental Science & Technology*, 33 (23), 4176-4187.

Squillace, P. J., Pankow, J. F., Korte, N. E., Zogorski, J. S. (1996) Environmental Behavior and Fate of Methyl Tert-butyl Ether (MTBE). U. S. Department of the Interior - U. S. Geological Survey – National Water Quality Assessment Program (NAWQA) 1-6.

Su, C., Hong, B.-Y., Tseng, C.-M. (2004) Sol-gel Preparation and Photocatalysis of Titanium Dioxide. *Catalysis Today*, 96, 119-216.

Sutherland, J., Adams, C., Kekobad, J. (2004) Treatment of MTBE by Air Stripping, Carbon Adsorption, and Advanced Oxidation: Technical and Economic Comparison for Five Groundwaters. *Water Research*, 38, 193-205.

Toride, N., Leij, F. J., van Genuchten, M. Th., 1999. The CXTFIT Code for Estimating Transport Parameters from Laboratory or Field Tracer Experiments. US Salinity Laboratory, Research report No. 137.

Turchi, C. S., Ollis, D. F. (1990) Photocatalytic Degradation of Organic Water Contaminants: Mechanisms Involving Hydroxyl Radical Attack. *Journal of Catalysis*, 122 (1), 178-192.

US EPA (2004) Technologies for Treating MtBE and Other Fuel Oxygenates. US EPA/National Service Centre for Environmental Publications (NSCEP), Cincinnati, U. S. A.

Vamathevan, V., Tse, H., Amal, R., Low, G., McEvoy, S. (2001) Effects of Fe<sup>3+</sup> and Ag<sup>+</sup> Ions on the Photocatalytic Degradation of Sucrose in Water. *Catalysis Today*, 68 (1), 201-208.

van Gerven, T., Mul, G., Moulijn, J., Stankiewicz, A. (2007) A Review of Intensification of Photocatalytic Processes. *Chemical Engineering and Processing*, 46 (9), 781-789.

Vella, G., Imoberdorf, G. E., Scalfani, A., Cassano, A. E., Alfano, O. M., Rizzuti, L. (2010) Modeling of a TiO<sub>2</sub>-coated Quartz Wool Packed Bed Photocatalytic Reactor. *Applied Catalysis B: Environmental*, 96 (3-4), 399-407.

Wang, S., Shiraishi, F., Nakano, K. (2002) Decomposition of Formic Acid in a Photocatalytic Reactor with a Parallel Array of Four Light Sources. *Journal of Chemical Technology & Biotechnology*, 77 (7), 805-810.

Wang, X. L., Pehkonen, S. O., Ray, A. K. (2004) Photocatalytic Reduction of Hg (II) on Two Commercial TiO<sub>2</sub> Catalysts. *Electrochimica Acta*, 49 (9-10), 1435-1444.

Warren, E. (2006) In Situ Remediation of Groundwater using Photocatalysis, MEng dissertation, University of Cambridge, UK.

- Watanabe, T., Nakajima, A., Wang, R., Minabe, M., Koizumi, S., Fujishima, A., Hashimoto, K. (1999) Photocatalytic Activity and Photoinduced Hydrophilicity of Titanium Dioxide Coated Glass. *Thin Solid Films*, 351 (1-2), 260-263.
- Xagas, A. P., Androulaki, E., Hiskia, A., Falaras, P. (1999) Preparation, Fractal Surface Morphology and Photocatalytic Properties of TiO<sub>2</sub> Films. *Thin Solid Films*, 357 (2), 173-178.
- Yan, Y. E., Schwartz, F. W. (1999) Oxidative Degradation and Kinetics of Chlorinated Ethylenes by Potassium Permanganate. *Journal of Contaminant Hydrology*, 37, 343-365.
- Yeh, C. K., Novak, J. T. (1995) The Effect of Hydrogen Peroxide on the Degradation of Methyl and Ethyl Tert-Butyl Ether in Soils. *Water Environment Research*, 67 (5), 828-834.
- Yu, J. C., Yu, J., Zhao, J. (2002a) Enhanced Photocatalytic Activity of Mesoporous and Ordinary TiO<sub>2</sub> Thin Films by Sulfuric Acid Treatment. *Applied Catalysis B: Environmental*, 36 (1), 31-43.
- Yu, J. G., Yu, J. C., Ho, W. K., Jiang, Z. T. (2002b) Effects of Calcination Temperature on the Photocatalytic Activity and Photo-induced Super-hydrophilicity of Mesoporous TiO<sub>2</sub> Thin Films. *New Journal of Chemistry*, 26, 607-613.
- Yu, J. G., Zhao, X. J., Zhao, Q. N. (2000) Effect of Surface Structure on Photocatalytic Activity of TiO<sub>2</sub> Thin Films Prepared by Sol-gel Method. *Thin Solid Films*, 379, 7-14.
- Yu, X.-Z., Gu, J.-D. (2006) Uptake, Metabolism, and Toxicity of Methyl Tert-butyl Ether (MTBE) in Weeping Willows. *Journal of Hazardous Material*, 137 (3), 1417-1423.

## List of Publications

Lim, L. L. P., Lynch, R. J., In, S.-I. (2009) Comparison of Simple and Economical Photocatalyst Immobilisation Procedure. *Applied Catalysis A: General*, 365 (2), 214-221.

Lim, L. L. P., Lynch, R. J. (2010a) A Proposed Photocatalytic Reactor Design for In-situ Groundwater Applications. *Applied Catalysis A: General*, 378 (2), 202-210.

Lim, L. L. P., Lynch, R. J. (2010b) In-situ Photocatalytic Attenuation of Organics in Groundwater. *Proceedings of the 11th International UFZ-Deltares/TNO Conference on Management of Soil, Groundwater and Sediment (ConSoil 2010)*, Salzburg Congress, Austria, 22-24 September.